2018-06-13

Conversion of Carbon Dioxide to Fuels using Dispersed Atomic-Size Catalysts

Satish Kumar Iyemperumal
Worcester Polytechnic Institute

Conversion of Carbon Dioxide to Fuels using Dispersed Atomic-Size Catalysts

by

Satish Kumar Iyemperumal

A Dissertation

Submitted to the Faculty of

Worcester Polytechnic Institute

In partial fulfillment of the requirements for the

Degree of Doctor of Philosophy

in

Chemical Engineering

by

June 2018

APPROVED

Dr. N. Aaron Deskins, Advisor Chemical Engineering Department, WPI	Dr. Ravindra Datta, Committee Member Chemical Engineering Department, WPI
Dr. George Kaminski, Committee Member Chemistry and Biochemistry Department, WPI	Dr. Michael Timko, Committee Member Chemical Engineering Department, WPI

Dr. Susan Roberts, Head of Department,
Chemical Engineering Department, WPI

Abstract

Record high CO_2 emissions in the atmosphere and the need to find alternative energy sources to fossil fuels are major global challenges. Conversion of CO_2 into useful fuels like methanol and methane can in principle tackle both these environment and energy concerns. One of the routes to convert CO_2 into useful fuels is by using supported metal catalyst. Specifically, metal atoms or clusters (few atoms large in size) supported on oxide materials are promising catalysts. Experiments have successfully converted CO_2 to products like methanol, using TiO_2 supported Cu atoms or clusters. How this catalyst works and how CO_2 conversion could be improved is an area of much research. We used a quantum mechanical tool called density functional theory (DFT) to obtain atomic and electronic level insights in the CO_2 reduction processes on TiO_2 supported metal atoms and clusters.

We modeled small Cu clusters on TiO_2 surface, which are experimentally synthesizable. Our results show that the interfacial sites in TiO_2 supported Cu are able to activate CO_2 into a bent configuration that can be further reduced. The Cu dimer was found to be the most reactive for CO_2 activation but were unstable catalysts. Following Cu, we also identified other potential metal atoms that can activate CO_2. Compared to expensive and rare elements like Pt, Au, and Ir, we found several early and mid transition metals to be potentially active catalysts for CO_2 reduction. Because the supported metal atom or cluster is a reactive catalyst, under reaction conditions they tend to undergo aggregation and/or oxidation to form larger less active catalysts. We chose Co, Ni, and Cu group elements to study their catalyst stability under oxidizing reaction conditions. Based on the thermodynamics of Cu oxidation and kinetics of O_2 dissociation, we found that TiO_2 supported Cu atom or a larger Cu tetramer cluster were the likely species observed in experiments. Our work provides valuable atomic-level insights into improving the CO_2 reduction activities and predicts potential catalysts for CO_2 reduction to valuable fuels.

Acknowledgements

A lot of people were involved directly or indirectly to make the journey of my PhD as smooth as possible. First and foremost I am very grateful to my advisor Prof. N. Aaron Deskins, whose guidance and support was unparalleled. I am also appreciative of Professors Ravindra Datta, George Kaminski, and Michael Timko for serving in my PhD committee and for their valuable suggestions and help. I would like to thank Prof. Gonghu Li and Tom Fenton from University of New Hamshire for the exciting collaborative research discussions. Professor Randy Paffenroth and Matt Wiess shared their data science expertise in one of my projects, which I also acknowledge.

I am grateful to Lida Namin for all her help and stimulating discussions over the course of my PhD. I also acknowledge valuable discussions with Junbo Chen, Thang Pham, Behnam Partopour, Azadeh Zaker, and Alex Maag. I also acknowledge Dr. Spencer Pruitt's assistance and computational support. Finally and most importantly, I am very grateful to all my family members, who have shown their continued support throughout my life.

Contents

List of Figures

List of Tables

Chapter 1

Introduction

Annual carbon dioxide atmospheric emissions were estimated to reach a new high at 41.6 billion metric tonnes in the year 2017.[1] Such high levels of carbon dioxide in the atmosphere bring risks associated with climate change and eventually human health. Large-scale technologies for carbon capture and storage (CCS) have high costs associated with lowering carbon dioxide concentrations in the environment.[2,3] Complementary technologies for carbon dioxide utilization, such as catalytic conversion of CO_2, direct utilization (e.g. in the food and beverage industry as a carbonating agent), and enhanced oil recovery can be powerful ways to lower the carbon footprint in our environment.[4] Specifically, catalytic conversion can generate valuable chemicals and fuels, such as methane and methanol, through CO_2 reduction. Suitable catalysts that carry out CO_2 reduction in the presence of sunlight (photocatalysis) can enable processes that are clean, green, and renewable.

The challenge of CO_2 photoreduction lies in finding a suitable photocatalyst which can convert CO_2 with high yield and selectivity. Recent papers[5,6] have shown that highly dispersed transition metal atoms or clusters on support materials, such as TiO_2 and Al_2O_3 can be active catalysts for CO_2 reduction to CO, CH_3OH, and CH_4. In Chapter 4, we discuss the CO_2 photoreduction activities of highly dispersed monoatomic Cu supported on TiO_2.

We collaborated with the group of Professor Gonghu Li, who performed experiments on Cu/TiO_2 photocatalysts, while we modeled such catalysts. Using density functional theory (DFT), a molecular modeling technique, we determined that the interfacial sites between Cu and TiO_2 are active sites for activating the CO_2 molecule. The activation of the CO_2 molecule is one of the early and important steps in the complete CO_2 reduction, since activation of CO_2 by one electron reduction is a energetically (redox potential $CO_2 + e^- \longrightarrow CO_2^-$ is -1.90 V vs RHE[7]) very unfavorable. In Chapter 5, we extended our DFT studies to understand CO_2 activation on Cu clusters with 1-4 atoms supported on TiO_2. We found that over all Cu clusters CO_2 was activated. Interestingly, the Cu dimer showed the largest activity for CO_2 activation owing to the unstable nature of Cu dimer, indicating a possible very active photocatalyst. In the subsequent Chapter 6, we screened potential photocatalysts for CO_2 reduction by modeling metal atoms adsorbed on TiO_2. We considered 29 transition metal and 8 post transition metal adatoms supported on TiO_2. Of all the catalysts, early transition metals activated CO_2 the largest indicating potential new catalysts, and explaining important trends in atomic catalysts.

Often during catalyst synthesis or under reaction conditions, oxidizing agents such as oxygen or water are present. Unless the reaction is controlled to eliminate oxidation reactions,[5] the supported metal catalyst may undergo oxidation. In Chapter 7, we study the role of reaction environment (such as oxygen and water) on the oxidation of TiO_2-supported late transition metal catalysts (Co, Ni, and Cu groups in the periodic table). For Cu/TiO_2 catalysts, we find that the thermodynamics of the oxidation by molecular oxygens is favorable. However, the availability of oxygen atoms through dissociation of O_2 limits the full oxidation of the supported Cu atom/cluster. We find that Cu clusters readily dissociate O_2, while lone Cu atoms cannot dissociate O_2. The kinetics of O_2 dissociation may thus lead to Cu^{1+} not Cu^{2+} being the dominant Cu species. In the final Chapter 8, is a summary of all the findings from the aforementioned projects.

Bibliography

[1] G. P. Peters, C. Le Quéré, R. M. Andrew, J. G. Canadell, P. Friedlingstein, T. Ilyina, R. B. Jackson, F. Joos, J. I. Korsbakken, G. A. McKinley, S. Sitch and P. Tans, *Nature Climate Change*, 2017, **7**, 848–850.

[2] J. C. Bergstrom and D. Ty, in *Recent Advances in Carbon Capture and Storage*, InTech, 2017, vol. 6, pp. 111–133.

[3] P. Psarras, H. Krutka, M. Fajardy, Z. Zhang, S. Liguori, N. M. Dowell and J. Wilcox, *Wiley Interdisciplinary Reviews: Energy and Environment*, 2017, **6**, 1–21.

[4] R. M. Cuéllar-Franca and A. Azapagic, *Journal of CO2 Utilization*, 2015, **9**, 82–102.

[5] C. Liu, B. Yang, E. Tyo, S. Seifert, J. DeBartolo, B. von Issendorff, P. Zapol, S. Vajda and L. A. Curtiss, *Journal of the American Chemical Society*, 2015, **137**, 8676–8679.

[6] J. H. Kwak, L. Kovarik and J. Szanyi, *ACS Catalysis*, 2013, **3**, 2094–2100.

[7] S. N. Habisreutinger, L. Schmidt-Mende and J. K. Stolarczyk, *Angewandte Chemie - International Edition*, 2013, **52**, 7372–7408.

Chapter 2

Background

2.1 Carbon dioxide conversion

Continued increasing levels of CO_2 in the atmosphere have dangerous global implications in terms of climate change and ocean acidification. Annual CO_2 emissions have been estimated to reach 41.6 billion metric tonnes in the year 2017.[1] A major portion of these emissions are from human-based industrial activities that contribute to ever-increasing levels of CO_2 in the atmosphere. Global emissions of CO_2 by burning coal and fossil fuels have reached 36.8 billion metric tonnes in 2017 (or 88.5% of total emissions).[1] The emitted CO_2 resides in any of three carbon sinks, including the atmosphere (45 %), land (30 %), or ocean (25 %). The high CO_2 emissions could result in harmful consequences to the environment and agriculture in terms of poor air and food quality which can have direct implications on human, plant, and animal life.

One of the common strategies to reduce CO_2 levels is through carbon capture and storage (or sequestration). However, current levels of CO_2 production are more than 150 times higher than the sum of current sequestration capacity and CO_2 utilization efforts.[2] Wilcox and coworkers have also reported several studies indicating the difficulties in carbon capture and

storage technologies.[3,4] For instance, CO_2 capture from low CO_2 concentration streams (such as air) is energy-intensive, suffers from low purity of the captured CO_2, and is economically expensive when compared to high concentration streams (such as exhaust of coal fired plant). Therefore, other technologies such as catalytic conversion of CO_2 to useful fuels can be valuable for utilizing and removing excess amounts of CO_2.

2.2 Heterogeneous catalysis of CO_2 to fuels

CO_2 reduction is a process of converting CO_2 to products such as CH_3OH and CH_4, often with a suitable source of H (H_2 or H_2O for instance). In the process of CO_2 (O=C=O) reduction to CH_4 or CH_3OH, two C=O bonds need to be cleaved and several C-H, C-O bonds, and O-H bonds need to be formed. Since CO_2 is stable closed-shell molecule, the energy required to cleave the bonds in CO_2 is very large. The other big challenge in CO_2 is to selectively cleave and form necessary bonds during CO_2 reduction such that the selectivity towards the desired products like CH_4 or CH_3OH is high. For instance, once C-O bonds are cleaved in CO_2, C-H, C-O, or O-H bonds may need to be formed to produce CH_4 or CH_3OH. A suitable catalyst which lowers the energetic costs for the reduction reaction and provides selectivity forms the basis for an ideal CO_2 reduction catalyst. Heterogeneous catalysts are especially attractive owing to the ease of separation of heterogeneous catalysts from reaction products (unlike the case of homogeneous catalysis).

Some common routes to reduce CO_2 to valuable chemicals and fuels are through thermal catalysis, electrocatalysis, and photocatalysis. In conventional thermal catalysis, elevated temperatures act as the driving force for the catalytic reactions. The thermal energy provides the energy required to break or form necessary bonds for the reduction of CO_2 to useful fuels. Electrocatalytic conversion of CO_2 to fuels has been also widely studied.[5] Here a set of metal electrodes in contact with a liquid electrolyte forms a cell. An external source of current

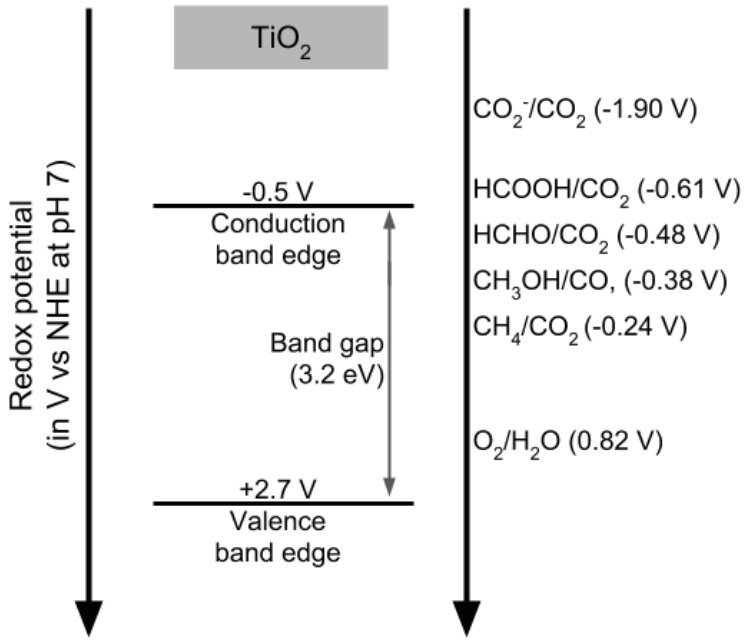

Figure 2.1: The redox potentials of several molecules, as well as the conduction band minimum and valence band maximum energy levels of TiO_2. Redox potential in parenthesis are given for CO_2 reduction products at pH 7 with reference to normal hydrogen electrode (NHE). The redox potentials are not drawn to scale.Figure adapted from Ref. [12]

drives the CO_2 electrochemical reduction at the surface of metal electrodes. In the case of photocatalysis, photons from sunlight act as the driving force for generating electron-hole pairs in a semiconductor, which participates in the redox chemistry of CO_2 reduction. Photocatalysis has an advantage over thermal catalysis, because typically photocatalysis occurs at room temperatures[6] which eliminates the requirement for external energy sources. CO_2 photocatalysis is also renewable and clean due to the the use of sunlight. One of the prototypical and widely used photocatalysts is titanium dioxide (TiO_2), which is used for various applications, such as self-cleaning surfaces, water purification, air purification, and transparent conducting oxides.[7] TiO_2 gained significant attention after Fujishima and Honda reported the electrochemical photolysis of water using TiO_2.[8] TiO_2 is also inexpensive, chemically stable, and non-toxic.[9–11]

CO_2 reduction using photocatalysts such as TiO_2 is a complicated reaction due to the

possibility of a variety of intermediates and products, depending upon the number of electrons and/or holes that participate in reduction of CO_2. Shown in Equations 2.2 - 2.7 are different possible CO_2 reduction products. Figure 2.1 shows the redox potentials of CO_2 reduction products compared to the corresponding conduction band minimum and valence band maximum energy levels of TiO_2. The redox potential indicates the tendency of a species to be reduced or oxidized. A large negative redox potential indicates a low tendency of the species to be reduced since electrons must have high energy (negative potential) to reduce the molecule. Electrons from a semiconductor may transfer from the conduction band to the appropriate redox potential to reduce the molecule on the semiconductor's surface. Equation 2.2, the one electron reduction of CO_2 to form a CO_2- anion, has a very high reduction potential of -1.90 V, which is much more negative than the conduction band minimum energy level of several different semiconductors. This indicates that the formation of CO_2- is an energetically unfavorable process since the electron must move energetically uphill from an excited conduction band state to transfer to CO_2. On the contrary however, the other reduction products in Equation 2.3- 2.7 have reduction potentials in the range of -0.61 V to -0.21 V, which are closer to the conduction band minimum energy level of TiO_2. This shows that the latter products are much easier to form thermodynamically compared to the single electron reduction of CO_2 to CO_2-.[12]

$$CO_2 + e^- \longrightarrow CO_2^- \tag{2.1}$$

$$CO_2 + 2H^+ + 2e^- \longrightarrow HCOOH \tag{2.2}$$

$$CO_2 + 2H^+ + 2e^- \longrightarrow CO + H_2O \tag{2.3}$$

$$CO_2 + 4H^+ + 4e^- \longrightarrow HCHO + H_2O \tag{2.4}$$

$$CO_2 + 6H^+ + 6e^- \longrightarrow CH_3OH + H_2O \tag{2.5}$$

$$CO_2 + 8H^+ + 8e^- \longrightarrow CH_4 + 2H_2O \tag{2.6}$$

$$2H^+ + 2e^- \longrightarrow H_2 \tag{2.7}$$

For a complete redox cycle, reduction and oxidation must occur. The other half of the CO_2 reduction catalytic cycle is the oxidation of water by photogenerated holes. Oxidation of water to generate O_2 as per Equation 2.8 is thermodynamically favorable on TiO_2, since the valence band maximum lies more positive (lower) in energy than the redox potential of water at 0.82 V.[12] Holes tend to move to more negative potentials, or from the semiconductor valence band edges to oxidize water. Although thermodynamically favorable, the requirement of 4 holes per O_2 produced during oxidation of water makes the water oxidation process also challenging,[13] similar to CO_2 reduction process. This dissertation focuses on the CO_2 reduction reaction, rather than both CO_2 reduction and water oxidation.

$$2H_2O + 4h^+ \longrightarrow O_2 + 4H^+ \tag{2.8}$$

2.3 TiO_2 Photocatalysts

TiO_2 has three common polymorphs, namely rutile, anatase, and brookite. The popular commercially-used Degussa P25 consists of primarily anatase (70 %) and 30 % rutile.

Anatase is the more stable and typically catalytically active polymorph of TiO_2 for nanoparticles below $\sim$ 14 nm.[14] Several aspects, such as polymorph choice, types of exposed surface facets, and defects in TiO_2 have been studied for CO_2 photoreduction.[15–18] For instance on pure TiO_2-based catalysts low photoreduction and quantum yields (of $\sim$ 55 μmol/g and 0.31 % respectively) for CO_2 reduction to CO, CH_3OH, and CH_4 have been reported.[17,19] The CO_2 reduction product yields and selectivity control of the products are very low[17,20] for commercial applications, which underscores the need for more work in this area.

Modifying pristine TiO_2 by addition of metal atoms, clusters, or nanoparticles has shown improved catalytic activities for CO_2 reduction with relatively high yields and efficiencies compared to pristine TiO_2.[15] Several interesting aspects of these oxide-supported metal catalysts could lead to increased CO_2 reduction activity. One possible explanation is that the presence of a co-catalyst with the TiO_2 (such as Pt, Au, Pd, or Cu) resulting in lowering electron hole recombination.[10,15] Recombination is a dominant phenomenon in photocatalysis (and photovoltaics), where a photogenerated electron combines with photogenerated hole to generate heat or radiation instead of participating in the catalytic reaction. Thus less recombination can improve the photocatalytic performance. The strong metal-support interactions could also stabilize metal clusters of various sizes on the support which could expose under-coordinated metal atoms, which are also correlated with improved catalytic activities.[21] In the case of CO_2 reduction, Cu is one of the most promising and inexpensive cocatalysts on TiO_2.[5,22–27] Cu/TiO_2 has been found to reduce CO_2 to CO and methane with similar activity compared to precious metals such as Au or Pt.[28,29]

2.4 Atomically Dispersed supported metal catalysts for CO_2 reduction

Supported metal catalysts are widely used for catalytic applications such as Fischer-tropsch reactions, three-way catalyst for CO oxidation in automobile exhaust, methanol production from syngas, and several other redox reactions.[30–33] Supported metal particles conventionally span few to hundreds of nanometers in size. These larger nanoparticles contain a large number of atoms, where most of the catalysis occurs on the surface, edge, or corners atoms of these nanoparticles. Most of the bulk atoms within such nanoparticles are not utilized for catalysis, which is inefficient and could waste expensive catalysts. The fraction of active sites in such a nanoparticle is small. The maximum achievable limit of the fraction of active sites becomes one when supported single atoms are used instead of nanoparticles. Depending upon the distribution of single atoms on the support, the catalysts can be termed either atomically dispersed supported metal catalyst (ADSMC) or a single atom catalyst (SAC). An ADSMC consists of monomers along with other larger clusters such as dimers, trimers, clusters, etc. while a SAC contains only monomers on the support (see schematic in Figure 2.2).[34–36]

ADSMC and SAC are reactive in nature and they tend to aggregate to form larger clusters or nanoparticles. In order to stabilize these atomically dispersed metal atoms, several strategies have been reported in the literature, such as lowering the metal loading, increasing the interactions with the support, or utilizing reactive defect sites such as oxygen vacancies in oxides. Flytzani-Stephanopolous and coworkers have reported the important role surface oxygen atoms to stabilize atomically dispersed catalysts through metal-oxygen linkages.[37] Although, low metal loading is beneficial to stabilize atomically dispersed catalysts, Liu et al.[38] reported a photochemical approach for increasing the metal loading (from a typical $\sim$0.5 % to 1.5 %) in Pd_1/TiO_2 with minimal metal aggregation. Pd1Cl2/TiO_2 can be easily prepared by wet chemistry synthesis where a metal precursor (H_2PdCl_4) reacts with TiO_2

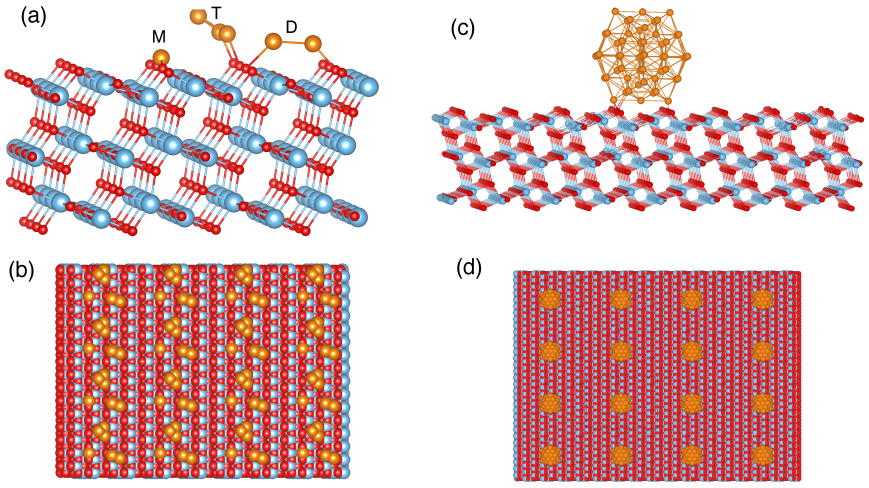

Figure 2.2: Schematic of dispersed atomic-size Cu (a,b) and a representative nanoparticle of of 1nm size containing 55 Cu atoms (c,d) deposited on TiO_2. Side view with a ball and stick model (a, c) and top view with periodically repeated space filling model (b,d) of Cu/TiO_2 catalysts. (a,b) represent dispersed atomic-size catalysts showing monomers (M), dimers (D), and trimers (T). Ti, O, and Cu are shown in blue, red, and gold spheres, respectively.

dispersed in water. Liu et al.[38] reported that the $Pd_1Cl_2 \longrightarrow Pd_1$ species formation can easily occur under UV light irradiation.

There are several examples in literature where atomically dispersed supported metal catalysts have demonstrated high catalytic activities for a variety of reactions such as CO oxidation, CO_2 reduction, water gas shift, H_2 evolution, and dehydrogenation reactions.[21,33,34,36,39–45] Several techniques have been used to synthesize atomically dispersed supported metal catalysts. (i) Mass/size selected soft-landing of metal clusters. Here, a magnetron sputtering source forms ion clusters from a gas phase metal cluster, which is passed through a mass selection filter and finally deposited on support materials. The technique is called soft-landing as the deposition energy of clusters are <0.2 eV per atom.[39] (ii) Leaching of metals from nanoparticles. This technique by Flytzani-Stephanopolous and coworkers uses cyanide-based solutions to leach out atoms from larger clusters or nanoparticles to form atomically dispersed metal atoms on the support. (iii) Solution deposition of metals. In our previous work we reported on the simple redox chemistry between Sn and Cu (Sn^{2+} +

$Cu^{2+} \longrightarrow Cu + Sn^{4+}$), where the Sn^{2+} was on a TiO_2 support. The Cu was exchanged with the Sn to produce highly dispersed on TiO_2.[22] Other techniques use solutions with metal cations to deposit metals on support. See Ref[34,46] for other synthesis techniques.

CO_2 reduction has been studied by several research groups using atomically dispersed supported metal catalysts. Liu et al.[47] showed that Cu_4 clusters on amorphous Al_2O_3 exhibited high activities for CO_2 reduction to methanol. They attributed the large activity to the presence of metallic Cu species present on the support. Similarly, CO_2 reduction to methanol was reported by them in another work where they studied size dependent CO_2 reduction using Cu_n/Al_2O_3 (n=3,4,20) catalysts.[48] They found Cu_4 to show the best CO_2 reduction activity. Kwak et al.[45] and Matsubu et al.[43] have reported the reduction of CO_2 to CO using atomically dispersed Pd on Al_2O_3 and Rh on TiO_2, respectively. The catalytic effect of interfacial sites or undercoordinated supported metal clusters using theoretical techniques such as density functional theory (DFT) has also been reported for CO_2 activation, dissocation, and hydrogenation on supported metal clusters such as Pt, Ag, Ni, Cu, Cu, Co, and Rh.[48–54] Atomically dispersed supported metal catalysts have had a surge of interest in other catalytic reactions such as CO oxidation, hydrogenation, and water gas shift.[33,37,40,41,44,55–57] It should be noted that a lot of work focuses on depositing late transition metal atoms on a support. As we will show in Chapter 6, early or mid transition metal atoms (which are also abundant and inexpensive) can also be catalytically active atomically dispersed supported metal catalysts.

Theoretical techniques such as DFT are essential for better understanding the metal-support interactions that determine how atomic/cluster species may diffuse and aggregate to form larger nanoparticles (thereby lowering the activity per metal atom). Alghannam et al. studied the diffusion of metal atoms on TiO_2 surface.[58] They reported that the activation barrier for adatoms in this order: Au < Ag < Cu < Pt < Rh < Ni < Co < Fe. These results suggest that the late transition metal adatoms can diffuse over the TiO_2 surface more than

the earlier transition metal atoms. Several other papers report the growth mechanisms from single atom catalysts to metallic clusters of larger sizes on TiO_2 anatase(101).[59–68] For instance, strong adsorption energies of Ag_n and Pt_n were reported for $n > 3$ and 1 respectively, which was reported to result in less tendency of these clusters to sinter and form larger clusters (range of n studied was ≤ 8).[59]

2.5 Reaction conditions and stability of atomically dispersed supported metal catalysts

Atomically dispersed supported metal catalysts have high chemical potential[69] such that there is a large tendency of these atomic-size species to aggregate or react with molecules under reaction/synthesis conditions. Typical synthesis and/or reaction conditions of atomically dispersed supported metal catalysts often result in oxidized metal species on support due to the presence of O_2 or H_2O. Depending upon the reaction environment the atomically dispersed supported metal catalysts may also undergo reduction due to the presence/treatment with H_2 as has been shown previously for supported metal nanoparticles[6] and supported metal clusters.[47] Several authors showed that depending upon the reaction conditions and reaction environment, both metallic and oxidized states of atomically dispersed species can exist and be responsible for high catalytic activity.[22,33,41,43,47,70]

Oxidized atomically dispersed supported Pt catalysts have been reported to be more active than metallic species for CO oxidation.[33,41,57] Oxidized silver trimers on alumina were also reported to be catalytically active for propylene epoxidation.[71] Single Pt atoms at high loading (1 wt%) were reported to be stabilized by Pt-O bonds in a square planar geometry on a phosphomolybdic acid modified carbon support.[72] Such a Pt-O geometry resulted in Pt being positively charged and exhibited good activity for nitrobenzene and cyclohexanone hydrogenation. In contrast, for CO_2 reduction the active state of Cu tetramer supported

on alumina was reported to be a metallic state.[47] Based on these studies and also other literature work by the groups of Stefan Vajda, Flytzani-Stephanopolous, Abhaya Datye, Phillip Christopher, Scott Anderson, Gonghu Li and others, different reaction synthesis techniques, operating reaction conditions, size of supported atom/cluster, type of support material, and the catalytic reaction under investigation can all contribute to the active site being either metallic or oxidized. With the potential high activity of atomically dispersed supported metal catalysts for various catalytic reactions, it is quite important to understand the role of oxidation state of adsorbed metal atoms or clusters on stability and reactivity.

Bibliography

[1] G. P. Peters, C. Le Quéré, R. M. Andrew, J. G. Canadell, P. Friedlingstein, T. Ilyina, R. B. Jackson, F. Joos, J. I. Korsbakken, G. A. McKinley, S. Sitch and P. Tans, *Nature Climate Change*, 2017, **7**, 848–850.

[2] Y. A. Daza and J. N. Kuhn, *RSC Advances*, 2016, **6**, 49675–49691.

[3] J. Wilcox, P. C. Psarras and S. Liguori, *Environmental Research Letters*, 2017, **12**, 065001.

[4] K. Z. House, A. C. Baclig, M. Ranjan, E. A. van Nierop, J. Wilcox and H. J. Herzog, *Proceedings of the National Academy of Sciences*, 2011, **108**, 20428–20433.

[5] J. L. White, M. F. Baruch, J. E. Pander, Y. Hu, I. C. Fortmeyer, J. E. Park, T. Zhang, K. Liao, J. Gu, Y. Yan, T. W. Shaw, E. Abelev and A. B. Bocarsly, *Chemical Reviews*, 2015, **115**, 12888–12935.

[6] B.-R. Chen, V.-H. Nguyen, J. C. S. Wu, R. Martin and K. Kočí, *Physical chemistry chemical physics : PCCP*, 2016, **18**, 4942–51.

[7] A. Fujishima, X. Zhang and D. A. Tryk, *Surface Science Reports*, 2008, **63**, 515–582.

[8] A. Fujishima and K. Honda, *Nature*, 1972, **238**, 37.

[9] J. Schneider, M. Matsuoka, M. Takeuchi, J. Zhang, Y. Horiuchi, M. Anpo and D. W. Bahnemann, *Chem. Rev.*, 2014, **114**, 9919–9986.

[10] A. L. Linsebigler, G. Lu and J. T. Yates, *Chemical Reviews*, 1995, **95**, 735–758.

[11] L. E. Oi, M.-Y. Choo, H. V. Lee, H. C. Ong, S. B. A. Hamid and J. C. Juan, *RSC Adv.*, 2016, **6**, 108741–108754.

[12] S. N. Habisreutinger, L. Schmidt-Mende and J. K. Stolarczyk, *Angewandte Chemie - International Edition*, 2013, **52**, 7372–7408.

[13] Á. Valdés, Z.-W. Qu, G.-J. Kroes, J. Rossmeisl and J. K. Nørskov, *The Journal of Physical Chemistry C*, 2008, **112**, 9872–9879.

[14] H. Zhang and J. F. Banfield, *Journal of Materials Chemistry*, 1998, **8**, 2073–2076.

[15] Y. Ma, X. L. Wang, Y. S. Jia, X. B. Chen, H. X. Han and C. Li, *Chemical Reviews*, 2014, **114**, 9987–10043.

[16] M. M. Rodriguez, X. Peng, L. Liu, Y. Li and J. M. Andino, *The Journal of Physical Chemistry C*, 2012, **116**, 19755–19764.

[17] L. Liu, Y. Jiang, H. Zhao, J. Chen, J. Cheng, K. Yang and Y. Li, *ACS Catalysis*, 2016, **6**, 1097–1108.

[18] L. Liu, H. Zhao, J. M. Andino and Y. Li, *ACS Catalysis*, 2012, **2**, 1817–1828.

[19] H. Zhao, F. Pan and Y. Li, *Journal of Materiomics*, 2017, **3**, 17–32.

[20] S. Kattel, P. Liu and J. G. Chen, *Journal of the American Chemical Society*, 2017, **139**, 9739–9754.

[21] S. Vajda, M. J. Pellin, J. P. Greeley, C. L. Marshall, L. a. Curtiss, G. a. Ballentine, J. W. Elam, S. Catillon-Mucherie, P. C. Redfern, F. Mehmood and P. Zapol, *Nature materials*, 2009, **8**, 213–216.

[22] C. Liu, S. K. Iyemperumal, N. A. Deskins and G. Li, *Journal of Photonics for Energy*, 2016, **7**, 012004.

[23] L. Liu, F. Gao, H. Zhao and Y. Li, *Applied Catalysis B: Environmental*, 2013, **134-135**, 349–358.

[24] M. Anpo, H. Yamashita, Y. Ichihashi and S. Ehara, *Journal of Electroanalytical Chemistry*, 1995, **396**, 21–26.

[25] I. H. Tseng, J. C. S. Wu and H. Y. Chou, *Journal of Catalysis*, 2004, **221**, 432–440.

[26] Slamet, H. Nasution, E. Purnama, S. Kosela and J. Gunlazuardi, *Catalysis Communications*, 2005, **6**, 313–319.

[27] L. Liu, C. Zhao and Y. Li, *Journal of Physical Chemistry C*, 2012, **116**, 7904–7912.

[28] O. K. Varghese, M. Paulose, T. J. LaTempa and C. A. Grimes, *Nano Letters*, 2009, **9**, 731–737.

[29] S. Neatu, J. A. Maciá-Agulló, P. Concepción and H. Garcia, *Journal of the American Chemical Society*, 2014, **136**, 15969–15976.

[30] J. Shi, *Chem. Rev.*, 2013, **113**, 2139–2181.

[31] M. Behrens, F. Studt, I. Kasatkin, S. Kuhl, M. Havecker, F. Abild-Pedersen, S. Zander, F. Girgsdies, P. Kurr, B.-L. Kniep, M. Tovar, R. W. Fischer, J. K. Norskov and R. Schlogl, *Science*, 2012, **336**, 893–897.

[32] Q. L. Tang and Z. P. Liu, *J. Phys. Chem. C*, 2010, **114**, 8423–8430.

[33] J. Jones, H. Xiong, A. T. DeLaRiva, E. J. Peterson, H. Pham, S. R. Challa, G. Qi, S. Oh, M. H. Wiebenga, X. I. Pereira Hernandez, Y. Wang and A. K. Datye, *Science*, 2016, **353**, 150–154.

[34] J. Liu, *ACS Catalysis*, 2017, **7**, 34–59.

[35] B. C. Gates, M. Flytzani-Stephanopoulos, D. A. Dixon and A. Katz, *Catal. Sci. Technol.*, 2017, **7**, 4259–4275.

[36] X. F. Yang, A. Wang, B. Qiao, J. Li, J. Liu and T. Zhang, *Accounts of Chemical Research*, 2013, **46**, 1740–1748.

[37] M. Yang and M. Flytzani-Stephanopoulos, *Catalysis Today*, 2017, **298**, 216–225.

[38] P. Liu, Y. Zhao, R. Qin, S. Mo, G. Chen, L. Gu, D. M. Chevrier, P. Zhang, Q. Guo, D. Zang, B. Wu, G. Fu and N. Zheng, *Science*, 2016, **352**, 797–800.

[39] S. Vajda and M. G. White, *ACS Catalysis*, 2015, **5**, 7152–7176.

[40] W. E. Kaden, T. Wu, W. A. Kunkel and S. L. Anderson, *Science*, 2009, **326**, 826–829.

[41] B. Qiao, A. Wang, X. Yang, L. F. Allard, Z. Jiang, Y. Cui, J. Liu, J. Li and T. Zhang, *Nature chemistry*, 2011, **3**, 634–641.

[42] M. Yang, L. F. Allard and M. Flytzani-Stephanopoulos, *Journal of the American Chemical Society*, 2013, **135**, 3768–3771.

[43] J. C. Matsubu, V. N. Yang and P. Christopher, *Journal of the American Chemical Society*, 2015, **137**, 3076–3084.

[44] L. DeRita, S. Dai, K. Lopez-Zepeda, N. Pham, G. W. Graham, X. Pan and P. Christopher, *Journal of the American Chemical Society*, 2017, **139**, 14150–14165.

[45] J. H. Kwak, L. Kovarik and J. Szanyi, *ACS Catalysis*, 2013, **3**, 2094–2100.

[46] T. Y. Chang, Y. Tanaka, R. Ishikawa, K. Toyoura, K. Matsunaga, Y. Ikuhara and N. Shibata, *Nano Letters*, 2014, **14**, 134–138.

[47] C. Liu, B. Yang, E. Tyo, S. Seifert, J. DeBartolo, B. von Issendorff, P. Zapol, S. Vajda and L. A. Curtiss, *Journal of the American Chemical Society*, 2015, **137**, 8676–8679.

[48] B. Yang, C. Liu, A. Halder, E. C. Tyo, A. B. F. Martinson, S. Seifert, P. Zapol, L. A. Curtiss and S. Vajda, *The Journal of Physical Chemistry C*, 2017, **121**, 10406–10412.

[49] C.-T. Yang, B. C. Wood, V. R. Bhethanabotla and B. Joseph, *J. Phys. Chem. C*, 2014, **118**, 26236–26248.

[50] C.-T. Yang, B. C. Wood, V. R. Bhethanabotla and B. Joseph, *Phys. Chem. Chem. Phys.*, 2015, **17**, 25379–25392.

[51] P. Schlexer, H.-Y. T. Chen and G. Pacchioni, *Catalysis Letters*, 2017, **147**, 1871–1881.

[52] L. Liu, Z. Liu, H. Sun and X. Zhao, *Applied Surface Science*, 2017, **399**, 469–479.

[53] T. Billo, F.-Y. Fu, P. Raghunath, I. Shown, W.-F. Chen, H.-T. Lien, T.-H. Shen, J.-F. Lee, T.-S. Chan, K.-Y. Huang, C.-I. Wu, M. C. Lin, J.-S. Hwang, C.-H. Lee, L.-C. Chen and K.-H. Chen, *Small*, 2018, **14**, 1702928.

[54] S. Ma, W. Song, B. Liu, H. Zheng, J. Deng, W. Zhong, J. Liu, X.-Q. Gong and Z. Zhao, *Catal. Sci. Technol.*, 2016, **6**, 6128–6136.

[55] G. Spezzati, Y.-Q. Su, J. P. Hofmann, A. D. Benavidez, A. T. DeLaRiva, J. McCabe, A. K. Datye and E. J. M. Hensen, *ACS Catalysis*, 2017, **7**, 6887–6891.

[56] Q. Fu, H. Saltsburg and M. Flytzani-Stephanopoulos, *Science*, 2003, **301**, 935–938.

[57] M. Moses-Debusk, M. Yoon, L. F. Allard, D. R. Mullins, Z. Wu, X. Yang, G. Veith, G. M. Stocks and C. K. Narula, *Journal of the American Chemical Society*, 2013, **135**, 12634–12645.

[58] A. Alghannam, C. L. Muhich and C. Musgrave, *Phys. Chem. Chem. Phys.*, 2017, **19**, 4541–4552.

[59] C. T. Yang, N. Balakrishnan, V. R. Bhethanabotla and B. Joseph, *J. Phys. Chem. C*, 2014, **118**, 4702–4714.

[60] H. Wang, T. An and A. Selloni, *J. Chem. Phys.*, 2017, **146**, 184703.

[61] J. Zhang, M. Zhang, Y. Han, W. Li, X. Meng and B. Zong, *The Journal of Physical Chemistry C*, 2008, **112**, 19506–19515.

[62] S.-t. Zhang, C.-m. Li, H. Yan, M. Wei, D. G. Evans and X. Duan, *The Journal of Physical Chemistry C*, 2014, **2**, 140211062045005.

[63] Y. Yan, Y. Yu, S. Huang, Y. Yang, X. Yang, S. Yin and Y. Cao, *The Journal of Physical Chemistry C*, 2017, **121**, 1089–1098.

[64] A. R. Puigdollers, P. Schlexer and G. Pacchioni, *The Journal of Physical Chemistry C*, 2015, **119**, 15381–15389.

[65] A. Vittadini, M. Casarin and A. Selloni, *Theoretical Chemistry Accounts*, 2007, **117**, 663–671.

[66] Y. Zhou, C. L. Muhich, B. T. Neltner, A. W. Weimer and C. B. Musgrave, *Journal of Physical Chemistry C*, 2012, **116**, 12114–12123.

[67] X.-q. Gong, A. Selloni, O. Dulub, P. Jacobson and U. Diebold, *Journal of the American Chemical Society*, 2008, **130**, 370–381.

[68] Y. Han, C. J. Liu and Q. Ge, *Journal of Physical Chemistry B*, 2006, **110**, 7463–7472.

[69] C. T. Campbell and Z. Mao, *ACS Catalysis*, 2017, **7**, 8460–8466.

[70] F. Dvoák, M. Farnesi Camellone, A. Tovt, N.-D. Tran, F. R. Negreiros, M. Vorokhta, T. Skála, I. Matolínová, J. Mysliveček, V. Matolín and S. Fabris, *Nature Communications*, 2016, **7**, 10801.

[71] Y. Lei, F. Mehmood, S. Lee, J. Greeley, B. Lee, S. Seifert, R. E. Winans, J. W. Elam, R. J. Meyer, P. C. Redfern, D. Teschner, R. Schlogl, M. J. Pellin, L. A. Curtiss and S. Vajda, *Science*, 2010, **328**, 224–228.

[72] B. Zhang, H. Asakura, J. Zhang, J. Zhang, S. De and N. Yan, *Angewandte Chemie - International Edition*, 2016, **55**, 8319–8323.

Chapter 3

Theoretical Background

3.1 Schrödinger's equation

The interactions between atomic and sub-atomic particles as well as other corresponding phenomena can be explained by the laws of quantum mechanics. The fundamental equation governing quantum mechanics was put forward in 1926 by Erwin Schrödinger. It consists of the Hamiltonian operator $\hat{\mathrm{H}}$, electronic wavefunction ψ, and the energy E corresponding to the system described in the Hamiltonian (equation 3.1). The Schrödinger equation is an eigenproblem, where E is the eigenvalue and ψ_{i} is the eigenvector. The wavefunction, ψ_{i}, is a function that describes the system of study and in principle can be used to derive properties of the system. For describing atoms, molecules, and solids, $\hat{\mathrm{H}}$ consists of the potential and kinetic energy contributions of electrons and nuclei (equation 3.2). The $\hat{\mathrm{H}}$ thus contains, in order, the kinetic energy of electrons, kinetic energy of nuclei, the potential energy of all electrons interacting with nuclei, the potential energy of all nuclear-nuclear interactions, and the potential energy corresponding to all electron-electron interaction. Here i,j runs over n electron system, while k and l runs over M nuclei system. This equation is reduced to a relatively simpler equation 3.3 using the Born-Oppenheimer approximation. This approxi-

mation is based on the fact that the electronic mass is much lighter (by at least 1800 times) than the mass of a proton or neutron in a nucleus. This allows the simplification of the Hamiltonian, $\hat{\mathrm{H}}$, to only consider the electronic interactions and electronic kinetic energy, while the nuclei are kept fixed during the solution of Schrödinger's equation in Equation 3.3. Note that application of Born-Oppenheimer approximation results in the second term in Equation 3.3 consisting of only the kinetic energy of electrons, electron-electron interactions, and electron-nuclear interactions.

$$\hat{\mathrm{H}}\psi = \mathrm{E}\psi \tag{3.1}$$

$$\Big[-\sum_{\mathrm{i}}^{\mathrm{n}} \frac{\hbar^2}{2\mathrm{m}} \nabla_{\mathrm{i}}^2 - \sum_{\mathrm{k}}^{\mathrm{M}} \frac{\hbar^2}{2\mathrm{M_k}} \nabla_{\mathrm{k}}^2 - \sum_{\mathrm{i}}^{\mathrm{n}} \sum_{\mathrm{k}}^{\mathrm{M}} \mathrm{V}(\mathrm{r_{ik}}) + \sum_{\mathrm{k}}^{\mathrm{M}} \sum_{\mathrm{l}\neq\mathrm{k}} \mathrm{V}(\mathrm{r_k}, \mathrm{r_l}) + \sum_{\mathrm{i}}^{\mathrm{n}} \sum_{\mathrm{j}\neq\mathrm{i}} \mathrm{V}(\mathrm{r_i}, \mathrm{r_j}) \Big] \psi = \mathrm{E}\psi \tag{3.2}$$

$$\Big[-\sum_{\mathrm{i}}^{\mathrm{n}} \frac{\hbar^2}{2\mathrm{m}} \nabla_{\mathrm{i}}^2 - \sum_{\mathrm{i}}^{\mathrm{n}} \mathrm{V}(\mathrm{r_i}) + \sum_{\mathrm{i}}^{\mathrm{n}} \sum_{\mathrm{j}\neq\mathrm{i}} \mathrm{V}(\mathrm{r_i}, \mathrm{r_j}) \Big] \psi = \mathrm{E}\psi \tag{3.3}$$

Equation 3.3 is an eigenvalue problem, where the eigenvector is the wavefunction ψ and eigenvalue is the ground state energy of the system. Here, the solution of the wavefunction is calculated, which can become computationally challenging for multi-electron system. For instance, a H_2 molecule contains two electrons such that ψ is a six dimensional function (three coordinates, xyz, for each electron). Another simple molecule such as CO_2, has a ψ that is now a function of 66 variables (three variables for each electron). Thus, solving Schrödinger's equation for a large molecule or collection of smaller molecules ($\sim$100 atom) becomes a computationally formidable task. Another important challenge in calculating the ground state of a multi-electron system is that the electrons are correlated. Electron correlation is due to the fact that when one electron moves spatially, all the other electrons can potentially change their spatial coordinates too (thereby changing the potential felt by

the first electron that moved). Since electrons are correlated, the solution of the Schrödinger equation of any electron is influenced by solution of Schrödinger equation of other electrons. This is called the many body problem, and since the exact form of such electron correlation is difficult to solve, solution of Equation 3.3 becomes computationally impractical for large systems.

3.2 Density functional theory

The electron density, or probability of an electron being a certain place in space, is related to the wavefunction by equation 3.4. The electron density is a function of the spatial coordinates, x, y, and z. Thomas-Fermi, in 1927, showed that the energy of a system can be obtained as a functional of electron density alone. A functional is a mathematical quantity that produces a scalar value (energy) from a given function (electron density). In the present context, the energy is a functional of the electron density, E[n(r)], and the electron density is a function of spatial coordinates. Thus, for a given electron density functional, the energy of a system (a scalar value) can be calculated. This paved way for the modern, so called density functional theory (DFT).[1,2] In 1964, Walter Kohn and Pierre Hohenberg proved two important theorems:

Theorem 1: The ground state energy from Schrödinger's equation is a unique functional of the electron density.

Theorem 2: The electron density that minimizes the energy of the overall functional is

the true electron density corresponding to the full solution of the Schrödinger equation.

$$\mathrm{n(r)} = \int \psi\psi^{*}\mathrm{dr} \tag{3.4}$$

$$\hat{\mathrm{h}}\psi_{\mathrm{i}} = \varepsilon_{\mathrm{i}}\psi_{\mathrm{i}} \tag{3.5}$$

$$\Big[-\frac{\hbar^2}{2\mathrm{m}}\nabla^2 + \mathrm{V(r)} + \mathrm{V_H} + \mathrm{V_{XC}}\Big]\psi_{\mathrm{i}} = \varepsilon_{\mathrm{i}}\psi_{\mathrm{i}} \tag{3.6}$$

$$\mathrm{V_{eff}} = \mathrm{V(r)} + \mathrm{V_H} + \mathrm{V_{xc}} \tag{3.7}$$

$$\mathrm{E} = \sum_{\mathrm{i}} \varepsilon_{\mathrm{i}} \qquad \psi = \prod_{\mathrm{i}} \psi_{\mathrm{i}} \tag{3.8}$$

Although theorem 1 said that there exists a unique functional of the electron density, the true functional was still unknown. A year later Walter Kohn and Liu Sham reported approximations for this true functional and the governing self consistent equations for DFT or Kohn-Sham equations (equation 3.6) to find the ground state energy of a system. The functional was approximated as the sum of a kinetic energy functional of non-interacting electrons, a functional of the electron-electron interactions, a functional of the electron-nuclei interactions, and an exchange correlation functional. The exchange and correlation functional captures the corrections to the approximations made in the energy functional (explained further in the next paragraph). Finding the true exchange correlation functional is the greatest challenge with DFT, as the exact form of the exchange correlation interactions is not known. Improving exchange correlation functionals is an active area of research (see Reference[3] for their performance over the past few decades). Overall, the Kohn-Sham equations are solved for the energy and wavefunction of each electron (rather than all the electrons as in Schrödinger's equation). The overall energy of the system and the wavefunction is then given by the sum of energy of each electron and Hartree product respectively (see Equation 3.8).

The terms in the Kohn-Sham equations (Equation 3.6) are the kinetic energy, electron-

nuclei potential, Hartree potential (electron-electron interactions), and exchange correlation potential. The kinetic energy of the electrons are approximated by the kinetic energy functional of non-interacting electrons. Because in a realistic system electrons are interacting, the correction to this non-interacting kinetic energy of electrons is accounted for in the exchange correlation potential. The electron-nuclei potential is an attractive Coulombic potential represented as the sum of electron-nuclei interactions. The Hartree potential accounts for the repulsive Coulombic electron-electron interactions. The last term takes into account the neglected interactions (or corrections) of all the previous terms in the form of electron exchange and electron correlation interactions. Physically, the electron exchange (or Pauli repulsion) describes the energy associated with two electrons occupying the same spatial site with degenerate electron energy levels. This is a consequence of the Pauli exclusion principle that up spin and down spin electrons are distinguishable. Note that in DFT, the exchange potential is approximated using the homogeneous electron gas model. The exchange interactions are incorrectly modeled as the homogeneous electron gas model results in the exchange interactions also including spurious correlation effects.[4,5] In order to model the exchange interactions correctly, exchange interactions are typically modeled using exact exchange such as the Hartree-Fock exchange. The electron correlation effects are due to the fact that when one electron moves spatially, all the other electrons can potentially change their spatial coordinates too. DFT does not describe this connection (or correlation) between electrons because it describes all the electrons by mean field potentials that change iteratively in response to other electrons.

The exchange correlation functional is key to density functional theory because it is the correction term that determines the accuracy of the method. Popular exchange correlation functionals such as local density approximation (LDA[2]) and generalized gradient approximations (GGA), including the popular Perdew-Burke-Ernzerhof (PBE[6]) functional, exist that approximate the exchange correlation interactions. In the LDA, the electron density at

a specified position (a small volume of in the unit cell) is assumed to be a function only of the electron position (Equation 3.9). This approximation can sometimes work well as the electron density in systems like solid materials can be a slowly varying function of the spatial coordinates. The exchange and correlation interactions ($E_{XC} = E_X + E_C$) are described by the homogeneous electron gas model. The homogeneous electron gas model includes non-interacting electrons moving in an average constant potential and coulomb repulsion between the electrons. The exchange energy (E_X) for a homogeneous electron gas has a simple analytical form that depends on electron density n as $n^{3/4}$. For the correlation energy (E_C), numerical techniques such as those reported by Ceperley and Alder[7] using Monte Carlo methods for a ground state solution of electrons are used to calculate the energy. In the case of the GGA, the exchange correlation energy also includes the gradient of the electron density as shown in Equation 3.10. This gives for instance improved predictions of binding energies of atoms and molecules in solids comparable to experimental values. More details about exchange correlation functionals can be found in Chapter 8 in Ref[8] and Chapter 3 in Ref.[9]

$$E_{XC}^{LDA} = \int n(r)\varepsilon_{XC}[n(r)] \quad d^3r \tag{3.9}$$

$$E_{XC}^{GGA} = \int n(r)\varepsilon_{XC}[n(r), \nabla n] \quad d^3r \tag{3.10}$$

Hohenberg-Kohn's second theorem showed that the true electron density results in a minimum of the overall energy functional. However, both the true electron density and the effective potential V_{eff} (sum of electron-ion, hartree, and exchange correlation potentials as shown in Equation 3.7) depend on each other. Therefore, in practice the minimization procedure to find the ground state energy involves an initial electron density guess followed by search for a self-consistent solution of the electron density and effective potential (Figure 3.1).

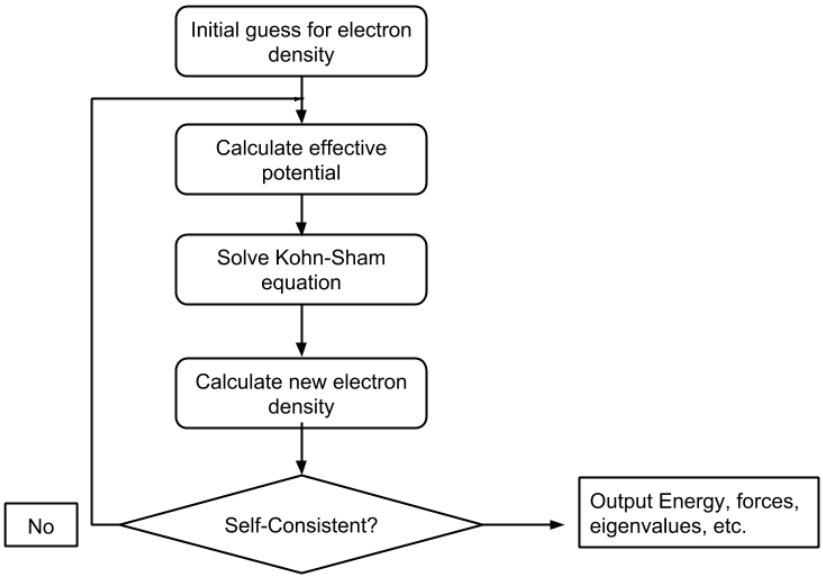

Figure 3.1: Flow diagram showing the self consistent procedure to obtain the ground state energy from the Kohn-Sham equations. This flow diagram is adapted from Ref.[8]

After the initial guess of the electron density, an V_{eff} is constructed, which enters the KS equations. The solution of the KS equations gives the the eigenvectors (wavefunctions) and eigenvalues (energies) for all the electrons in the system. Based on Equation 3.4, the wavefunctions obtained from KS solution generates a new electron density. This new electron density is now used for the second (and subsequent) iterations to ultimately find the ground state energy of the system.

Solving the DFT equations involves computer, numerical solutions, rather than analytical solutions. To do so a form or mathematical equation must be assumed for the wavefunctions. The wavefunctions are commonly described in terms of localized Gaussian basis sets or by periodic plane wave basis sets. The Gaussian basis sets are a common choice when working with computational chemistry based problems where the task is to describe a non-periodic molecular system. In contrast, plane waves are well suited for describing solid materials (materials with periodic unit cells), which require periodic properties. Typical localized Gaussian functions are of the form $\exp(-x^2)$, while periodic basis sets are of the

form exp(ix) = cos(x) + isin(x) (i represents the imaginary unit). Detailed information on this can be found in Chapter 1 in Ref.[10]

Chemical bonding and reactions involve primarily the valence electrons of the atoms. Therefore, solving the KS equations for the core electrons is not chemically meaningful and at the same time can make computations impractical due solving the KS equation for too many electrons. For instance, a 100-atom supercell of Pt (78 electrons per atom) would require solving the set of KS equations for 7800 electrons. In contrast, pseudopotentials can reduce the number to 1000, where the 68 core electrons are replaced by pseudopotentials.[10] This has led to the widespread use of pseudopotentials, where the core electrons' influence is mimicked by a pre-calculated potential derived in an atomic environment. This potential is then suitably combined with the valence electrons to describe the complete potential interactions in an atom. Several flavors of pseudopotentials exist such as norm-conserving, ultrasoft, and projector augmented wave pseudopotentials.[10–12]

3.3 Modeling Solids and Surfaces

Computational chemistry packages (such as NWChem[13]) are commonly used to model isolated molecular systems using localized Gaussian type basis sets. To model solids however, using a plane wave basis set is the most common approach. A plane wave basis set can be represented by a periodic function like Ae^{-iBx} , while a Gaussian type basis set takes the form Ce^{-Dx^2}. In these functions x is the spatial coordinate, while the constants A and C are determined by solving the KS equation. Constants B and D are pre-determined before the simulation. The solid (for instance bulk Pt in Figure 3.2) is simply described by a repeating cell of the material. This demonstrates the concept of periodic boundary conditions. The plane waves are used to describe the electron wavefunctions only in the cell. However due to periodic boundary conditions, an extended 3-dimensional bulk solid is modeled, since any

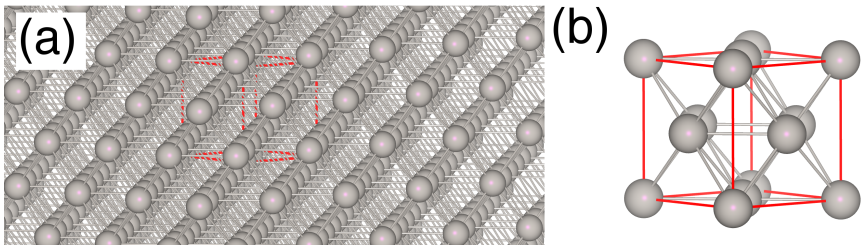

Figure 3.2: Bulk solid Pt with indicated unit cell in red (a) and the corresponding face centered cubic unit cell without repetition (b).

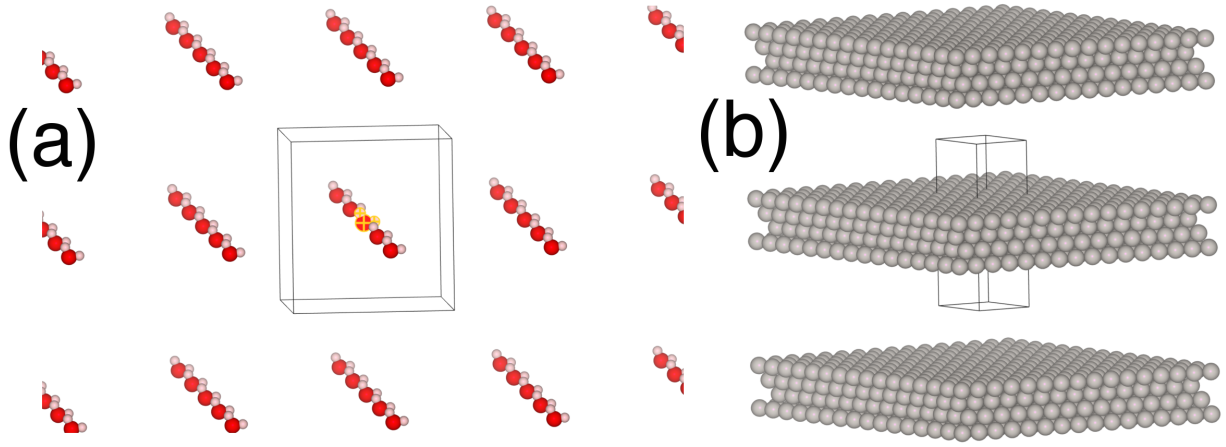

Figure 3.3: Demonstration of modeling an isolated water molecule (a) and slab approach of modeling the Pt(111) surface (b) using periodic boundary conditions. The cell is shown using black solid lines. The H_2O inside the unit cell is highlighted in yellow.

solution within the cell is repeated in infinite directions.

Periodic boundary conditions also allow one to model isolated molecules and 2-dimensional surfaces. This is shown in Figure 3.3. Because the electron density of isolated molecules approach zero far from the molecule, a large unit cell with well separated periodic images of this molecule represents an isolated molecule that can be described by plane waves. In the case of modeling surfaces, the surface normal direction of the cell is well separated by vacuum to avoid interactions between periodic images. This approach is the slab approach as the surface is described by infinite periodic 2-dimensional slabs, while the surface normal direction contains vacuum.

Bibliography

[1] P. Hohenberg and W. Kohn, *Physical Review*, 1964, **136**, B864–B871.

[2] W. Kohn and L. J. Sham, *Physical Review*, 1965, **140**, A1133–A1138.

[3] M. G. Medvedev, I. S. Bushmarinov, J. Sun, J. P. Perdew and K. A. Lyssenko, *Science*, 2017, **355**, 49–52.

[4] A. D. Becke, *The Journal of Chemical Physics*, 1993, **98**, 1372–1377.

[5] J. Heyd, G. E. Scuseria and M. Ernzerhof, *Journal of Chemical Physics*, 2003, **118**, 8207–8215.

[6] J. P. Perdew, K. Burke and M. Ernzerhof, *Phys. Rev. Lett.*, 1996, **77**, 3865–3868.

[7] D. M. Ceperley and B. J. Alder, *Physical Review Letters*, 1980, **45**, 566–569.

[8] R. M. Martin, *Electronic Structure*, Cambridge University Press, Cambridge, 2004.

[9] F. Giustino, *Materials Modelling using Density Functional Theory*, Oxford University Press, 1st edn., 2014.

[10] D. Sholl, J. A. Steckel and Sholl, *Density Functional Theory : A Practical Introduction*, Wiley-Interscience, Hoboken, NJ, USA, 2009, pp. 2–4.

[11] D. Vanderbilt, *Physical Review B*, 1990, **41**, 7892–7895.

[12] G. Kresse and D. Joubert, *Physical Review B*, 1999, **59**, 1758–1775.

[13] M. Valiev, E. J. Bylaska, N. Govind, K. Kowalski, T. P. Straatsma, H. J. J. Van Dam, D. Wang, J. Nieplocha, E. Apra, T. L. Windus and W. a. De Jong, *Computer Physics Communications*, 2010, **181**, 1477–1489.

Chapter 4

CO_2 Reduction on Dispersed Cu_1/TiO_2 catalysts

4.1 Introduction

Atomically dispersed supported metal catalysts form a new class of highly active and efficient catalysts.[1,2] Vajda and coworkers have shown that Cu based size-selective clusters deposited on support have shown good photocatalytic activity for CO_2 reduction to form methanol.[3,4] One of the important and energetically unfavorable reaction step in CO_2 reduction is the CO_2 activation step,[5,6] where a linear CO_2 undergoes electron reduction to form a bent CO_2 ($\sim 130^o$). Therefore, a catalyst that stabilizes bent CO_2 is favorable for CO_2 reduction reaction.

Supported Cu based catalysts (atoms, clusters and nanoparticles) have been reported to reduce CO_2 to form CO, methane, and methanol.[3,7–9] However, atomic level understanding from theoretical modeling is still lacking. In this present work, we modeled atomic Cu supported on TiO_2 to simulate the atomically dispersed Cu/TiO_2 photocatalyst that was

experimentally found to reduce CO_2 to CO with high catalytic activity compared to pure TiO_2.

4.2 Methodology

Periodic density functional theory (DFT) simulations of Cu/TiO_2 systems were performed using the Vienna ab initio simulation package.[10,11] All calculations were conducted as spin-polarized. We specifically modeled a (1x2) supercell of the anatase (101) surface, which is the most stable anatase surface, with a single Cu atom adsorbed on the surface. The surface was treated by the slab approach and had ∼15 Å of vacuum between slabs. The surface slab consisted of six O-Ti-O trilayers (9Å thick) and had lattice vectors 10.4 Å by 7.6 Å parallel to the surface. The bottom two trilayers of the slab were frozen in bulk positions. The slab had a total of 24 Ti atoms and 48 O atoms. Similar models were used in previous DFT studies. A 2x2x1 k-point mesh was used in this study. All calculations used the PerdewBurkeErnzerhof exchange-correlation functional.[12] The valence electrons were treated by a plane-wave basis set with a cutoff of 450 eV, while core electrons were treated by projector augmented-wave pseudopotentials[13] with cores being: O ($1s^2$), Ti ($1s^2 2s^2 2p^6 3s^2 3p^6$), C ($1s^2$), and Cu ($1s^2 2s^2 2p^6 3s^2 3p^6$). This larger core for Ti has been shown to give very similar results compared to smaller electronic cores while allowing faster computational time.[14] We applied the DFT+U correction method to Ti (U_{eff} = 4.5 eV) and Cu (U_{eff} = 5eV) to improve electronic description. Similar values were used in previous works.[15–17]

4.3 Results

Experimental results showed that the photocatalytic activity for reduction of CO_2 to form CO was much higher on Cu/TiO_2 compared to that on pure TiO_2 (see our published work in

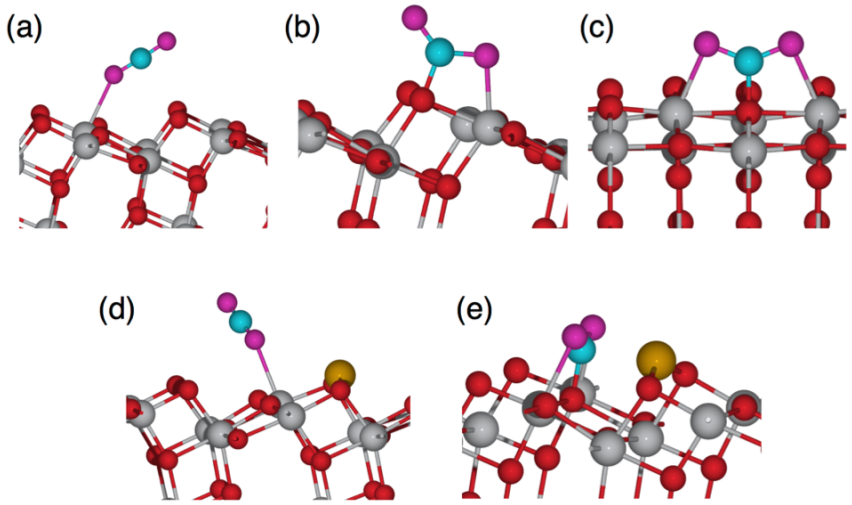

Figure 4.1: Modeling results for CO_2 adsorption on (ac) TiO_2 and (d and e) Cu/TiO_2. The calculated adsorption energies are (a) 0.25, (b) 0.05, (c) 0.06, (d) 0.23, and (e) 0.25 eV. Color code: Ti (gray), O in TiO_2 (red), Cu (dark yellow), O in CO_2 (magenta), and C (blue).

Ref[18] for details on the experimental results). In order to explain the observed experimental trends, we first calculated the most stable binding site of Cu atom on TiO_2. The most preferred site was found to be between two surface O atoms, in agreement with the work by Seriani et al.[17] We modeled CO_2 adsorption over the bare anatase surface and over Cu/TiO_2, as shown in Figure 4.1. Other possible geometries were also investigated, but we report only the most stable results herein. On the anatase (101) surface, adsorption of CO_2 occurs preferentially on Ti atoms, with relatively weak binding energies (0.25 eV), which is similar to the previously reported value of 0.20 eV.[19] When Cu is present on the surface, the binding is still relatively weak, but the presence of surface Cu atoms significantly stabilizes the adsorption of bent CO_2 (Figures 4.1e). This is important since the difficulty for single-electron CO_2 reduction originates from a possible large reorganization energy between the linear and bent configuration.[6] Thus, the presence of Cu may contribute to stabilizing surface adsorption of CO_2 for subsequent photocatalysis.

After the photocatalytic CO_2 reduction, experiments showed that CO was adsorbed on Cu/TiO_2 catalysts as indicated by CO vibrational frequency shifts corresponding to adsorbed

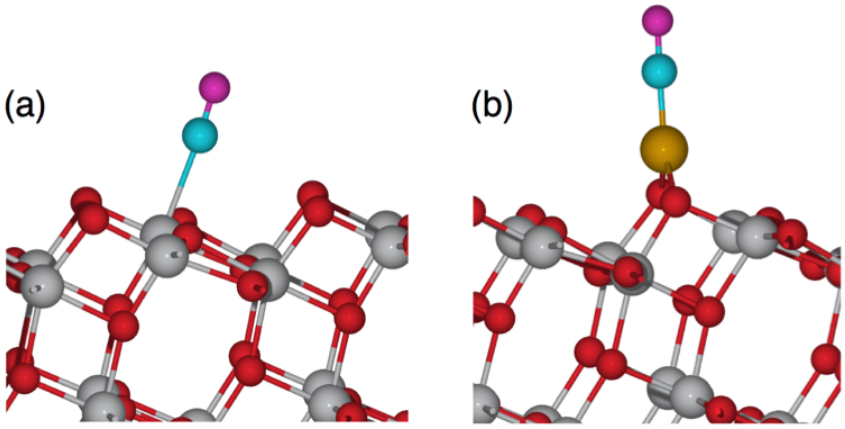

Figure 4.2: Modeling of CO adsorption on TiO_2 and Cu/TiO_2. The calculated adsorption energies are (a) 0.36 eV on TiO_2 and (b) 1.04 eV on Cu/TiO_2.

CO. Consistent with experiments, modeling CO adsorption clearly showed that adsorption of CO was very stable on Cu/TiO_2 (Figure 4.2b) compared to that on pure TiO_2 (Figure 4.2a).

4.4 Conclusion

We studied CO_2 reduction over Cu/TiO_2 catalysts to understand the effect of Cu in improving the photocatalytic activity. The improved activity was attributed to the stabilization the bent CO_2 over linear CO_2 on Cu/TiO_2 catalysts when compared to pure TiO_2.

Bibliography

[1] M. Flytzani-Stephanopoulos and B. C. Gates, *Annual Review of Chemical and Biomolecular Engineering*, 2012, **3**, 545–574.

[2] B. C. Gates, M. Flytzani-Stephanopoulos, D. A. Dixon and A. Katz, *Catal. Sci. Technol.*, 2017, **7**, 4259–4275.

[3] C. Liu, B. Yang, E. Tyo, S. Seifert, J. DeBartolo, B. von Issendorff, P. Zapol, S. Vajda and L. A. Curtiss, *Journal of the American Chemical Society*, 2015, **137**, 8676–8679.

[4] M. Yang and M. Flytzani-Stephanopoulos, *Catalysis Today*, 2017, **298**, 216–225.

[5] H.-J. Freund and M. W. Roberts, *Surface Science Reports*, 1996, **25**, 225–273.

[6] E. E. Benson, C. P. Kubiak, A. J. Sathrum and J. M. Smieja, *Chem. Soc. Rev.*, 2009, **38**, 89–99.

[7] D. Liu, Y. Fernández, O. Ola, S. Mackintosh, M. Maroto-Valer, C. M. Parlett, A. F. Lee and J. C. Wu, *Catalysis Communications*, 2012, **25**, 78–82.

[8] R. Passalacqua, S. Parathoner, G. Centi, A. Halder, E. C. Tyo, B. Yang, S. Seifert and S. Vajda, *Catal. Sci. Technol.*, 2016, **6**, 6977–6985.

[9] B.-R. Chen, V.-H. Nguyen, J. C. S. Wu, R. Martin and K. Kočí, *Physical chemistry chemical physics : PCCP*, 2016, **18**, 4942–51.

[10] G. Kresse and J. Furthmüller, *Computational Materials Science*, 1996, **6**, 15–50.

[11] G. Kresse and J. Furthmüller, *Physical review. B, Condensed matter*, 1996, **54**, 11169–11186.

[12] J. P. Perdew, K. Burke and M. Ernzerhof, *Phys. Rev. Lett.*, 1996, **77**, 3865–3868.

[13] P. E. Blöchl, *Physical Review B*, 1994, **50**, 17953–17979.

[14] N. Aaron Deskins, *Chemical Physics Letters*, 2009, **471**, 75–79.

[15] B. Bukowski and N. A. Deskins, *Physical chemistry chemical physics : PCCP*, 2015, **17**, 29734–46.

[16] J. C. Garcia, M. Nolan and N. Aaron Deskins, *J. Chem. Phys.*, 2015, **142**, year.

[17] N. Seriani, C. Pinilla and Y. Crespo, *J. Phys. Chem. C*, 2015, **119**, 6696–6702.

[18] C. Liu, S. K. Iyemperumal, N. A. Deskins and G. Li, *Journal of Photonics for Energy*, 2016, **7**, 012004.

[19] H. He, P. Zapol and L. A. Curtiss, *J. Phys. Chem. C*, 2010, **114**, 21474–21481.

Chapter 5

CO_2 Reduction on Dispersed $Cu_{1–4}/TiO_2$ catalysts

5.1 Introduction

One approach to mitigating greenhouse gases like CO_2 is the conversion of such gases to other chemicals. Reducing CO_2 into chemical fuels such as methane and methanol can in principle help solve these environmental issues while also producing useful fuels. Photocatalytic conversion of CO_2 makes this process renewable and clean. Although photocatalytic reduction of CO_2 appears feasible, reported CO_2 conversion efficiencies have been low,[1–5] limiting the potential of this process. More active photocatalysts are needed for commercialization of CO_2 conversion processes. TiO_2 is one of the widely used photocatalysts due to its low cost, chemical stability, and low toxicity.[6] Metal-supported TiO_2 photocatalysts such as Cu/TiO_2 have attracted considerable interest due to several reports of promising CO_2 photoreduction activities.[4,5,7–12] Cu/TiO_2 catalysts have shown better selectivity for CO_2 photoreduction to methane with formation rates of methane comparable or larger than

Au/TiO_2[13] or Pt/TiO_2[11,14] photocatalysts. Moreover, the abundant availability and low cost of Cu makes Cu/TiO_2 a desirable photocatalyst for CO_2 photoreduction.

Dispersed Cu catalysts have shown strong reactivity for CO_2 photoreduction[10,15] and water gas shift activity.[16] Small clusters (i.e. less than 10 to 20 atoms) as catalysts are of especial interest due to several factors. Such small clusters adsorbed on a support have a high concentration of reaction sites, high activity to catalyst loading ratio, and possible favorable metal-support interactions. Several reports have appeared recently where supported single metal atom catalysts have been synthesized for several reactions like CO_2 reduction, H_2 evolution, NO removal, and CO oxidation.[17–20] Other synthesis techniques such as the size-selected soft landing approach have also been successfully used to control the number of atoms in the cluster.[21] Of particular interest for the present work are supported Cu clusters. Tanizawa et al. synthesized size-selected Cu_3 and Cu_6 clusters that were adsorbed on a TiO_2 rutile (110) surface.[22] Vajda and coworkers synthesized Cu clusters between three and twenty atoms supported on Al_2O_3 that efficiently reduced CO_2 to methanol.[23,24] Results using Cu_5 and Cu_{20} clusters showed that Cu_5 resulted in CO_2 electrochemical reduction with lower overpotential compared to Cu_20.[25] Well dispersed small Cu clusters and nanoparticles on TiO_2 rutile (110) surface with cluster heights less than around 0.5[16] and 1.0[26]nm were also found to be reactive for CO oxidation. Small Cu species with measured diameters of less than around 1 nm deposited on Ceria showed high conversion of dimethyl carbonate to methanol.[27] Several other clusters consisting of noble metal atoms like Pt, Pd, Au, and Ag on the order of one to several tens of atoms have also been deposited on various supports.[20,28–32] Previous work by the current authors[15] highlighted photocatalysts for CO_2 reduction consisting of dispersed Cu atoms/clusters on TiO_2. Experimental work thus illustrates that small Cu clusters on metal oxide support can be synthesized as potential catalysts for CO_2 reduction.

CO_2 is a stable molecule and activation of the molecule is a key challenge for CO_2

reduction. The activation of CO_2 on metal oxides (such as TiO_2) has been of significant interest.[33–39] The initial activation step is believed to occur through one electron reduction of CO_2 forming a CO_2 radical anion (CO_2^-).[39–41] This CO_2 activation step structurally transforms the linear CO_2 to a bent CO_2 radical anion and the energy associated with such transformation is strongly unfavorable. Catalysts which can lower this energetic penalty to transform linear to bent CO_2 are desired. Our recent report[15] showed that monoatomic Cu adsorbed on TiO_2 may promote bent CO_2 formation, and that higher photoactivity of Cu/TiO_2 compared to TiO_2 was observed. The higher activity was attributed to the presence of Cu as Cu^{1+} species on TiO_2. Using density functional theory (DFT), we showed that Cu atoms offered binding sites for both the reactant (CO_2) and product (CO) that stabilized these molecules compared to pure TiO_2 surfaces. In a study by Liu et al.,[23] they showed using both DFT and experiments that Cu^0 species were the active sites for CO_2 reduction to methanol on Cu_4 supported on Al_2O_3. What oxidation state the Cu clusters may have on supports like TiO_2 is still an important question for CO_2 reduction.

DFT-based studies have focused on modeling CO_2 adsorption as well as possible CO_2 anion formation on various TiO_2 surfaces. Using DFT, He et al.[34,42] reported the formation of bent CO_2 on TiO_2 anatase (101), which resembled a CO_2 anion. It was reported that the activation of CO_2 to bent CO_2 was the rate limiting step with a barrier of 0.87 eV in the formation of formic acid.[34] Sorescu et al.[43,44] used dispersion-corrected DFT to identify bent CO_2 structures on TiO_2 anatase (101) and rutile (110) surfaces with and without the presence of co-adsorbed oxidizing species, like water and OH. They found that adsorption of bent CO_2 could be stabilized in the presence of oxidizing species.[44] Indrakanti et al.[3] reported that electron transfer to CO_2 from TiO_2 anatase and rutile cluster surfaces was energetically unfavorable due to the energy level of the lowest unoccupied molecular orbital (LUMO) of CO_2 lying above the highest occupied molecular orbital (HOMO) of the TiO_2 surfaces.

Several DFT studies have focused on supported metal atoms. In our previous work[15] we modeled a single Cu atom on anatase (101) and found that Cu favors the formation of bent activated CO_2. Liu et al.[23] studied CO_2 reduction to methanol, CO, and methane on Cu_4/Al_2O_3. In their study the reactions proceeded by the formation of HCOO and COOH species which involved the presence of structurally bent O-C-O moiety). This again suggests the importance of activating linear CO_2 into its bent form for efficient CO_2 reduction. Uzunova et al. showed that the Cu_2O (001) surface reconstructs and results in Cu dimers on the surface, which stabilized bent CO_2 and were found to be the active sites for CO_2 reduction to methanol.[45] Yang et al.[46,47] modeled CO_2 adsorption on $Pt_{4,6,8}$ and $Ag_{4,8}$ clusters, all supported on a TiO_2 anatase (101) surface. They reported strong adsorption of bent CO_2 anions. Similar strong adsorption of bent CO_2 on Cu_{10} and Ru_{10} on TiO_2 anatase(101) was also reported by Schlexer et al. recently.[48] Shanmugam et al. used ab-initio molecular dynamics simulation and reported that various gas-phase Cu clusters (sizes of up to 7 atoms) were not able to stabilize the adsorption of bent CO_2.[49] In another report, Liu et al. reported an unfavorable adsorption energy of 0.27 eV for bent CO_2 on a lone Cu_4 cluster.[50] These results on unsupported Cu clusters show that Cu alone does not stabilize bent CO_2, but that a support such as TiO_2 may significantly alter CO_2 reduction activity.

In the present work we modeled using DFT Cu_x (x=1-4) clusters on an anatase (101) surface to further understand how and if Cu clusters could activate CO_2. This titania surface is the most stable facet of anatase, which often displays more photocatalytic activity than rutile.[51,52] We characterized the nature of the supported Cu clusters, including morphology and oxidation state. We also determined how Cu_x/titania may interact with adsorbed CO_2 and CO molecules, and possibly activate CO_2. Since CO_2 activation is a very important step in CO_2 reduction, we focus specifically on this step in our present work. Future work may focus on CO2 dissociation and/or hydrogenation reactions to form CO_2 reduction products such as formic acid, methanol, and methane. Our work aims to show how small Cu clusters

supported on TiO_2 may be good catalysts for CO_2 reduction.

5.2 Methodology

All spin-polarized DFT calculations were performed using the CP2K package,[53,54] which uses the Gaussian and Plane Wave (GPW) approach.[55] We used the generalized gradient approximation (GGA) PBE exchange correlation functional.[56] Valence electrons were described using molecularly optimized (MOLOPT[57]) double ζ basis sets and core electrons were described using Goedecker-Teter-Hutter (GTH) norm conserving pseudopotentials.[58] A plane wave cutoff energy of 300 Ry was used, similar to previous work.[59] The number of valence electrons used for Cu, Ti, O, and C were 11, 12, 6, and 4, respectively. Electronic and ionic relaxations were performed until energies and maximum forces converged below $1E^{-6}$ Ha and 0.05 eV/Å, respectively. Since dispersion interactions have been reported to be important in adsorption of CO_2 on TiO_2 surfaces,[44,60] we included the D3 dispersion correction[61] with Becke-Jonsson damping. The CP2K program is limited to sampling k-space only at the gamma point, so we used large supercells to minimize errors related to k-space sampling.

Bulk anatase was modeled with a 3x3x2 supercell containing 216 atoms to determine appropriate lattice constants. The optimized lattice constants of bulk anatase were determined to be 3.78 and 9.58Å, which are in good agreement with previous DFT (3.76 and 9.52Å)[62] and experimental (3.78 and 9.51Å)[63] work. The (101) surface of anatase was modeled as a (2x4) rectangular surface slab with six O-Ti-O layers, resulting in a supercell with a total of 288 atoms (see Figure 5.1). The bottom two layers in this slab were frozen. This super cell had lattice vectors of 20.6 Å and 15.1Å parallel to the surface, and 30.0Å perpendicular to the surface. The thickness of the slab was 9.4Å, resulting in a vacuum spacing of $\sim$ 20.6Å. A similar slab thickness was used in previous work.[34,43,64,65] Test calculations using

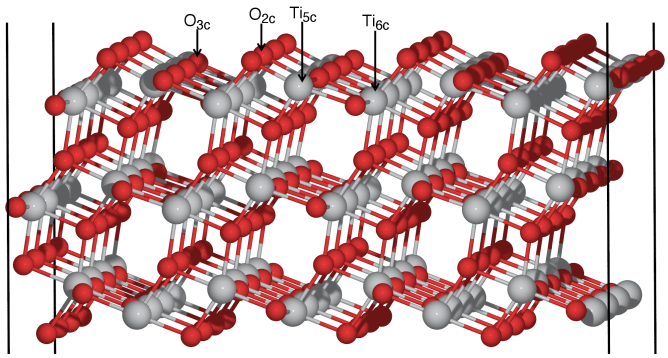

Figure 5.1: TiO_2(101) surface supercell with two (2c), three (3c), five (5c), and six (6c) coordinated surface O and Ti atoms indicated.

eight O-Ti-O layers showed that the adsorption energies of Cu and CO_2 on the TiO_2(101) surface changed by $\leq$0.08 eV compared to a six layer slab (refer Table A.1 in Supporting Information). We therefore used a six layer slab for the current work.

We used DDEC6 charge analysis[66,67] in our work. In order to obtain accurate electron density, we performed single point calculations on the optimized geometries with a very fine grid spacing by setting a large plane wave cutoff of 1600 Ry. DDEC6 derived charges were extensively tested and compared to the widely used Bader charge method.[68,69] We found the DDEC6 program to generate atomic charges in close agreement with those determined using Bader charges for both molecular and condensed systems (see Table A.2). Vibrational frequencies were calculated using finite differences to obtain numerical frequencies. We used a larger plane wave cutoff of 600 Ry and a tighter electronic convergence of $1E^{-7}$ Ha to calculate vibrational frequencies, since we determined these settings were necessary to obtain good agreement with experimental gas-phase frequencies and previous DFT frequencies of adsorbed CO_2 (more details in Table A.4). Due to the increase in computational cost with the higher cutoff energy of 600Ry, we only relaxed 40-50 atoms from the adsorption site during our vibrational frequency calculations (atoms within 6-7Å of the C atom). As shown in Table A.4, the results obtained by relaxing 40-50 atoms near the adsorption site are very close to the results when two/four layer slabs were relaxed (see SI for more details).

We modeled CO_2 adsorption on Cu_x/TiO_2 where the entire system is neutral. Upon adsorption of CO_2 however, electron transfer from the surface to CO_2 may occur, resulting in the adsorbed CO_2 becoming charged. The Cu_x/TiO_2 geometries are all reported for the most stable spin state, which we found to be the lowest spin state (singlet or doublet). We ran calculations of higher spin states, but found these energies to always be larger than the low spin state solutions. Comparison of the low and high spin state energies are provided in the Supporting Information in Table A.5.

The adsorption energies (ΔE_{ads}) of Cu clusters are given by Equation 5.1

$$\Delta E_{ads-Cu_x} = \frac{1}{x}(E_{Cu_x/TiO_2} - E_{TiO_2} - xE_{Cu}) \tag{5.1}$$

where, E_{Cu_x/TiO_2}, E_{TiO_2}, and xE_{Cu} are the energies of Cu_x/TiO_2, pure TiO_2, and atomic Cu respectively. Here x is the number of Cu atoms in the Cu_x cluster and x ranges from 1 to 4. The adsorption energy of CO_2 or CO is given by Equation 5.2

$$\Delta E_{ads-CO_n} = E_{CO_n/Cu_x/TiO_2} - E_{Cu_x/TiO_2} - E_{CO_n}[n = 1, 2] \tag{5.2}$$

where, $E_{CO_n/Cu_x/TiO_2}$ is the energy of adsorbed CO_n (n=1,2), E_{Cu_x/TiO_2} is the energy of the surface without CO_n, E_{CO_n} is the energy of gas phase CO_n. A negative adsorption energy indicates an exothermic adsorption process.

Standard DFT employing exchange correlation functionals like GGA often suffers from self-interaction errors[70] in correlated materials like TiO_2. We therefore performed tests using the DFT+U[71] formalism and compared results obtained using DFT. These are discussed in the Supporting Information and show that DFT and DFT+U give similar results for adsorption energies and charges. Similar conclusions were also previously reported for CO_2 adsorption on Pt/TiO_2,[46] and metal cluster adsorption (Au and Pt) on TiO_2.[72] Adsorption energies and charges are reported using DFT in this paper. Analysis of the electronic struc-

ture (i.e. density of states) however showed that DFT+U gives a better description (see the Supporting Information), so our analysis of the density of states (Section 5.3.3) used the DFT+U method.

5.3 Results and Discussion

5.3.1 Cu Clusters on Titania

The first step in our work was to identify the most stable gas phase Cu cluster geometries. Several DFT studies have reported Cu geometries.[73,74] We tested these geometries as well as several others. We found that linear Cu_2, triangular Cu_3, and rhombus-shaped Cu_4 were the most stable geometries (see Figure 5.2). The linear Cu dimer had a bond distance of 2.2 Å. The most stable Cu trimer cluster had bond distances of 2.3, 2.4, and 2.4 Å with angles of 57.8°, 59.9°, and 62.3°. We also modeled the Cu trimer in an equilateral triangle structure, but the geometry changed to the triangle just described. In the case of Cu_4, all four peripheral bond distances were ∼2.4 Å in the rhombus, but the cluster was not completely planar (see Figure 5.2). The most stable geometries that we found were also the most stable Cu geometries reported earlier.[73,74] We calculated the binding energy per atom of these Cu clusters to be $1/x\ [\ E_{Cu_x} - x\ E_{Cu}\ ]$ where, E_{Cu_x} and E_{Cu} are the energies of the Cu cluster with x atoms and atomic Cu, respectively. The calculated binding energies were -1.15 eV for Cu_2, -1.25 eV for Cu_3, and -1.64 eV for Cu_4. Our results are close to the values reported by Jiang et al.,[73] which were -1.04, -1.13, and -1.48 eV, respectively,

Although several DFT studies have focused on TiO_2-supported metal clusters,[38,75,76] only a few studies focused on Cu adsorption over the TiO_2 anatase (101) surface.[65,77] In contrast, Cu over the TiO_2 rutile (110) surface has been studied in several papers.[26,78–81] Seriani et al.[65] already reported Cu adsorption sites on the anatase (101) surface for cluster sizes of 1-4 atoms, similar to our work. In addition to the geometries reported by Seriani et

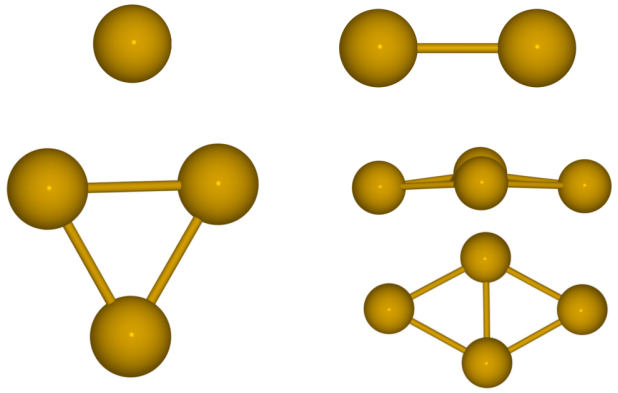

Figure 5.2: Most stable gas phase Cu_x (x=1,2,3,4) clusters. For Cu_4, the top and side views of the non-planar structure are shown.

al., we modeled Cu clusters at several other adsorption sites on the TiO_2 surface in order to fully assess Cu adsorption. We report only the most stable geometries. The most stable adsorbed geometries for each cluster are shown in Figure 5.3. Bulk Cu has Cu-Cu bond distances of 2.6 Å and we used 2.6Å as the cutoff distance to determine whether an atom was coordinated to a Cu atom. By determining which atoms were coordinated to Cu atoms, we could calculate coordination numbers of the Cu atoms.

Atomic Cu prefers to adsorb at a bridge site between O atoms that are two-coordinated (denoted hereafter as O_{2c} atoms) with an ΔE_{ads} of -2.56 eV. These O_{2c} atoms move towards the Cu atom by ∼0.1 Å, such that both Cu-O_{2c} bond distances were 1.89 Å. Atomic Cu on TiO_2 lies very close to the surface (0.56Å above the surface), and has a coordination number of 3. Our ΔE_{ads} is in good agreement with the earlier reported value of -2.30 eV,[65] which also found the bridge site to be most stable for atomic Cu. Luo et al.[77] also found the bridge site to be the most stable site for the adsorption of atomic Cu. They however reported a smaller ΔE_{ads} value of -1.5 eV. In their work they represented the anatase surface as a cluster (not periodic) and also used different DFT parameters (i.e. hybrid exchange correlation functional and Gaussian basis sets), which could explain the difference in adsorption energies between our work and theirs.

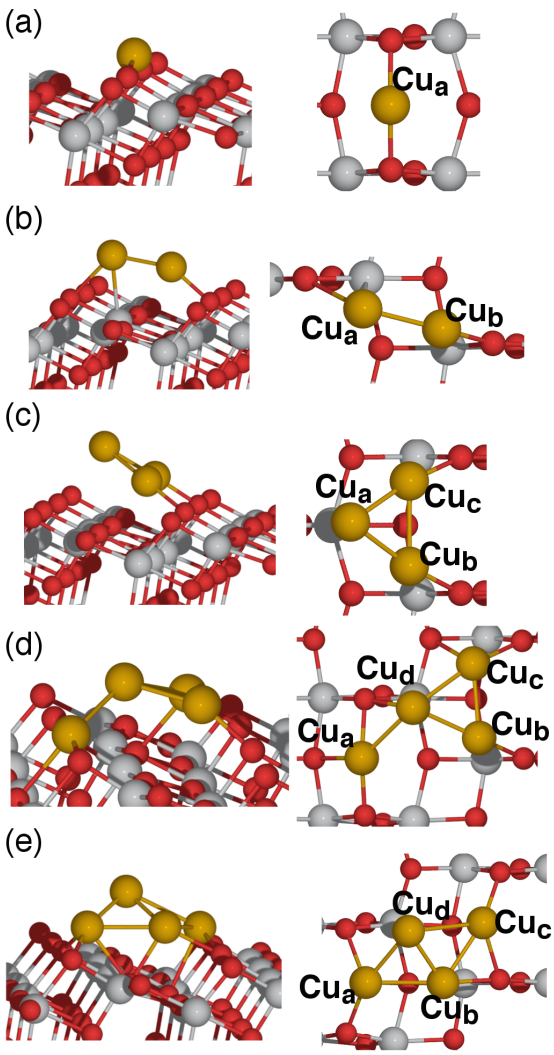

Figure 5.3: Most stable adsorption sites for Cu (a), Cu_2 (b), Cu_3 (c), and two different Cu_4 clusters (d,e) on the TiO_2 anatase (101) surface. The two Cu_4/TiO_2 are represented as Cu_4(I) (d) and Cu_4(II) (e).

Similar to Cu, the Cu atoms in Cu_2 prefer to bond to O_{2c} atoms on the TiO_2 surface. Upon adsorption, the Cu_a-Cu_b bond distance slightly increases to 2.3 Å compared to the gas phase value of 2.2 Å. Each of the Cu atoms bonds to a O_{2c} atom along different O_{2c}-rows as shown in Figure 5.3b. The Cu_a atom bonds to an O_{2c} atom lying above a five-coordinated surface Ti atom (Ti_{5c}), while the other Cu_b atom bonds to an O_{2c} atom lying above a subsurface six-coordinated Ti atom (Ti_{6c}) atom. The former Cu_a atom also interacts with the Ti_{5c} atom beneath it (having a Cu-Ti_{5c} bond distance of 2.6Å), while also interacting with the O_{2c} atom (Cu-O_{2c} bond distance of 2.4Å). The Cu_b atom has a Cu-O_{2c} bond distance of 1.9Å. The ΔE_{ads} of Cu_2 was calculated to be -2.09 eV. The Cu binding energy of the Cu_2 cluster on the TiO_2 surface, defined as E_{Cu_x/TiO_2} + (x-1) E_{TiO_2} - x E_{Cu/TiO_2}, was calculated to be 0.94 eV, indicating that clustering of adsorbed Cu atoms to form Cu_2 is energetically unfavorable. Cu_a and Cu_b atoms lie away from surface (1.7 and 1.3Å), which results in a small coordination numbers of 3 and 2 respectively. A different structure for Cu_2 (and also for Pd_2[82]) on the TiO_2 anatase (101) surface was reported earlier[65] to be most stable. This other structure had one Cu atom at a bridge site between two O_{2c} atoms, while the other Cu atom was above a Ti_{5c} atom. We found this structure to be 0.09 eV less stable than the structure reported in Figure 5.3b. We also found that two other structures had adsorption energies close to our most stable geometry: Cu_2 bound to two O_{2c} atoms along the same row (ΔE_{ads} of -2.05 eV) and a Cu_2 structure with Cu atoms bound to O_{2c} and O_{3c} atoms (ΔE_{ads} of -2.03 eV). There are thus multiple Cu_2 structures which are close in energy, but we used the geometry shown in Figure 5.3b for this work since we determined it to be the most stable. Similar to the conclusion by Seriani et al., we found the Cu_2 cluster (compared to Cu, Cu_3, and Cu_4) to have the weakest binding to the TiO_2 surface.

We modeled several different structures for Cu_3 adsorption on the TiO_2 surface. Compared to the most stable geometry in Figure 5.3c, all other geometries were typically less stable by 0.15 eV to 1.39 eV. We also modeled a linear Cu_3 trimer, where each Cu atom

was bound to one oxygen atom, and found that the linear Cu_3 is strongly unstable by 2.0 eV compared to the most stable triangular Cu_3. In the most stable adsorption configuration Cu_3 adsorbs with two of its Cu atoms (indicated as Cu_b and Cu_c) bound to two O_{2c} atoms, while the third Cu_a atom does not interact with any surface atoms (see Figure 5.3c). The Cu_a-Cu_b, Cu_b-Cu_c, and Cu_c-Cu_a bond distances were 2.3, 2.4, and 2.3Å respectively, which were similar to the gas phase values (2.3, 2.4, and 2.4 Å). The bond distances of Cu_b and Cu_c with O_{2c} were ∼1.9Å, while the Cu_a atom lies 3.1Å above a Ti_{5c} atom. The associated coordination numbers were calculated to be 2, 4, 4 for Cu_a, Cu_b, and Cu_c respectively. The binding energy of the Cu_3 cluster was calculated to be -0.03 eV, which shows that Cu trimers and Cu adatoms on the surface are energetically similar. The ΔE_{ads} of Cu_3 was found to be -2.57 eV, which is in close agreement with the reported value of -2.48 eV.[65] Similar stable structures of metal trimers with two metal atoms bound to two O_{2c} atoms have been reported earlier for Au_3 and Pt_3 on the TiO_2 anatase (101) surface,[76] as well as Cu_3 on the TiO_2 rutile (110) surface.[80]

Similar to Cu_3, we considered several different geometries for Cu_4/TiO2. Compared to the most stable Cu_4/TiO_2 geometry shown in Figure 5.3d, all the other tested geometries were less stable by 0.57 to 2.64 eV. For instance these clusters were rotated or translated in various configurations on the surface. We also modeled linear Cu_4/TiO_2, with each Cu atom bound to one oxygen atom in different orientations, and found it to be less stable by 2.6-2.8 eV when compared to the most stable Cu_4/TiO_2 in Figure 5.3d. After testing several different adsorption sites for Cu_4, we found two different stable Cu_4 tetramers on the surface as shown in Figure 5.3d and 5.3e. The more stable structure Cu_4(I), is shown in Figure 5.3d (ΔE_{ads} of -2.67 eV), while the second most stable structure Cu_4(II) is shown in Figure 5.3e (ΔE_{ads} of -2.52 eV). The more stable Cu_4(I) geometry undergoes structural changes so that the Cu_4 cluster does not resemble a rhombus shape, and one Cu-Cu bond between Cu_a and Cu_b breaks upon adsorption. The slightly less stable structure Cu_4(II)

keeps its basic rhombus shape intact upon adsorption. In Cu_4(I) the Cu_a atom sits at the bridge site between two O_{2c} atoms and bonds to a single Cu atom (Cu_a-Cu_d). In the Cu_4(II) structure Cu_a and Cu_c atoms are at the bridge sites between O_{2c} atoms, while Cu_b interacts with O_{2c}/O3c atoms. Cu_d atom is positioned away from the surface and only interacts with other Cu atoms. We found that the coordination numbers of Cu_a, Cu_b, Cu_c, and Cu_d in Cu_4(I) were 5, 3, 4, and 4. In Cu_4(II) the coordination numbers of Cu_a, Cu_b, Cu_c, and Cu_d were 5 , 5, 4, and 2. Upon adsorption of Cu_4 cluster, the Cu-Cu bond distances in Cu_4(I) and Cu_4(II) geometries were elongated. Compared to the gas phase Cu-Cu bond distances of around 2.4 Å in the gas-phase Cu tetramer, when Cu_4(I) adsorbs, two of the four edge bond distances (Cu_a-Cu_b and Cu_d-Cu_a) increased to 3.9 and 2.6Å. Likewise for Cu_4(II) adsorption, the Cu_a-Cu_b and Cu_c-Cu_d distances increased to 2.6 and 2.8 Å compared to the gas phase cluster edge bond distances of 2.4 Å. The binding energy of the Cu_4 clusters on the TiO_2 surface were -0.42 for Cu_4(I) and 0.16 eV for Cu_4(II). Unlike the Cu dimer and Cu trimers, the negative binding energy of Cu_4(I) shows the preference of Cu tetramer cluster formation on TiO2 compared to isolated Cu adatoms. We considered both Cu_4(I) and Cu_4(II) structures since they are very close in energy. The Cu_4(II) structure in Figure 5.3e, while slightly less stable, represents the case where the Cu_4 structure stays intact upon adsorption.

Seriani et al.[65] reported a tetrahedral Cu_4 to be the most stable geometry on TiO_2 and found it to be more stable by ∼0.5 eV compared to the flat structure depicted in Figure 5.3e. We found, however the adsorption energy of our flat Cu_4 structures to be more stable by 0.38 (Figure 5.3e) and 0.24 eV (Figure 5.3d) compared to an adsorbed Cu_4 tetrahedron. The flat Cu_4 cluster prefers to remain flat when adsorbed. This difference in flat versus tetrahedral geometry is largely due to the use of dispersion corrections in the present work, which increase favorable interactions between Cu atoms and the surface. We calculated that without the use of dispersion corrections, the adsorption energy of Cu_4 in Figure 5.3e was only 0.10 eV

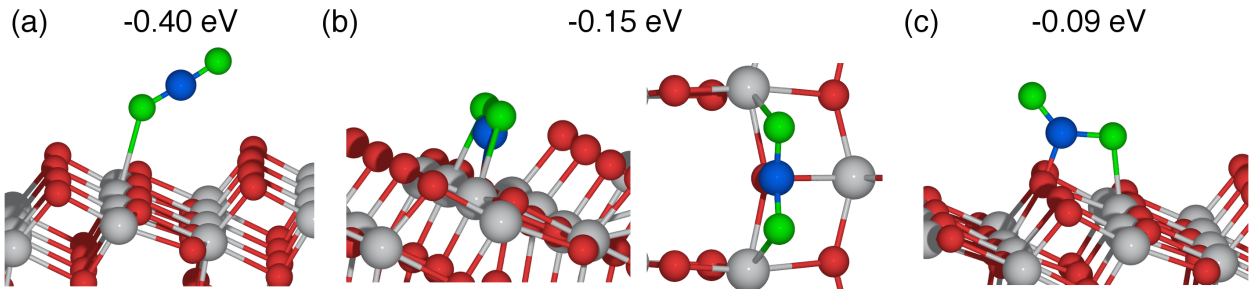

Figure 5.4: Most stable adsorbed CO_2 on TiO_2 in linear (a) and bent (b,c) configurations. Both side and top views are shown for the structure in (b). The numbers correspond to the adsorption energies of CO_2. The Ti and O atoms of TiO_2 are shown as gray and red spheres, while C and O atoms of CO_2 are shown as blue and green spheres.

more stable than the tetrahedral geometry reported by Seriani et al., compared to the flatter Cu_4 structure being 0.38 eV more stable than the tetrahedral structure with dispersion corrections applied. Without dispersion corrections, both the flatter Cu_4 and tetrahedral Cu_4 are close in energy (0.1 eV) and within the accuracy limits of DFT. Puigdollers et al. reported that the ordering of stability of metal cluster isomers on a TiO_2 surface can change with inclusion of dispersion corrections.[83] They reported that flat tetramers of Ag (similar to our Cu_4) on the TiO_2 anatase (101) surface were strongly stabilized when dispersion corrections were included in their DFT calculations. Similar to our flat Cu_4 clusters on the TiO_2 surface, other DFT reports exist for flat Cu_4 adsorption on Al_2O_3[23] and flat Ag_4 on the anatase (100) surface.[84] Our results of Cu cluster adsorption are also consistent with the experimental work by Tong et al.[85] Similar to our findings for Cu adsorption, they reported that Au dimers, trimers, and tetramers prefer to adsorb flat on the TiO_2 rutile (110) surface. An experimental study by Kaden et al. also reported the presence of flat Pd_n clusters on TiO_2 rutile (110) for $n \leq 10$ atoms.[32]

5.3.2 CO_2 adsorption over Cu Clusters and TiO_2

The adsorption of CO_2 on metal oxides such as TiO_2 has been widely studied in order to identify potential catalysts for CO_2 reduction.[33–39] Geometrical parameters such as bond angle of CO_2 and bond distance of the C-O bonds have been used to identify CO_2 activation on a catalyst surface.[39,46,86] Neutral CO_2 is a stable molecule with a linear structure as its ground state geometry. When neutral CO_2 undergoes one electron reduction, a CO_2 anion is formed that has a bent CO_2 geometry.[39] The bent configuration may lead to increased reactivity of CO_2, including possible C-O bond breaking.[13,39] Activation of CO_2 to form the bent structure is believed to be the initial step in the photoreduction of CO_2, and it has a large reorganizational energy cost for the transformation from a linear to bent geometry.[41] In this section we report on adsorption of CO_2 in linear and bent forms on TiO_2, as well as over supported Cu_x clusters. This allows us to identify the potential role of Cu and titania in activating the CO_2 molecule.

We modeled linear and bent CO_2 as neutral species adsorbed on Cu_x/TiO_2 by considering multiple adsorption sites. We modeled CO_2 adsorbed directly to Cu atoms, surface TiO_2 sites, and interfacial sites, where CO_2 interacts with both the Cu atom(s) and TiO_2 atoms. Bent CO_2 on these different sites was modeled by considering structures that had C-M (M=Cu,Ti,O) and O_{CO_2}-N (N=Cu,Ti) interactions, or in other words geometries with O_{CO_2} and C atoms interacting with surface O, Cu, and Ti atoms. Linear CO_2 geometries on Cu clusters, surface TiO_2 sites, and interfacial sites were modeled by considering various O_{CO_2}-Y (Y=Ti,Cu) interactions. Considering this variety of potential adsorption geometries allowed us to determine several possible configurations. In the following we report the most stable bent and linear CO_2 adsorption geometries.

CO_2 adsorption on TiO_2

The most stable linear and bent configurations of CO_2 on the clean TiO_2 surface have been reported earlier.[15,42,43] In our work, we modeled the reported most stable configurations as shown in Figure 5.4. In the linear adsorption mode (with the O-C-O bond angle close to 180^o), CO_2 binds to TiO_2 with a bond between an O_{CO_2} atom and a Ti_{5c} atom at the surface. The bond distance between O_{CO_2} and Ti_{5c} was found to be 2.5 Å and the ΔE_{ads} was -0.40 eV. We give a summary in Table 5.1 of adsorption energies and geometry information for the most stable linear and bent CO_2 configurations over the various studied surfaces. In the case of bent adsorption on pure anatase (with the O-C-O bond angle considerably smaller than 180^o), two binding modes having close ΔE_{ads} values (-0.15 and -0.09 eV) are shown in Figure 5.4b, c. Both bent structures resemble carbonate (CO_3) geometries. Previous work[15,42,43] however reported that the carbonate-like structure in Figure 5.4c was more stable than the structure in Figure 5.4b by 0.1 to 0.2 eV. This observed difference in the most stable bent CO_2 structure may be due to using different computational parameters, such as basis set, pseudopotential, or dispersion corrections. Nonetheless, we found the difference in adsorption energies between these two carbonate structures to be only 0.06 eV, which may be close to the accuracy of our DFT method. Our results are consistent with previous results that show bent CO_2 to have weaker adsorption energies compared to linear CO_2 on the anatase surface. For example, Sorescu et al. reported ΔE_{ads} values of -0.48 and -0.16 eV for the most stable linear and bent CO_2 on anatase, similar to our values.

CO_2 adsorption over Cu/TiO_2

The adsorption geometries of the most stable linear and bent CO_2 configurations over Cu/TiO_2 are shown in Figure 5.5. In the most stable linear configuration (Figure 5.5a), CO_2 interacts with a Ti_{5c} atom through an O_{CO_2} atom with an ΔE_{ads} of -0.40 eV (the same value when no Cu is present). In this configuration CO_2 does not even directly in-

Table 5.1: Structural parameters of the most stable adsorbed bent and linear CO_2 molecules. The last two columns show distances between CO_2 atoms and closest surface atoms (designated M and N). The closest surface atom types are given in parenthesis. 4(I) and 4(II) refer to the two Cu_4 clusters in Figure 5.3d,e respectively.

x (Cu_x)	**CO_2** Configuration	ΔE_{ads} (eV)	**C-O Bond** Length (Å)	**O-C-O angle** (°)	**C-M** Distance (Å)	**O-N** Distance (Å)
	CO_2 (gas)		1.17, 1.17	180.0		
0	bent	-0.15	1.25, 1.25	135.1	1.42 (O_{3c})	2.18, 2.22 (Ti_{5c})
	linear	-0.40	1.16, 1.18	177.4	3.37, 3.47 (O_{2c})	2.47 (Ti_{5c})
1	bent	-0.38	1.24, 1.28	132.1	1.39 (O_{3c})	2.05 (Cu); 2.27, 2.40 (Ti_{5c})
	linear	-0.40	1.17, 1.18	176.8	3.20, 3.30 (O_{2c})	2.59 (Ti_{5c})
2	bent	-0.84	1.23, 1.30	128.4	2.01, 2.04 (Cu)	2.42 (Cu); 2.05 (Ti_{5c})
	linear	-0.49	1.17, 1.18	177.4	3.01,3.15 (O_{2c})	2.71 (Ti_{5c})
3	bent	-0.56	1.23, 1.27	128.7	1.45 (O_{2c})	1.93 (Cu); 2.83 (Ti_{5c})
	linear	-0.46	1.17, 1.18	176.3	2.67 (O_{2c})	2.28 (Cu)
4(I)	bent	-0.32	1.27, 1.22	133.0	1.54 (O_{2c})	1.99 (Cu); 2.85 (Ti_{5c})
	linear	-0.38	1.18, 1.17	178.0	3.36 (O_{2c})	2.57 (Ti_{5c})
4(II)	bent	-0.54	1.26, 1.28	128.7	2.57 (Cu); 1.37 (O_{2c})	2.00 (Cu); 2.07 (Ti_{5c})
	linear	-0.48	1.17, 1.18	179.2	3.17 (O_{2c})	2.48 (Cu); 2.72 (Ti_{5c})

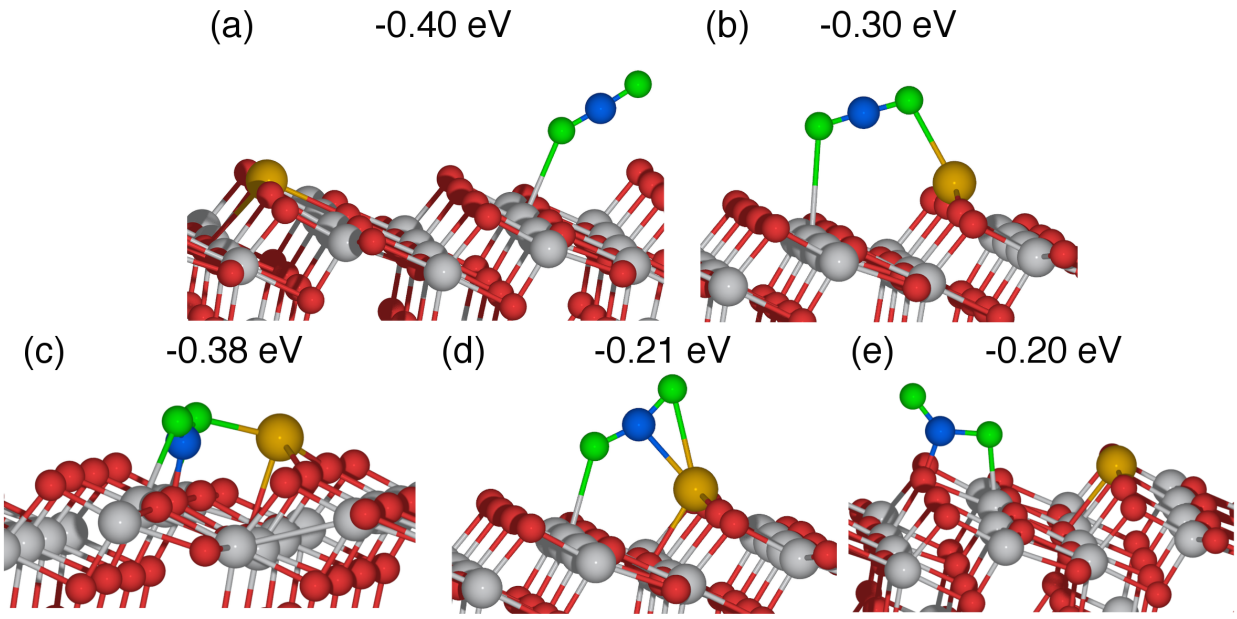

Figure 5.5: Stable adsorbed CO_2 on Cu/TiO_2 in linear (a,b) and bent (c,d,e) configurations. The numbers indicate adsorption energies of the CO_2 molecules.

teract with the Cu atom and is actually far from it on the surface. When a linear CO_2 interacts directly with Cu and Ti_{5c} atoms (Figure 5.5b), the calculated adsorption energy is weaker, being -0.30 eV. This indicates that the presence of Cu does not significantly affect the adsorption of linear CO_2, as the CO_2 prefers to interact directly with the titania surface. In the bent CO_2 geometry, the most stable adsorption occurs at the Cu/TiO_2 interface (Figure 5.5c), where the primary interactions occur between CO_2 and Ti_{5c}/O_{3c} atoms, while secondary interactions occur between O_{CO_2} and Cu. When CO_2 adsorbs on the surface, a strong displacement of the Cu atom towards CO_2 by $\sim$1.0Å occurs. The short bond distances of (C-O_{3c} = 1.39Å, O_{CO_2}-Cu = 2.05Å, and O-Ti_{5c}=2.3,2.4Å) between CO_2 and the surface atoms indicate strong interactions. In contrast, in linear CO_2 adsorption the distances between CO_2 and surface atoms are large (O_{CO_2}-Ti_{5c}=2.59Å and C-O_{2c} > 3.1Å), indicative of weak adsorption. Table 5.1 also shows that the C-O bonds in CO_2 are elongated to 1.24 and 1.28 Å compared to the gas phase value of 1.17 Å. The O-C-O bond angle was also bent to 132^o. The ΔE_{ads} of bent CO_2 over Cu/TiO_2 (-0.38 eV) is significantly stronger than just over pure TiO_2 (-0.15 eV). Thus, a Cu atom stabilizes the bent CO_2 structure. This conclusion is similar to our previous work, where we also found a Cu atom to promote bent CO_2 adsorption.[15] It has also been reported[87] that bent CO_2 molecules over metal atoms (Rh, Ru, Pd) supported on TiO_2 anatase(101) surfaces have strong adsorption energies (in the range of -0.5 to -0.9 eV).

Two other bent CO_2 structures are shown in Figure 5.5. CO_2 binding at the interface site, shown in Figure 5.5d (ΔE_{ads} of -0.21 eV) had the C atom and one of the O_{CO_2} atoms both interacting with the Cu atom and the O-C-O angle in CO_2 was slightly bent (159^o). The other bent CO_2 structure with a ΔE_{ads} of -0.20 eV preferred to bind to just the titania surface, away from the Cu atom in a carbonate-like structure (Figure 5.5e). Both these structures were not as stable as the most stable carbonate-like structure in Figure 5.5c, where the CO_2 structure has primary interactions with TiO_2 along with secondary interactions with

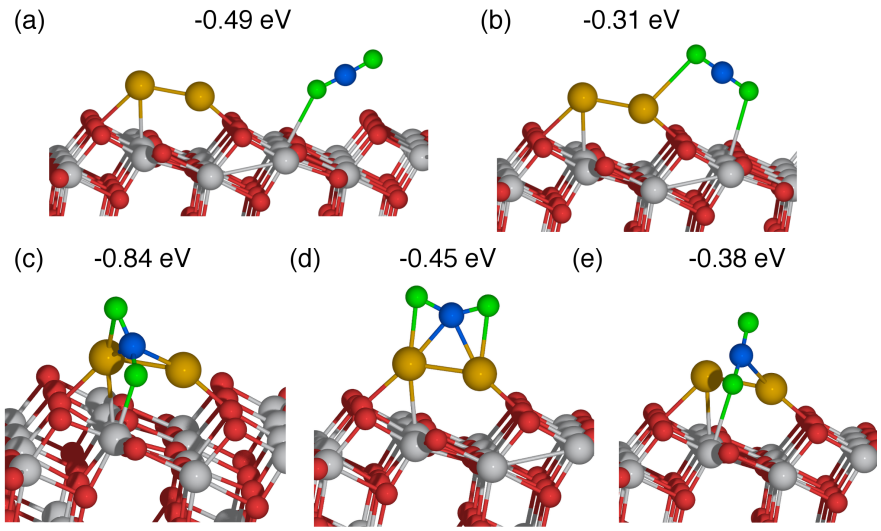

Figure 5.6: Several stable adsorbed CO_2 on Cu_2/TiO_2 in linear (a,b) and bent (c,d,e) configurations. The numbers indicate adsorption energies of the CO_2 molecules.

the Cu atom.

CO_2 adsorption on Cu_2/TiO_2

The two most stable linear CO_2 adsorption geometries on Cu_2/TiO_2 were found to occur at the TiO_2 surface and at the Cu_2/TiO_2 interface (see Figure 5.6a,b). Adsorption over the TiO_2 surface involved O_{CO_2} binding to a Ti_{5c} atom, similar to other linear geometries. This structure had a ΔE_{ads} of -0.49 eV, which is slightly more negative than that on pure TiO_2 (-0.40 eV). The large bond distance of 2.71 Å between O_{CO_2}-Ti_{5c} further suggests weak adsorption. The other linear CO_2 was adsorbed at an interface site, and was arranged with one O_{CO_2} atom interacting with Ti_{5c} while the other one O_{CO_2} atom interacted with a Cu atom. Linear CO_2 at the interfacial site was less stable with a ΔE_{ads} of -0.31 eV. The large bond distances of 2.9 and 2.7 Å between CO_2 and the surface also showed that linearly bound CO_2 at the interfacial site was weakly adsorbed.

Uzunova et al. reported on the role of Cu dimers in CO_2 conversion to methanol over Cu_2O.[45] They reported that Cu dimers formed on the $Cu_2O(001)$ surface, as well as $Cu_{32}O_{16}$

and $Cu_{14}O_7$ nanoclusters, due to surface reconstruction. These dimers served as active sites for strong adsorption of bent CO_2. We observed similar strong adsorption of bent CO_2 over Cu_2 on the anatase (101) surface. The most stable bent CO_2 (Figure 5.6c) binds strongly at a Cu_2/TiO_2 interface with an ΔE_{ads} of -0.84 eV. In this structure the C atom interacts with both Cu atoms. One O_{CO_2} atom interacts with a Ti_{5c} atom while the other O_{CO_2} atom interacts with a Cu atom. The short bond distances of around 2.0 Å (see Table 5.1) between atoms of CO_2 and the surface atoms are indicative of stronger adsorption. The bent CO_2 also displays strong bending (128°) and C-O_{CO_2} bond distances of 1.23/1.30 Å (compared to gas phase CO_2 values of 1.17/1.17 Å).

Besides the most stable CO_2 bent configuration, two other bent CO_2 structures (directly over Cu_2 and at the interface) also exist. The bent CO_2 molecule directly interacting with the Cu cluster (Figure 5.6d) has a ΔE_{ads} value of -0.45 eV. The last bent CO_2 structure has a ΔE_{ads} value of -0.38 eV and binds at an interfacial site (Figure 5.6e). The O-C-O angle of CO_2 in this configuration is 163°, which indicates an intermediate state between the bent and linear CO_2 structures. This structure slightly resembles the most stable configuration, however it adsorbs with a significantly weaker ΔE_{ads}. Further, the bonds formed between CO_2 and the surface are significantly larger (C-Cu = 2.59 and O_{CO_2}-Ti5c = 2.49 Å) compared to the most stable adsorption configuration. The later geometry in Figure 5.6e only interacts with one Cu atom, while the more stable geometry in Figure 5.6c interacts with two Cu atoms, which may explain why it is weaker. Incidentally the two bent configurations in Figure 5.6d,e have ΔE_{ads} values that are similar to linear CO_2 adsorption on pure TiO_2 (-0.40 eV). Thus, the Cu dimer is able to stabilize several possible bent CO_2 structures.

CO_2 adsorption on Cu_3/TiO_2

The most stable linear geometry on Cu_3/TiO_2 (ΔE_{ads} = -0.46 eV) was found to occur with CO_2 directly interacting with the Cu cluster through the top Cu_a atom (see Figure 5.7a).

The second most stable linear CO_2 adsorption configuration has CO_2 bound to the surface without directly interacting with Cu atoms (see Figure 5.7b), similar to other linear adsorption modes. The two linear adsorption energies are very close in energy (0.03 eV difference), and are both close to the adsorption energy over pure TiO_2 (-0.40 eV). Among all the adsorbed linear CO_2 structures, only for the case of Cu_3 did linear CO_2 interact with the Cu cluster in its most stable configuration.

In the case of bent CO_2 adsorption over Cu_3/TiO_2, the most stable geometry occurs at an interfacial site with ΔE_{ads} being -0.56 eV. Figure 5.7c shows this geometry, which resembled a carbonate structure. Here, the C atom was bound to an O_{2c} and the O_{CO_2} atoms were bound to either a Cu or Ti_{5c} atom. The short bond distances for C-O_{2c} (1.45 Å) and O_{CO_2}-Cu (1.93 Å) are indicative of strong interactions. Our results show that the top Cu_a atom in Cu_3 is the preferred site for both the most stable bent and linear adsorption structures. This is likely due to the top Cu_a atom having the least coordination number of 2 compared to the other Cu atoms (coordination number of 4), and is therefore most reactive. This top Cu atom is only coordinated to two other Cu atoms.

The other two bent CO_2 structures (see Figure 5.7d,e) were less strongly adsorbed, with ΔE_{ads} values of -0.28 and -0.16 eV. The former had a carbonate-like geometry that was adsorbed at an O_{2c} site in the vicinity of the Cu cluster. The shortest O_{CO_2}-Cu_b distance was 3.23Å indicating that any interactions between the CO_2 molecule and Cu cluster were indirect. This carbonate-like structure was similar to the bent adsorption structure on Cu/TiO_2 (Figure 5.5e) and pure TiO_2 (Figure 5.4c). Our results show that in the presence of Cu or Cu_3 on TiO_2, this carbonate-like geometry had slightly stronger adsorption energies (-0.20 and -0.28 eV respectively) when compared to that on pure TiO_2 (-0.09 eV). Since the Cu atom/clusters only indirectly interacted with these carbonate-like CO_2, this suggests that Cu may have changed the surface and electronic properties in its vicinity.

The other bent structure was also a carbonate-like structure but it occurred at an inter-

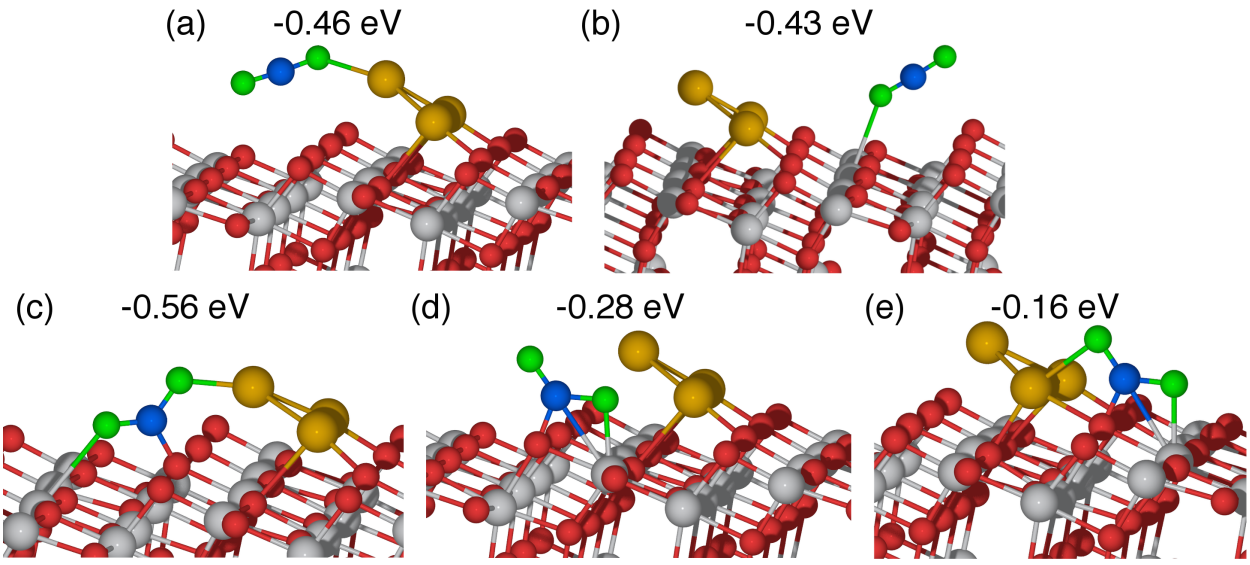

Figure 5.7: Several stable CO_2 adsorption configurations on Cu_3/TiO_2 in linear (a,b) and bent (c,d,e) configurations. The numbers indicate adsorption energies of the CO_2 molecules.

facial site with one O_{CO_2} atom bonding to a Ti_{5c} while the other O_{CO_2} atom was bound to a Cu atom. This geometry was weakly bound to the surface (ΔE_{ads} = -0.16 eV) which demonstrates that not all interfacial sites lead to stabilization of bent CO_2. The Cu atom involved in this structure was more fully coordinated, in contrast to the structure in Figure 5.5c where the CO_2 interacted with the lone under-coordinated Cu atom and exhibited strong adsorption. This suggests that the coordination of the Cu atoms may play a role in how well they bind to CO_2.

CO_2 adsorption on Cu_4/TiO_2

CO_2 adsorption on Cu_4(I)/TiO_2 structure We modeled CO_2 adsorption over the most stable Cu_4 cluster (I) and the slightly less stable Cu_4(II) cluster. Over Cu_4(I) the two most stable linear CO_2 had similar ΔE_{ads} of -0.38 (Figure 5.8a) and -0.36 eV (Figure 5.8b). A very similar adsorption structure (not shown) to Figure 5.8a, where CO_2 was adsorbed far away from Cu_4 also had a close ΔE_{ads} of -0.37 eV. All these structures bind to Ti_{5c}. For the geoemetry in Figure 5.8b the CO_2 also interacts with a Cu_d atom. The ΔE_{ads} of these most

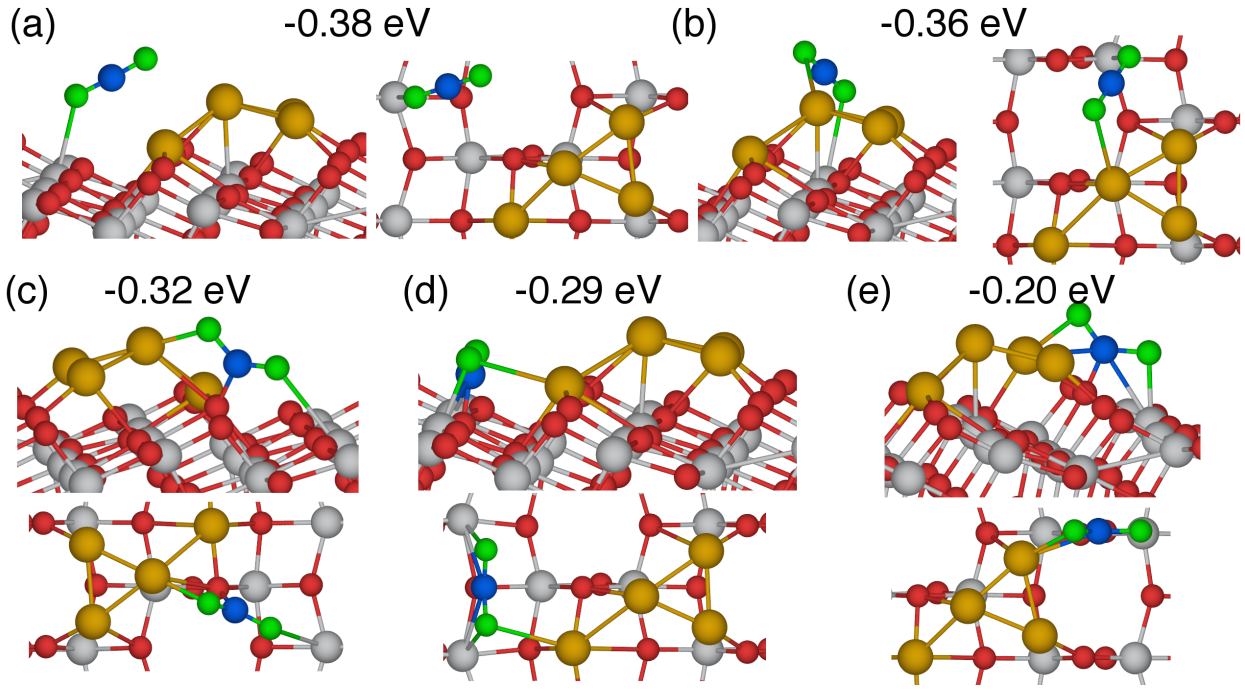

Figure 5.8: Several stable adsorbed CO_2 on $Cu_4(I)/TiO_2$ (the most stable Cu_4 structure as shown in Figure 5.3d) in linear (a,b) and bent (c,d,e) configurations. Both side and top views have been shown. The numbers indicate adsorption energies of the CO_2 molecules.

two linear CO_2 were similar to when no Cu was present on the TiO_2 surface (ΔE_{ads}=0.40 eV). In the case of bent CO_2 adsorption on $Cu_4(I)/TiO_2$, we found three different adsorption geometries at the interfacial site with ΔE_{ads} differing by around 0.1 eV (see Figure 5.8c-e). All these geometries appeared carbonate like. ΔE_{ads} of the most stable bent CO_2 consisted of each of the O_{CO_2} binding to Cu_d or Ti_{5c} atom. This adsorption configuration was similar to that on Cu_3/TiO_2 (ΔE_{ads}=-0.56 eV), however the ΔE_{ads} of -0.32 eV on $Cu_4(I)$ was significantly smaller than that on Cu_3. Interestingly, over $Cu_4(I)$, the ΔE_{ads} of the most stable bent and linear CO_2 were similar in energy.

The ΔE_{ads} (-0.29 eV) of the next most stable bent CO_2 over $Cu_4(I)$ was close in energy to the most stable bent structure. These two geometries were similar, except the CO_2 interacted with different Cu atoms. The third stable bent CO_2 had a geometry similar to that on Cu_3/TiO_2 (see Figure 5.8e and Figure 5.7e). Here, the O_{CO_2} bind with either Cu or Ti_{5c} atoms, while the C atoms bond to surface O_{2c}.

CO2 adsorption on Cu_4(II)/TiO_2 structure We now discuss the second most stable Cu_4/TiO_2 structure (II) (see Figure 5.3e). The most stable linear CO_2 was found to occur at the interface (ΔE_{ads}=-0.48) where the O_{CO_2} atoms bond to Cu_d and Ti_{5c} atoms (see Figure 5.9a). Another linear CO_2 structure had an ΔE_{ads} of -0.40 eV, where O_{CO_2} was bound to a Ti_{5c} atom. Interestingly, our results show that all the most stable linear structures on Cu_x/TiO_2 had ΔE_{ads} that were close to that of linear structures on pure TiO_2 (within 0.1 eV). This would again suggest that Cu clusters do not significantly affect linear CO_2 adsorption for activating CO_2.

The most stable bent CO_2 geometry was found to occur at an interfacial site (Figure 5.9c) and had a carbonate-like structure with ΔE_{ads} of -0.54 eV. Here the C atom was bonded to an O_{2c} atom and the O_{CO_2} atoms bonded to either Cu_b or Ti_{5c} atoms. Although this structure resembled a geometry on Cu_3/TiO_2 (Figure 5.7e) and $Cu_4(I)/TiO_2$ (Figure 5.8e),

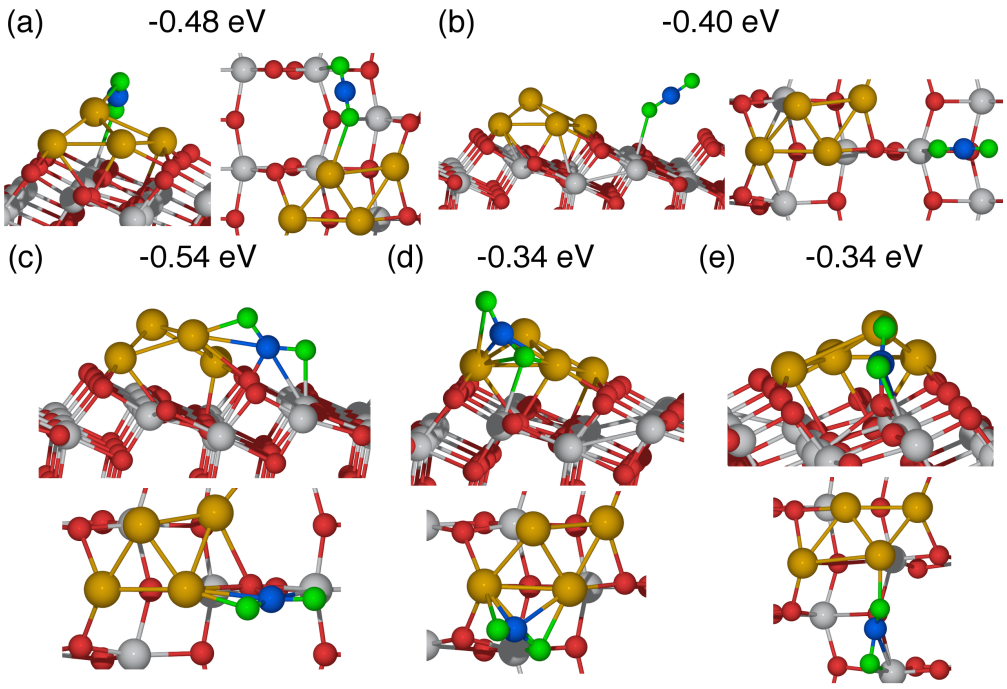

Figure 5.9: Several stable adsorbed CO_2 on $Cu_4(II)/TiO_2$ in linear (a,b) and bent (c,d,e) configurations. Both side and top views have been shown. The numbers indicate adsorption energies of the CO_2 molecules.

the adsorption energy of -0.54 eV was significantly stronger (∼-0.2 eV). When CO_2 adsorbs, the Cu_b atom displaces 0.8Å away from the surface to allow the favorable adsorption. Over Cu_3 and Cu_4(I) this displacement does not occur. We find that Cu_4(II) stabilizes the bent CO_2 slightly more than linear CO_2. In contrast, linear CO_2 is preferred compared to bent CO_2 over Cu_4(I). Yang et al.[47] reported that bent CO_2 on Pt_4/TiO_2 adsorbed through direct Pt_4 interactions (without CO_2 interacting with TiO_2) with a ΔE_{ads} of -0.22 eV. Over pure TiO_2 they found linear CO_2 to have an adsorption energy of -0.14 eV, indicating a difference of 0.08 eV between their Pt_4 and pure TiO_2 adsorption energies. The difference in energy between bent CO_2 on Cu_4(II) and linear CO_2 on pure TiO_2 was 0.14 eV in our work, a similar difference to the Pt_4 work of Yang et al. However, our adsorption energies were much stronger. Yang et al. did not use dispersion corrections which could be why they obtained smaller absolute adsorption energies compared to our results.

Figure 5.9d,e shows two other bent CO_2 structures, whose ΔE_{ads} were both -0.34 eV. These structures both adsorb at interfacial sites. The bent CO_2 shown in Figure 5.9d resembles the bent CO_2 geometry on Cu_2/TiO_2 (Figure 5.6c), but is less stable. The atoms in the Cu_4(II) cluster have higher coordination than the Cu_2 cluster, which could explain why Cu_2 has stronger adsorption. The last bent CO_2 structure is shown in Figure 5.9e. Here, the C atom was bound to an O_{3c} atom, while the O_{CO_2} atoms were bound to either Cu_d or Ti_{5c} atoms.

Comparison of CO_2 Adsorption

We show in Figure 5.10a a comparison of the most stable bent and linear CO_2 adsorption energies on Cu_x/TiO_2. On pure TiO_2, adsorption of linear CO_2 is more stable than bent CO_2. However, in the presence of Cu bent CO_2 is always strongly stabilized. Over atomic Cu linear CO_2 is slightly more stable than bent CO_2 (by only 0.02), while over Cu_4(I) linear CO_2 is also slightly more stable than bent CO_2 (by 0.06 eV). Over Cu_2, Cu_3, and Cu_4(II)

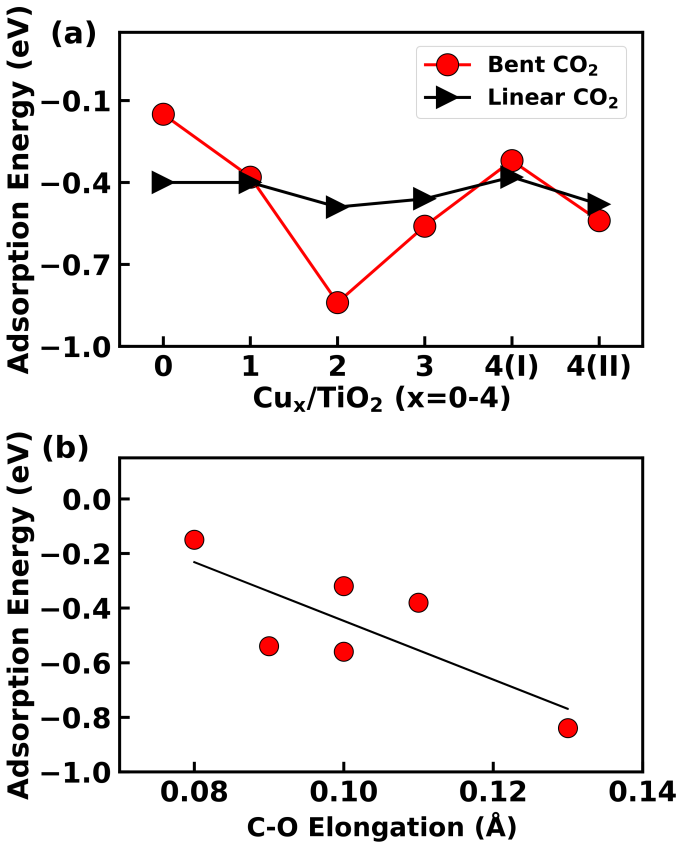

Figure 5.10: (a) Adsorption energies (ΔE_{ads}) of the most stable bent and linear CO_2 on the different Cu_x/TiO_2 surfaces. (b) The correlation between adsorption energies of bent CO_2 (ΔE_{ads}) on Cu_x/TiO_2 surfaces, and the C-O bond elongation (for the largest bond) upon adsorption. The solid line is the best linear fit to the data.

bent CO_2 is always preferred. The most stable bent CO_2 occurs over Cu_2 with a very strong adsorption energy of -0.84 eV. In contrast, the Cu_2 dimer had the lowest adsorption energy among the Cu_x clusters on TiO_2 (see Section 5.3.1, suggesting that lower adsorption energy of the Cu cluster on TiO_2 results in a larger adsorption energy of bent CO_2. A review by Campbell[88] discussed an inverse correlation between adsorption strength of metals on oxide support and the adsorption strength of small adsorbates like O_2, similar to what we find in our work. We discuss more details of Cu_2 later in this article. Of similar note, Kaden et al. reported CO oxidation activity as a function of Pd cluster size for Pd adsorbed on TiO_2 rutile(110).[32] They found the Pd_2 cluster to have the largest activity out of Pd_x clusters (x=0,1,2,4). We further found the trends in ΔE_{ads} values for bent CO_2 to be related to C-O elongation upon adsorption, which could be indicative of CO_2 activation. The largest bond change in adsorbed bent CO_2 correlates with ΔE_{ads}, as shown in Figure 5.10b. This indicates that increased interactions between CO_2 and the surface weaken the C-O bond (presumably as CO_2/surface bonds form) and lead to its elongation.

The ΔE_{ads} of adsorbed bent CO_2 consists approximately of two competing energy terms, the interaction energy between CO_2 and surface, and the reorganization energy for the formation of bent CO_2 from a linear CO_2 (i.e. energy to bend linear CO_2 to a bent structure). This can be written as: $\Delta E_{ads} \sim E_{CO_2\text{–}Cu_x/TiO_2\,\text{interaction}} + E_{CO_2\,\text{reorganization}}$. For linear CO_2 adsorption, the reorganization energy is essentially zero. We can assume that the reorganization energies are close to each other for the bent adsorption modes since the angles are similar to each other. On pure TiO_2, bent CO_2 had a weak ΔE_{ads} value (-0.15 eV), which indicates that the interaction energy is slightly more exothermic than the reorganization energy. However, the interaction energy term is much larger than the reorganization energy term when Cu clusters are present, such that the overall ΔE_{ads} values become more exothermic for bent CO_2 on Cu_x/TiO_2 compared to pure TiO_2. Cu_x has strong interactions with CO_2, as we show in our analysis of the electronic states in Section 5.3.3.

We found that the most stable bent CO_2 geometries were at interfacial sites with CO_2 interacting with both the TiO_2 surface atoms (O_{3c}, O_{2c}, Ti_{5c}) and Cu cluster. For example see geometries in Figure 5.5c, Figure 5.6c, Figure 5.7c, Figure 5.8c, and Figure 5.9c. Graciani et al.[89] also reported also reported that activated bent CO_2 was present at Cu-Ceria interfacial sites using infrared reflection absorption spectroscopy (IRRAS). In previous DFT studies bent CO_2 adsorption was reported to occur at the interfacial sites of TiO_2 anatase(101) supported Cu_{10},[48] Ag_8,[46] Pt_6[47] and Pt_8.[46] On Cu_{10}, Pt_6, and Pt_8/TiO_2, the most stable adsorption sites consisted of C-metal(Cu/Pt) interactions, while on Ag_8/TiO_2, the most stable site was a carbonate-like structure at the interfacial site. In our work, except for Cu_2 with C-Cu interactions, the most stable bent CO_2 adsorbed in carbonate-like structures. Experimental studies using infrared spectroscopy involving titania supported Cu or Rh have also reported the formation of carbonate-like structures,[90,91] as well as bent CO_2 with C-Rh interactions.[92,93] CO_2 as carbonate-like species were also observed on $CeO_x/Cu(111)$ catalysts using infrared reflection absorption spectroscopy.[89]

The strong adsorption energy of bent CO_2 on Cu_2/TiO_2 can be related to each Cu atom in Cu_2/TiO_2 having low coordination (coordination numbers of 3 and 2 for Cu_2). This low coordination makes the Cu_2 cluster very reactive towards CO_2 adsorption and activation. Other Cu_x structures however, while being active for bent CO_2 formation, are likely less reactive than Cu_2 due to having larger coordination numbers, ranging from 3-5 (except Cu_a atom in Cu_3, which has coordination number of 2). Silaghi et al. also found that bent CO_2 was stabilized strongly at the low coordinated edge and corner sites of alumina supported Ni clusters.[94] Strong adsorption of bent CO_2 on Pt_n/TiO_2 (n=4,6,8) was found to occur at under-coordinated Pt sites.[46,47]

5.3.3 Characterization of Adsorbed CO_2

Vibrational Frequencies of Adsorbed CO_2

Experimentally, the presence of bent or linear form of CO_2 is often identified by techniques based on infrared or Raman spectroscopy.[39,92,95–97] Several DFT papers have assisted experimental observations by clarifying the structure of adsorbed CO_2 (linear, bent, carbonate, or bicarbonate) using calculated vibrational frequencies.[15,42,44,60,86,98,99] In this section we report calculated vibrational frequencies of the most stable adsorbed linear and bent CO_2 geometries.

We first calculated the vibrational frequencies of gas phase CO_2, which has several modes: asymmetric stretching (one bond elongates and other contracts), symmetric stretching (both bonds elongate/contract in unison), and in/out plane bending modes (O-C-O bond angle increases/decreases from 180^o). For the asymmetric, symmetric, and bending modes, our calculated frequencies of 2380, 1308, and 657 cm^{-1} agree well with the experimentally reported values of 2349, 1333, and 667 cm^{-1} respectively.[100] Upon adsorption of CO_2 on TiO_2 P25 (which is predominantly anatase), the experimentally reported vibrational frequencies become 2355 (asymmetric stretch), 1379 (symmetric stretch), and 1271 cm^{-1} (first overtone of bending mode).[101] In another experimental paper, Mino et al. reported the asymmetric stretching frequency of linearly adsorbed CO_2 on the anatase (101) surface to be 2357 cm^{-1}.[99] Our calculated frequencies of the stretching modes for linear CO_2 on the (101) surface, 2367 (asymmetric) and 1351 (symmetric) cm^{-1}, are comparable to these experimental values. The bending overtone at 1271 cm^{-1} was a result of the Fermi resonance between the symmetric stretching mode and the first overtone of the bending mode, which shifts the bending frequency to higher values.[86,99] DFT does not capture these resonance effects, as only the normal vibration modes are calculated, and our calculated bending modes were 667 and 688 cm^{-1}. Two types of bending modes are determined from our calculations: a parallel

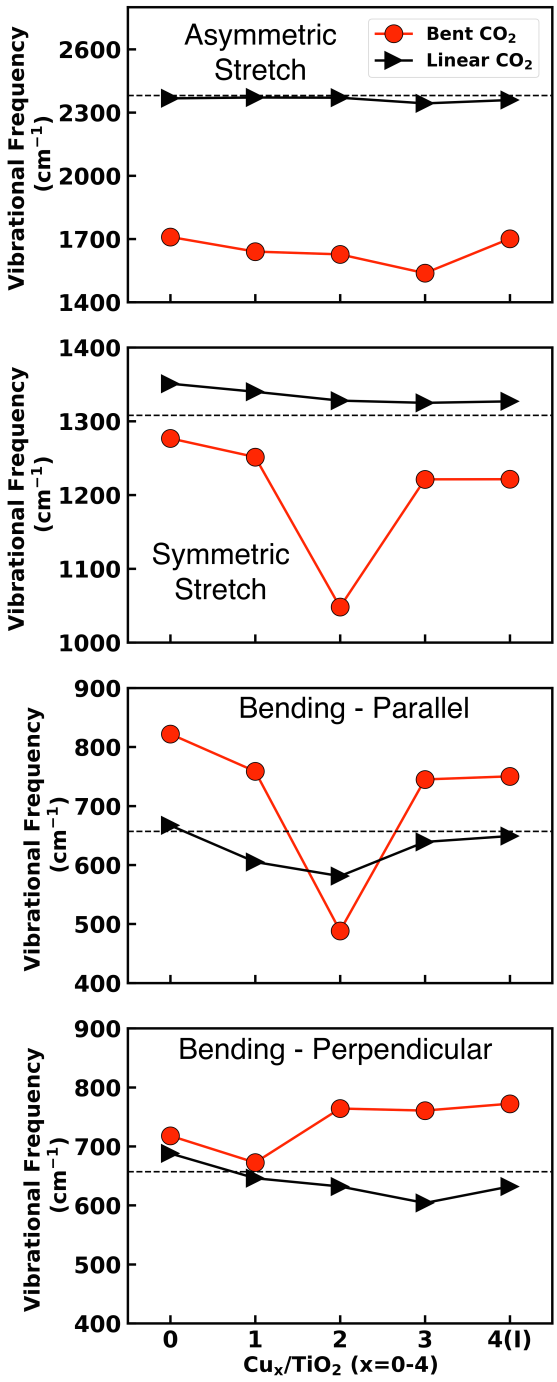

Figure 5.11: Vibrational frequencies of CO_2 for the most stable adsorbed linear and bent CO_2 configurations on Cu_x/TiO_2 surfaces. The vibrational frequencies from top to bottom are the asymmetric stretching, symmetric stretching, bending parallel, and bending perpendicular modes. The dashed line indicates the calculated gas phase CO_2 vibrational frequencies.

bending mode occurs when the CO_2 bends primarily in the plane of the surface, while a perpendicular bending mode occurs when CO_2 bends primarily perpendicular to the surface. We visually examined the two calculated bending modes, and assigned them based on which mode best appeared to be parallel/perpendicular. Our calculated vibrational frequencies for adsorbed linear CO_2 are also close to previous DFT results. Comparing to several previous papers we find mean absolute differences of 13,[99] 18,[42] 26,[43] 24[86]cm^{-1} when comparing the four vibrational modes. For example, Mino et al.[99] reported the asymmetric, symmetric, and bending frequencies to be 2359, 1340, and 642/641 cm^{-1} respectively, which are comparable to our calculated values.

Figure 5.11 shows the various vibrational frequencies of adsorbed CO_2. We note that in this section we only report the results for most stable Cu_4(I) geometry. All the asymmetric and symmetric stretching modes of bent CO_2 have lower frequencies (red shifted) compared to linear CO_2. This strong difference ranges from 658 to 806 cm^{-1} for the asymmetric stretch and 74 to 280 cm^{-1} for the symmetric stretch. Such strong red shifts for bent adsorbed CO_2 are due to the strong interaction of the CO_2 molecule with the surface atoms. In contrast, for adsorbed linear CO_2 weak interactions between CO_2 and surface occur, so that the asymmetric and symmetric stretching frequencies are very close to gas phase frequencies. In the case of bent CO_2 adsorbed on the Cu_2/TiO_2 surface, the symmetric stretching frequency is significantly red shifted to 1048 cm^{-1}. We attribute this large shift to the distinct strong C-Cu interactions between CO_2 and Cu_2, which do not occur in the carbonate-like structures observed on other Cu_x/TiO_2 surfaces. The bending frequencies however for bent CO_2 are higher compared to linear CO_2 (blue shifted). An exception occurs for the parallel bending mode on Cu_2/TiO_2, where a low vibrational frequency of 488 cm^{-1} is observed, which again can be attributed to the distinct strong C-Cu interactions occurring with Cu_2. Overall, we generally observe large shifts in the stretching frequencies of bent CO_2, with red shifts of $\sim$600-800 cm^{-1} (asymmetric) and $\sim$100-300 cm^{-1} (symmetric) occurring, while bending

modes have blue shifts of ∼100 cm^{-1} compared to linear CO_2 frequencies.

In-situ FTIR and diffuse reflectance infrared spectra on Cu/TiO_2 catalysts show the formation of bent carboxylate species with asymmetric stretching frequencies corresponding to peaks at 1567 and 1595 cm^{-1}.[102,103] In the work by Neatu et al.,[13] in-situ time resolved IR spectra showed that reactive bent CO_2 intermediates had an asymmetric stretching frequency of 1589 cm^{-1} (carboxylate species) and 1674 cm^{-1} (carbonate species) when adsorbed on a titania supported Au-Cu nanoalloy. In other experimental work, the asymmetric and symmetric stretching frequencies of 1610-1680 cm^{-1} and 1220-1290 cm^{-1} were reported for activated bent CO_2 adsorbed on defective TiO_2, $CeO_x/Cu(111)$, and titania based nanotubes.[89,92,96,104,105] Our calculated bent CO_2 species on Cu_x/anatase(101) showed predominantly a range of vibrational frequencies being 1537-1709 cm^{-1} and 1048-1277 cm^{-1} for asymmetric and symmetric stretch respectively, which were similar to these earlier reported experimental values. Using DFT, Yang et al.[46,47] reported the vibrational frequencies of bent CO_2 at the interfacial sites on Ag_8, Pt_6, and Pt_8/TiO_2 to be in the range of 1510-1750 cm^{-1} (asymmetric stretch), 1150-1270 cm^{-1} (symmetric stretch) and 700-850 cm^{-1} (bending). Another DFT work by Mudiyanselage et al.[104] reported that at the of $CeO_x/Cu(111)$ interface, the asymmetric stretching frequency of bent CO_2 species was 1610 cm^{-1}. The vibrational frequency ranges for bent CO_2 at the Cu_x/TiO_2 interface calculated in our present work fall in a similar range of vibrational frequencies compared to these earlier DFT results.

Charge Analysis of Adsorbed CO_2

Activation of CO_2 to form a negative anion is believed to be the first step in the CO_2 reduction reaction.[39,40] He et al. identified bent CO_2 structures on neutral and negatively charged anatase (101) surfaces (similar to Figure 5.4). On a neutral TiO_2 surface bent CO_2 become moderately charged as -0.11 indicating the possibility of CO_2 anion formation. However, on a negatively charged TiO_2 surface (designed to mimic the surface with photoexcited

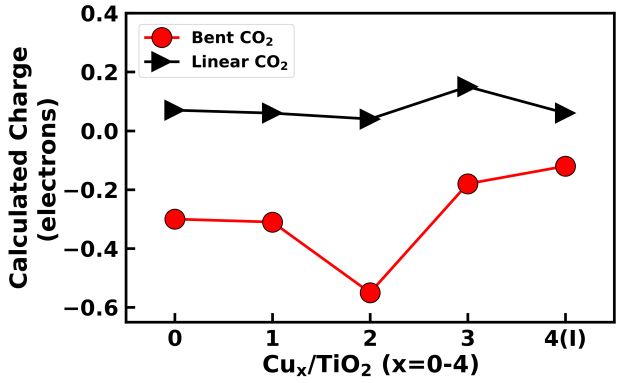

Figure 5.12: Calculated charges using the DDEC6 method of CO_2 when adsorbed on Cu_x/TiO_2.

electron), He et al. found a new adsorption structure for bent CO_2 that showed formation of CO_2 anion species. TiO_2 surfaces with oxygen vacancies have also been reported to form CO_2 anions when CO_2 was adsorbed in the vicinity of the vacancy.[42,43,46,47,60] Yang et al. reported CO_2 adsorption on Pt_x (x = 4,6,8) and Ag_8 clusters supported on anatase (101) surfaces.[46,47] They found that bent CO_2 with an electron gain by up to $\sim$ -0.6 was stabilized (up to -1.0 eV) by the presence of these metal clusters. Therefore, in order to identify the possible formation of CO_2 anions when Cu clusters are present on TiO_2 anatase(101) surface, we calculated the charges of adsorbed CO_2.

We used the density derived electrostatic and chemical (DDEC6) approach[106] to calculate atomic charges. Further details on the method and comparison with the Bader approach are given in the Supporting Information. We first looked at the charge transfer from Cu_x atoms to the TiO_2 surface. We find that when a Cu atom is close to two O_{2c} atoms, as in the case of Cu/TiO_2 (Cu_a), Cu_b/Cu_c in Cu_3/TiO_2, $Cu_a/Cu_b/Cu_c$ in $Cu_4(I)/TiO_2$, or Cu_a/Cu_c in $Cu_4(II)/TiO_2$, the Cu atom has significant electron transfer to the support, in the range of 0.20-0.53 electrons. All the other Cu atoms in Cu_x/TiO_2 show only a weak charge transfer to/from the support. Similar conclusions have also been reported earlier, where they find that electron transfer occurs from metal to the oxide support when the metal atoms lie closer

to the surface.[20,23]

The calculated charges using DDEC6 shown in Figure 5.12 clearly indicate that CO_2 in a bent configuration on any Cu_x/TiO_2 surface gained electrons (negative charge values). The charges on CO_2 ranged from $\sim$ -0.3 (for pure TiO_2 and single Cu atom) to -0.55 (over Cu_2), with $\sim$ -0.2 over Cu_3 and Cu_4. In contrast to bent CO_2, linear CO_2 molecules were slightly cationic. He et al.[42] reported a +0.10 charge for adsorbed bent CO_2 on a TiO_2 surface built as a cluster, while 0.00 charge for adsorbed bent CO_2 on a TiO_2 surface using periodic boundary conditions (slab model). The bond angles in the bent CO_2 are close to the experimental gas phase CO_2 anion angle of 127 ± 8^o:[107] 135^o over TiO_2, 132^o over Cu/TiO_2, 128^o over Cu_2/TiO_2, 129^o over Cu_3/TiO_2, and 129^o over Cu_4/TiO_2. Bent CO_2 on Cu_2/TiO_2 showed the largest gain of electrons, suggesting stronger formation of anions when compared to other Cu_x/TiO_2 surfaces.

In order to better understand the degree of electron transfer to CO2 upon formation of the bent structure, we compared the calculated DDEC6 charges of adsorbed bent CO_2 to reference molecules having anionic CO_2^-. Calculated charges will typically not match formal charges, so comparison to species with known formal charges can help in analyzing the calculated DDEC6 charges. We modeled CO_2 interacting with electron donors such as H, Li, and Ba^+ to form OCOH (carboxylate), Li-CO_2, and [Ba-CO_2]$^+$, respectively. Due to the electron-donating nature of H, Li, and Ba^+, the CO_2 molecule would be expected to formally gain an electron. We used Ba^+ instead of Ba, since Ba typically gives up two electrons to form Ba^2+, and using Ba^+ would lead to one electron transferred to CO_2. The calculated charges of CO_2 were -0.37 (OCOH), -0.66 (Li-CO_2), and -0.46 ([Ba-CO_2]$^+$). The calculated charges of adsorbed bent CO_2 were -0.31 (Cu), -0.56 (Cu_2), -0.18 (Cu_3), and -0.19 e^- (Cu_4). Thus the DDEC6 charges would suggest that either one electron (in the case of the Cu dimer) or less than one electron is transferred to CO_2. Furthermore, we also compared the geometrical parameters of gas phase CO_2, CO_2^-, and CO_2^{2-} to the adsorbed

CO_2. The calculated C-O bond distances were 1.17 (CO_2), 1.26 (CO_2^-), and 1.34 Å (CO_2^{2-}), while O-C-O bond angles were found to be 180° (CO_2), 132° (CO_2^-), and 112° (CO_2^{2-}). The adsorbed bent CO_2 had C-O bond distances of 1.24/1.28 (Cu), 1.23/1.30 (Cu_2), 1.23/1.27 (Cu_3), and 1.26/1.28 Å (Cu_4). The corresponding O-C-O bond angles of adsorbed bent CO2 were 132° (Cu), 128° (Cu_2), 129° (Cu_3), and 129° (Cu_4). The geometrical analysis is consistent with this conclusion of one or less than one electron transfer to CO_2, as all adsorbed CO_2 had similar bond lengths and angles to gas-phase CO_2^-.

We next analyze the charges on individual atoms. The atomic charges of CO_2 and Cu_x are given in Table A.6. We found that over Cu_2/TiO_2 the C atom in bent CO_2 primarily gained electrons, as its charge become +0.33 from the gas-phase value of +0.75. The O_{CO_2} bonding with a Ti_{5c} atom also gained 0.23 e^- resulting in an overall large electron gain for bent CO_2 on Cu_2/TiO_2. Analysis of the atomic charges of Cu_2/TiO_2 indicated that Cu atoms become oxidized upon the adsorption of bent CO_2. The atomic charges of Cu were +0.13 and -0.07 (before adsorption) and +0.29 and +0.30 (after adsorption). For bent CO_2 on Cu_2/TiO_2, the electrons are primarily transferred from Cu atoms to the C atom of bent CO_2. The direct electron transfer for Cu_2 may be related to its adsorption geometry, where the C atom binds directly to the Cu_2. We also found evidence for electron transfer to C atoms in other structures where C-Cu interactions occurred. For example, the bent CO_2 on Cu_2 with an adsorption energy of -0.45 eV (Figure 5.6d) and the bent CO_2 on Cu_4 with an adsorption energy of -0.34 eV (Figure 5.9d) both had C-Cu interactions. In both these cases the C atom gained 0.38 and 0.41 e^- respectively when compared to gas phase CO_2. In contrast to Cu_2, on other Cu_x/TiO_2 the O atoms of the most stable bent CO_2 were primarily reduced. In these cases, the C atoms were slightly oxidized (electron loss of <0.1 e^-). The charges on Cu_x atoms for x = 1, 3, and 4 before and after bent CO_2 adsorption showed insignificant ($\leq$0.1 e^-) changes (see Table A.6). This indicates that on Cu_x/TiO_2 (x=0,1,3,4) the charge transfer occurred from the TiO_2 surface to the bent CO_2.

Our calculated charges for CO_2 are similar to those reported by Yang et al.[46,47] They used Bader charge analysis and reported the number of electrons gained by bent CO_2 on Ptx/TiO_2 with x=4, 6, and 8 to be 0.3, 0.5, and 0.6, respectively. The adsorption geometries consisted of C-Pt interactions which led to electron gain primary by the C atom in bent CO_2. Our results for bent CO_2 on Cu_x/TiO_2 (x=0,1,2) showed that the electron gained by bent CO_2 is comparable to the values reported by Yang et al., while on other larger Cu_x/TiO_2 (x=3,4), the electron gain is relatively weaker. In another DFT paper by Silaghi et al.[94] they reported a large gain of electrons (0.9 e^-) by bent CO_2 at the interfacial sites of alumina supported Ni_{13} and Ni_{55} clusters.

Electronic States of CO_2 on Cu_x/TiO_2

Electronic properties of correlated systems like TiO_2 suffer from self interaction errors[70] as explained earlier. To avoid these self interaction errors, we used DFT+U formalism to calculate the PDOS. We used a U value of 5.0 eV applied to Ti 3d electrons as discussed further in the Supporting Information. The most stable linear and bent CO_2 structures were reoptimized at the level DFT+U. We found that applying the U correction resulted in essentially the same geometries. For instance the bond distances between adsorbed CO_2 and Cu_x/TiO_2 changed by <0.1Å for CO_2 linear and bent adsorption when compared to the structures reported using DFT in Figure 5.3.

We analyzed the site-projected density of states (DOS) of linear and bent CO_2 as shown Figure 5.13 to understand different orbitals associated with different atoms. Only the Cu and Cu_2 DOS are given in the figure, while DOS for the remaining Cu_x/TiO_2 systems are given in the Supporting Information. DOS for Cu_3 and Cu_4 are very similar to Cu_1. The Cu states are strongly localized near the valence band edge from 0 to ∼-2 eV. Similar strongly localized states were also reported previously for clusters of Pt (1-4,8), Ag (2,4,8) and Au (1,2,3) on the TiO_2 anatase(101) surface.[46,47,72,108] Cu states deeper in the valence band

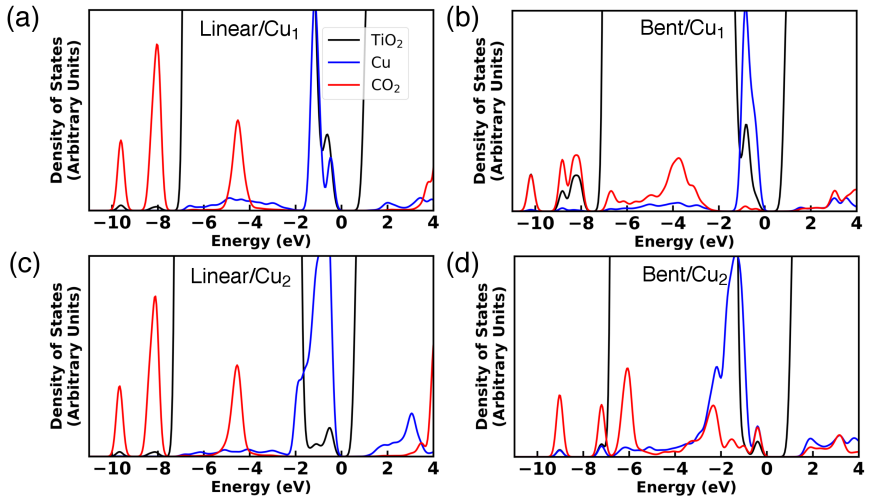

Figure 5.13: Sited-projected density of states (DOS) for linear and bent CO_2 adsorbed on Cu1 and Cu_2. The left plots show linear CO_2 while the right plots show bent CO_2. The valence band edge has been set to 0 eV.

consist of shallow delocalized states extending up to -8 eV. The conduction band is composed predominantly of TiO_2 states. The DOS of linear CO_2 on all Cu_x/TiO_2 show two localized peaks between -8 and -10 eV. Another characteristic peak for linear CO_2 is between -4 and -6 eV that appears consistently for all the Cu_x/TiO_2 surfaces. The localized linear CO_2 peaks have little overlap with the Cu states which indicates weak interactions between CO_2 and Cu states.

In contrast, for bent CO_2 on Cu_x/TiO_2 the characteristic CO_2 bands become hybridized with Cu states. On all the Cu_x/TiO_2 surfaces, we find that bent CO_2 states become more delocalized within the valence band and start to overlap with Cu states. The broad energy range of overlap between CO_2 states with Cu states indicates strong hybridization between Cu and bent CO_2. Since bent CO_2 states extend up to the valence band edge (unlike linear CO_2), activation of bent CO_2 upon light absorption by photoexcited electrons is more possible. Similar to our results, the states of bent CO_2 on Ag and Pt/TiO_2 also extended close to the valence band edge.

While strong interactions occur between Cu_2 and bent CO_2, Cu_2 has slightly different

DOS when compared to the other Cu_x/TiO_2 systems. The bent CO_2 states for Cu_2/TiO_2 (Figure 5.13d) are shifted to higher energy (by ∼0.4 eV) when compared to the other Cu_x/TiO_2 surfaces. This shift results in more states of bent CO_2 near the valence band maximum compared to other Cu_x/TiO_2. We attribute this special behavior to the distinct C-Cu interactions on Cu_2/TiO_2, unlike the carbonate-like CO_2 that form on other Cu_x/TiO_2 surfaces. The large number of bent CO_2 states near the valence band edge indicates strong possible photocatalytic activation on Cu_2/TiO_2. In contrast, for the case of Pt_8 on TiO_2, bent CO_2 had only weak hybridization with Pt close to the valence band maximum edge.[46] This may indicate the strong potential photocatalytic activity of smaller clusters.

5.3.4 Oxidation state of Cu Clusters

Several reports have shown the oxidation state of the metal to be an important catalytic property. Reports focusing on the photocatalytic reduction of CO_2 to methanol or CO showed the presence of Cu^{1+} and/or Cu^{2+} to be active sites on Cu/TiO_2 catalysts.[5,7–9] The coexistence of Cu^0 and Cu^{1+} species was also reported by other authors[4,12,23] to be favorable for CO_2 photoreduction to methane. Chen et al.[12] reported favorable photocatalytic activity as a result of the different oxidation states of Cu leading to efficient electron-hole separation between different Cu atoms, and accompanying lowered electron-hole recombination. Interactions of the support and adsorbed metals may lead to charge transfer, which may reduce or oxidize the metals. What oxidation state the Cu clusters may have on supports like TiO_2 that may serve as an active site is still an important question for CO_2 reduction.

Determination of Cu oxidation state using CO vibrational frequencies

Experimentally, the oxidation state of supported metals can be correlated to changes in CO vibrational frequencies upon adsorption.[4,15,109–112] For example, adsorbed CO on Cu/TiO_2 can be used to assign different oxidation states based on the CO vibrational frequency:[4] 2050-

Table 5.2: Determination of Cu oxidation state from adsorbed CO vibrational frequencies and DDEC6 charge analysis. Shown are adsorbed CO vibrational frequencies and assigned oxidation state of the Cu atom(s) bonding to the CO. DDEC6 charges are given for each Cu atom in the cluster. The DDEC6 charge analysis is for the bare clusters (no adsorbates present). The bold numbers indicate charges/oxidation states of the same Cu atom(s) from the vibrational analysis.

Cu_x/ TiO_2	**ν_{CO} cm^{-1}**	**Assigned Oxidation state from ν_{CO}**	**DDEC6 Cu Charges**	**Assigned Oxidation state from DDEC6 Charges**
1	2097	Cu^0	**0.53**	**Cu^{2+}**
2	1788	–	**-0.07, 0.13**	**Cu^0, Cu^0**
3	2104	Cu^0/Cu^{1+}	**0.03**, 0.24, 0.24	**Cu^0**, Cu^{1+}, Cu^{1+}
4(I) top	2069	Cu^0	0.52, 0.20, 0.23, **-0.07**	Cu^{2+}, Cu^{1+}, Cu^{1+}, **Cu^0**

2100 cm^{-1} (Cu^0), 2100-2150 cm^{-1} (Cu^{1+}), or 2190-2200 cm^{-1} (Cu^{2+}). The experimental vibrational frequency of CO is 2169 cm^{-1}.[100] These frequencies equate to CO vibrational shifts of -119 to -69 cm^{-1} over Cu^0, -69 to -19 cm^{-1} over Cu^{1+}, and 21 to 31 cm^{-1} over Cu^{2+}. In the following section we assigned the oxidation state of Cu atoms that are bonded to CO molecules based on the adsorbed CO vibrational frequencies. In order to calculate the CO vibrational frequencies, we first determine the most stable CO adsorption sites on these photocatalysts as detailed in the Supporting Information. Our results show the most stable sites to have adsorption energies between -1.7 and -2.1 eV with the C atom bonding directly to Cu atoms, rather than TiO_2 atoms. Several other reports also show similar bonding where the C atom of CO is directly bonded to oxide-supported metal atoms such as Cu[79,113] and Ag/Pd.[114]

On Cu/TiO_2, CO prefers to bind directly with the Cu atom (ΔE_{ads}=-1.96 eV). The vibrational frequency of CO adsorbed on Cu/TiO_2(101) was 2097 cm^{-1}, which is a shift of -81 cm^{-1} from the calculated gas-phase value. This red shift from gas phase CO suggests an oxidation state of Cu0 based on the assignments of Liu et al.[4] as discussed above. See Table 5.2 for a summary of vibrational frequencies and assigned oxidation states. In the case of Cu_2/TiO_2, CO adsorbed strongly (ΔE_{ads}=-2.10 eV) at the bridge site between two Cu atoms. The vibrational frequency of 1788 cm^{-1} was significantly shifted. Such a lowered vibrational frequency for the bridge site bonding can be explained on the basis of Blyholder model,[115] where back donation of electron occurs from the metal atom (Cu) to the antibonding orbital of CO, which is accompanied by a C-O bond elongation by 0.06 Å (compared to gas phase C-O bond distance of 1.14 Å) such that the vibrational frequency is lowered. Previous experimental work[4,15] on Cu/TiO_2 catalysts did not find such a strongly red shifted CO vibrational frequency so we could not assign the oxidation state of the Cu atoms in Cu_2 based on CO vibrational frequency. The absence of such strong red shifts in the experimental work suggests the absence of Cu_2 dimers on TiO_2. We discuss more on the stability of Cu_2 dimers later in the paper. We also note that similar to our calculated strong red shifts for CO at the Cu_2 bridge site, strong red shifts of more than 100 cm^{-1} were also observed for CO adsorption at a bridge site on Pd/Al_2O_3[116] and Pt/FeO_x.[20]

CO was found to adsorb to the Cu_3 cluster (through C-Cu_a bond) with a ΔE_{ads} value of -1.72 eV, and had a large vibrational frequency (2104 cm^{-1}) for adsorbed CO. This CO stretch frequency corresponds to a frequency shift of -74 cm^{-1} compared to calculated gas phase CO frequency. Since this frequency shift is close to the shifts corresponding to both Cu^0 and Cu^{1+} species, the Cu_a atom could not be definitively assigned. On $Cu_4(I)/TiO_2$, the most stable adsorption site was found to be at the bridge site bridge site between Cu_a and Cu_d of Cu_4 with an ΔE_{ads} = -1.91 eV. The vibrational frequency of this bridged CO was calculated to be 1955 cm^{-1}. This frequency has a large shift of -223 cm^{-1}, again (similar

to Cu_2/TiO_2) can be explained on the basis of the Blyholder model. Unfortunately this shift could not be used to assign the oxidation state of Cu. A second top CO site over the Cu_4(I) cluster was only 0.23 eV less stable than the bridge site, indicating that CO atoms may adsorb in the top configuration over Cu_4(I). In Table 5.2 we report the vibrational frequency of CO adsorbed at this top site (with a C-Cu_c bond). The vibrational frequency of CO at the top site on Cu_4(I) was 2069 cm^{-1} which corresponds to a vibrational frequency shift of -109 cm^{-1} compared to gas phase CO value. This shift suggests the Cu_c atom to have a Cu^0 oxidation state.

Determination of oxidation state using DDEC6 charge analysis

The other approach that we used to determine the oxidation state of the Cu atoms was DDEC6 charge analysis.[66,67] Details comparing this method with the common Bader method are found in the Supporting Information. In order to assign Cu oxidation state, we calculated the DDEC6 charges of Cu in several reference molecular and condensed systems with known Cu^{1+} and Cu^{2+} oxidation states, as detailed in the Supporting Information. The average calculated DDEC6 charge for Cu^{1+} and Cu^{2+} was 0.36 and 0.85 e^- respectively. The DDEC6 charges of Cu1+ species ranged from 0.25 to 0.52 while DDEC6 charges of Cu^{2+} species ranged from 0.44 to 1.10. We used these calculated charges to help assign formal oxidation states to the Cu clusters.

We were able to calculate the charges of all Cu atoms (as opposed to the CO adsorption method in the previous section which only provided information on select Cu atoms), and these results are shown in Table 5.2. The calculated DDEC6 charges fall into three range of values. In the first case, the charge of the Cu atom is significantly positive ∼0.5, while in the second case the Cu charge is close to ∼0.2, while in the last case the Cu charge is ∼0. The calculated charge of 0.5, 0.2, and 0 can be assigned to formal oxidation states of Cu^{2+}, Cu^{1+}, and Cu^0, respectively. DDEC6 based assignments show that the closer the Cu atoms are to

the TiO_2 surface, the more the Cu atoms are oxidized. The Cu_a atoms that lie close to the TiO_2 surface in Cu1 and Cu_4(I) have calculated charges near 0.5, indicative of Cu^{2+} species. The other set of Cu atoms close to the TiO_2 surface are Cu_b and Cu_c in Cu_3 and Cu_4(I), with calculated charges near 0.2 which correspond to Cu^{1+} species. Finally, the rest of Cu atoms which lie the farthest from the surface in Cu_2, Cu_3, Cu_4(I) have calculated charges in the range of -0.07 to 0.13 which correspond to Cu^0 species. Our results are consistent with the results of Liu et al., where they used Bader analysis and showed that when Cu in Cu_4/Al_2O_3 was closer (or farther) to the surface O atoms, Cu existed as Cu^{1+} (or Cu^0) species.[23] Our CO_2 adsorption results showed that Cu_a, Cu_a/Cu_b, Cu_a, and Cu_d atoms in Cu_1 through Cu_4(I) respectively were able to stabilize bent CO_2 (see Section 5.3.2). Except for the case of the lone Cu atom, these Cu atoms were located away from the surface and had DDEC6 charges of -0.07, 0.13 (Cu_a/Cu_b in Cu dimer), 0.03 (Cu_a in Cu_3), and -0.07 (Cu_d in Cu_4(I)). These charges are indicative of a Cu^0 oxidation state, which would indicate that Cu0 atoms interact most strongly with bent CO_2 molecules. The lone Cu_a atom in Cu/TiO_2 had significant charge transfer (0.53 calculated charge) and had a formal oxidation state of Cu^{2+}.

Overall we find that assigned oxidation states from CO vibrational shifts are Cu^{1+}/Cu^0, while assigned oxidation states from DDEC6 analysis are $Cu^{2+}/Cu^{1+}/Cu^0$. The DDEC6 method provides information on all Cu atoms in the cluster, not just those bound to CO. Discrepancies between the two methods could be attributed to charge transfer effects and/or DFT accuracy. First, adsorption can change the charges of Cu clusters due to electron transfer between adsorbate and Cu cluster. This charge transfer can lead for instance to the oxidation state of Cu being different before and after CO adsorption. We indeed observed that when CO was adsorbed on Cu_2/TiO_2, there was significant charge transfer from Cu_2 to CO. The same was true for CO_2 adsorption (see Table A.6). Before CO adsorption, the two Cu atoms in Cu_2 had charges of 0.13 and -0.07, while after adsorption the charges

became 0.44 and 0.39, indicating that Cu_2 changed from Cu^0/Cu^0 states to Cu^{1+}/Cu^{1+} states. Sterrer et al. also reported charge transfer between CO and Au/MgO and reported that the probe molecule (CO) measured only the final state charges (after CO adsorption) instead of the bare catalyst (without CO adsorption).[109] Charge transfer effects between a probe molecule and catalyst must be considered as this may change the oxidation state of the catalyst, although only the Cu_2 cluster charges changed upon CO adsorption. All the other clusters essentially had the same charges before and after CO adsorption. Second, the accuracy of calculated vibrational frequencies using DFT must also be considered. An error in DFT calculated frequencies (possibly up to ~ 40[117] cm^{-1}) could lead to inaccurate assignments, especially for frequencies near the cutoff between two oxidation state ranges.

5.3.5 The Special Case of Cu_2

Our results for Cu_2/TiO_2 indicating strong CO_2 adsorption along with large charge transfer to bent CO_2 indicate the peculiarities of the Cu_2 dimer compared to other Cu clusters (see Figure 5.6c and Figure 5.10 for instance). Several papers have also reported transition metal dimers on different supports as potential reactive sites. The experimental work by Kaden et al.[32] reported that Pd_2 on TiO_2 had substantial CO oxidation activity when compared to other Pd clusters of size $\leq$10 atoms. Pd_2 was found using DFT to have a lower barrier for CO oxidation compared to Pd_1.[118] Kydd et al.[119] also reported large CO oxidation activity for Cu_2 dimers adsorbed on ceria. Metal dimers, like Cu_2, may therefore be very reactive sites.

It is unclear, however, whether the Cu_2 dimer is stable on the TiO_2 surface. Indeed, the calculated CO vibrational frequency over Cu_2 is near 1788 cm^{-1}, and such a frequency was not observed in previous experimental work on Cu clusters over TiO_2.[15] However, Qiao et al.[20] reported the CO frequency to be 1860 cm^{-1} for a bridge-bonded CO over a Pt_2 dimer on FeO_x, while they reported CO adsorption on a monomer Pt site to have a frequency

of 2030 cm^{-1}, similar to our findings over Cu_x clusters. Since the frequencies for CO/Cu_2 species were not experimentally observed for Cu/TiO_2, this would suggest that Cu_2 dimers may not be stable on TiO_2. We calculated the dimer formation energy ($Cu \longrightarrow Cu_2$) to be 0.94 eV, or an endothermic process. We further calculated the barrier for Cu atom diffusion across the anatase (101) surface to be 0.99 eV along the [010] direction and 1.63 eV along the [101] direction (see the Supporting Information for more details). This value along the [010] direction is close to the previous reported value of 1.23 eV for Cu adatom diffusion on the TiO_2 anatase(101) surface.[120] Thus, Cu_2 formation is thermodynamically unfavorable and also hard to form because of the high barrier for Cu diffusion on the surface. This would explain why Cu_2 dimers did not appear in experimental work.[15] Our results suggest that if an experimental technique could synthesize and stabilize these dimers, this could lead to a very active CO_2 photoreduction catalyst that readily activates CO_2.

5.4 Conclusions

We used density functional theory calculations to determine how TiO_2-supported Cu clusters (Cu_x, x = 1 to 4) could activate CO_2 for reduction. We found that Cu promotes the activation of CO_2 on all Cu_x/TiO_2 surfaces as shown by the strong adsorption energies of bent form of CO_2 when compared to linear form of CO_2. In contrast, on pure TiO_2, the bent CO_2 was less stable when compared to the linear CO_2. Charge transfer analysis showed that bent CO_2 on Cu_x/TiO_2 gained significant electrons (0.2 to 0.5 e^-) from the Cu_x/TiO_2 surfaces, indicating the formation of activated CO_2 anion species. Further analysis showed that bent CO_2 had strong vibrational frequency shifts (>100 cm^{-1}) when compared to linear CO_2 on Cu_x/TiO_2. Projected density of states showed evidence that the bent CO_2 interacts strongly with the Cu clusters through mixing of CO_2 and Cu electronic states. Charge and vibrational analysis indicates that Cu atoms had formally assigned oxidation states between

Cu^0 and Cu^{2+}, but that Cu atoms that interacted with CO_2 molecules predominantly had charges of Cu^0 or Cu^{1+}, depending on the oxidation state characterization technique (charge analysis or CO vibrational shifts). Finally, we analyzed the Cu dimer; bent CO_2 adsorption was very strong over the Cu dimer, suggesting that the Cu dimer could potentially be a very active catalyst. Cu dimer formation however is endothermic and has a high activation barrier. A synthesis technique that could stabilize these dimers could lead to very active catalysts. Several experimental studies on the synthesis of small Cu clusters (up to 20 atoms large) on oxide surfaces have been reported.[21,23–25] These reports have shown that small clusters can be highly active for CO_2 reduction. Our work highlights the potential of Cu clusters for CO_2 reduction, and provides motivation for further studies on these catalysts.

Bibliography

[1] M. Anpo, H. Yamashita, K. Ikeue, Y. Fujii, S. G. Zhang, Y. Ichihashi, D. R. Park, Y. Suzuki, K. Koyano and T. Tatsumi, *Catal. Today*, 1998, **44**, 327–332.

[2] H. Yamashita, Y. Fujii, Y. Ichihashi, S. G. Zhang, K. Ikeue, D. R. Park, K. Koyano, T. Tatsumi and M. Anpo, *Catal. Today*, 1998, **45**, 221–227.

[3] V. P. Indrakanti, H. H. Schobert and J. D. Kubicki, *Energy Fuels*, 2009, **23**, 5247–5256.

[4] L. Liu, F. Gao, H. Zhao and Y. Li, *Applied Catalysis B: Environmental*, 2013, **134-135**, 349–358.

[5] M. Anpo, H. Yamashita, Y. Ichihashi and S. Ehara, *Journal of Electroanalytical Chemistry*, 1995, **396**, 21–26.

[6] J. Schneider, M. Matsuoka, M. Takeuchi, J. Zhang, Y. Horiuchi, M. Anpo and D. W. Bahnemann, *Chem. Rev.*, 2014, **114**, 9919–9986.

[7] I. H. Tseng, J. C. S. Wu and H. Y. Chou, *Journal of Catalysis*, 2004, **221**, 432–440.

[8] Slamet, H. Nasution, E. Purnama, S. Kosela and J. Gunlazuardi, *Catalysis Communications*, 2005, **6**, 313–319.

[9] L. Liu, C. Zhao and Y. Li, *Journal of Physical Chemistry C*, 2012, **116**, 7904–7912.

[10] D. Liu, Y. Fernández, O. Ola, S. Mackintosh, M. Maroto-Valer, C. M. Parlett, A. F. Lee and J. C. Wu, *Catalysis Communications*, 2012, **25**, 78–82.

[11] O. K. Varghese, M. Paulose, T. J. LaTempa and C. A. Grimes, *Nano Letters*, 2009, **9**, 731–737.

[12] B.-R. Chen, V.-H. Nguyen, J. C. S. Wu, R. Martin and K. Kočí, *Physical chemistry chemical physics : PCCP*, 2016, **18**, 4942–51.

[13] S. Neatu, J. A. Maciá-Agulló, P. Concepción and H. Garcia, *Journal of the American Chemical Society*, 2014, **136**, 15969–15976.

[14] Q. Zhai, S. Xie, W. Fan, Q. Zhang, Y. Wang, W. Deng and Y. Wang, *Angew. Chem., Int. Ed.*, 2013, **52**, 5776–5779.

[15] C. Liu, S. K. Iyemperumal, N. A. Deskins and G. Li, *Journal of Photonics for Energy*, 2016, **7**, 012004.

[16] J. B. Park, J. Graciani, J. Evans, D. Stacchiola, S. D. Senanayake, L. Barrio, P. Liu, J. F. Sanz, J. Hrbek and J. A. Rodriguez, *J. Am. Chem. Soc.*, 2010, **132**, 356–363.

[17] K. Fujiwara and S. E. Pratsinis, *AIChE J.*, 2017, **63**, 139–146.

[18] X. F. Yang, A. Wang, B. Qiao, J. Li, J. Liu and T. Zhang, *Accounts of Chemical Research*, 2013, **46**, 1740–1748.

[19] J. H. Kwak, L. Kovarik and J. Szanyi, *ACS Catalysis*, 2013, **3**, 2094–2100.

[20] B. Qiao, A. Wang, X. Yang, L. F. Allard, Z. Jiang, Y. Cui, J. Liu, J. Li and T. Zhang, *Nature chemistry*, 2011, **3**, 634–641.

[21] S. Vajda and M. G. White, *ACS Catalysis*, 2015, **5**, 7152–7176.

[22] Y. Tanizawa, T. Shido, W.-J. Chun, K. Asakura, M. Nomura and Y. Iwasawa, *J. Phys. Chem. B*, 2003, **107**, 12917–12929.

[23] C. Liu, B. Yang, E. Tyo, S. Seifert, J. DeBartolo, B. von Issendorff, P. Zapol, S. Vajda and L. A. Curtiss, *Journal of the American Chemical Society*, 2015, **137**, 8676–8679.

[24] B. Yang, C. Liu, A. Halder, E. C. Tyo, A. B. F. Martinson, S. Seifert, P. Zapol, L. A. Curtiss and S. Vajda, *The Journal of Physical Chemistry C*, 2017, **121**, 10406–10412.

[25] R. Passalacqua, S. Parathoner, G. Centi, A. Halder, E. C. Tyo, B. Yang, S. Seifert and S. Vajda, *Catal. Sci. Technol.*, 2016, **6**, 6977–6985.

[26] J. A. Rodriguez, J. Evans, J. Graciani, J. B. Park, P. Liu, J. Hrbek and J. F. Sanz, *J. Phys. Chem. C*, 2009, **113**, 7364–7370.

[27] M. Tamura, T. Kitanaka, Y. Nakagawa and K. Tomishige, *ACS Catal.*, 2016, **6**, 376–380.

[28] S. Lee, C. Fan, T. Wu and S. L. Anderson, *Journal of the American Chemical Society*, 2004, **126**, 5682–5683.

[29] L. Benz, X. Tong, P. Kemper, Y. Lilach, A. Kolmakov, H. Metiu, M. T. Bowers and S. K. Buratto, *The Journal of Chemical Physics*, 2005, **122**, 081102.

[30] Y. Lei, F. Mehmood, S. Lee, J. Greeley, B. Lee, S. Seifert, R. E. Winans, J. W. Elam, R. J. Meyer, P. C. Redfern, D. Teschner, R. Schlogl, M. J. Pellin, L. A. Curtiss and S. Vajda, *Science*, 2010, **328**, 224–228.

[31] S. Vajda, M. J. Pellin, J. P. Greeley, C. L. Marshall, L. a. Curtiss, G. a. Ballentine, J. W. Elam, S. Catillon-Mucherie, P. C. Redfern, F. Mehmood and P. Zapol, *Nature materials*, 2009, **8**, 213–216.

[32] W. E. Kaden, T. Wu, W. A. Kunkel and S. L. Anderson, *Science*, 2009, **326**, 826–829.

[33] H.-J. Freund and G. Pacchioni, *Chem. Soc. Rev.*, 2008, **37**, 2224–2242.

[34] H. He, P. Zapol and L. a. Curtiss, *Energy Environ. Sci.*, 2012, **5**, 6196.

[35] J. A. Rodriguez, P. Liu, D. J. Stacchiola, S. D. Senanayake, M. G. White and J. G. Chen, *ACS Catal.*, 2015, **5**, 6696–6706.

[36] W. Tu, Y. Zhou and Z. Zou, *Adv. Mater.*, 2014, **26**, 4607–4626.

[37] C. C. Yang, Y. H. Yu, B. Van Der Linden, J. C. S. Wu and G. Mul, *J. Am. Chem. Soc.*, 2010, **132**, 8398–8406.

[38] Y. Ma, X. L. Wang, Y. S. Jia, X. B. Chen, H. X. Han and C. Li, *Chemical Reviews*, 2014, **114**, 9987–10043.

[39] H.-J. Freund and M. W. Roberts, *Surface Science Reports*, 1996, **25**, 225–273.

[40] G. Centi and S. Perathoner, *Catal. Today*, 2009, **148**, 191–205.

[41] E. E. Benson, C. P. Kubiak, A. J. Sathrum and J. M. Smieja, *Chem. Soc. Rev.*, 2009, **38**, 89–99.

[42] H. He, P. Zapol and L. A. Curtiss, *J. Phys. Chem. C*, 2010, **114**, 21474–21481.

[43] D. C. Sorescu, W. A. Al-Saidi and K. D. Jordan, *J. Chem. Phys.*, 2011, **135**, 124701.

[44] D. C. Sorescu, J. Lee, W. a. Al-Saidi and K. D. Jordan, *J. Chem. Phys.*, 2012, **137**, 074704.

[45] E. L. Uzunova, N. Seriani and H. Mikosch, *Phys. Chem. Chem. Phys.*, 2015, **17**, 11088–11094.

[46] C.-T. Yang, B. C. Wood, V. R. Bhethanabotla and B. Joseph, *J. Phys. Chem. C*, 2014, **118**, 26236–26248.

[47] C.-T. Yang, B. C. Wood, V. R. Bhethanabotla and B. Joseph, *Phys. Chem. Chem. Phys.*, 2015, **17**, 25379–25392.

[48] P. Schlexer, H.-Y. T. Chen and G. Pacchioni, *Catalysis Letters*, 2017, **147**, 1871–1881.

[49] R. Shanmugam, A. Thamaraichelvan, T. K. Ganesan and B. Viswanathan, *Applied Surf. Sci.*, 2017, **396**, 444–454.

[50] C. Liu, H. He, P. Zapol and L. A. Curtiss, *Phys. Chem. Chem. Phys.*, 2014, **16**, 26584–99.

[51] L. Kavan, M. Grätzel, S. E. Gilbert, C. Klemenz and H. J. Scheel, *J. Am. Chem. Soc.*, 1996, **118**, 6716–6723.

[52] H. Zhang and J. F. Banfield, *Journal of Materials Chemistry*, 1998, **8**, 2073–2076.

[53] J. Vandevondele, M. Krack, F. Mohamed, M. Parrinello, T. Chassaing and J. Hutter, *Comput. Phys. Commun.*, 2005, **167**, 103–128.

[54] http://cp2k.berlios.de, *CP2K developers home page*, 2016.

[55] G. Lippert, J. Hutter and M. Parrinello, *Mol. Phys.*, 1997, **92**, 477–488.

[56] J. P. Perdew, K. Burke and M. Ernzerhof, *Phys. Rev. Lett.*, 1996, **77**, 3865–3868.

[57] J. VandeVondele and J. Hutter, *J. Chem. Phys.*, 2007, **127**, 0–9.

[58] S. Goedecker, M. Teter and J. Hutter, *Phys. Rev. B*, 1996, **54**, 1703–1710.

[59] N. A. Deskins, R. Rousseau and M. Dupuis, *J. Phys. Chem. C*, 2009, **113**, 14583–14586.

[60] D. C. Sorescu, S. Civiš and K. D. Jordan, *J. Phys. Chem. C*, 2014, **118**, 1628–1639.

[61] S. Grimme, S. Ehrlich and L. Goerigk, *J. Comput. Chem.*, 2011, **32**, 1456–1465.

[62] J. C. Garcia and N. A. Deskins, *J. Phys. Chem. C*, 2012, **116**, 16573–16581.

[63] J. K. Burdett, T. Hughbanks, G. J. Miller, J. W. Richardson and J. V. Smith, *J. Am. Chem. Soc.*, 1987, **109**, 3639–3646.

[64] H. Cheng and A. Selloni, *The Journal of Chemical Physics*, 2009, **131**, 054703.

[65] N. Seriani, C. Pinilla and Y. Crespo, *J. Phys. Chem. C*, 2015, **119**, 6696–6702.

[66] T. A. Manz and N. G. Limas, *RSC Adv.*, 2016, **6**, 47771–47801.

[67] N. G. Limas and T. A. Manz, *RSC Adv.*, 2016, **6**, 45727–45747.

[68] R. F. Bader, *Atoms in molecules: a quantum theory*, 1990.

[69] G. Henkelman, A. Arnaldsson and H. Jónsson, *Comput. Mater. Sci.*, 2006, **36**, 354–360.

[70] G. Pacchioni, *J. Chem. Phys.*, 2008, **128**, 182505.

[71] S. L. Dudarev, S. Y. Savrasov, C. J. Humphreys and a. P. Sutton, *Phys. Rev. B*, 1998, **57**, 1505–1509.

[72] H. Wang, T. An and A. Selloni, *J. Chem. Phys.*, 2017, **146**, 184703.

[73] M. Jiang, Q. Zeng, T. Zhang, M. Yang and K. A. Jackson, *J. Chem. Phys.*, 2012, **136**, 104501.

[74] B. H. Cogollo-Olivo, N. Seriani and J. A. Montoya, *Chem. Phys.*, 2015, **461**, 20–24.

[75] C. L. Pang, R. Lindsay and G. Thornton, *Chem. Rev.*, 2013, **113**, 3887–3948.

[76] X.-q. Gong, A. Selloni, O. Dulub, P. Jacobson and U. Diebold, *Journal of the American Chemical Society*, 2008, **130**, 370–381.

[77] D. Luo, Y. Bi, W. Kan, N. Zhang and S. Hong, *J. Mol. Struct.*, 2011, **994**, 325–331.

[78] L. Giordano, G. Pacchioni, T. Bredow and J. F. Sanz, *Surf. Sci.*, 2001, **471**, 21–31.

[79] A. M. Márquez, J. Graciani and J. F. Sanz, *Theoretical Chemistry Accounts*, 2009, **126**, 265–273.

[80] D. Pillay and G. S. Hwang, *J. Mol. Struct.*, 2006, **771**, 129–133.

[81] S.-F. Peng and J.-J. Ho, *Phys. Chem. Chem. Phys.*, 2011, **13**, 20393–400.

[82] J. Zhang, M. Zhang, Y. Han, W. Li, X. Meng and B. Zong, *The Journal of Physical Chemistry C*, 2008, **112**, 19506–19515.

[83] A. R. Puigdollers, P. Schlexer and G. Pacchioni, *The Journal of Physical Chemistry C*, 2015, **119**, 15381–15389.

[84] A. S. Mazheika, T. Bredow, V. E. Matulis and O. A. Ivashkevich, *The Journal of Physical Chemistry C*, 2011, **115**, 17368–17377.

[85] X. Tong, L. Benz, P. Kemper, H. Metiu, M. T. Bowers and S. K. Buratto, *Journal of the American Chemical Society*, 2005, **127**, 13516–13518.

[86] H. Y. T. Chen, S. Tosoni and G. Pacchioni, *Surf. Sci.*, 2016, **652**, 163–171.

[87] S. Ma, W. Song, B. Liu, H. Zheng, J. Deng, W. Zhong, J. Liu, X.-Q. Gong and Z. Zhao, *Catal. Sci. Technol.*, 2016, **6**, 6128–6136.

[88] C. T. Campbell, *Acc. Chem. Res.*, 2013, **46**, 1712–1719.

[89] J. Graciani, K. Mudiyanselage, F. Xu, A. E. Baber, J. Evans, S. D. Senanayake, D. J. Stacchiola, P. Liu, J. Hrbek, J. F. Sanz and J. A. Rodriguez, *Science*, 2014, **345**, 546–550.

[90] J. C. S. Wu and C. W. Huang, *Front. Chem. Eng. China*, 2010, **4**, 120–126.

[91] N. Nomura, T. Tagawa and S. Goto, *Appl. Catal., A*, 1998, **166**, 321–326.

[92] J. Rasko and F. Solymosi, *J. Phys. Chem.*, 1994, **98**, 7147–7152.

[93] C. W. Lee, R. Antoniou Kourounioti, J. C. S. Wu, E. Murchie, M. Maroto-Valer, O. E. Jensen, C. W. Huang and A. Ruban, *J. CO2 Util.*, 2014, **5**, 33–40.

[94] M.-C. Silaghi, A. Comas-Vives and C. Copéret, *ACS Catal.*, 2016, **6**, 4501–4505.

[95] A. M. Turek, I. E. Wachs and E. DeCanio, *J. Phys. Chem.*, 1992, **96**, 5000–5007.

[96] W. Taifan, J.-F. Boily and J. Baltrusaitis, *Surf. Sci. Rep.*, 2016, **71**, 595–671.

[97] W. Su, J. Zhang, Z. Feng, T. Chen, P. Ying and C. Li, *J. Phys. Chem. C*, 2008, **112**, 7710–7716.

[98] V. P. Indrakanti, J. D. Kubicki and H. H. Schobert, *Energy Fuels*, 2008, **22**, 2611–2618.

[99] L. Mino, G. Spoto and A. M. Ferrari, *J. Phys. Chem. C*, 2014, **118**, 25016–25026.

[100] T. Shimanouchi, *Natl. Bur. Stand.*, 1972.

[101] G. Ramis, G. Busca and V. Lorenzelli, *Mater. Chem. Phys.*, 1991, **29**, 425–435.

[102] S. Kattel, B. Yan, Y. Yang, J. G. Chen and P. Liu, *J. Am. Chem. Soc.*, 2016, **138**, 12440–12450.

[103] K. K. Bando, K. Sayama, H. Kusama, K. Okabe and H. Arakawa, *Appl. Catal., A*, 1997, **165**, 391–409.

[104] K. Mudiyanselage, S. D. Senanayake, L. Feria, S. Kundu, A. E. Baber, J. Graciani, A. B. Vidal, S. Agnoli, J. Evans, R. Chang, S. Axnanda, Z. Liu, J. F. Sanz, P. Liu, J. A. Rodriguez and D. J. Stacchiola, *Angew. Chem., Int. Ed.*, 2013, **52**, 5101–5105.

[105] W. Wu, K. Bhattacharyya, K. Gray and E. Weitz, *J. Phys. Chem. C*, 2013, **117**, 20643–20655.

[106] T. A. Manz and D. S. Sholl, *J. Chem. Theory Comput.*, 2010, **6**, 2455–2468.

[107] K. O. Hartman and I. C. Hisatsune, *J. Chem. Phys.*, 1966, **44**, 1913–1918.

[108] C. T. Yang, N. Balakrishnan, V. R. Bhethanabotla and B. Joseph, *J. Phys. Chem. C*, 2014, **118**, 4702–4714.

[109] M. Sterrer, M. Yulikov, T. Risse, H. J. Freund, J. Carrasco, F. Illas, C. Di Valentin, L. Giordano and G. Pacchioni, *Angew. Chem., Int. Ed.*, 2006, **45**, 2633–2635.

[110] S. D. Senanayake, N. A. Pappoe, T.-D. Nguyen-Phan, S. Luo, Y. Li, W. Xu, Z. Liu, K. Mudiyanselage, A. C. Johnston-Peck, A. I. Frenkel, I. Heckler, D. Stacchiola and J. A. Rodriguez, *Surf. Sci.*, 2016, **652**, 206–212.

[111] B. Yoon, H. Häkkinen, U. Landman, A. S. Wörz, J.-M. Antonietti, S. Abbet, K. Judai and U. Heiz, *Science*, 2005, **307**, 403–407.

[112] A. S. Wörz, U. Heiz, F. Cinquini and G. Pacchioni, *J. Phys. Chem. B*, 2005, **109**, 18418–18426.

[113] Z. Helali, A. Jedidi, A. Markovits, C. Minot and M. Abderrabba, *Theoretical Chemistry Accounts*, 2015, **134**, 50.

[114] J. Blomqvist, L. Lehman and P. Salo, *Phys. Status Solidi B*, 2012, **249**, 1046–1057.

[115] G. Blyholder, *J. Phys. Chem. A*, 1964, **68**, 2772–2777.

[116] H. Unterhalt, G. Rupprechter and H. J. Freund, *J. Phys. Chem. B*, 2002, **106**, 356–367.

[117] K. E. Riley, B. T. Op't Holt and K. M. Merz, *J. Chem. Theory Comput.*, 2007, **3**, 407–433.

[118] S. Li, X. Zhao, J. L. Shi, Y. Jia, Z. Guo, J.-H. Cho, Y. Gao and Z.-y. Zhang, *Phys. Chem. Chem. Phys.*, 2016, **18**, 24872–24879.

[119] R. Kydd, W. Y. Teoh, K. Wong, Y. Wang, J. Scott, Q. H. Zeng, A. B. Yu, J. Zou and R. Amal, *Adv. Funct. Mater.*, 2009, **19**, 369–377.

[120] A. Alghannam, C. L. Muhich and C. Musgrave, *Phys. Chem. Chem. Phys.*, 2017, **19**, 4541–4552.

Chapter 6

Quantifying Support Interactions and Reactivity Trends of Single Metal Atom Catalysts over TiO_2

6.1 Introduction

Atomically dispersed catalysts represent the pinnacle for achieving high activity with minimal loading.[1–6] A characteristic atomically dispersed catalyst contains a single metal atom as the active center on a support such as metal oxide, and is often described in the literature as "single-atom catalysts".[2,5,6] Each metal atom interacts with the support, and interfacial effects may potentially lead to even more favorable catalysis.[7–10] In the literature, single-atom catalysts have been synthesized for various applications such as CO_2 reduction, CO oxidation, methane oxidation, hydrogenation of organic molecules, water gas shift, and methanol steam reforming.[6,11–13] A number of single-atom catalysts have been synthesized, such as Cu, Au, Pd, Pt, Ru, or Rh, over supports such as TiO_2, CeO_2, or FeO_x.[8–10,14–22] Under-

standing and characterizing metal-support interactions is key to designing and synthesizing new, better single-atom catalysts since the support plays such a crucial role in stabilizing the individual catalyst atoms and affecting chemical reactivity.

Insight on supported dispersed metals is also important in understanding the formation of larger clusters and nanoparticles, as metals may aggregate during synthesis and reaction conditions.[10,23,24] If the metal-support interactions are strong, then aggregation may be hindered, while if metal-support interactions are weak metal diffusion is fast and aggregation of metal atoms more readily occurs.[21,25,26] For instance, Aydin et al.[27] reported that certain clusters (Ir) on MgO were resistant to sintering, while others (Pt and Au) were not. Thus different interactions with the support for different metal atoms/clusters can occur to influence stability and structure of single metal atoms. Several reports have focused on the stability of supported small metal clusters or single atom catalysts.[8,26,28] Theoretical methods such as density functional theory (DFT) can provide valuable insight on supported single atom catalysts.

DFT has been used to model metal atoms and clusters on several metal oxide supports, such as TiO_2, Al_2O_3, or CeO_2.[29–33] Several DFT reports exist on metal cluster-oxide interactions and/or growth of late transition metal atom to form larger clusters on TiO_2.[15,25,34–45] DFT studies have provided valuable insights on the stability of supported metal atoms/clusters, diffusion and activation barriers, charge transfer effects and other structural and electronic properties. Nonetheless, these accounts were primarily focused on the adsorption of late transition metal atoms (or clusters). A complete analysis of all transition metals is lacking, which is the focus of the current work.

The goal of this work was to understand the principles of how single metal atoms interact with a model metal oxide surface, the TiO_2 anatase (101) surface. Noble metals are often used as single-atom catalysts, but these metals are rare and costly, which underscores the importance of identifying catalysts that are more abundant and inexpensive. Therefore, we

have modeled the binding of all transition metals (3d, 4d, and 5d metals) to the surface and explain the nature of the metal-support interactions. We have also studied the activation of CO_2, important for CO_2 reduction, in order to further predict how these single-atom catalysts may behave. We briefly discuss results for post-transition metals. Our work provides a systematic analysis of supported transition and post-transition metals, and will be useful in further design of single-atom catalysts.

6.2 Methodology

We performed all spin-polarized DFT calculations with the Vienna Ab Initio Simulation Package (VASP).[46–49] The valence electrons were represented by plane waves with a cutoff energy of 450 eV. Core electrons were treated by projector augmented wave (PAW) potentials.[50,51] O had 6 valence electrons, while C had 4 valence electrons. For the metals we used the following number of valence electrons: 5 (Sb), 7 (Re), 8(Fe, Os), 9 (Co, Ir), 10 (Ti, Ni, Pd, Hf, Pt), 11 (Sc, Y, Ta, Cu, Ag, Au), 12 (Cr, Zn, Zr, Cd, Hg, W), and 13 (V, Ga, In, Mn, Nb, Tc, Tl), 14 (Ge, Mo, Pb, Ru, Sn), and 15 (Bi, Rh).

Reciprocal space was sampled with a k-point mesh of 2x2x1. Electronic states were converged below a threshold of 10^{-5} eV, while geometries were converged below a threshold of 2×10^{-2} eV/Å. We used the Perdew-Burke-Ernzerhof (PBE) exchange correlation functional.[52] The PBE exchange correlation suffers from self interaction errors for strongly correlated systems like TiO_2. To improve the quality of the electronic structure, such as correct localization of electrons and band gaps,[53–55] we used Hubbard U corrections. The +U corrections were applied to Ti d orbitals with an effective U value of 4.5 eV, similar to previous work.[56–58] For accurately determining the adsorption energies of weakly binding adsorbates such as CO_2 on TiO_2, inclusion of dispersion forces is important.[59–62] To better model dispersion interactions, we used the Grimme D3 dispersion correction with Becke-Jonson

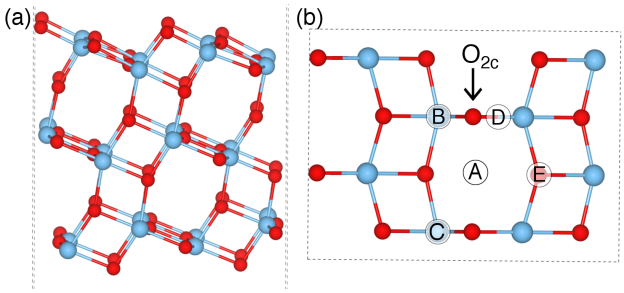

Figure 6.1: The side (a) and top (b) views of the anatase (101) surface slab used in the present work. In the top view, only the surface atoms are shown for clarity. The labels A, B, C, D, and E indicate the most stable metal adsorption sites. The distinction between Site B and C is shown in Figure 6.2. Blue spheres represent Ti atoms, while red spheres represent O atoms.

damping.[63,64] All the reported values (unless explicitly mentioned) are at the PBE+D3+U level.

We modeled the anatase (101) surface with the simulation cell shown in Figure 6.1. This cell was a (2x1) representation of the surface, having dimensions of 10.3 Å × 7.6 Å (72 atoms). The slab was ∼9.6 Å thick, or had six TiO_2 layers. The bottom two TiO_2 layers of the slab were kept frozen. A vacuum space of ∼15 Å was set between periodic slabs. The surface consisted of several types of atoms, such as two-coordinated O atoms (O_{2c}), three-coordinated O atoms (O_{3c}), and five-coordinated Ti atoms (Ti_{5c}). Equation 6.1 shows how adsorption energies were calculated.

$$\Delta E_{ads-M} = E_{M/TiO_2} - E_{TiO_2} - E_M. \tag{6.1}$$

E_{M/TiO_2} is the energy of a TiO_2 surface with metal atom adsorbed, E_{TiO_2} is the energy of a bare TiO_2 surface, and E_M is the energy of a lone metal atom M. We used the E_M values corresponding to the most stable spin state for each atom M, as determined by our calculations. A similar approach was used to calculate adsorption energies for CO_2.

6.2.1 Adsorption Energies of Metal Atoms

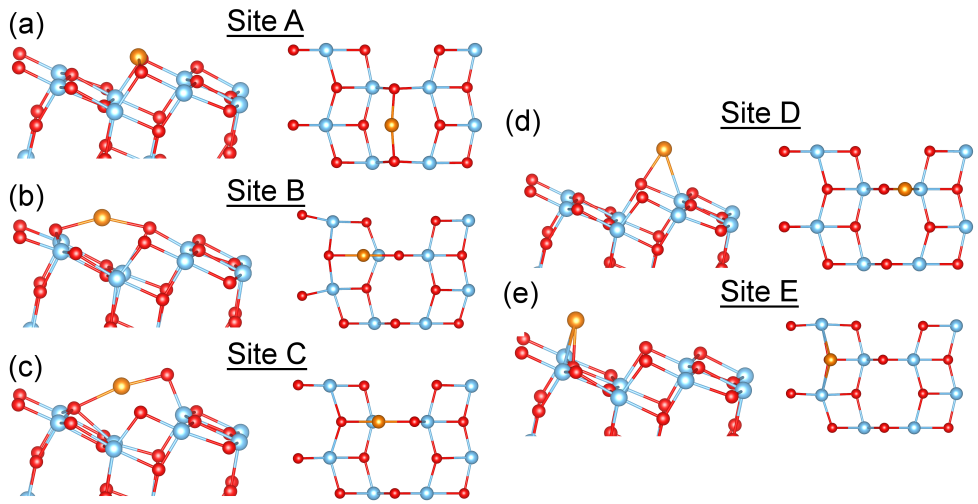

Figure 6.2: Various adsorption configurations for metal atoms on the TiO_2 anatase (101) surface. The adsorbed metal atom is displayed as gold. Shown are top and side views of the surfaces.

In Figure 6.2 we show the various possible adsorption geometries for stable metal adsorption. These sites are similar to previous work[37,39,45] which also modeled metal atom adsorption over the anatase (101) surface. We considered other sites, but after optimization, all these geometries converged to one of the five configurations shown in Figure 6.2. Site A involves bridging between two O_{2c}, and is the most stable adsorption geometry for the metals. Site B involves the metal atom binding between a surface O_{2c} atom and a surface O_{3c} atom. Site C is similar to site B but an O_{2c} becomes very distorted from its normal position by ~ 1 Å(on average) upon metal atom adsorption. This anomalous geometry has been previously discussed in the papers by Alghannam et al.[37] and Wang et al.[45] Site D involves an O_{2c} atom and Ti_{5c} atom. Site E occurs with the metal atom on top of O_{3c} atom and interacting with two Ti_{5c} atoms. We modeled all configurations for each metal, but not all configurations were stable for every metal and would sometimes converge to other geometries.

Figure 6.3 shows the adsorption energies for each atom at the various adsorption sites.

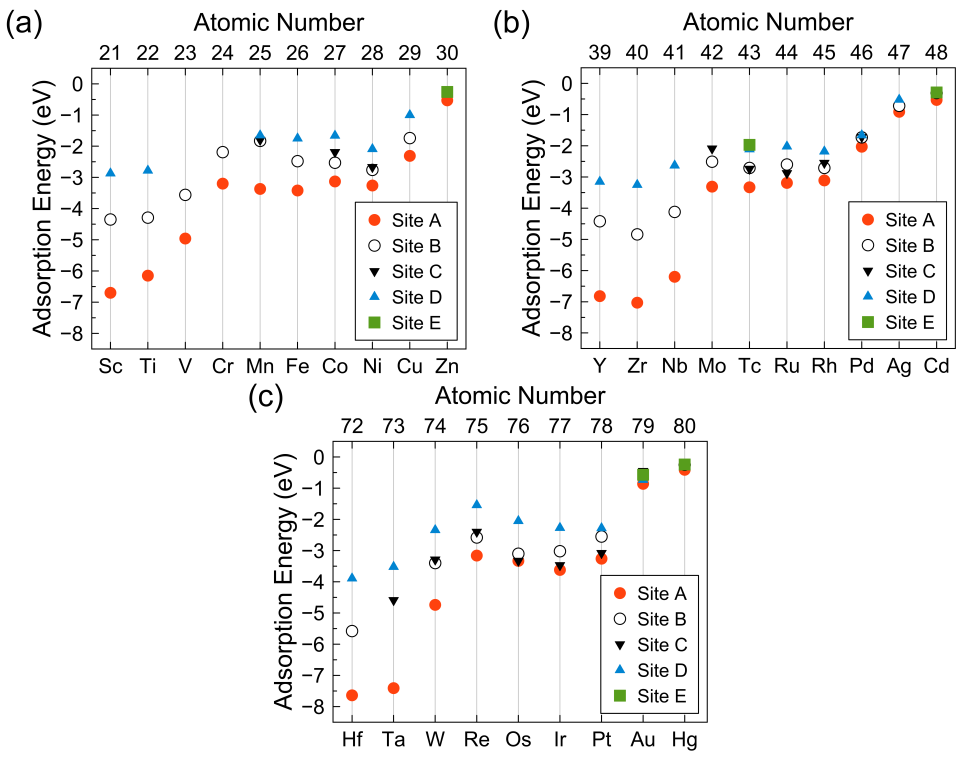

Figure 6.3: Adsorption energies of transition metal atoms in rows 4 (a), 5 (b), and 6 (c) on TiO_2 for the stable adsorption configurations as shown in Figure 6.2.

Only energies for converged structures are reported. For every transition metal, site A was the most stable adsorption mode. This configuration involved only under-coordinated O_{2c} atoms binding to the adsorbed metal. Other stable configurations that existed for nearly every metal were site B and D, which involved O_{2c} and O_{3c} atoms for site B, and O_{2c} and Ti_{5c} atoms for site D. Site C, which had a large distortion of the O_{2c} atom out of the surface, was mostly stable for mid- to late transition metal atoms such as Mn-Ni (except Fe) in row 4, Mo-Pd in row 5, and Ta-Au in row 6. Site E, where the metal atom adsorbed on top of an O_{3c} atom while simultaneously bonding to two Ti_{5c} atoms, was only stable for metals with half filled or completely filled d-orbitals such as Zn (d^{10}), Tc (d^5), Au (d^{10}), and Hg (d^{10}). Based on this data we conclude that adsorbed transition metal atoms bind strongest to O_{2c} atoms (site A), while binding at sites involving Ti_{5c} atoms (Sites D and E) is essentially the

least preferred.

Adsorption energies depended upon whether the transition metal atom was early, middle, or late in the periodic table. Adsorption energies of the middle transition metals tended to be near -3 eV, while the adsorption energies increased with atomic number for the early and late transition metals. Adsorption energies for site A were very stable (-7.6 to -5.0 eV) for early transition metals, moderately stable (-3.4 to -2.0 eV) for mid to late transition metals (with the exception of W at -4.7 eV), and less stable (-0.4 to -0.9 eV) for late transition metals (with the exception of Cu at -2.3 eV). All the metals in their atomic configuration have d electrons to interact with the surface, except for the Cu and Zn group transition metals which have filled d orbitals. Cu group metals have stronger adsorption energies compared to Zn group metals. Cu group metals hybridize with TiO_2 while the Zn group elements do not, as shown by the state in the range of -1 to -7 eV in Figure B.1. Cu binds much stronger than the other metals in the Cu group (Ag and Au). This observation can be rationalized by the PDOS of lone Cu group atoms. Gas-phase Cu bands are much higher in energy (-0.4 eV below the conduction band) compared to gas-phase Ag and Au (around -2.5 and -1.3 eV below the conduction band respectively). See Figure B.2 for these plots. Upon adsorption these bands in Cu shift to lower energy to hybridize with the TiO_2 bands as bonds form (Figure B.1). Such a large shift stabilizes the Cu atom significantly as high energy orbitals become more stable lower energy orbitals. Such a shift is not seen in Ag or Au, and therefore Ag and Au do not bind as strongly to TiO_2 as Cu.

Overall, the adsorption energies decrease in strength with increasing atomic number, with the exception of the near constant adsorption energies of the middle transition metals. This decrease may be attributed to the weaker interactions with TiO_2 for transition metals that have more filled d bands and/or fewer unpaired electrons as was reported previously by Wang et al. for late transition metal atom adsorption on TiO_2.[65] For instance, early transition metals have more unpaired electrons compared to the later transition metals,

such that the former has a larger tendency to pair up their unpaired electrons with TiO_2 resulting in stronger interactions with TiO_2. Of note is that several metals typically relevant for catalysis (e.g. middle to late transition metals) have adsorption energies between -3.5 and -2 eV, or rather stable binding to the surface.

Our results agree with previous simulations of metal atom adsorption on the anatase (101) surface. We calculated the adsorption energy of Cu to be -2.31 eV, which is similar to other reported values of -2.30 eV[44] and -2.26 eV,[37] as well as our reported value of -2.56 eV.[36] Our values of -3.26 and -0.86 eV for Pt and Au are also close to the values of -3.08 and -0.81 eV reported by Wang et al.[45] Zhang et al.[43] reported the Ru adsorption energy to be -3.59, while we calculated an adsorption energy of -3.19 eV. Zhang et al. used a different basis set (double numerical basis set with polarization) and also did not include a dispersion correction, which may explain the small differences for Ru. Alghannam et al.[37] also found the most adsorption stable site of eight different transition metal atoms to be at the bridge site between two O_{2c} atoms (our site A). The mean absolute difference between our adsorption energies and their reported values was 0.15 eV.

Diffusion of transition metal adatoms on support materials can have important consequences in terms of sintering and aggregation to form larger clusters or nanoparticles.[37,66] Metal atoms that readily diffuse may not be stable single atom catalysts. Calculating the diffusion barrier for many metal atoms can be involved,[37] and rather we can use a proxy to estimate diffusion barriers. A large energy difference between the most stable site and the next most stable site indicates that the most stable site has a very deep energy well and to move to the second most stable site, or across the surface, requires significant energy. For instance the energy difference for Cu is the difference in adsorption energies of site A and site B, and has a value of 0.57 eV. A good correlation ($R^2 = 0.76$) between literature diffusion barriers and the energy difference between the two most stable adsorption sites ($\Delta E_{ads–1–2}$) is given in Figure B.3. Thus, knowing the $\Delta E_{ads–1–2}$ value can provide an estimate of the

barrier for diffusion.

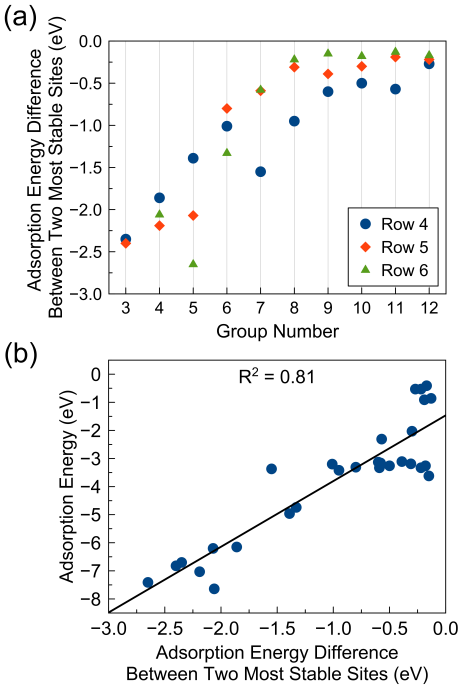

Figure 6.4: Diffusion analysis for metal atoms on TiO_2. (a) The energy difference between the two most stable sites is plotted against group number for all the transition metal atoms supported on TiO_2. (b) Comparison of the most stable adsorption energy at site A with the difference in adsorption energy between the two most stable sites. This energy difference between the two most stable sites can be used as a proxy for the activation barrier for diffusion as discussed in the Supporting Information.

In Figure 6.4a, we show the $\Delta E_{ads-1-2}$ values for all transition metals. Early transition metals (group 3-5) show significantly negative $\Delta E_{ads-1-2}$, which increases to more positive values for mid-transition metals (groups 6-8). Groups 9-12 transition metals show only moderate $\Delta E_{ads-1-2}$. These results show that early transition metals are trapped in deep energy wells with low probability to diffuse to the next most stable adsorption site on the TiO_2 surface. Moving along each row of the transition metals, this trapping becomes less pronounced. For late transition metals the trapping is weak, indicating easier diffusion. In

Figure 6.4b, we show the correlation of the most stable adsorption energies (site A) with the $\Delta E_{ads-1-2}$ values. Our results show that the stronger the adatom binds to the TiO_2 surface, the more difficult it will be to diffuse on the surface. Incidentally Iachella et al.[67] reported that a stronger adsorption energy of Cu compared to Au resulted in higher diffusion barrier of Cu (0.57 eV) compared to Au (0.26 eV) on the stoichiometric TiO_2 surface, similar to the current work. Our results demonstrate the efficient use of simple adsorption energy calculations to estimate diffusion barriers, and that earlier transition metals may be more stable than later transition metals on the surface.

6.2.2 Geometry Analysis of Adsorbed Metal Atoms

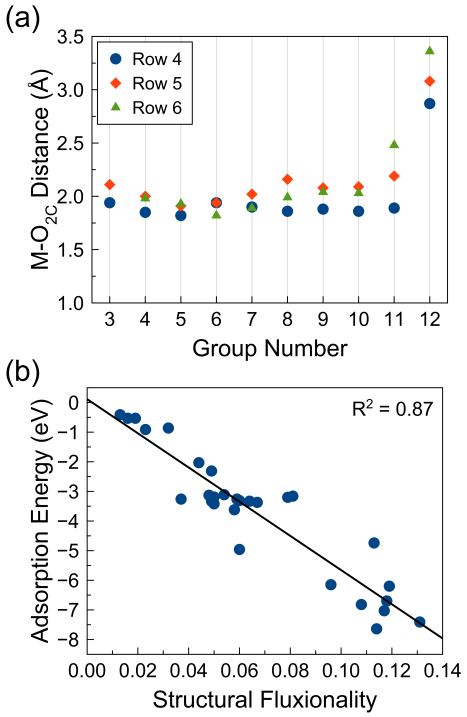

Figure 6.5: Comparison of metal adsorption energies with (a) M-O_{2c} distances and (b) surface fluxionality. Shown are results for the most stable site, or site A.

We analyzed the geometries upon transition metal atom adsorption for the most stable site A, and summarize this information in Figure 6.5. Figure 6.5a shows the bond distances between the transition metal atom and nearby O_{2c} atoms (M-O_{2c}) for each group. In site A the metal atoms are bonded only to the O_{2c} atoms. There appears to be no direct correlation between the M-O_{2c} bond distances and group number. There is also no correlation between metal adsorption energy and M-O_{2c} distance. Rather, all M-O_{2c} bond distances appear to be near 2 Å, with the exception of late transition metals which have large M-O_{2c} bond distances. Similar bond distances near 2 Å were reported by Alghannam et al.[37] for adsorption of eight transition metal atoms on the TiO_2 anatase (101) surface. Experiment also provides evidence based on EXAFS (extended x-ray absorption fine structure spectroscopy) results for group 7 and 8 transition metal-oxygen bond distances to be around 2.1 Å for supported single atoms over metal oxides or in zeolites.[68] The atomic Cu and Zn group transition metals have d^{10} electronic configurations. Despite having filled d states, Cu and Ag bonded to O_{2c} of TiO_2 with short bond distances (1.89 Å for Cu and 2.19 Å for Ag). An Au atom adsorbs on TiO_2 with large bond distances as the bonding interaction of Au involves primarily polarization and dispersion interactions with little charge transfer, unlike Cu and Ag. Larger charge transfer to TiO_2 from Cu and Ag (0.68 and 0.62 e-, respectively) compared to that of Au (0.2 e-) occurs. Similar bonding interactions were described by Wang et al.[45] for Au_1/TiO_2.

We also analyzed how much the surface distorted upon metal atom adsorption for the most stable adsorption site A. The distortions of surface TiO_2 atoms were larger for early transition metals compared to the mid or late transition metals. For instance, upon adsorption of numerous early transition metals (Sc, Ti, Y, Zr, Nb, Hf, Ta, W), several of the surface atoms (typically four to seven) undergo >0.2 Å displacements. These transition metals had strong adsorption energies as Figure 6.3 shows. Upon adsorption of other metals, only a handful of surface atoms (less than four) were displaced by >0.2 Å. The atoms that distorted upon adsorption were typically the O_{2c} and O_{3c} atoms. Typical distortions of surface

O_{2c} and O_{3c} atoms involve these atoms moving out of the surface plane and towards the metal adatom. The distortions of surface Ti atoms were always small (<0.2 Å).

We also analyzed the surface fluxionality, which is a measurement of how much the surface changed upon adsorption. We used the approach of Yang et al.,[69] where they analyzed how a geometry changed between two different states. We calculated how much the surface changed upon metal atom adsorption through the fluxionality value. Figure 6.5b shows the calculated surface fluxionality values compared to the adsorption energies of the metals. A strong correlation exists, where higher surface distortion (or fluxionality) is correlated to stronger adsorption energy. Again this indicates that strong interactions between the metal and the surface, as evidenced by the surface distortions, lead to increased binding.

Sites B and C had similar geometries, where the metal atom bonds to O_{2c} and O_{3c} atoms. However, site C involved significant distortion of the O_{2c} atom, while site B did not. The largest distortions (up to ∼0.4 Å) for site B primarily involved O3c and O2c atoms bonded to the metal adatom. Site C, which involved the most dramatic changes of the TiO_2 surface, where an O_{2c} atom moved significantly out of the surface (∼1 Å), was not a stable site for several of the transition metals (see Figure 6.3). Often an initial geometry for site C converged back to site B or was less stable than other adsorption sites. The large distortions of the O_{2c} atoms decidedly limited the stability of site C.

6.2.3 Electronic Analysis of Adsorbed Metals

In order to further understand the electronic nature of the metal adsorbate-surface interactions, we calculated the projected density of states (PDOS) and show representative results in Figure 6.6. See Figure B.4 in the Supporting Information for PDOS of all adsorbed elements. The adsorption of transition metal atoms on TiO_2 results in surface or gap states. Similar observations have been reported earlier.[45,70–73] Figure 6.6a shows results for Hf (an early transition metal), which introduces a gap state around -1 eV and also populates the

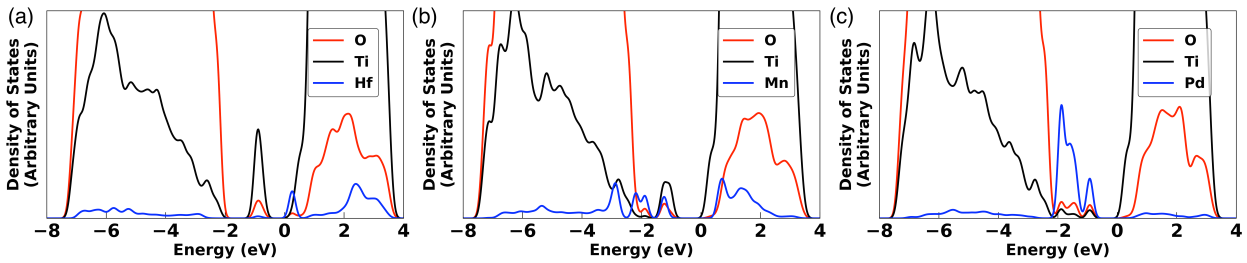

Figure 6.6: Projected density of states of representative early (a, Hf), mid (b, Mn), and late (c, Pd) transition metal atoms adsorbed on TiO_2. The energies are shifted so that 0 eV is at the bottom of the conduction band. Bands below 0 eV are filled states.

conduction band edge with Hf states. Similar to other early transition metals (Sc, Ti, and V group elements), Hf introduces gap states that consist significantly of TiO_2 states. However, in the case of Mn (a mid transition metal) and Pd (a late transition metal), electronic states of these metal atoms are localized in the gap or near the top of the valence band edge. The localized gap states exist within the band gap between -0.8 and -1.6 eV for Mn/TiO_2 and between -0.6 and -2.2 eV for Pd/TiO_2. The gap states were a hybridization of metal adatom, Ti, and O as seen from the overlap of electronic states between the three types of atoms. This behavior was similar to several other mid to late (Cr to Cu group elements) transition metal atoms. We note that metal bands significantly spread across the valence band region ($\sim$ -2 to -8 eV) for all metals except Zn group metals which have filled shells. For several transition metals (like Mn, Co, Ag, W, Pt, and Au) the band gaps, or difference between conduction band edge and valence band edge of the M/TiO_2 system, were lowered by 0.2 to 0.8 eV compared to a pure TiO_2 surface.

During catalytic and photocatalytic reactions over these supported single metal atoms, the high energy gap states may play an important role as these states are likely to interact (or hybridize) with the adsorbed reaction intermediates. For instance, in our previous work the valence band edge states of Cu clusters over TiO_2 interacted with CO_2 to stabilize the activated, bent form of CO_2.[36] Similar conclusions have been reported by others for both CO_2 reduction[71,74] and CO oxidation reactions.[75] The energy level of a gap state can be

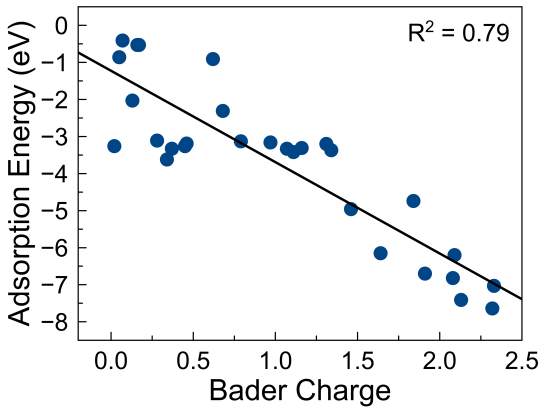

Figure 6.7: Comparison of transition metal atom adsorption energies to calculated Bader charges of adsorbed transition metal atoms at Site A.

be crucial for enabling reduction or oxidation reactions. Several mid-transition metals (see PDOS of Fe, Co, Mo, Cr, Rh, and W) and a few early/late transition metals (V and Ni) had gap states lying very close to the conduction band edge. Since these gap states are close to the conduction band they may more readily participate in reactions with high reduction potential. Wang et al.[76] showed a similar example using TiO_2-supported Pt nanoparticles. The 1 nm Pt particle energy levels, as opposed to larger particles, were close to the CO_2/CH_4 redox potential and was this energy proximity was proposed to increase the activity for CO_2 reduction. Several gap states lie near the valence band (see PDOS of Mn, Fe, Co, Cu, Tc, Ru, Rh, Pd, W, Re, Ir) and after photoexcitation occurs holes may migrate to these metals to enable oxidation reactions with relatively lower potential. Yan et al.[38] performed experiments and calculations to propose a similar phenomena with high and low energy gaps states from adsorbed metals. Finally, the presence of gap states and reduction of band gap can also be beneficial for visible light photocatalysis as reported by Nolan and coworkers.[71]

For all adsorbed transition metals, the metal atoms became positively charged upon adsorption, as determined by Bader charge analysis.[77,78] Electrons transfered to the TiO_2 surface upon adsorption. We found that the metal atom adsorption energies are correlated

with the adatom charges, as Figure 6.7 shows. Metal atoms with large charge transfer interact with the surface strongly, as reflected by stronger adsorption energies. The metal atom charges were also correlated with the metal-oxygen bond dissociation energies (R^2 = 0.73). Metals that formed stronger metal-oxygen bonds had larger degree of charge transfer from the metal adatom to TiO_2 surface due to strong interactions.

The Bader charges of the metal atoms were between +0.02 and +2.32 e^-. The early transition metals (group 3 to 5) had the largest charges, in the range of +1.5 to +2.3 e^-. The mid transition metals had charges between +0.3 and +1.8 e^-, while late transition metals had charges between +0.02 and +0.8 e^-. The larger charge transfer occurring with early and mid-transition metals can be attributed to the presence of a large number of unpaired electrons for these atoms, which upon adsorption can readily transfer to the TiO_2 surface. Moving across a transition metal row, this charge transfer tendency decreased as the transition metals approached stable s^2d^{10} configurations (see Figure B.5 in the Supporting Information). Of note, the charges of the row 4 transition metals decreased along the row more gradually than row 5 and 6 transition metals.

6.2.4 Further Explanation of Metal Atom Adsorption

We further aimed to understand the adsorption energy trends for the transition metals by correlating our adsorption data with known independent quantities. We have already shown that the adsorption energies correlate with the surface distortions (Figure 6.5) and metal atom charge (Figure 6.7). Such quantities, while useful for understanding adsorption behavior, cannot be determined a priori without modeling adsorption and may be of limited use in predicting adsorption behavior. We considered 11 different tabulated properties of transition metals, such as number of d electrons, atomic radii, electronegativity, cohesive energy, workfunction, polarizability, etc. See Table B.1 in the Supporting Information for properties considered. We used the Lasso shrinkage model[79] to identify important descriptors and

performed linear regression using the identified descriptors (metal-oxygen dissociatin energy, number of d electrons, electronegativity) . Compared to univariate regression, the use of multiple descriptors improved the R^2 values only slightly, so we report only univariate linear regression to avoid overfitting. Several of the descriptors we considered did not correlate well with the adsorption energy data (see Table B.2).

The group number correlated strongly ($R^2 = 0.85$) with metal atom adsorption energy, as well as the number of d electrons in the transition metal atom ($R^2 = 0.84$). Moving to the right of the transition metal series resulted in weaker binding to the TiO_2 surface. The d-band center of the lone adsorbed transition metal atom also correlated well with the adsorption energy (R^2=0.80). The d-band model by Nørskov and coworkers[80,81] has been used to explain catalytic activity of different metals. A higher d-band center of the transition metal atom leads to stronger interactions with the surface. Note that the d-band center of the lone adsorbed metal atom is related to the the group number and the number of d electrons so that these descriptors are not independent. Linear regression of d-band center against both the group number and number of d electrons resulted in an R^2 values of 0.88. Group number was also reported as an important property in the prediction of d-band center of bimetallic compounds.[82]

The property that correlated best with the adsorption energies ($R^2 = 0.86$) was the tabulated M-O bond dissociation energies,[83] or the energy to break the M-O bond in a diatomic gas phase MO molecule, as Figure 6.8 shows. A similar correlation was found earlier for metal adsorption on the rutile (110) surface.[84] Essentially metal atoms that form strong M-O bonds (manifested by large M-O dissociation energies) will have large adsorption energies because these metal atoms interact strongly with surface oxygen atoms upon adsorption. We expect that a correlation between adsorption energy and M-O bond dissociation energy may exist over other metal oxide surfaces where formation of metal-oxygen bonds occurs. The correlation involving M-O dissociation energy also echoes work on the oxophilicity of transition

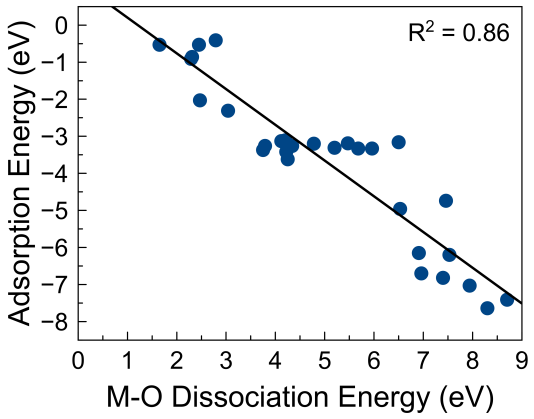

Figure 6.8: Comparison of transition metal atom adsorption energies to M-O (metal-oxygen) bond dissociation energy of gas phase diatomic MO molecules.[83]

metals, or the tendency of the metals to bond with oxygen. Campbell and coworkers,[85,86] using microcalorimetric experiments, correlated the metal oxophilicity with adhesion energy of metal nanoparticles over different metal oxide surfaces.

6.2.5 Effect of DFT Method

Our results so far have been at the DFT+D3+U level, or including dispersion corrections and the +U correction, as indicated in the Methodology section. We performed further tests without such corrections to assess their affect on the adsorption energies of the transition metal atoms. Figure 6.9 shows calculated adsorption energies at four levels of theory: DFT+U+D3, DFT+U, DFT+D3, and DFT. The trends in adsorption energies are the same using all four methods. Early transition metals bind strongly to the surface. The adsorption energies of the middle transition metals all have similar values within a row. Late transition metals bind weakly. We have summarized the differences in the adsorption energies for the four methods in Table B.3.

Compared to the PBE results, the inclusion of dispersion corrections (D3) stabilized the metal atoms by an average of 0.38 eV. V actually destabilized by 0.06 eV, while Nb was most

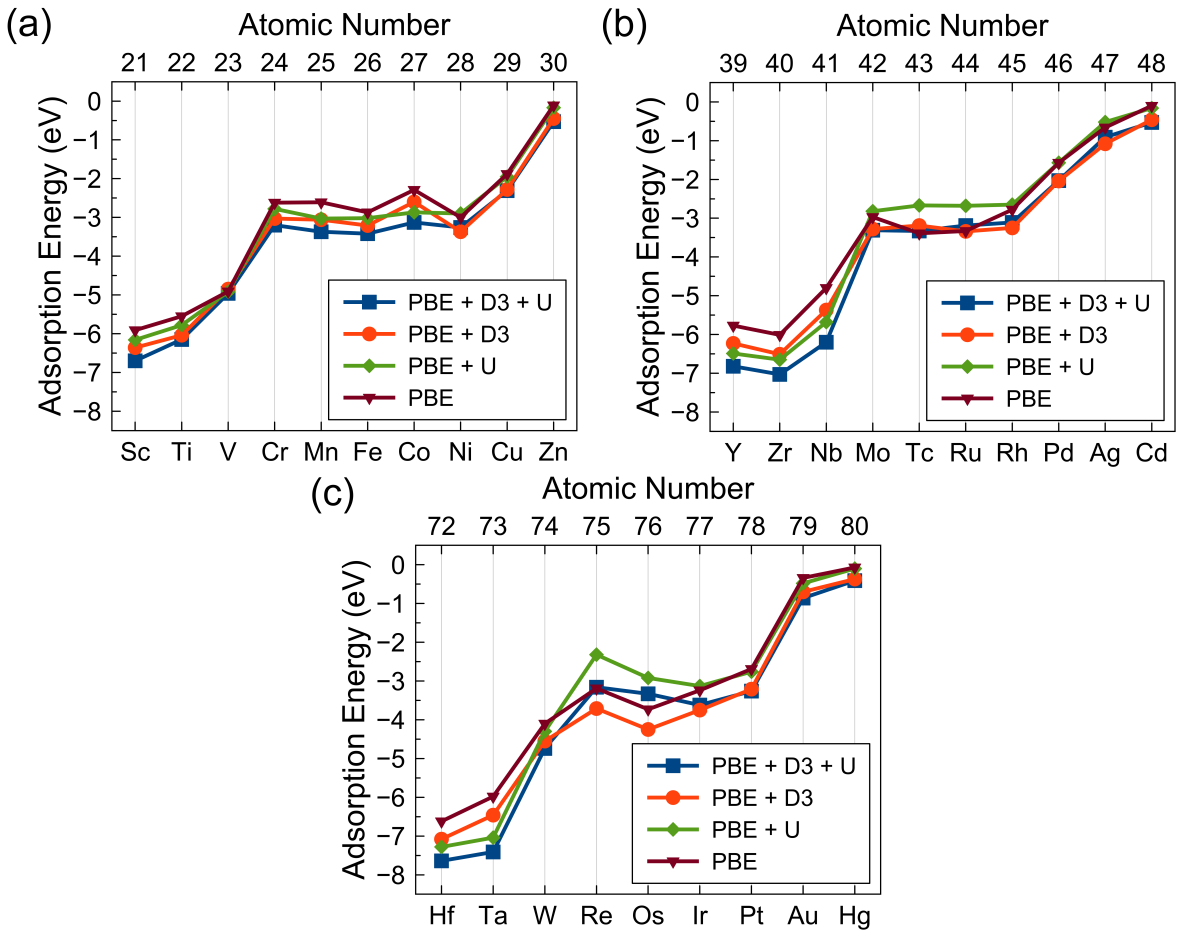

Figure 6.9: Comparison of four different levels of theory for the adsorption energies of row 4 (a), row 5 (b), and row 6 (c) transition metals. Results are for site A over the TiO_2 surface.

stabilized by 0.57 eV. A similar stabilizing effect using D2 dispersion corrections of 0.3 to 0.6 eV was also reported for Au and Ag atom adsorption on the TiO_2 anatase (101) surface.[60] In contrast, when U corrections were applied to PBE, some atoms were stabilized (up to 1.06 eV for Ta) while others were destabilized (down to 0.87 eV for Re). Most atoms however appeared to be stabilized by the +U corrections. Finally, when both D3 and U corrections were applied to PBE, all the adsorption energies were more exothermic, except for a few metals (Tc, Ru, Re, and Os) which were destabilized by $\leq$0.40 eV. The D3 correction will change the adsorption energies as will the U correction. The change in adsorption energies for D3 calculations and change in adsorption energies for U calculations are largely independently additive, since we find for most of the transition metals that adding the two changes from the two separate types of calculations differs by < 0.2 eV from adsorption energy differences for combined D3+U calculations, or $\Delta E_{ads(PBE+D3+U)} - \Delta E_{ads(PBE)} \sim [\Delta E_{ads(PBE+U)} - \Delta E_{ads(PBE)}] + [\Delta E_{ads(PBE+D3)} - \Delta E_{ads(PBE)}]$.

6.2.6 CO_2 Activation over Supported Metal Atoms

CO_2 reduction is an important reaction for curtailing this greenhouse gas and potentially converting it to useful fuels.[87–91] CO_2 reduction to CO or CH_4 has been reported recently using single metal atom catalysts such as Cu/TiO_2,[15,38,92] Rh/TiO_2,[17] Ir/TiO_2,[93] Pd/Al_2O_3,[7,94] Pd/TiO_2,[38] Mn/TiO_2,[38] and Co in a metal oxide framework (MOF).[95] During CO_2 reduction, the activation of a stable linear CO_2 molecule by one electron reduction to form bent CO_2^- anion is one of the initial steps. However, this reaction step is well known to be highly unfavorable (redox potential of -1.9 V vs NHE[90]). Without CO_2 activation, further reduction of the CO_2 molecule can be difficult, if not impossible. The importance of CO_2 activation in the CO_2 reduction reaction has been emphasized by both experimental and theoretical studies.[15,36,96–101]

We modeled adsorption of both linear (non-activated) and bent (activated) CO_2 over the

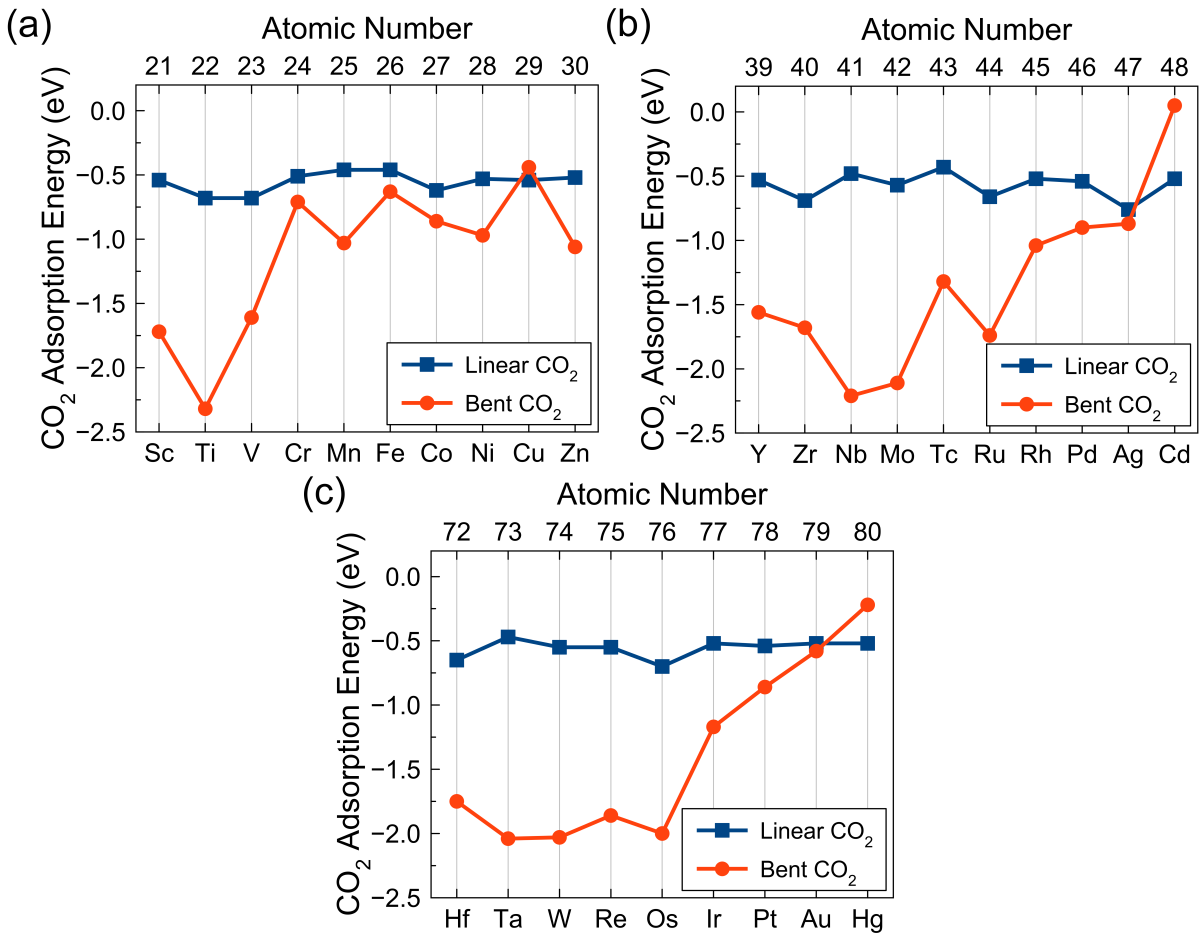

Figure 6.10: Adsorption energies of the most stable bent and linear CO_2 on all the metal atom/TiO_2 surfaces.

metal atom/TiO_2 surfaces. In Figures B.6 and B.8 we show stable adsorption sites for linear and bent CO_2 that were found, while Figures B.7 and Figure B.9 show all the adsorption energies for CO_2 over the different metal/TiO_2 surfaces. All of the CO_2 adsorption geometries we modeled were with a metal in site A since this was found to be the most stable site for all transition metals. All the most stable bent CO_2 geometries occurred with CO_2 binding at interfacial sites except Hg/TiO_2, where CO_2 interacted with just TiO_2. The interfacial sites consisted of the C atom interacting with the transition metal adatom, surface O_{2c}, or O_{3c} atom near the transition metal adatom. In the case of linear adsorption, the CO_2 adsorbed with O_{CO_2}-M bonds, where M was either a surface Ti_{5c} atom or the transition metal adatom. Further discussion of the various CO_2 geometries we modeled can be found in the Supporting Information.

A comparison of the most stable linear and bent CO_2 adsorption energies is shown in Figure 6.10. Notable is the fact that all linear adsorption energies are in a narrow energy range of -0.43 and -0.76 eV with an average adsorption energy of -0.56 eV. There appears little trend in the linear CO_2 adsorption energies with respect to the various transition metals. These results are indicative of the uniform nature of the interactions between linear CO_2 and the surface. We further examined the effect of dispersion forces on linear CO_2 adsorption energies. We modeled linear CO_2 adsorption for the Row 4 transition metals without the dispersion correction (only PBE+U) and found the adsorption energies became more unstable by 0.06 to 0.36 eV. The average linear CO_2 PBE+U adsorption energy over the row 4 transition metals was -0.34 eV, compared to the average PBE+D3+U adsorption energy for row 4 transition metals of -0.56 eV. This indicates that dispersion forces can be important for binding linear CO_2.

Bent CO_2 adsorption however was much stronger and very much depended upon the adsorbed metal. Row 4 transition metal atoms on TiO_2 behaved differently compared to row 5 and row 6 metal atoms. For bent CO_2 adsorption over row 4 metals, only the early

transition metals had very large bent CO_2 adsorption energies being -1.72 eV, -1.61 eV, and -2.3 eV, for Sc, Ti, and V, respectively. For the rest of the row 4 metals, the bent CO_2 adsorption energies were more moderate, between -0.4 and -1.1 eV. In contrast, both the early and mid-transition metals in row 5 (Y to Ru) and row 6 (Hf to Os) elements stabilized the bent CO_2 significantly stronger than the later transition metals. These adsorption energies were in the range of -1.3 to -2.2 eV. Except for some late transition metals (Cu, Cd, Hg), bent CO_2 was more stable than linear CO_2 on all the supported transition metal atoms. This may indicate the potential strong reactivity of these single atom catalysts since activated bent CO_2 could lead to further CO_2 reduction.[15,36,99] We further examined the charge transfer to the most stable bent CO_2 adsorption structures. We found that interaction between the metal adatom and C atom is important for significant (0.43 to 1.02 e-) electron transfer to CO_2 forming CO_2 anion species (see Figure B.10 and associated discussion).

One could expect that a catalyst which binds bent CO_2 strongly could be reactive for CO_2 reduction, while a catalyst that binds bent CO_2 weakly would be less reactive. For instance, Matsubu et al.[17] reported high CO_2 reduction activity for single atom Rh/TiO_2 catalysts. Consistent with Matsubu et al.'s work, we find bent CO_2 adsorption on Rh/TiO_2 to be strongly stabilized (-1.04 eV) compared to the linear (-0.52 eV) adsorption. In a study comparing three different transition metal atoms supported on TiO_2 (Mn, Cu, and Pd), Yan et al.[38] reported CO_2 photoreduction to CO and CH_4. Compared to pure TiO_2, the photocatalytic reduction activities improved with a 1.79 to 2.92-fold increase for CO_2 conversion to CH_4 using the three catalysts. Our results are consistent with Yan et al. where we show that bent CO_2 was strongly stabilized on Mn, Cu, and Pd/TiO_2. Yan et al.[38] also showed that for CO_2 reduction Mn/TiO_2 and Pd/TiO_2 were excellent catalysts. Our results, based on bent CO_2 adsorption energies, also showed that Mn (-1.03 eV) and Pd (-0.90 eV) have strong binding energies, indicating activation of CO_2. We showed that TiO_2 supported early and mid transition metals could be potentially active for CO_2 reduction. A similar

conclusion on early and mid transition metals was reached by Li et al.,[102] although for CO oxidation over FeO_x-supported metal atoms.

Experimental results of atomic-size Cu on TiO_2 indicated increased CO_2 photoreduction activity compared to just TiO_2.[15] Our previous modeling results[15,36] showed that on a TiO_2 surface, bent CO_2 was less stable than linear CO_2 by 0.2-0.25 eV. Bent CO_2 was stabilized by atomic Cu, but was still less stable by ∼0.1 eV compared to linear CO_2.[15,36] This indicates that at least for the case of Cu, lone atoms may not be the most reactive sites for CO_2 reduction. Rather, small Cu clusters[36] (i.e. dimers, trimers) or other surface features (such as defects[92] or step edges) may contribute to the CO_2 reduction activity of supported atomic-size Cu. We also note a similar conclusion that was reported recently.[103] They showed that alkyne hydration reactions in solution occurred only when Au clusters with 3 to 5 atoms in size were formed.

We further considered several possible descriptors that could be used to explain the bent CO_2 adsorption energy trends. We examined several easily available and tabulated transition metal atom properties such as atomic number, atomic radius, electronegativity, ionization energy, electron affinity, number of d electrons, metal oxygen dissociation energy, polarizability, and group number. We also considered bulk transition metal properties such as cohesive energy and workfunction. Finally, from our DFT calculations we obtained other properties such as d-band centers and adsorption energies of transition metals on TiO_2. A list of descriptors and values that we considered is found in Table B.1.

We analyzed the descriptors and CO_2 adsorption energies by developing simple linear regression models using one independent descriptor variable. A model comparing the most stable CO_2 adsorption energies and group number gave an R^2 value of 0.59. A similar weak correlation existed between the metal adsorption energy and bent CO_2 adsorption energy with a R^2 value of 0.53. Other models we considered had relatively weak correlations ($0.56 \geq R^2 \leq 0.61$), such as using number of d electrons, metal cohesive energy, and d-band center.

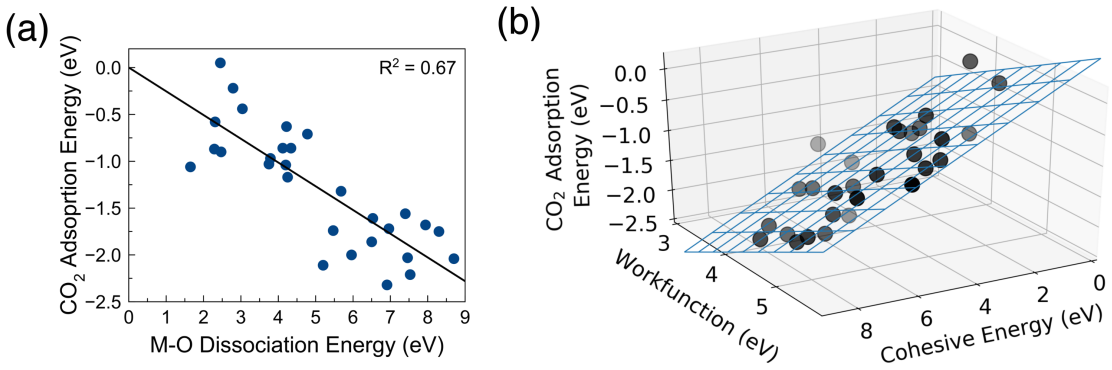

Figure 6.11: Regression models analyzing bent CO_2 adsorption. (a) Bent CO_2 adsorption energies compared to dissociation energies of M-O molecules.[83] (b) Bent CO_2 adsorption energies compared with two predictors, transition metal cohesive energy and workfunction.

A summary of models we considered is found in Table B.4. Our best simple regression model showed a roughly linear correlation (R^2 of 0.67) between bent CO_2 adsorption energies and tabulated M-O (M is a transition metal) dissociation energies of gas phase MO molecules,[83] as Figure 6.11a shows. This behavior can be rationalized from the adsorption configurations of bent CO_2 (see Figure B.8). 22 out of 29 transition metals had O_{CO_2} interacting directly with the transition metal atom with O_{CO_2}-M bond distances < 2.4 Å. Metals that form strong O bonds (large M-O dissociation energies) tend to bind CO_2 strongly through a M-O_{CO_2} bond.

We expanded our analysis to include Lasso regression with the Scikit-learn[104] code to develop models with multiple descriptors. To determine the best set of descriptors (i.e. feature selection), we used the shrinkage model called Lasso,[79] which selects (based on L1 regularization) the best set of features by shrinking the coefficients of less important descriptors to zero. The best model with two descriptors had an adjusted R^2 of 0.76 and used the cohesive energies and workfunctions of the transition metals as independent variables (see Figure 6.11b). We rationalize this model as follows. A large cohesive energy indicates that a metal prefers to form bonds with other atoms compared to the atomic state. Metals with large cohesive energy also strongly bound to CO_2, as reflected by larger bent CO_2 adsorption

energies. A linear correlation between metal cohesive energies and bent CO_2 energies had a R^2 value of 0.58. The second parameter in this model was the metal workfunction. The workfunction is the energy cost of transferring an electron from the fermi level to vacuum level. In the case of an adsorbate interacting with a transition metal, a smaller workfunction indicates that the metal atom more readily gives up electrons to the adsorbate. In our work metals with smaller workfunctions have a larger tendency to transfer electrons to stabilize bent CO_2, which explains why the metal workfunction correlates with the bent CO_2 adsorption energies. This model thus predicts that metals which (1) prefer to bond with other atoms and (2) more readily give up electrons will bind strongly to CO_2.

6.2.7 Post-Transition Metals

Our analysis has focused on transition metals and we briefly discuss the trends of post-transition metals. We modeled adsorption of several post-transition metals: row 4 (Ga, Ge), row 5 (In, Sb, Sb), and row 6 (Tl, Pb, Bi). We found Site A to be the most stable adsorption site for all the post-transition metal atoms, similar to our previous calculations. The adsorption energies ranged between -1.64 eV to -3.55 eV (see Figure B.11). We also calculated the Bader charges of the adsorbed atoms (see Figure B.12). Bader charges were in the range of +0.75 to +1.30 e^-, indicating significant electron transfer from the metal atoms to the TiO_2 surface. Metals with only one valence p electron (Ga, In, Tl) transferred a smaller number of electrons (in the range of 0.75 to 0.79 e-) compared to other post-transition metals with more (2 or 3) electrons. Compared to the transition metals, the adsorption energies and Bader charges of post-transition metals had a smaller range. Transition metal adsorption energies and charges were in the range of -0.41 to -7.64 eV and +0.02 to +2.33 e^-, respectively. Using Lasso feature selection, we found a good correlation (adjusted R^2=0.92) between the adsorption energies and two descriptors: M-O dissociation energy and group number. The values for various descriptors considered are given in Table B.5.

We also modeled CO_2 adsorption over the post-transition adatoms. Compared to the transition metals, there was much less variation in the CO_2 adsorption energies for both bent and linear CO_2 configurations (See Figures B.13). The adsorption energies of the most stable linear CO_2 ranged between -0.51 and -0.60 eV and occurred through O_{CO_2}-Ti_{5c} interactions. We also modeled linear CO_2 adsorption through O_{CO_2}-M interactions, but these geometries were always unstable for the post-transition metals and did not result in bound CO_2. In the case of bent CO_2, adsorption energies ranged between -0.39 and -0.84 eV. In contrast to linear CO_2, for most of the metals the most stable bent CO_2 configurations were at an interfacial site, where CO_2 interacted with both TiO_2 and the metal adatom (see Figure B.14). Only for Ga and In did CO_2 prefer to adsorb on TiO_2 far from Ga or In (the shortest O_{CO_2}-adatom distance was 2.6 or 2.7 Å for Ga or In, respectively).

Adsorbed CO_2 Bader charges were neutral for linear CO_2 while negative for bent CO_2, similar to the transition metal atoms, as Figure B.15 shows. The bent CO_2 charges for the post-transition metals were similar to the CO_2 charges over transition metals. We found that when bent CO_2 interacted with the C atom bonding to the post-transition metal atom (e.g. Sb and Bi), the charge transfer was significantly large (0.95 and 0.77 e-). On other post-transition metals, where bent CO_2 interacted with the C bonded to surface O_{2c} or O_{3c} atoms, less charge transfer occurred, $\sim$0.2 e-. Using Lasso, we found the atomic number and ionization energy of the post-transition metal atoms be be important descriptors for estimating CO_2 adsorption energies. Linear regression using these two descriptors gave an adjusted R^2 of 0.72, which is a weaker correlation than the best transition metal correlation (based on workfunction and cohesive energy). Univariate regression showed poor correlations (see Table B.6), again in contrast with the transition metal results.

6.3 Conclusions

We modeled adsorption of all 29 transition metal atoms on the TiO_2 anatase (101) surface. The most stable adsorption configuration involved bridging between two O_{2c} atoms (denoted as site A in our work) for all the adsorbed metal atoms. The adsorption energy of the transition metal atoms weakened going from early to mid to late transition metal atoms. The adsorption energies ranged between -7.6 and -0.4 eV. Using Lasso shrinkage models, the trends in adsorption energies were correlated to several descriptors like metal-oxygen bond dissociation energy, structural fluxionality, Bader charges, d-band center, and group number. Based on the adsorption energies we developed a correlation to predict diffusion energies, and show that early transition metals had the highest diffusion barriers while later transition metals had lower diffusion barriers. Density of states analysis showed that metal atom adsorption introduced gap states at various energy levels within the band gap of TiO_2. The gap states primarily consisted of TiO_2 states for early transition metals, while metal adatom states for mid and late transition metals.

We also modeled adsorption of bent CO_2, a first step in CO_2 activation. Early and mid transition metal atoms stabilized bent CO_2 anions with adsorption energies up to -2.2 eV. Suitable descriptors such as workfunction and cohesive energies were identified using the Lasso shrinkage model to explain the CO_2 adsorption energy trends. We also modeled post-transition metals and found that in general metal atom adsorption and bent CO_2 adsorption energies were weaker compared to the transition metals. Our results provide important insights into the trends of metal-support interactions across all the transition and several post-transition metals. Reactivity trends for CO_2 activation predicted that the early and mid transition metal atoms, which can be both abundant and inexpensive, to be catalytically active. Our work serves as important motivation to further explore several early to mid-transition metals as atomically dispersed catalysts.

Bibliography

[1] B. C. Gates, *Chem. Rev.*, 1995, **95**, 511–522.

[2] H. Zhang, G. Liu, L. Shi and J. Ye, *Adv. Energy Mater.*, 2018, **8**, 1701343.

[3] L. Liu and A. Corma, *Chem. Rev.*, 2018, **118**, 4981–5079.

[4] M. Flytzani-Stephanopoulos and B. C. Gates, *Annu. Rev. Chem. Biomol. Eng.*, 2012, **3**, 545–574.

[5] X. F. Yang, A. Wang, B. Qiao, J. Li, J. Liu and T. Zhang, *Acc. Chem. Res.*, 2013, **46**, 1740–1748.

[6] J. Liu, *ACS Catal.*, 2017, **7**, 34–59.

[7] J. H. Kwak, L. Kovarik and J. Szanyi, *ACS Catal.*, 2013, **3**, 2094–2100.

[8] M. Yang and M. Flytzani-Stephanopoulos, *Catal. Today*, 2017, **298**, 216–225.

[9] L. DeRita, S. Dai, K. Lopez-Zepeda, N. Pham, G. W. Graham, X. Pan and P. Christopher, *J. Am. Chem. Soc.*, 2017, **139**, 14150–14165.

[10] J. Jones, H. Xiong, A. T. DeLaRiva, E. J. Peterson, H. Pham, S. R. Challa, G. Qi, S. Oh, M. H. Wiebenga, X. I. Pereira Hernandez, Y. Wang and A. K. Datye, *Science*, 2016, **353**, 150–154.

[11] E. C. Tyo and S. Vajda, *Nat. Nanotechnol.*, 2015, **10**, 577–588.

[12] M. Dhiman and V. Polshettiwar, *ChemCatChem*, 2018.

[13] S. Vajda and M. G. White, *ACS Catal.*, 2015, **5**, 7152–7176.

[14] J. Xing, J. F. Chen, Y. H. Li, W. T. Yuan, Y. Zhou, L. R. Zheng, H. F. Wang, P. Hu, Y. Wang, H. J. Zhao, Y. Wang and H. G. Yang, *Chem. - Eur. J.*, 2014, **20**, 2138–2144.

[15] C. Liu, S. K. Iyemperumal, N. A. Deskins and G. Li, *J. Photonics Energy*, 2016, **7**, 012004.

[16] W. E. Kaden, T. Wu, W. A. Kunkel and S. L. Anderson, *Science*, 2009, **326**, 826–829.

[17] J. C. Matsubu, V. N. Yang and P. Christopher, *J. Am. Chem. Soc.*, 2015, **137**, 3076–3084.

[18] T. Y. Chang, Y. Tanaka, R. Ishikawa, K. Toyoura, K. Matsunaga, Y. Ikuhara and N. Shibata, *Nano Lett.*, 2014, **14**, 134–138.

[19] G. Spezzati, Y.-Q. Su, J. P. Hofmann, A. D. Benavidez, A. T. DeLaRiva, J. McCabe, A. K. Datye and E. J. M. Hensen, *ACS Cat.*, 2017, **7**, 6887–6891.

[20] Q. Fu, H. Saltsburg and M. Flytzani-Stephanopoulos, *Science*, 2003, **301**, 935–938.

[21] B. Qiao, A. Wang, X. Yang, L. F. Allard, Z. Jiang, Y. Cui, J. Liu, J. Li and T. Zhang, *Nat. Chem.*, 2011, **3**, 634–641.

[22] P. Liu, Y. Zhao, R. Qin, S. Mo, G. Chen, L. Gu, D. M. Chevrier, P. Zhang, Q. Guo, D. Zang, B. Wu, G. Fu and N. Zheng, *Science*, 2016, **352**, 797–800.

[23] C. Carrillo, T. R. Johns, H. Xiong, A. Delariva, S. R. Challa, R. S. Goeke, K. Artyushkova, W. Li, C. H. Kim and A. K. Datye, *J. Phys. Chem. Lett.*, 2014, **5**, 2089–2093.

[24] E. D. Goodman, J. A. Schwalbe and M. Cargnello, *ACS Cat.*, 2017, **7**, 7156–7173.

[25] R. P. Galhenage, H. Yan, S. A. Tenney, N. Park, G. Henkelman, P. Albrecht, D. R. Mullins and D. A. Chen, *J. Phys. Chem. C*, 2013, **117**, 7191–7201.

[26] Y. Chen, Z. Huang, Z. Ma, J. Chen and X. Tang, *Catal. Sci. Technol.*, 2017, **7**, 4250–4258.

[27] C. Aydin, J. Lu, N. D. Browning and B. C. Gates, *Angew. Chem.*, 2012, **51**, 5929–5934.

[28] B. C. Gates, M. Flytzani-Stephanopoulos, D. A. Dixon and A. Katz, *Catal. Sci. Technol.*, 2017, **7**, 4259–4275.

[29] G. Pacchioni, *Phys. Chem. Chem. Phys.*, 2013, **15**, 1737–57.

[30] D. Cheng, F. R. Negreiros, E. Aprà and A. Fortunelli, *ChemSusChem*, 2013, **6**, 944–965.

[31] J. Paier, C. Penschke and J. Sauer, *Chem. Rev.*, 2013, **113**, 3949–3985.

[32] E. Jimenez-Izal and A. N. Alexandrova, *Annu. Rev. Phys. Chem.*, 2018, **69**, 377–400.

[33] E. Fako, Z. Łodziana and N. López, *Catal. Sci. Technol.*, 2017.

[34] X. Tong, L. Benz, S. Chrétien, P. Kemper, A. Kolmakov, H. Metiu, M. T. Bowers and S. K. Buratto, *J. Chem. Phys.*, 2005, **123**, 204701.

[35] S. V. Ong and S. N. Khanna, *J. Phys. Chem. C*, 2012, **116**, 3105–3111.

[36] S. K. Iyemperumal and N. A. Deskins, *Phys. Chem. Chem. Phys.*, 2017, **19**, 28788–28807.

[37] A. Alghannam, C. L. Muhich and C. Musgrave, *Phys. Chem. Chem. Phys.*, 2017, **19**, 4541–4552.

[38] Y. Yan, Y. Yu, S. Huang, Y. Yang, X. Yang, S. Yin and Y. Cao, *J. Phys. Chem. C*, 2017, **121**, 1089–1098.

[39] X.-q. Gong, A. Selloni, O. Dulub, P. Jacobson and U. Diebold, *J. Am. Chem. Soc.*, 2008, **130**, 370–381.

[40] Y. Han, C. J. Liu and Q. Ge, *J. Phys. Chem. B*, 2006, **110**, 7463–7472.

[41] C. T. Yang, N. Balakrishnan, V. R. Bhethanabotla and B. Joseph, *J. Phys. Chem. C*, 2014, **118**, 4702–4714.

[42] Y. Zhou, C. L. Muhich, B. T. Neltner, A. W. Weimer and C. B. Musgrave, *J. Phys. Chem. C*, 2012, **116**, 12114–12123.

[43] S.-t. Zhang, C.-m. Li, H. Yan, M. Wei, D. G. Evans and X. Duan, *J. Phys. Chem. C*, 2014, **118**, 3514–3522.

[44] N. Seriani, C. Pinilla and Y. Crespo, *J. Phys. Chem. C*, 2015, **119**, 6696–6702.

[45] H. Wang, T. An and A. Selloni, *J. Chem. Phys.*, 2017, **146**, 184703.

[46] G. Kresse and J. Hafner, *Phys. Rev. B*, 1993, **47**, 558–561.

[47] G. Kresse and J. Hafner, *Phys. Rev. B*, 1994, **49**, 14251–14269.

[48] G. Kresse and J. Furthmüller, *Comput. Mater. Sci.*, 1996, **6**, 15–50.

[49] G. Kresse and J. Furthmüller, *Phys. Rev. B*, 1996, **54**, 11169–11186.

[50] P. E. Blöchl, *Phys. Rev. B*, 1994, **50**, 17953–17979.

[51] G. Kresse and D. Joubert, *Phys. Rev. B*, 1999, **59**, 1758.

[52] J. P. Perdew, K. Burke and M. Ernzerhof, *Phys. Rev. Lett.*, 1996, **77**, 3865–3868.

[53] F. De Angelis, C. Di Valentin, S. Fantacci, A. Vittadini and A. Selloni, *Chem. Rev.*, 2014, **114**, 9708–9753.

[54] M. Capdevila-Cortada, Z. Łodziana and N. López, *ACS Cat.*, 2016, **6**, 8370–8379.

[55] G. Pacchioni, *J. Chem. Phys.*, 2008, **128**, 182505.

[56] M. T. Curnan and J. R. Kitchin, *J. Phys. Chem. C*, 2015, **119**, 21060–21071.

[57] N. A. Deskins, J. Du and P. Rao, *Phys. Chem. Chem. Phys.*, 2017, **19**, 18671–18684.

[58] J. C. Garcia and N. A. Deskins, *J. Phys. Chem. C*, 2012, **116**, 16573–16581.

[59] N. Marom, A. Tkatchenko, M. Rossi, V. V. Gobre, O. Hod, M. Scheffler and L. Kronik, *J. Chem. Theory Comput.*, 2011, **7**, 3944–3951.

[60] A. R. Puigdollers, P. Schlexer and G. Pacchioni, *J. Phys. Chem. C*, 2015, **119**, 15381–15389.

[61] D. C. Sorescu, J. Lee, W. a. Al-Saidi and K. D. Jordan, *J. Chem. Phys.*, 2012, **137**, 074704.

[62] D. C. Sorescu, S. Civiš and K. D. Jordan, *J. Phys. Chem. C*, 2014, **118**, 1628–1639.

[63] S. Grimme, J. Antony, S. Ehrlich and H. Krieg, *J. Chem. Phys.*, 2010, **132**, 154104.

[64] S. Grimme, S. Ehrlich and L. Goerigk, *J. Comput. Chem.*, 2011, **32**, 1456–1465.

[65] Y. Wang, Y. Su, M. Zhu and L. Kang, *RSC Adv.*, 2015, **5**, 16582–16591.

[66] T. E. James, S. L. Hemmingson and C. T. Campbell, *ACS Cat.*, 2015, **5**, 5673–5678.

[67] M. Iachella, T. Le Bahers and D. Loffreda, *J. Phys. Chem. C*, 2018, **122**, 3824–3837.

[68] J. A. van Bokhoven and C. Lamberti, *X-Ray Absorption and X-Ray Emission Spectroscopy : Theory and Applications*, John Wiley & Sons, Incorporated, New York, 2016, pp. 773–808.

[69] C.-T. Yang, B. C. Wood, V. R. Bhethanabotla and B. Joseph, *Phys. Chem. Chem. Phys.*, 2015, **17**, 25379–25392.

[70] Q. Jin, M. Fujishima, A. Iwaszuk, M. Nolan and H. Tada, *J. Phys. Chem. C*, 2013, **117**, 23848–23857.

[71] M. Nolan, A. Iwaszuk, A. K. Lucid, J. J. Carey and M. Fronzi, *Adv. Mater.*, 2016, **28**, 5425–5446.

[72] K. C. Schwartzenberg, J. W. J. Hamilton, A. K. Lucid, E. Weitz, J. Notestein, M. Nolan, J. A. Byrne and K. A. Gray, *Catal. Today*, 2017, **280**, 65–73.

[73] N. Umezawa, H. H. Kristoffersen, L. B. Vilhelmsen and B. Hammer, *J. Phys. Chem. C*, 2016, **120**, 9160–9164.

[74] M. Fronzi, W. Daly and M. Nolan, *Appl. Catal., A*, 2016, **521**, 240–249.

[75] S. Li, X. Zhao, J. L. Shi, Y. Jia, Z. Guo, J.-H. Cho, Y. Gao and Z.-y. Zhang, *Phys. Chem. Chem. Phys.*, 2016, **18**, 24872–24879.

[76] W.-N. Wang, W.-J. An, B. Ramalingam, S. Mukherjee, D. M. Niedzwiedzki, S. Gangopadhyay and P. Biswas, *J. Am. Chem. Soc.*, 2012, **134**, 11276–11281.

[77] R. F. W. Bader, *Atoms in molecules: a quantum theory*, 1990.

[78] G. Henkelman, A. Arnaldsson and H. Jónsson, *Comput. Mater. Sci.*, 2006, **36**, 354–360.

[79] R. Tibshirani, *J. R. Stat. Soc.: Ser. B*, 1996, **58**, 267–288.

[80] A. Ruban, B. Hammer and J. K. Norskov, *J. Mol. Catal. A: Chem.*, 1997, **115**, 421.

[81] B. Hammer and J. Norskov, *Adv. Catal.*, 2000, **45**, 71–129.

[82] I. Takigawa, K.-i. Shimizu, K. Tsuda and S. Takakusagi, *RSC Adv.*, 2016, **6**, 52587–52595.

[83] *CRC Handbook of Chemistry and Physics*, ed. J. R. Rumble, CRC Press/Taylor & Francis, Boca Raton, FL., 98th edn., 2017.

[84] A. M. Asaduzzaman and P. Kruger, *J. Phys. Chem. C*, 2008, **112**, 19616–19619.

[85] S. L. Hemmingson and C. T. Campbell, *ACS Nano*, 2017, **11**, 1196–1203.

[86] C. T. Campbell and Z. Mao, *ACS Cat.*, 2017, **7**, 8460–8466.

[87] Y. Li, S. H. Chan and Q. Sun, *Nanoscale*, 2015, **7**, 8663–8683.

[88] H. Li, L. Wang, Y. Dai, Z. Pu, Z. Lao, Y. Chen, M. Wang, X. Zheng, J. Zhu, W. Zhang, R. Si, C. Ma and J. Zeng, *Nat. Nanotechnol.*, 2018, **13**, 411–417.

[89] Y. Ma, X. L. Wang, Y. S. Jia, X. B. Chen, H. X. Han and C. Li, *Chem. Rev.*, 2014, **114**, 9987–10043.

[90] S. N. Habisreutinger, L. Schmidt-Mende and J. K. Stolarczyk, *Angew. Chem., Int. Ed.*, 2013, **52**, 7372–7408.

[91] S. Kattel, P. Liu and J. G. Chen, *J. Am. Chem. Soc.*, 2017, **139**, 9739–9754.

[92] L. Liu, C. Zhao and Y. Li, *J. Phys. Chem. C*, 2012, **116**, 7904–7912.

[93] X. Chen, X. Su, H.-Y. Su, X. Liu, S. Miao, Y. Zhao, K. Sun, Y. Huang and T. Zhang, *ACS Cat.*, 2017, **7**, 4613–4620.

[94] X. Wang, H. Shi and J. Szanyi, *Nat. Commun.*, 2017, **8**, 513.

[95] H. Zhang, J. Wei, J. Dong, G. Liu, L. Shi, P. An, G. Zhao, J. Kong, X. Wang, X. Meng, J. Zhang and J. Ye, *Angew. Chem., Int. Ed.*, 2016, **55**, 14310–14314.

[96] S. Ma, W. Song, B. Liu, W. Zhong, J. Deng, H. Zheng, J. Liu, X. Q. Gong and Z. Zhao, *Appl. Catal., B*, 2016, **198**, 1–8.

[97] S. Neatu, J. A. Maciá-Agulló, P. Concepción and H. Garcia, *J. Am. Chem. Soc.*, 2014, **136**, 15969–15976.

[98] J. A. Rodriguez, P. Liu, D. J. Stacchiola, S. D. Senanayake, M. G. White and J. G. Chen, *ACS Cat.*, 2015, **5**, 6696–6706.

[99] H. He, P. Zapol and L. A. Curtiss, *J. Phys. Chem. C*, 2010, **114**, 21474–21481.

[100] H. He, P. Zapol and L. a. Curtiss, *Energy Environ. Sci.*, 2012, **5**, 6196.

[101] S. Kattel, B. Yan, J. G. Chen and P. Liu, *J. Catal.*, 2016, **343**, 115–126.

[102] F. Li, Y. Li, X. C. Zeng and Z. Chen, *ACS Cat.*, 2015, **5**, 544–552.

[103] J. Oliver-Meseguer, J. R. Cabrero-Antonino, I. Dominguez, A. Leyva-Perez and A. Corma, *Science*, 2012, **338**, 1452–1455.

[104] F. Pedregosa, G. Varoquaux, A. Gramfort, V. Michel, B. Thirion, O. Grisel, M. Blondel, P. Prettenhofer, R. Weiss, V. Dubourg, J. Vanderplas, A. Passos, D. Cournapeau, M. Brucher, M. Perrot and E. Duchesnay, *J. Mach. Learn. Res*, 2011, **12**, 2825–2830.

Chapter 7

The Fate of Supported Atomic-Size Catalysts in Reactive Environments

7.1 Introduction

Sub-nanometer metal catalysts have attracted interest as potentially active atomic-size catalysts for applications such as chemical synthesis, energy production, and emissions control.[1–8] Sub-nanometer or atomically dispersed catalysts are advantageous because they can have a high density of active sites and therefore a large activity to catalyst loading ratio. A number of such small clusters have been synthesized, such as Cu, Pt, Pd, Ag, and Au.[4,5] Specific recent reactions that have been studied using such catalysts include CO oxidation,[9–11] CO_2 reduction,[12–14] and the water gas shift reaction.[15,16] It has been a challenge to synthesize and correctly identify sub-nanometer clusters, and specialized synthesis techniques such as size-selected cluster (soft-landing) deposition, metal leaching, and wet chemistry methods have been used.[4,11] Indeed, stabilizing atoms or clusters in certain sizes or oxidation states is key to controlling their catalytic activity. The current report focuses on understanding

the nature of cluster stability (i.e. oxidation state and size), and how this in turn affects catalyst properties.

Supported metal atoms or clusters can sinter at elevated temperatures,[1,2,17–21] and the catalytic activity of supported metal clusters often depend on the size of the metal clusters.[7,22,23] For instance, high activity of small clusters has been reported for CO oxidation,[10] CO_2 reduction,[24] hydrogenation,[25] oxidative dehydrogenation of propane,[26] and propylene epoxidation.[8] Still, reports also exist where catalytic activity of small supported clusters were reported to be smaller than supported nanoparticles. In the case of toluene hydrogenation, Ir_4 and Ir_6 clusters showed lower activity than a larger Ir_{20} particle, which was attributed to strong H_2 chemisorption and hence poisoning of these smaller clusters.[27] Interestingly, Ir_4 clusters readily formed Ir_{20} aggregates on Al_2O_3 but not on MgO, indicating the importance of cluster-support interactions in stabilizing clusters of particular sizes.

Furthermore, metal clusters can become oxidized during synthesis or reaction conditions.[2,11,19,28–31] In some cases oxidation of metal clusters may be favorable while for other cases oxidation may have detrimental catalytic effects. DeRita et al.[11] showed that isolated Pt atoms on TiO_2 were active for CO oxidation, while platinum oxide clusters bound CO too strongly which resulted in no CO oxidation activity. On the other hand, Spezzati et al.[3] reported that atomically dispersed PdO and PdO_2 species on ceria improved CO oxidation activity. In the presence of excess oxygen, NO_x reduction by NH_3 was reported to selectively occur when CuO existed as dispersed species on alumina.[32] In the presence of H_2 metallic clusters and nanoparticles of Ir[33] and Cu[13,34] were reported to be stable and active towards hydrogenation and CO_2 reduction reactions. Understanding the chemical state of a supported cluster (metallic or oxidized) is crucial in understanding and characterizing dispersed catalysts.

Theory has been an essential tool to study sub-nanometer catalysts. Density functional theory (DFT) studies have examined metal atom diffusion,[35] metal cluster growth,[36–38]

cluster size effects,[39,40] and oxidation of metal clusters[8,41–45,45–47] supported on various oxides like TiO_2, MgO, and Al_2O_3. Huber et al.[41] used DFT to show that small Pd clusters supported on magnesia readily dissociate O_2 to become oxidized, more so than similar Pd clusters in the gas phase. Ong and Khanna[44] also reported that in the presence of small Pd clusters ($\leq$ 7 atoms) supported on TiO_2, O_2 molecules preferred to exist on the surface in an activated or dissociated form. In a recent study by Concepcion et al.,[48] they reported that a smaller Cu_5 cluster showed less tendency to oxidize compared to larger Cu_8 or Cu_{20} clusters, thereby highlighting the role of cluster size dependent oxidation. These reports demonstrate the utility of molecular modeling in characterizing supported or gas phase metal clusters. Such tools can clarify the nature of supported clusters, especially in oxidative reaction conditions, and provide better understanding on the stability of clusters (i.e. resistance to oxidation or aggregation).

This goal of this work was to address the issues related to finding the stable state of supported clusters (i.e. metallic or oxidized) under oxidizing conditions using a combination of modeling (density functional theory) and experiments. Precisely identifying the chemical state of potential supported clusters is important in order to design better catalysts with high catalytic activity and stability. The state of Cu clusters on TiO_2 (a prototypical support) under oxidizing reaction environments was identified and characterized by considering the kinetics of O_2 dissociation/oxidation along with the thermodynamics of Cu oxidation/aggregation. Our main focus was on Cu, but we also report on aggregation and/or oxidation processes of other metals in groups 9, 10, and 11.

7.2 Methodology

7.2.1 Computational Methodology

We report all our results using spin polarized DFT with the CP2K code.[49,50] CP2K employs a hybrid Gaussian and Plane Wave (GPW) approach.[51] We used the generalized gradient approximation exchange correlation functional of Perdew Burke Ernzerhof (PBE).[52] Molecularly optimized (MOLOPT) double ζ basis sets[53] were used to describe the valence electrons, while the core electrons were described by norm conserving Goedecker-Teter-Hutter (GTH) pseudopotentials.[54] The number of valence electrons used for were as follows: C (4), O (6), Ti(12), Co/Rh/Ir (17), Ni/Pd/Pt (18), Cu/Ag/Au (11). The electronic and ionic relaxation convergence criteria were 1E-6 Ha and 0.05 eV/Å, respectively, similar to our previous work.[40] We used a plane wave cutoff energy of 300 Ry for our calculations. We also used Grimme's D3[55,56] dispersion corrections with Becke-Jonsson damping in our study, as dispersion was found to be important for accurately identifying the most stable geometries of supported clusters.[57] Previous reports have shown that high spin states for Cu and Pt oxide clusters are more stable than lower spin state clusters.[58,59] We therefore tested multiple spin states for all the gas-phase and TiO_2-supported clusters and report only the most stable spin states herein.

We modeled the TiO_2 anatase (101) surface as a (2x4) rectangular slab consisting of six O-Ti-O layers for a total of 288 atoms. This slab had lattice vectors of 20.6Å and 15.1 Å parallel to the surface, and a lattice vector 30.0 Å normal to the surface. The thickness of the slab was 9.4 Å, which gave a vacuum space of $\sim$21 Å. The bottom two layers of the slab were frozen in bulk positions. More details on this model can be found in our previous work,[40] which used a similar slab. This slab is shown in Figure C.1. In order to calculate the degree of electron transfer and oxidation state of atoms, we used DDEC6 charge analysis.[60,61] DDEC6 charges were compared extensively with Bader charges in our previous work[40] for

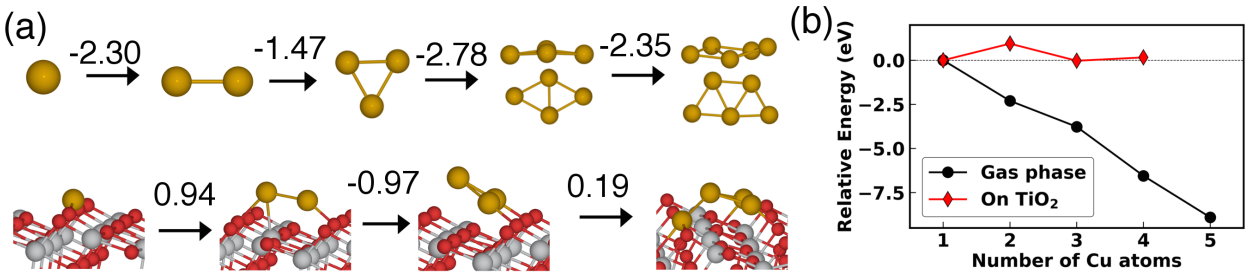

Figure 7.1: (a) Cu aggregation geometries and corresponding reaction energies (in eV) in the gas-phase and over TiO_2. (b) Relative energies of clusters of various sizes in gas-phase and on TiO_2

several periodic and molecular systems, and we found the DDEC6 and Bader methods to give similar partial atomic charges. To generate accurate DDEC6 charges, we calculated the electron density using a very large plane wave cutoff energy of 1600 Ry. The climbing image nudged elastic band method (CI-NEB)[62] was used to calculate the activation energy of O_2 dissociation on TiO_2 supported Cu clusters. We used at least 7 images to model O_2 dissociation.

7.3 Results and Discussion

7.3.1 Thermodynamics of Cu aggregation and oxidation

Cu aggregation

We first modeled Cu atom addition (or $Cu_x + Cu \longrightarrow Cu_{x+1}$) in the gas phase. Figure 7.1 shows the reaction energies and energies of clusters of various sizes. The large negative reaction energies (-1.4 to -2.8 eV) clearly indicate the strong preference of Cu atoms to aggregate and form larger Cu clusters. We note that the most stable Cu cluster geometries consist of planar configurations, which was also reported previously (the transition to 3D structures occurs for clusters $\geq$ 7 atom).[63]

In order to understand Cu aggregation on the TiO_2 anatase (101) surface, we adsorbed the

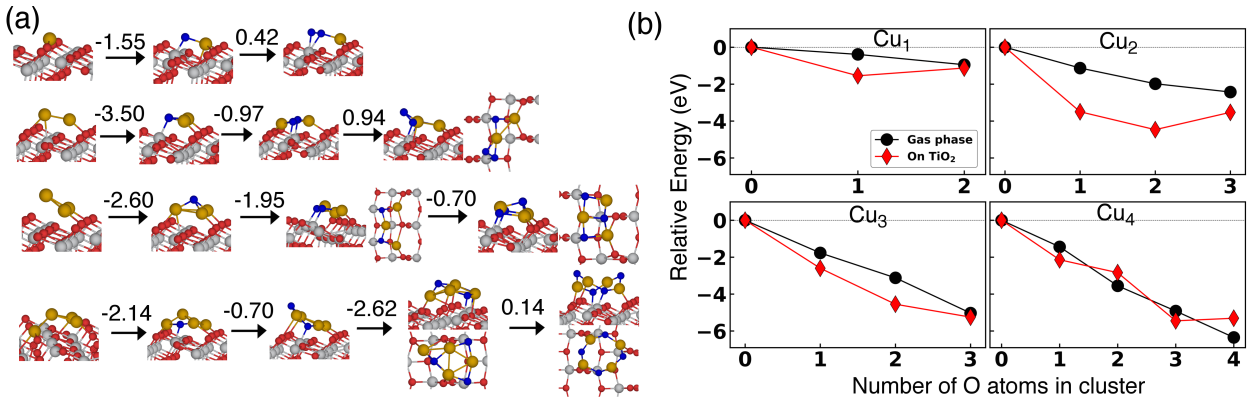

Figure 7.2: Results for oxidation of Cu clusters. (a) The most stable geometries for oxidized Cu clusters on TiO_2. The numbers (in eV) are reaction energies for each O addition step. (b) Relative energies of oxidized clusters in gas phase and supported on TiO_2. The source of O for oxidation was O_2 for gas phase calculations and O_2 adsorbed on TiO_2 for supported cluster calculations.

most stable geometries of Cu_x (x=1-4) clusters on TiO_2. Several adsorption configurations were modeled with Cu atoms interacting with surface O_{2c} and/or O_{3c} atoms, similar to previous reports.[40,64] The most stable configurations are reported in Figure 7.1a. These configurations consisted of Cu atoms bound to surface oxygen atoms, that is at a bridge site between two O_{2c} atoms or coordinating with only one O_{2c} atom. The first Cu addition step was unfavorable with a reaction energy of 0.94 eV. Similar results were seen in our earlier work[40] where it was shown that the Cu dimer is unstable. The reaction energy for $Cu_2 \longrightarrow Cu_3$ was -0.97 eV, while the reaction energy for $Cu_3 \longrightarrow Cu_4$ was 0.19 eV. Diffusion of Cu atoms is however slow on TiO_2, with a diffusion barrier of 1 eV.[40] Thus Cu atoms interact with TiO_2 strongly which limits their aggregation to form larger clusters, such as the dimer or larger clusters. Compared to gas-phase aggregation, aggregation of the supported clusters is slow due to unfavorable reaction energies and slow diffusion of Cu atoms. These trends can be seen in Figure 7.1b which shows the relative energies of different clusters.

Cu oxidation

In order to understand Cu growth in the presence of oxidants, such as O_2, we modeled oxidation of Cu clusters in the gas phase and on TiO_2. For these calculations the source of O was taken as O_2 for gas phase calculations and O_2 adsorbed on TiO_2 for supported cluster calculations. We show the gas phase geometries of oxidized Cu clusters in Figure C.2. Our most stable geometries are consistent with literature,[58,63,65–67] as discussed further in the Supporting Information. We used a similar approach to Nolan et al.[68] to find the most stable adsorbed configurations of these Cu oxide clusters. The most stable Cu oxide gas phase clusters were first identified, which were then adsorbed on TiO_2 in several different configurations to find the most stable adsorption configuration. Figure 7.2a shows geometries and reaction energies of oxidized supported clusters while Figure 7.2b gives relative energies for oxidized gas phase and supported clusters. For the gas-phase clusters, all oxidation steps ($Cu_x + \frac{1}{2}O_2 \longrightarrow Cu_xO$) were exothermic, regardless of the cluster. Compared to a lone Cu atom, the reaction energies of clusters were much more exothermic, indicating that the Cu clusters were easier to oxidize. For instance, $Cu_1 \longrightarrow Cu_1O$, $Cu_2 \longrightarrow Cu_2O$, $Cu_3 \longrightarrow Cu_3O$, and $Cu_4 \longrightarrow Cu_4O$ have reaction energies of -0.39, -1.13, -1.77, and -1.44 eV, respectively.

Most of the adsorbed oxidized Cu clusters formed flat configurations. Exceptions were the Cu_3O^* and $Cu_3O_3^*$ geometries where one oxygen atom protruded out of the cluster away from the surface in a 3D-like configuration. In all the adsorbed structures, the bonding interactions consisted predominantly of Cu-O_{2c} and $O_{cluster}$-Ti_{5c} bonding. Nolan and coworkers[45,46,69] modeled $CuO/Cu_2O/Cu_4O_4$ on the anatase (001)/(101) surfaces and Sn_4O_4/Zr_3O_6 nanoclusters on the anatase (101) surface. They reported the primary mode of interactions between nanocluster and surface atoms to be through M-O_{2c} and $O_{cluster}$-Ti_{5c} bonding, similar to our work. Sharma et al.[69] also reported flat structures of Cu_4O_3 and Cu_4O_4 clusters on the TiO_2 anatase (101) surface. Their most stable geometry of Cu_4O_3 was similar to our geometry, but they reported a more "closed" structure for the Cu_4O_4 cluster.

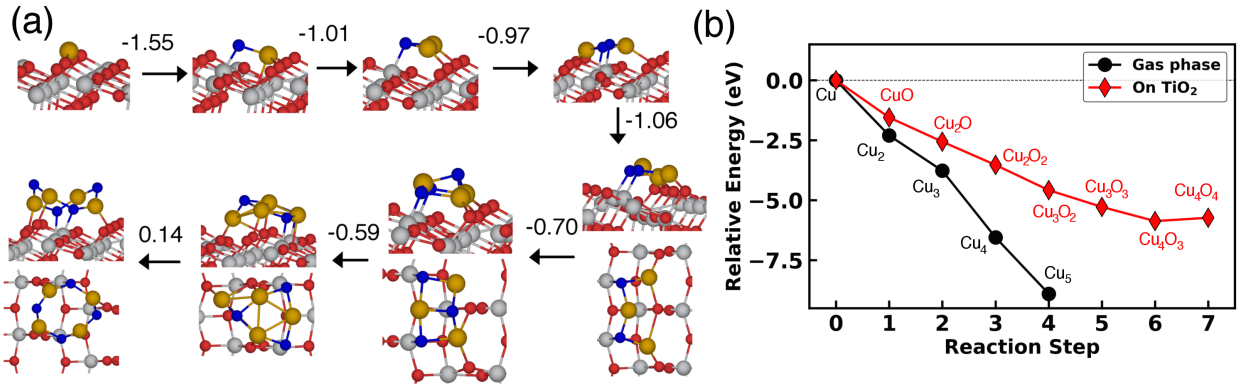

Figure 7.3: The adsorption geometries of the most stable combined aggregation oxidation growth pathway of Cu_1/TiO_2 (a). Numbers represent the reaction energy in eV. Relative energy of the most stable growth pathway in gas phase (b) and on TiO_2 (d). The reference for oxidation steps was O_2 adsorbed on TiO_2.

Nonetheless the adsorption energies were similar between our work (-3.55 eV) and theirs (-3.27 eV). A ring-like Cu_4O_4 in the gas phase was reported to be the most stable geometry by Bae et al.[58] Our results on the ring-like Cu_4O_4 structure (with Cu and O alternating in the ring) were similar to the structure reported by Jin et al.[45] on the anatase (001) surface. Finally, some of our adsorbed Cu oxide geometries (Cu_2O, Cu_2O_2, and Cu_3O) resembled the corresponding Pt oxide geometries on the rutile (110) surface.[70]

Figure 7.2b shows the relative energies of the gas phase and adsorbed oxidized clusters. Several trends can be seen. For example, oxidation of the adsorbed clusters is more exothermic than the gas phase clusters. Also, oxidation of a lone Cu atom is much less exothermic than the bigger Cu clusters. Additionally, the initial oxidation steps were all energetically downhill. However, the final oxidation steps of several adsorbed clusters were uphill, or endothermic: $Cu_1O \longrightarrow Cu_1O_2$, $Cu_2O_2 \longrightarrow Cu_2O_3$, and $Cu_4O_3 \longrightarrow Cu_4O_4$. In contrast, all oxidation steps were exothermic for the gas phase clusters. Overall, the unfavorable final oxidation steps of the adsorbed clusters indicate that more fully oxidized clusters may not be thermodynamically stable on the TiO_2 surface.

So far we have considered metal aggregation or metal oxidation steps separately. During

synthesis or in a reaction environment, but processes are likely to occur depending on the environmental conditions. In Figure 7.3, we show the thermodynamically preferred growth pathway of supported Cu when both oxidation and Cu aggregation may occur (Cu_xO_y* + $1/2O_2$* $\longrightarrow$ Cu_xO_{y+1}* and Cu_xO_y* + Cu* $\longrightarrow$ $Cu_{x+1}O_y$*). The preferred growth pathway involves sequential oxidation and metal addition steps: $Cu_1 \longrightarrow Cu_1O \longrightarrow Cu_2O \longrightarrow Cu_2O_2 \longrightarrow Cu_3O_2 \longrightarrow Cu_3O_3 \longrightarrow Cu_4O_3 \longrightarrow Cu_4O_4$. Figure 7.3b shows the relative energies of these processes. As the supported Cu oxide clusters get bigger, the reaction energies decrease, as indicated by the increasing slope with increasing cluster size. These results suggest that TiO_2 stabilizes small metal oxide cluster growth but that formation of larger oxide clusters may be hindered.

In contrast to the supported clusters, the thermodynamically preferred growth of gas phase clusters involves only metal addition. The preferred growth of the clusters is simply: $Cu_1 \longrightarrow Cu_2 \longrightarrow Cu_3 \longrightarrow Cu_4 \longrightarrow Cu_5$. All growth steps (metal atom addition) are highly exothermic, more so than the supported clusters. Metal-support interactions stabilize the supported smaller clusters, while no such stabilization occurs for the gas phase clusters. Our results are consistent with the experimental findings of Matsuda et al.,[71] where they performed laser ablation of a copper metal foil. They found that laser ablation of the foil produced Cu clusters that were resistant to oxidation, similar to our results.

We characterized the oxidation state of the supported Cu_xO_y clusters in Figure 7.4 using DDEC6 charge analysis.[60,61] The DDEC6 method partitions the electron density to assign charges to each atom and also reproduces the electostatic potential generated generated by the molecule. We have previously calculated the DDEC6 charges corresponding to formal Cu^0, Cu^{1+}, and Cu^{2+} species by calculating the DDEC6 charges of reference Cu complexes.[40] Cu^{1+} and Cu^{2+} oxidation states were assigned to Cu when DDEC6 charges of Cu were close to 0.36 and 0.85 e^- respectively.

As expected, as the number of oxygen atoms in the supported Cu oxide clusters increased,

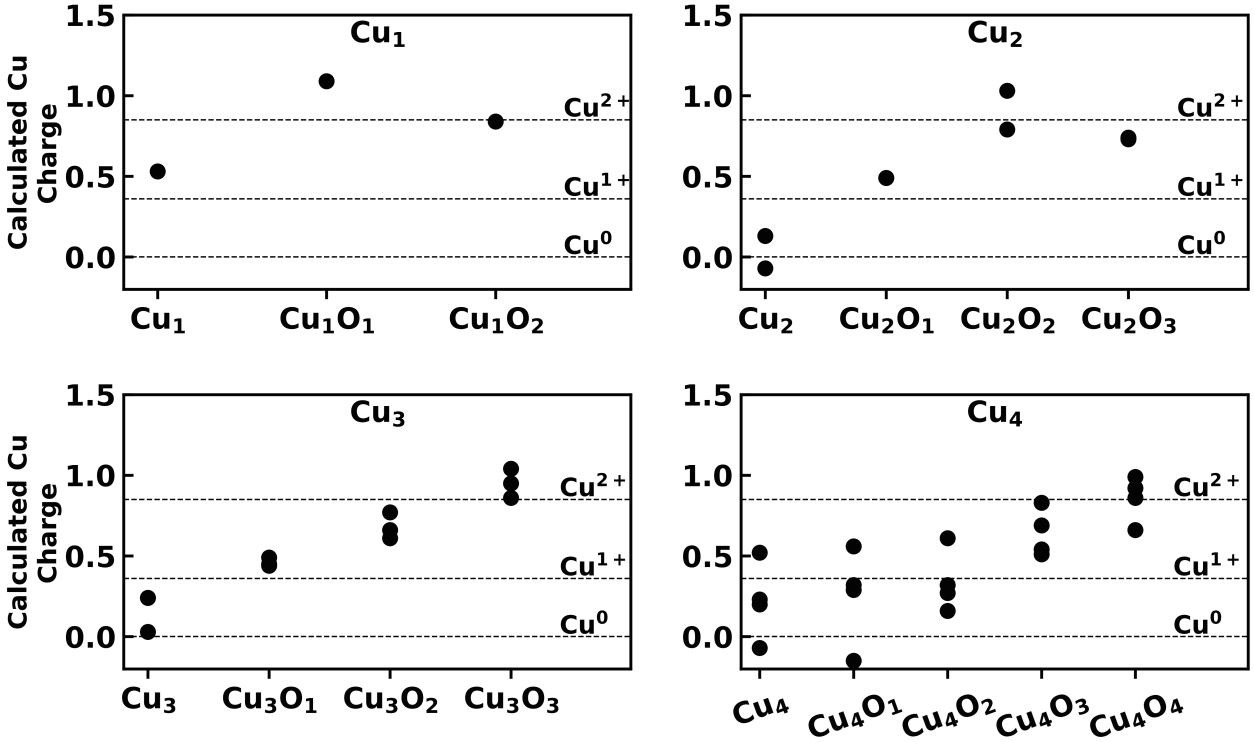

Figure 7.4: Calculated DDEC6 charges of the Cu atoms for the adsorbed copper/copper oxide clusters. Dotted lines show average Cu charges (+0.36 and +0.85) for reference molecules with formal Cu^{1+} and Cu^{2+} species.[40]

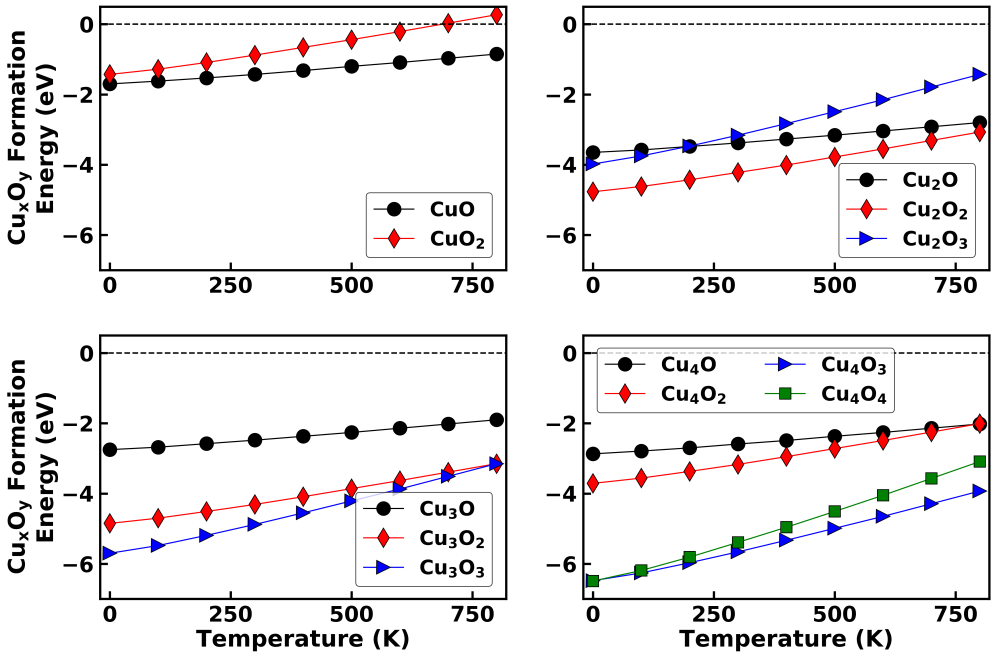

Figure 7.5: Calculated formation energies of oxidized supported Cu clusters in the presence of gas phase O_2 (at 1 atm) as a function of temperature. Formation energies are found from Equation 7.1, or according to the reaction $Cu_x^* + \frac{y}{2}\ O_2 \longrightarrow Cu_xO_y^*$.

the Cu charges became more positive. For instance, with Cu_2 and Cu_3, the Cu charges clearly become more positive with increasing number of O atoms in the cluster. The Cu_3 data are very linear. Of particular notes is that a lone adsorbed Cu atom was already oxidized, having a DDEC6 charge of 0.53 e^- which was assigned as Cu1+. The Cu atom interacted with surface O_{2c} atoms and was acted as a metal oxide cluster. The Cu_4 case is much more interesting, with a significant spread in the Cu oxidation states within each cluster. For instance, in the Cu_4 and Cu_4O clusters both Cu^0 and Cu^{1+} are observed. Cu_4O_2 had Cu^{1+} atoms, but also had atoms that could be classified as Cu^0 or Cu^{1+}. Cu_4O_3 had a mixture of Cu^{1+}/Cu^{2+} atoms, while Cu_4O_4 was predominantly Cu^{2+}. Similar observations have been experimentally reported. For instance, Liu et al. showed that size selected Cu_4 clusters supported on alumina consisted of Cu atoms with observed oxidation states of Cu^0, Cu^{1+}, and Cu^{2+}.[13] Chen et al.[34] also showed that Cu nanoparticles supported on TiO_2 had Cu

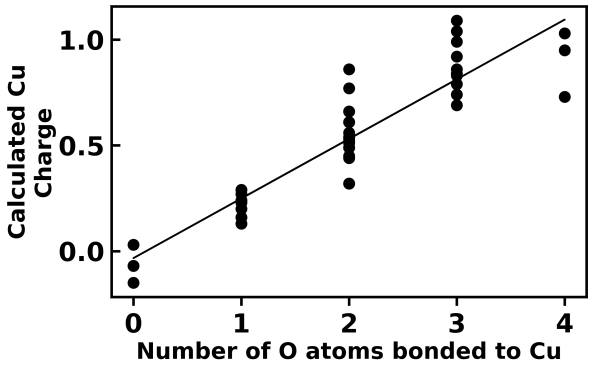

Figure 7.6: Relationship between DDEC6 calculated Cu charges and number of nearest oxygen atom bonded to a Cu atom.

with multiple oxidation states: Cu^0, Cu^{1+}, and Cu^{2+}.

The charge of each Cu atom in the clusters was correlated to how many oxygen atoms it bonded to, as Figure 7.6 shows. Assigning atoms as bonded can be ambiguous as there is no well defined cutoff radius to determine whether an atom was bonded to another atom. Nonetheless, we considered a cutoff of 2.2 Å, which was close to the experimental value of $\sim$ 2 Å for Cu-O bonds in copper oxide nanoparticles/composites as determined from extended X-ray absorption fine structure (EXAFS) spectroscopy.[72] This correlation explains why in the larger clusters, like Cu_4, there is a wide range of observed Cu oxidation states. The Cu atoms in Cu_4 bind to O atoms in several distinct configurations (see Figure 7.2 for the geometry). This variation in the Cu-O coordination leads to the variation in Cu oxidation states.

In order to better understand the cluster stability, we used ab initio thermodynamics[73] to determine the effect of temperature. The catalyst stability was characterized by calculating the Cu_xO_y* formation energy as given by Equation 7.1.

$$\Delta E_{form}(T, p) = E_{Cu_xO_y^*} - E_{Cu_x^*} - y\mu_O(T, p) \tag{7.1}$$

where, $E_{Cu_xO_y^*}$, $E_{Cu_x^*}$, and μ_O are the energies of an adsorbed Cu_xO_y cluster, of an adsorbed

Cu_x clusters, and the chemical potential of atomic O, taken as as $\mu_{O_2}/2$). Temperature dependent entropy and enthalpies of gas phase O_2 were obtained from tabulated values.[74]

We show the temperature dependent Cu_xO_y formation energies for gas phase clusters in Figure C.3. We found that the stability trends of oxidized Cu_1 and Cu_2 clusters were different from larger Cu_3 and Cu_4 clusters. At low temperatures, strongly oxidized CuO_2 and Cu_2O_3 were the most stable small clusters. The more oxidized Cu_2O_3 became less stable above $\sim$ 400 K, such that Cu_2O_2 was the most stable cluster between 400 to 800 K. At larger temperatures from 800 - 1100 K, Cu_2O was the most stable oxidized cluster of Cu_2. However, at higher temperatures metallic Cu_1 (500 K) and Cu_2 (1100 K) were more stable. In contrast, Cu_3O_3 and Cu_4O_4 were highly stable up to 1400 K, beyond which less oxidized Cu_3 and Cu_4 clusters became more stable.

In Figure 7.5 we show the formation energies of the supported Cu oxide clusters in the presence of O_2, a common oxidizing species, at temperatures up to 800 K. All the Cu oxide clusters were stable over the 0-800 K range, as determined by the negative formation energies. The exception was CuO_2* above 700 K. Likewise, extrapolation of the CuO* formation energy indicated that above $\sim$ 1500 K the adsorbed CuO cluster was unstable. The Cu_2O_2 cluster as the most stable Cu_2 oxide cluster within 0-800 K range. Nonetheless, at higher temperature of $>$ 900 K, the less oxidized Cu_2O was more stable. A transition for the Cu_3 clusters occurs around 800 K, where below 800 K Cu_3O_3 clusters are most stable, while above 800 K Cu_3O_2 are more stable. Further extrapolation of energies to temperatures $>$ 1000 K indicates that the Cu_2O cluster was the most stable cluster of all we studied at elevated temperatures. Based on the DDEC6 charges presented in Figure 7.4, the average Cu charges of the most stable clusters in this temperature range (CuO*, Cu_2O_2*, Cu_3O_3* and Cu_4O_3*) corresponded to $\sim$ Cu^{2+} oxidation states. We expect, at least based on thermodynamics, that Cu^{2+} would be a dominant species in the presence of O_2. Mengwa et al.[75] also found more oxidized CuO stoichiometric clusters on the anatase (101) surface

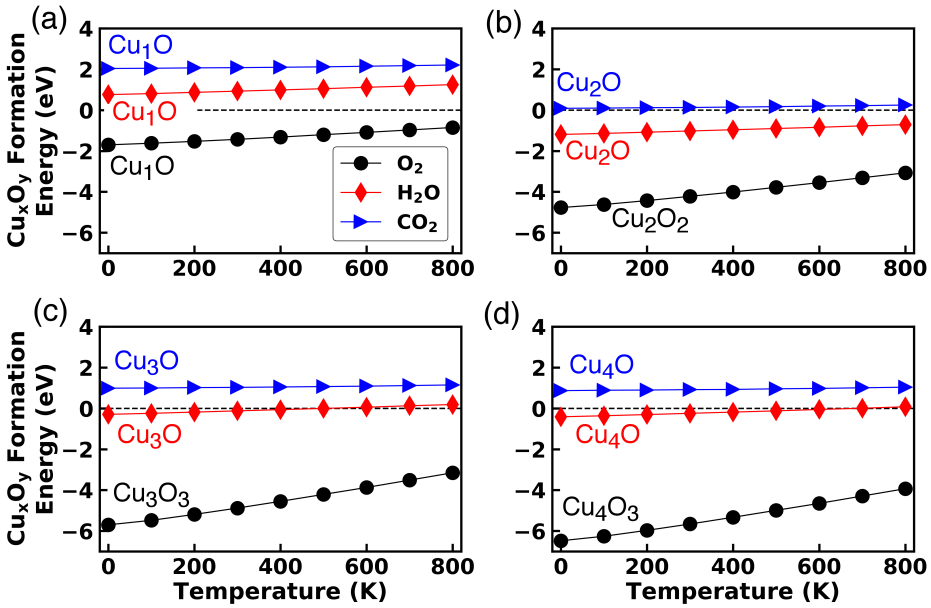

Figure 7.7: Formation energies of oxidized supported Cu clusters in the presence of various oxidants as a function of temperature. Each curve shows the formation energy of the most stable oxidized cluster after reacting with the indicated oxidant. I.e. $Cu_x^* + \frac{y}{2}\ O_2 \longrightarrow Cu_xO_y^*$, $Cu_x + yH_2O \longrightarrow Cu_xO_y + yH_2$, or $Cu_x + yCO_2 \longrightarrow Cu_xO_y + yCO$.

to be more stable than less oxidized Cu_2O clusters.

We also considered the effect of other oxidants like H_2O or CO_2 on Cu cluster oxidation (see Figure 7.7). The chemical potential of O to oxidize the clusters was calculated as μ_{H_2O} - μ_{H_2} or μ_{CO_2}-μ_{CO}. The chemical potentials for these gas phase species were obtained from tabulated values.[74] Copper oxide formation energies were most negative (exothermic) in the presence of O_2 indicating the strong oxidizing power of O_2. In the case of H_2O, some formation energies were positive (Cu_1, elevated temperatures for Cu_3 and Cu_4), while negative formation energies only occurred for Cu_2. This indicates that H_2O is a weak oxidizing agent of the supported Cu clusters. The most stable clusters in the presence of H_2O were Cu_1, Cu_2O, Cu_3O, Cu_4O at 300 K. Based on the DDEC6 charges of Cu (see Figure 7.4), the average Cu oxidation states of these clusters were all 1+. The associated DDEC6 charges were 0.53, 0.49, 0.46, and 0.25 e^- for Cu_1, Cu_2O, Cu_3O, and Cu_4O, respectively. At higher

temperatures (> 500 K) in the presence of water, the most stable clusters were Cu_1, Cu_2O, Cu_3, and Cu_4, with corresponding average oxidation states of $\sim Cu^{1+}$ (Cu_1), Cu^{1+} (Cu_2O), Cu^0/Cu^{1+} (Cu_3), and Cu^0/Cu^{1+} (Cu_4). These oxidation states were assigned based on the corresponding DDEC6 charges of 0.53, 0.49, 0.17, and 0.22 e- respectively. Thus, for all the Cu clusters, H_2O tended to only oxidize Cu to the Cu^{1+} oxidation state, while O_2, as a stronger oxidant, led to Cu^{2+} as the preferred oxidation state. Irrespective of the oxidant being H_2O or O_2, Cu^{1+} was the preferred oxidation state for Cu_1 on TiO_2. We also note that oxidation by H_2O is the opposite of reduction with H_2 (for instance, $Cu_xO + H_2 \longrightarrow Cu_x + H_2O$), so that an endothermic H_2O oxidation energy would correspond to an exothermic H_2 reduction energy. Indeed, our results show that reduction of Cu_1O (Cu^{2+}) by H_2 to form less oxidized Cu_1 ($\sim Cu^{1+}$) was similar to the trends observed in studies with TiO_2 supported Cu nanoparticles.[34,76] On these catalysts the reduction of Cu^{2+} species to form Cu^{1+} and/or Cu^0 species in the presence of H_2 occurred. CO_2 was the weakest oxidant, and was only able to oxidize Cu_2 to Cu_2O. Our results thus show that oxidation is very likely to occur using O_2, possibly using H_2O, and very unlikely using CO_2.

7.3.2 Kinetics of Cu Cluster Oxidation

The results presented so far have focused on the thermodynamics of Cu oxidation and aggregation. These calculations showed that oxidation of Cu clusters using O_2 or O_2* should readily occur based on the thermodynamic analysis. In this section we expand our analysis to consider the kinetics of Cu cluster oxidation. Indeed depending upon the reaction conditions like temperature and O_2 exposure to catalyst, the kinetics of O_2 dissociation on TiO_2 supported size-selected Pd_n clusters (n=4,7,10,20) were reported to be slow or fast.[77] Experiments and DFT calculations show that O_2 binds very weakly to TiO_2 and that dissociation of O_2 (which is necessary to oxidize the Cu clusters) does not readily occur over clean stoichiometric TiO_2.[78–80] If O_2 is not able to bind or dissociate on the Cu/TiO_2 surface,

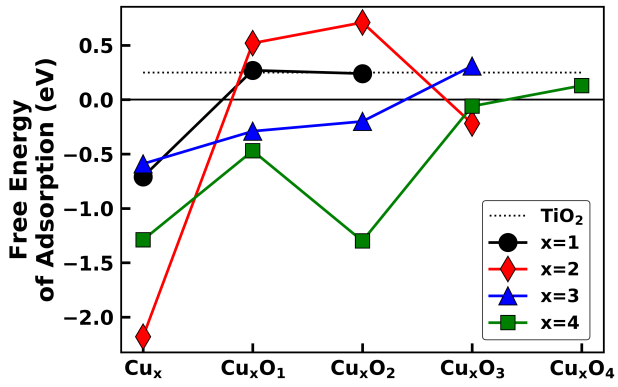

Figure 7.8: Free energies of O_2 adsorption at 300 K for Cu Clusters with various sizes and number of O atoms.

oxidation of Cu will not occur. We therefore investigated how the Cu clusters may aid in the adsorption and dissociation of O_2, which is necessary for the oxidation of the Cu.

In Figure 7.8, we report calculated adsorption free energies of O_2 at 300 K over the various clusters. The free energies were calculated as $\Delta G_{ads} \sim E_{(Cu_xO_y+O_2)*} - E_{Cu_xO_y*} - G_{O_2}$, where the first and second terms correspond to the DFT energies of Cu_xO_y* with adsorbed O_2, and lone Cu_xO_y* respectively. G_{O_2} was calculated by using the DFT energy of O_2 and including enthalpy and entropy corrections at 300 K from tabulated values.[74] O_2 adsorption was strongest over the non-oxidized Cu clusters, or the Cu_x clusters. In general, as the Cu clusters became more oxidized, O_2 adsorption weakened, and even became endothermic on several oxidized clusters. O_2 Adsorption on oxidized Cu clusters such as Cu_1O, Cu_1O_2, Cu_2O, Cu_2O_2, Cu_3O_3, and Cu_4O_4 were all unfavorable with positive O_2 adsorption energies. These results demonstrate that since O_2 will not bind to more oxidized clusters, oxidation may be limited to the clusters with fewer O atoms (e.g. Cu_1, Cu_2O, Cu_3O_2, Cu_4O_3) since a source of O will not be readily available for further oxidation.

We next calculated dissociation barriers for O_2* dissociation over the Cu clusters using the climbing image nudged elastic band method (CI-NEB).[62] Figure 7.9 shows these results how O_2 dissociation over a Cu atom was thermodynamically and kinetically unfavorable,

with a reaction energy of 0.93 eV and dissociation barrier 1.88 eV. However for Cu clusters, O_2 dissociation was thermodynamically downhill in energy and kinetically favorable with negligible barriers of $\leq$ 0.20 eV. Our results show that O_2* dissociation readily occurs over Cu clusters but was difficult over lone Cu atoms. After O_2 dissociation, the Cu_xO_2 clusters in Figure 7.9 could further rearrange to form the stable Cu_xO_2 geometries shown in Figure 7.2a. Transformation to the geometries in Figure 7.2a was exothermic for all clusters being -1.49 (Cu_2), -0.51 (Cu_3), and -0.97 eV (Cu_4). The most likely states of the clusters were found to be Cu_2O_2, Cu_3O_2, and Cu_4O_2. Since, O* formation was kinetically limited on Cu_1, the most likely state of a single Cu atom was in its unoxidized state (no additional O atoms). Once these atoms/clusters formed, further oxidation may be hindered since O_2 adsorption was weak to these clusters. An exception may be Cu_4O_2, where O_2 adsorption was relatively strong over the cluster (-1.30 eV). Further oxidation of the partially oxidized clusters however could be limited by slow O_2 dissociation kinetics. For example, Hang et al.[81] compared the O_2 adsorption and dissociation (reaction energies and barriers) between metallic Pt_8/TiO_2 and oxidized Pt_8O_8/TiO_2. The adsorption energy of O_2 was 1.81 eV higher on Pt_8O_8 compared to Pt_8. The dissociation energy (O_2* $\longrightarrow$ 2O*) was 1.24 eV higher on Pt_8O_8 compared Pt_8, while the dissociation barrier was slightly higher over Pt_8O_8 (0.13 eV higher than Pt_8). This indicates the difficulty to adsorb and dissociate O_2 over oxidized Pt clusters. Also, Wang et al.[82] showed that as TiO_2 supported Au_{20} oxidized more, the CO assisted dissociation barrier of O_2 (CO*+O_2* $\longrightarrow$ CO_2*+O*) increased from 0.37 to 0.72 eV.

When we considered the kinetics of Cu oxidation, we may reach different conclusions than when only thermodynamics was considered. In the thermodynamic limit (no kinetic limitations for O_2 dissociation), we found that Cu easily oxidized on TiO_2 and existed as Cu_1O, Cu_2O_2, Cu_3O_3, and Cu_4O_3 (see Figures 7.3 and 7.5). The average calculated Cu charges for the the species correspond to Cu in formal $\sim$ Cu^{2+} oxidation states. However, in the kinetic limit, where O_2 adsorption and dissociation were considered, we found the

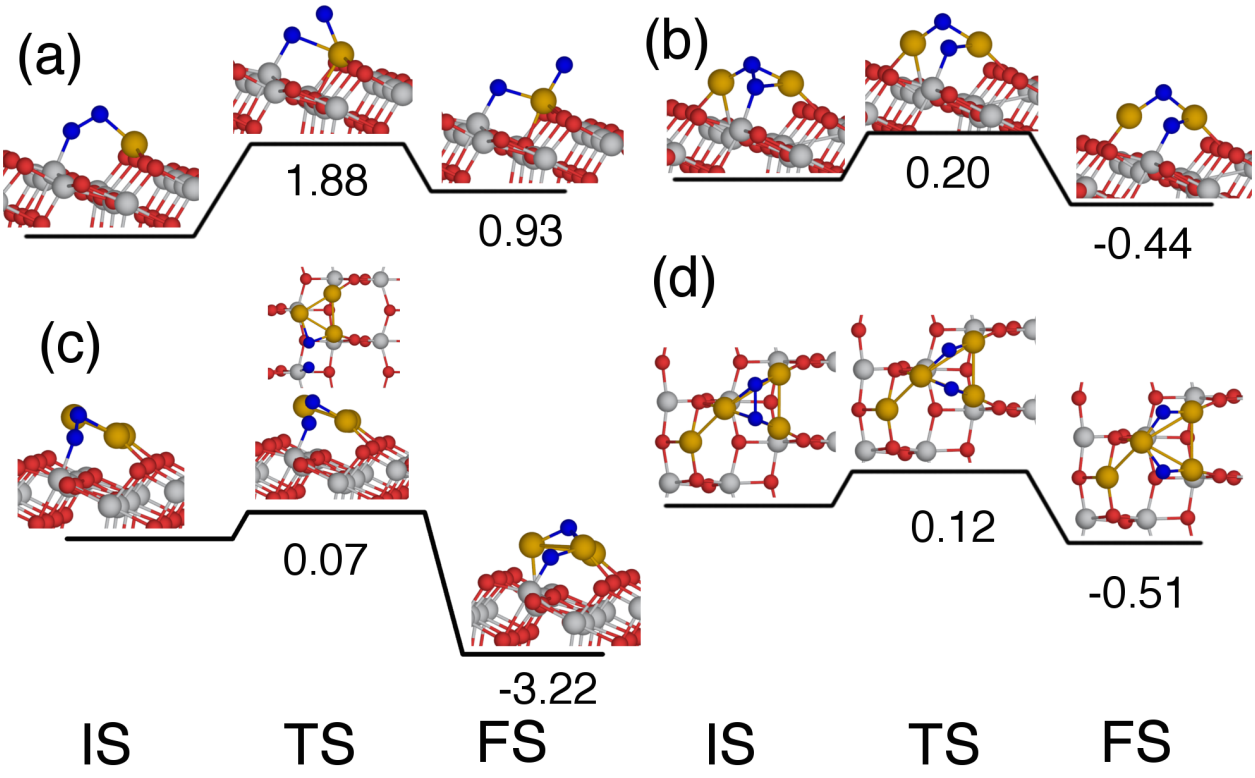

Figure 7.9: Reaction and activation energies for O_2 dissociation on supported Cu clusters. The initial states (IS), transition states (TS), and final states (FS) are indicated. Results are for (a) Cu_1 (b), Cu_2 (c), Cu_3, and Cu_4. O_2 dissociation is negligible on TiO_2. For example the reported dissociation barrier over TiO_2 assisted by H atoms was 1.78 eV.[83]

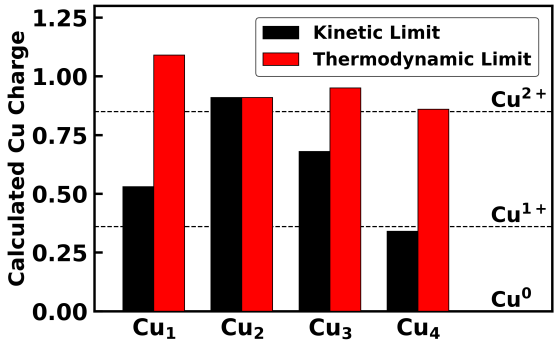

Figure 7.10: Comparison of the average Cu DDEC6 charges of the most stable Cu clusters on TiO_2 in the kinetic and thermodynamic limits. The labels within each bar shows the most stable oxidized cluster under each limit.

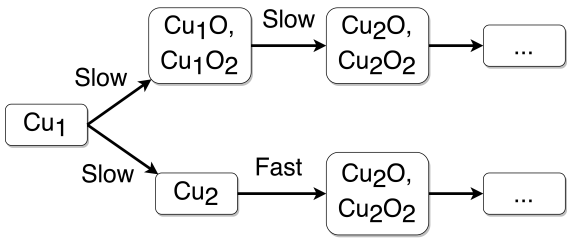

Figure 7.11: Schematic of the growth pathway of Cu on TiO_2 on the basis of kinetics of cluster growth and O_2 dissociation.

most likely Cu species on TiO_2 to be Cu_1, Cu_2O_2, Cu_3O_2, and Cu_4O_2. Calculated DDEC6 charges for these species correspond to Cu in formal Cu^{1+} and Cu^{2+} states, depending on the atom/cluster. The most likely oxidation states of the supported clusters based on the thermodynamic and kinetic limits are shown in Figure 7.10.

We show in Figure 7.11 a suggested path for cluster growth based on the kinetics of cluster growth and O_2 dissociation. O_2 dissociation is slow over lone Cu atoms, while Cu_2 formation is also slow due to a high Cu diffusion barrier[40] and has a highly endothermic dimerization energy. A synthesis technique that produces lone supported Cu atoms will not likely lead to further Cu growth or oxidation, and may require surfaces with defects (which will produce O*[78,84]), extreme oxidizing conditions, or much higher temperatures to oxidize the Cu atoms. On the other hand if the synthesis technique produces larger Cu_x clusters, then further oxidation may proceed quite readily. Our results provide important insights to corroborate experimental results[31] which showed formation of atomic Cu^{1+} species rather than Cu^{2+}. Synthesis of Cu/TiO_2 even under O_2 gave Cu^{1+} species in that work.[31] Further oxidation to Cu^{2+} was not observed. This suggests that the experimental results may be producing lone Cu atoms on the surface, which exist as Cu^{1+} (see Figure 7.10), rather than larger copper oxide clusters which exist as Cu^{2+}.

7.3.3 Metal aggregation and oxidation of Pt

Besides Cu, supported Pt atom or clusters have also been synthesized recently for applications like CO oxidation reactions.[2,85] Under reaction conditions the Pt atom/clusters were reported to oxidize to form Pt oxide clusters. In this section, we study the growth of TiO_2 supported Pt to form metal aggregated clusters (Pt_x) or oxidized clusters (Pt_xO_y).

In the gas phase, similar to Cu, we found that Pt prefers to aggregate and form metallic Pt clusters (see Figure C.4 for the geometries). The Pt addition steps were always more favorable than oxidation steps. The reaction energies for Pt aggregation and oxidation were in the range of -3.05 to -3.95 and -1.31 to -2.24 eV, respectively. The geometries of the adsorbed Pt clusters are shown in Figure 7.12a. Also indicated are reaction energies for either Pt addition or oxidation. These reaction energies were calculated using adsorbed O_2. We found that some Pt oxide clusters, like Pt_2O_2 and Pt_3O_3, preferred to adsorb on TiO_2 with the clusters pointing away from the surface, unlike other clusters that lay flat on TiO_2. For the Pt oxide clusters that were flat on the surface, the number of cluster-TiO_2 interactions were larger than less flat clusters, thereby stabilizing these flat clusters compared to the less flat clusters. For instance, the adsorption energy of Pt_2O_2 (not flat) was -3.02 eV, while Cu–$2O_2$ (flat) was -4.68 eV (see Table C.1 for all the adsorption energies). These less flat structures were not observed with the Cu clusters. Similar to Cu oxide clusters, the main interactions for Pt oxide clusters with TiO_2 were through Pt-O_{2c}/O_{3c} and $O_{Pt_xO_y}$-Ti_{5c} bonds.

In the gas phase Pt aggregation ($Pt_x + Pt \longleftrightarrow Pt_{x+1}$, x=1,2) was strongly exothermic being $\sim$ -3.7 eV for both aggregation processes. In contrast, Pt aggregation on TiO_2 was significantly less exothermic with Pt aggregation energies of -0.4 to -0.9 eV. The gas phase Pt oxidation energies in gas phase were between -1.3 to -2.3 eV. The corresponding Pt oxidation energies on TiO_2 were predominantly more positive than gas phase oxidation energies by 0.18 to 1.46 eV. The exception being $Pt_3O \longrightarrow Pt_3O_2$, where on TiO_2, the oxidation energy

was 0.9 eV more negative than in the gas phase. For the first oxidation step occurring on TiO_2 (M $\longrightarrow$ MO), oxidation was much weaker for Pt (-0.39 eV) compared to Cu (-1.55 eV). In contrast, Pt atoms can undergo aggregation (Pt* + Pt* $\longrightarrow$ Pt_2*) on TiO_2 (-0.43 eV), while Cu atom aggregation over TiO_2 was unfavorable (0.94 eV). These results show that over TiO_2 Pt clusters or Pt oxide clusters were most likely, while for Cu lone atoms were most likely to occur.

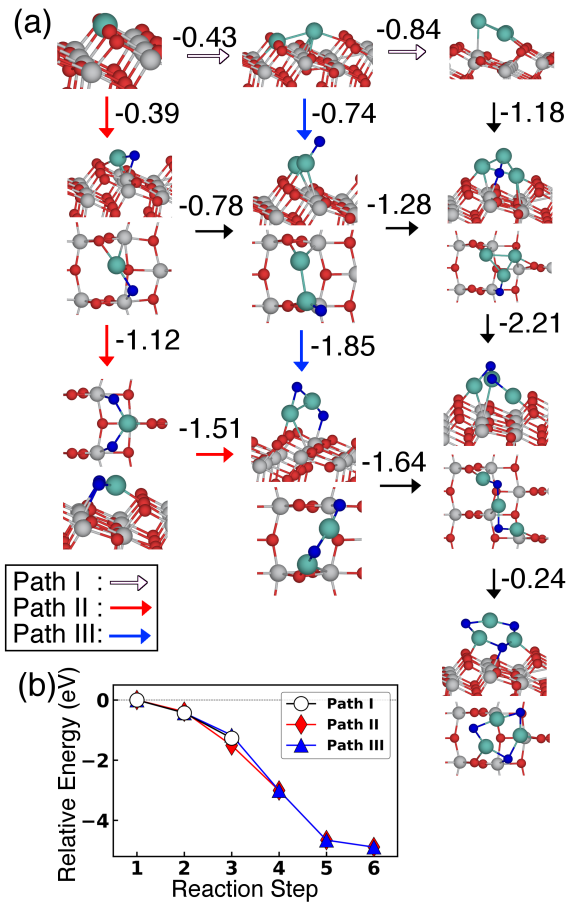

Figure 7.12: Results for adsorption and growth of supported Pt clusters. (a) Geometries showing how cluster growth may occur through Pt addition or oxidation. The numbers are reaction energies in eV for Pt addition (horizontal arrows) and O addition (vertical arrows). (b) Relative energies for different Pt species on the surface. Three reaction pathways are indicated in the graph and correspond to those shown in (a). All reaction paths have similar energies Adsorbed O_2 on TiO_2 was used as reference for oxidation steps.

As Figure 7.12 shows, there is no clear thermodynamically preferred reaction pathway, and three pathways have similar energies. These three pathways are indicated as Path I ($Pt_1 \longrightarrow Pt_2 \longrightarrow Pt_3$), Path II ($Pt_1 \longrightarrow Pt_1O \longrightarrow Pt_1O_2 \longrightarrow Pt_2O_2 \longrightarrow Pt_3O_2 \longrightarrow Pt_3O_3$), and Path III ($Pt_1 \longrightarrow Pt_2 \longrightarrow Pt_2O \longrightarrow Pt_2O_2 \longrightarrow Pt_3O_2 \longrightarrow Pt_3O_3$). Therefore, in the presence

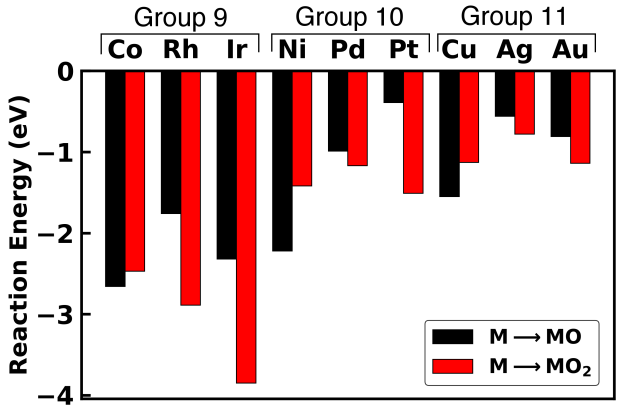

Figure 7.13: Reaction energies for the initial oxidation steps of selected transition metal metal atoms on TiO_2. Adsorbed O_2 on TiO_2 was used as reference for the oxidation steps.

of Pt* or O_2*, both Pt clusters and Pt oxide clusters are thermodynamically favorable on TiO_2. This result is important because the presence of non-oxidized Pt clusters may facilitate the dissociation of O_2 (assuming non-oxidized Pt clusters are better for O_2 dissociation like we have shown for Cu) to form Pt oxide clusters. In fact, Anderson and coworkers have reported that O_2 dissociation occurred easily on size-selective Pd (a Pt group element) clusters on TiO_2.[44,77] Unlike Cu, where Cu^{1+} species were most likely to occur owing to limiting O_2 dissociation kinetics, Pt clusters may get oxidized more easily due to faster kinetics of O_2 dissociation. Consistent with this argument, DeRita et al.[11] have reported Pt atoms to exist in a more oxidized Pt^{2+} state on TiO_2. Similar strongly oxidized Pt atom/clusters have also been reported on other oxide supports.[2,85]

7.3.4 Oxidation of Other Supported Metals

In this final section, we modeled the oxidation of group Co (group 9), Ni (group 10), and Cu group (group 11) atoms supported on TiO_2. In each case, we considered only the initial oxidation steps of M* to form either MO* or MO_2* clusters. For all 9 atoms, we found that oxidation of metal atoms to MO* and MO_2* was thermodynamically favorable as shown

by the negative oxidation energies in Figure 7.13. MO* formation was more favorable than MO_2* formation for the row 4 atoms (Co, Ni, and Cu). However, MO_2* was more favored for the larger atoms in row 5 (Rh, Pd, and Ag) and row 6 (Ir, Pt, and Au). Oxidation of group 9 elements was much more exothermic than oxidation of group 10 and 11 elements. These results show that several atoms (like group 9 atoms) have oxidation energies much more exothermic than Cu, and may not have thermodynamic or kinetic limitations for oxidation. Experimental results have identified, for instance, the more reactive nature of Co and Ni clusters towards oxidation compared to Cu clusters for cluster sizes of 2-60 atoms.[86,87] Moreover, experimentally synthesized atomic species show strong oxidized states: 3+ (Rh),[88] 2+ (Pd),[89] 2+ (Pt).[11]

7.4 Conclusions

Using DFT and experiments we identified and characterized the growth and oxidation states of Cu atoms and clusters on anatase. In the gas phase, Cu and Pt preferred to aggregate and form larger metallic clusters. On TiO_2 however, metal-support interactions stabilized lone Cu atoms and prevented Cu aggregation. We found that Cu atoms/clusters however preferred to oxidize based on thermodynamic analysis. In general as the number of O atoms in the copper oxide clusters increased, Cu became more oxidized from Cu^0 to Cu^{1+} to Cu^{2+}. The Cu oxidation state was directly related to the number of Cu-O bonds the Cu atom had, and more O bonds led to higher oxidation states. Cu oxidation thermodynamics showed that the most stable Cu oxide clusters formed $\sim Cu^{2+}$ species. However, experiments based on previous our work[31] showed only Cu^{1+} species, even under oxidizing conditions.

We found that thermodynamics alone could not explain the experimental results. O_2 adsorption and dissociation kinetics was found to play an important role in the cluster oxidation process. As the Cu clusters oxidized more, the O_2 adsorption strength weakened.

O_2 readily dissociated over the Cu clusters, but would not dissociate over lone adsorbed Cu atoms. However, Cu aggregation to form Cu_2 and larger clusters is kinetically and thermodynamically limited. Thus, taking into account the difficulty of O_2 dissociation, which is necessary for Cu oxidation, we predict that lone atoms are the most likely Cu species (with an oxidation state of +1), while other kinetically limited clusters have oxidation states of 2+, 1+/2+, and 1+ for Cu2, Cu3, and Cu4 respectively. Since Cu adatom diffusion was unfavorable, aggregation to form larger clusters was also unfavorable. Our results suggest the dominant Cu species on TiO_2 were Cu lone atoms. Kinetics may thus explain why Cu^{1+}, not Cu^{2+}, is the dominant species observed in experiment. In contrast to Cu, Pt clusters may oxidize to form Pt^{2+} species, as the kinetics of O_2 dissociation on Pt group clusters are known to be fast. Finally, among Co, Ni, and Cu group elements, Co group elements showed a much stronger tendency for initial oxidation to form MO/MO_2 (M=Co, Rh, Ir) on TiO_2. Our results provide important insights into the nature of metal cluster oxidation and growth, and especially the important role of support interactions in cluster stability and structure.

Bibliography

[1] M. Flytzani-Stephanopoulos and B. C. Gates, *Annual Review of Chemical and Biomolecular Engineering*, 2012, **3**, 545–574.

[2] J. Jones, H. Xiong, A. T. DeLaRiva, E. J. Peterson, H. Pham, S. R. Challa, G. Qi, S. Oh, M. H. Wiebenga, X. I. Pereira Hernandez, Y. Wang and A. K. Datye, *Science*, 2016, **353**, 150–154.

[3] G. Spezzati, Y.-Q. Su, J. P. Hofmann, A. D. Benavidez, A. T. Delariva, J. McCabe, A. K. Datye and E. J. M. Hensen, *ACS Catalysis*, 2017, acscatal.7b02001.

[4] J. Liu, *ACS Catalysis*, 2017, **7**, 34–59.

[5] S. Vajda and M. G. White, *ACS Catalysis*, 2015, **5**, 7152–7176.

[6] W. E. Kaden, T. Wu, W. A. Kunkel and S. L. Anderson, *Science*, 2009, **326**, 826–829.

[7] X. F. Yang, A. Wang, B. Qiao, J. Li, J. Liu and T. Zhang, *Accounts of Chemical Research*, 2013, **46**, 1740–1748.

[8] Y. Lei, F. Mehmood, S. Lee, J. Greeley, B. Lee, S. Seifert, R. E. Winans, J. W. Elam, R. J. Meyer, P. C. Redfern, D. Teschner, R. Schlogl, M. J. Pellin, L. A. Curtiss and S. Vajda, *Science*, 2010, **328**, 224–228.

[9] B. Qiao, A. Wang, X. Yang, L. F. Allard, Z. Jiang, Y. Cui, J. Liu, J. Li and T. Zhang, *Nature chemistry*, 2011, **3**, 634–641.

[10] S. Lee, C. Fan, T. Wu and S. L. Anderson, *Journal of the American Chemical Society*, 2004, **126**, 5682–5683.

[11] L. DeRita, S. Dai, K. Lopez-Zepeda, N. Pham, G. W. Graham, X. Pan and P. Christopher, *Journal of the American Chemical Society*, 2017, **139**, 14150–14165.

[12] B. Yang, C. Liu, A. Halder, E. C. Tyo, A. B. F. Martinson, S. Seifert, P. Zapol, L. A. Curtiss and S. Vajda, *The Journal of Physical Chemistry C*, 2017, **121**, 10406–10412.

[13] C. Liu, B. Yang, E. Tyo, S. Seifert, J. DeBartolo, B. von Issendorff, P. Zapol, S. Vajda and L. A. Curtiss, *Journal of the American Chemical Society*, 2015, **137**, 8676–8679.

[14] R. Passalacqua, S. Parathoner, G. Centi, A. Halder, E. C. Tyo, B. Yang, S. Seifert and S. Vajda, *Catal. Sci. Technol.*, 2016, **6**, 6977–6985.

[15] M. Yang, L. F. Allard and M. Flytzani-Stephanopoulos, *Journal of the American Chemical Society*, 2013, **135**, 3768–3771.

[16] M. Yang and M. Flytzani-Stephanopoulos, *Catalysis Today*, 2017, **298**, 216–225.

[17] Y. Dai, P. Lu, Z. Cao, C. T. Campbell and Y. Xia, *Chemical Society Reviews*, 2018.

[18] S. Duan, R. Wang and J. Liu, *Nanotechnology*, 2018, **29**, 204002.

[19] C. Carrillo, T. R. Johns, H. Xiong, A. Delariva, S. R. Challa, R. S. Goeke, K. Artyushkova, W. Li, C. H. Kim and A. K. Datye, *Journal of Physical Chemistry Letters*, 2014, **5**, 2089–2093.

[20] E. D. Goodman, J. A. Schwalbe and M. Cargnello, *ACS Catalysis*, 2017, **7**, 7156–7173.

[21] L. Benz, X. Tong, P. Kemper, Y. Lilach, A. Kolmakov, H. Metiu, M. T. Bowers and S. K. Buratto, *The Journal of Chemical Physics*, 2005, **122**, 081102.

[22] Y. Lykhach, S. M. Kozlov, T. Skála, A. Tovt, V. Stetsovych, N. Tsud, F. Dvoák, V. Johánek, A. Neitzel, J. Mysliveček, S. Fabris, V. Matolín, K. M. Neyman and J. Libuda, *Nature Materials*, 2016, **15**, 284–288.

[23] E. C. Tyo and S. Vajda, *Nat. Nanotechnol.*, 2015, **10**, 577–588.

[24] J. H. Kwak, L. Kovarik and J. Szanyi, *ACS Catalysis*, 2013, **3**, 2094–2100.

[25] T. Imaoka, Y. Akanuma, N. Haruta, S. Tsuchiya, K. Ishihara, T. Okayasu, W.-J. Chun, M. Takahashi and K. Yamamoto, *Nature Communications*, 2017, **8**, 688.

[26] S. Vajda, M. J. Pellin, J. P. Greeley, C. L. Marshall, L. a. Curtiss, G. a. Ballentine, J. W. Elam, S. Catillon-Mucherie, P. C. Redfern, F. Mehmood and P. Zapol, *Nature materials*, 2009, **8**, 213–216.

[27] Z. Xu, F.-S. Xiao, S. K. Purnell, O. Alexeev, S. Kawi, S. E. Deutsch and B. C. Gates, *Nature*, 1994, **372**, 346–348.

[28] G. S. Parkinson, Z. Novotny, G. Argentero, M. Schmid, J. Pavelec, R. Kosak, P. Blaha and U. Diebold, *Nature Materials*, 2013, **12**, 724–728.

[29] S. Lee, L. M. Molina, M. J. López, J. A. Alonso, B. Hammer, B. Lee, S. Seifert, R. E. Winans, J. W. Elam, M. J. Pellin and S. Vajda, *Angewandte Chemie - International Edition*, 2009, **48**, 1467–1471.

[30] R. Addou, T. P. Senftle, N. O'Connor, M. J. Janik, A. C. van Duin and M. Batzill, *ACS Nano*, 2014, **8**, 6321–6333.

[31] C. Liu, S. K. Iyemperumal, N. A. Deskins and G. Li, *Journal of Photonics for Energy*, 2016, **7**, 012004.

[32] J. H. Kwak, R. Tonkyn, D. Tran, D. Mei, S. J. Cho, L. Kovarik, J. H. Lee, C. H. F. Peden and J. Szanyi, *ACS Catalysis*, 2012, **2**, 1432–1440.

[33] C. Aydin, J. Lu, N. D. Browning and B. C. Gates, *Angewandte Chemie - International Edition*, 2012, **51**, 5929–5934.

[34] B.-R. Chen, V.-H. Nguyen, J. C. S. Wu, R. Martin and K. Kočí, *Physical chemistry chemical physics : PCCP*, 2016, **18**, 4942–51.

[35] A. Alghannam, C. L. Muhich and C. Musgrave, *Phys. Chem. Chem. Phys.*, 2017, **19**, 4541–4552.

[36] X.-q. Gong, A. Selloni, O. Dulub, P. Jacobson and U. Diebold, *Journal of the American Chemical Society*, 2008, **130**, 370–381.

[37] S.-t. Zhang, C.-m. Li, H. Yan, M. Wei, D. G. Evans and X. Duan, *The Journal of Physical Chemistry C*, 2014, **118**, 3514–3522.

[38] J. Zhang, M. Zhang, Y. Han, W. Li, X. Meng and B. Zong, *The Journal of Physical Chemistry C*, 2008, **112**, 19506–19515.

[39] M.-C. Silaghi, A. Comas-Vives and C. Copéret, *ACS Catalysis*, 2016, **6**, 4501–4505.

[40] S. K. Iyemperumal and N. Deskins, *Phys. Chem. Chem. Phys.*, 2017, **DOI:10.1039/C7CP05718K**, year.

[41] B. Huber, P. Koskinen, H. Häkkinen and M. Moseler, *Nature materials*, 2006, **5**, 44–47.

[42] H. Tada, Q. Jin, A. Iwaszuk and M. Nolan, *The Journal of Physical Chemistry C*, 2014, **118**, 12077–12086.

[43] Q. Jin, M. Fujishima, M. Nolan, A. Iwaszuk and H. Tada, *The Journal of Physical Chemistry C*, 2012, **116**, 12621–12626.

[44] S. V. Ong and S. N. Khanna, *The Journal of Physical Chemistry C*, 2012, **116**, 3105–3111.

[45] Q. Jin, M. Fujishima, A. Iwaszuk, M. Nolan and H. Tada, *Journal of Physical Chemistry C*, 2013, **117**, 23848–23857.

[46] M. Fronzi, W. Daly and M. Nolan, *Applied Catalysis A: General*, 2016, **521**, 240–249.

[47] F. Dvoák, M. Farnesi Camellone, A. Tovt, N.-D. Tran, F. R. Negreiros, M. Vorokhta, T. Skála, I. Matolínová, J. Mysliveček, V. Matolín and S. Fabris, *Nature Communications*, 2016, **7**, 10801.

[48] P. Concepción, M. Boronat, S. García-García, E. Fernández and A. Corma, *ACS Catalysis*, 2017, **7**, 3560–3568.

[49] J. Vandevondele, M. Krack, F. Mohamed, M. Parrinello, T. Chassaing and J. Hutter, *Computer Physics Communications*, 2005, **167**, 103–128.

[50] http://cp2k.berlios.de, *CP2K developers home page*, 2016.

[51] G. Lippert, J. Hutter and M. Parrinello, *Mol. Phys.*, 1997, **92**, 477–488.

[52] J. P. Perdew, K. Burke and M. Ernzerhof, *Phys. Rev. Lett.*, 1996, **77**, 3865–3868.

[53] J. VandeVondele and J. Hutter, *Journal of Chemical Physics*, 2007, **127**, 0–9.

[54] S. Goedecker, M. Teter and J. Hutter, *Phys. Rev. B*, 1996, **54**, 1703–1710.

[55] S. Grimme, J. Antony, S. Ehrlich and H. Krieg, *The Journal of Chemical Physics*, 2010, **132**, 154104.

[56] S. Grimme, S. Ehrlich and L. Goerigk, *J. Comput. Chem.*, 2011, **32**, 1456–1465.

[57] A. R. Puigdollers, P. Schlexer and G. Pacchioni, *The Journal of Physical Chemistry C*, 2015, **119**, 15381–15389.

[58] G. T. Bae, B. Dellinger and R. W. Hall, *Journal of Physical Chemistry A*, 2011, **115**, 2087–2095.

[59] Y. Xu, W. A. Shelton and W. F. Schneider, *The Journal of Physical Chemistry A*, 2006, **110**, 5839–5846.

[60] T. A. Manz and N. G. Limas, *RSC Adv.*, 2016, **6**, 47771–47801.

[61] N. G. Limas and T. A. Manz, *RSC Adv.*, 2016, **6**, 45727–45747.

[62] G. Henkelman, B. P. Uberuaga and H. Jónsson, *The Journal of Chemical Physics*, 2000, **113**, 9901–9904.

[63] M. Jiang, Q. Zeng, T. Zhang, M. Yang and K. A. Jackson, *The Journal of Chemical Physics*, 2012, **136**, 104501.

[64] N. Seriani, C. Pinilla and Y. Crespo, *Journal of Physical Chemistry C*, 2015, **119**, 6696–6702.

[65] G.-T. Bae, *Bulletin of the Korean Chemical Society*, 2016, **37**, 638–642.

[66] L.-s. Wang, H. Wu, S. R. Desai and L. Lou, *Physical Review B*, 1996, **53**, 8028–8031.

[67] B. Dai, L. Tian and J. Yang, *The Journal of chemical physics*, 2004, **120**, 2746–51.

[68] M. Nolan, A. Iwaszuk and K. A. Gray, *Journal of Physical Chemistry C*, 2014, **118**, 27890–27900.

[69] P. K. Sharma, M. A. L. Cortes, J. W. Hamilton, Y. Han, J. A. Byrne and M. Nolan, *Catalysis Today*, 2018.

[70] A. C. Reber, S. N. Khanna, F. S. Roberts and S. L. Anderson, *The Journal of Physical Chemistry C*, 2016, **120**, 2126–2138.

[71] Y. Matsuda, D. N. Shin and E. R. Bernstein, *Journal of Chemical Physics*, 2004, **120**, 4165–4171.

[72] A. Sharma, M. Varshney, J. Park, T.-K. Ha, K.-H. Chae and H.-J. Shin, *RSC Adv.*, 2015, **5**, 21762–21771.

[73] K. Reuter and M. Scheffler, *Physical Review B*, 2001, **65**, 035406.

[74] D. R. Stull and H. Prophet, *JANAF thermochemical tables*, 1971.

[75] V. Meng'wa, N. Makau, G. Amolo, S. Scandolo and N. Seriani, *The Journal of Physical Chemistry C*, 2017, **121**, 20359–20365.

[76] L. Liu, F. Gao, H. Zhao and Y. Li, *Applied Catalysis B: Environmental*, 2013, **134-135**, 349–358.

[77] W. E. Kaden, W. A. Kunkel, M. D. Kane, F. S. Roberts and S. L. Anderson, *Journal of the American Chemical Society*, 2010, **132**, 13097–13099.

[78] M. Setvin, U. Aschauer, P. Scheiber, Y.-F. Li, W. Hou, M. Schmid, A. Selloni and U. Diebold, *Science*, 2013, **341**, 988–991.

[79] G. Mattioli, F. Filippone and A. A. Bonapasta, *Journal of the American Chemical Society*, 2006, **128**, 13772–13780.

[80] C. L. Muhich, Y. Zhou, A. M. Holder, A. W. Weimer and C. B. Musgrave, *Journal of Physical Chemistry C*, 2012, **116**, 10138–10149.

[81] Y. Hang Li, J. Xing, Z. Jia Chen, Z. Li, F. Tian, L. Rong Zheng, H. Feng Wang, P. Hu, H. Jun Zhao and H. Gui Yang, *Nature Communications*, 2013, **4**, 1–7.

[82] Y. G. Wang, Y. Yoon, V. A. Glezakou, J. Li and R. Rousseau, *Journal of the American Chemical Society*, 2013, **135**, 10673–10683.

[83] L. Liu, Q. Liu, Y. Zheng, Z. Wang, C. Pan and W. Xiao, *Journal of Physical Chemistry C*, 2014, **118**, 3471–3482.

[84] M. D. Rasmussen, L. M. Molina and B. Hammer, *Journal of Chemical Physics*, 2004, **120**, 988–997.

[85] H. Yoshida, S. I. Nonoyama, Y. Yazawa and T. Hattori, *Catalysis Today*, 2010, **153**, 156–161.

[86] M. Andersson, J. L. Persson and A. Rosén, *The Journal of Physical Chemistry*, 1996, **100**, 12222–12234.

[87] G. Nieman, E. Parks, S. Richtsmeier, K. Liu, L. Pobo and S. Riley, *High temperature science*, 1986, **22**, 115–138.

[88] S. Kitano, M. Sadakiyo, K. Kato, M. Yamauchi, H. Asakura, T. Tanaka, K. Hashimoto and H. Kominami, *Applied Catalysis B: Environmental*, 2017, **205**, 340–346.

[89] Y. Yan, Y. Yu, S. Huang, Y. Yang, X. Yang, S. Yin and Y. Cao, *The Journal of Physical Chemistry C*, 2017, **121**, 1089–1098.

Chapter 8

Conclusions

The conversion of carbon dioxide to useful chemicals on catalyst surfaces was studied using a quantum mechanical modeling tool density functional theory (DFT). Collaboration with experimentalists showed that photocatalytic reduction of CO_2 to CO was possible using atomically dispersed Cu on TiO_2. Motivated by these results, we sought to understand (i) CO_2 activation using a Cu_1/TiO_2 photocatalyst, (ii) the role of Cu clusters (1-4 atoms in size) supported on TiO_2 in activating CO_2, (iii) the trends in metal-support interactions across the periodic table (37 elements) and how they affect CO_2 activation, and (iv) the stability under reaction conditions for TiO_2-supported metal clusters.

CO_2 activation is one of the important initial reactions in CO_2 reduction, where a linear CO_2 molecule forms bent CO_2 species. Cu_1/TiO_2 catalysts were found to stabilize bent CO_2 anion species and potentially active CO_2. We next studied the role of clusters of Cu on TiO_2 and how they activated CO_2. Similar to Cu_1, all clusters of Cu (2-4) were found to activate CO_2 as shown by the bent CO_2 adsorption energies being stronger than the linear CO_2 on all Cu_x/TiO_2 (x=1-4) surfaces. The stabilization of bent CO_2 was also accompanied by electronic charge transfer to CO_2 forming CO_2 anion species on all TiO_2-supported Cu clusters. Out of the four Cu clusters, the Cu dimer was found to activate CO_2 the most.

However, the formation of Cu dimers by diffusion of Cu monomers on TiO_2 surface was found to be unfavorable (both thermodynamically and kinetically) suggesting that the Cu dimer is a reactive but unstable catalyst. Experimental efforts to stabilize the Cu dimer could lead to highly active catalysts.

In the literature, many atomically dispersed catalysts that have been studied are expensive late transition metals such as Rh, Ru, Pt, Ir, or Au. One of the important challenges in the field of atomically dispersed catalysts is the stabilization of the supported metal atom. In our work we elucidated the trends in metal-support interactions by modeling adsorption of 38 metal atoms (all transition and several post-transition metals) on TiO_2. Binding of the metals ranged from very strong (early transition metals) to weak (late transition metals). Using statistical learning methods like the Lasso shrinkage model, we identified important descriptors that can estimate the metal atom adsorption energies. Important descriptors or properties in describing metal adsorption were metal-oxygen bond dissociation energy, structural fluxionality, d-band center, Bader charge, and group number in the periodic table.

We also determined the CO_2 adsorption/activation trends for the 38 studied metals. In order to explain the trends in CO_2 activation, Lasso again was used to identify the d-band center, metal-oxygen bond dissociation energy, group number, cohesive energy and workfunction of the metal as the important descriptors for CO_2 adsorption. In terms of the trends in CO_2 activation, we again found that early and mid transition metal atoms activated CO_2 strongly and thus can potentially be active catalysts for CO_2 reduction. Our results encourage experimental synthesis of the abundant and inexpensive elements from early and mid transition metal atoms that are predicted to be potentially stable and active catalysts.

Under reaction or synthesis conditions, a supported metal atom or cluster can undergo aggregation and/or oxidation that can affect the catalyst's activity. Stabilizing these small clusters in a desired state is crucial for developing stable and catalytically active catalysts.

In order to understand the stability of supported atoms of small clusters, we modeled metal aggregation and metal oxidation on TiO_2 surfaces for clusters of common transition metal atoms (Co, Ni, and Cu group elements). Cu and Pt atoms/clusters in gas phase favored metal aggregation compared to oxidation. The thermodynamically preferred growth pathway of Cu_1/TiO_2 to form larger clusters involved sequential oxidation and metal aggregation (Cu_1 $\longrightarrow$ Cu_1O $\longrightarrow$$Cu_2O$ $\longrightarrow$ Cu_2O_2, etc.). In the case of Pt_1/TiO_2, the Pt aggregation and Pt oxidation growth pathways were both favorable and were close in energy. We found that O_2 adsorption and dissociation are important for the oxidation of Cu_x/TiO_2. Although, oxidation by O_2 is thermodynamically favorable to form Cu^{2+} species, kinetics of O_2 dissociation showed that O_2 dissociation was favorable only on Cu clusters. Overall, considering both kinetics of O_2 dissociation and thermodynamics of oxidation, Cu^{1+} was the stable oxidation state of all Cu atom/clusters on TiO_2. Our results were in agreement with experimental results, where the presence of O_2 resulted in oxidation of Cu to form Cu^{1+} species (instead of complete oxidation to form Cu^{2+}). In the case of other transition metal atoms studied, we found Co group elements to more strongly oxidize on TiO_2, compared to Cu and Ni group elements.

The current work has raised several interesting questions that can be pursued in future research directions. (i) So far, we have only modeled the activation of CO_2. However, in order to understand the selectivity and formation of various reaction product like carbon monoxide, formic acid, formaldehyde, methanol, and methane, the complete CO_2 reduction mechanism should be considered. We modeled only the anatase (101) surface and understanding the role of different TiO_2 surface facets (including step edges) on the selectivity of CO_2 reduction products is also crucial for a better catalyst design. (ii) In order to better understand the oxidation of supported metal atoms and clusters, more kinetic data of the O_2 dissociation reaction may be required. (iii) We have only considered the possibility of O_2, H_2O, or CO_2 in oxidizing the small supported clusters using chemical potential of the gas phase molecules.

Under experimental conditions, these molecules may however react with the supported metal cluster catalyst resulting in radical species such as H, OH, and O, which can be important in understanding the stable oxidation state of the catalyst.

Robust quantum mechanical modeling tools such as DFT are essential for providing valuable structural, energetic, and electronic insights, which are difficult to probe experimentally. We have provided several examples where DFT was used to provide fundamental understanding of catalysts and also to predict potentially active catalysts that experimentalists can synthesize and validate. Theoretical tools therefore are important for designing better catalysts more efficiently, rather than trial and error based experimental synthesis.

Appendix A

Supporting Information - CO_2 Reduction on Dispersed Cu_{1-4}/TiO_2 catalysts

A.1 Effect of TiO_2 Slab Thickness

We tested the effect of the TiO_2 slab thickness as given in Table A.1. We modeled a single Cu atom adsorbed in the bridge site between two O_{2c} atoms, and the adsorption energy changed by only 0.08 eV between six and eight layer slabs. Adsorption energies for linear and bent CO_2 molecules over pure TiO_2 changed by ≤ 0.03 eV between six and eight layer slabs. We thus used a six layer slab in all of our work.

Table A.1: Effect of TiO_2 slab thickness on the adsorption energies (in eV) of a Cu atom, linear CO_2, and bent CO_2. See main text for geometries.

	6 Layers	**8 Layers**
Cu	-2.56	-2.64
CO_2 linear	-0.40	-0.43
CO_2 bent	-0.15	-0.14

A.2 Comparison of DDEC6 charges with Bader charges

We used DDEC6 charge analysis[1,2] in the present work as the DDEC6 code provides reference core charge densities that are easily augmented with the valence electron densities generated from CP2K. Core densities are necessary to ensure that proper charges on atoms are calculated. DDEC6 iteratively calculates partial atomic charges from the ground state electron density while simultaneously accurately reproducing electrostatic potentials from the electron density of the system.[2] The challenge for any charge analysis technique is that there is no unique way to define atomic charge. Another complication is that calculated charges may not match formal charges due to ionocovalent bonding or limitations of the charge analysis technique. For example, Ti and O atoms in bulk TiO_2 anatase have DDEC6 charges of +2.28 and -1.14, respectively. Formally Ti has a +4 charge, while O has a -2 charge. We note however that the oxidation state of Ti and O in TiO_2 has been recently suggested to be rather +3 and -1.5,[3] in contrast to the traditionally assigned charges in TiO_2.

Nevertheless, charge analysis can provide useful insight on charge transfer during an adsorption process. Another widely used method is Bader charge analysis,[4,5] where the electron density of a material is partitioned by determining the zero flux surfaces around each atom. We compared the charges calculated from DDEC6 with Bader for several molecules

like CO_2, CO_2-, CO, O_2, OH, and OH^-, as well as periodic solid systems like CO_2, $LiTiO_2$, $LiTi_2O_4$, CuO, and Cu_2O in Table A.2. We show in this table also results calculated using a common periodic DFT code, VASP.[6,7] For the bulk crystals, calculated charges using DDEC6+CP2K and Bader+VASP gave a mean absolute difference of 0.08 e^-. For molecules, the mean absolute difference was 0.43 e^-. For determining trends in charge transfer the DDEC6 method is fully adequate.

Table A.2: DDEC6 and Bader charges calculated using CP2K and VASP for bulk and molecular systems.

	System	Atoms	CP2K + DDEC6	VASP + DDEC6	VASP + Bader
Bulk	TiO_2 anatase	Ti	2.28	2.25	2.16
		O	-1.14	-1.12	-1.08
	$LiTiO_2$	Li	0.87	0.89	0.89
		Ti	1.73	1.65	1.57
		O	-1.30	-1.27	-1.23
	$LiTi_2O_4$	Li	0.90	0.90	0.91
		Ti	1.95	1.94	1.84
		O	-1.20	-1.19	-1.15
	CuO	Cu	0.94	0.94	1.00
		O	-0.94	-0.94	-0.99
	Cu_2O	Cu	0.33	0.33	0.54
		O	-0.65	-0.66	-1.08
	CO_2	C	0.71	0.71	2.01
		O	-0.35	-0.35	-0.99
	CO_2^-	C	0.21	0.28	1.50
		O	-0.61	-0.64	-1.18
	CO	C	0.11	0.11	1.03
		O	-0.11	-0.11	-1.00
	O_2	O	0.00	0.00	-0.05/0.07
	OH	O	-0.33	-0.33	-0.59
		H	0.33	0.33	0.61

Table A.2: Continued: DDEC6 and Bader charges calculated using CP2K and VASP for bulk and molecular systems.

	System	Atoms	CP2K + DDEC6	VASP + DDEC6	VASP + Bader
Molecules	OH-	O	-1.20	-1.21	-1.46
		H	0.20	0.21	0.51
	CuO	Cu	0.44	0.46	0.59
		O	-0.44	-0.46	-0.55
	Cu_2O	Cu	0.28	0.28	0.44
		O	-0.59	-0.56	-0.81
	Cu_3O	Cu	0.16	0.16	0.32
		O	-0.50	-0.49	-0.85
	CuO_2	Cu	0.59	0.70	0.99
		O	-0.30	-0.35	-0.48

A.3 Vibrational Frequency Calculations

We determined the effect of several simulation parameters on the vibrational frequency calculations of CO adsorbed on Cu/TiO_2, and linear/bent CO_2 on TiO_2 surfaces. These include the plane wave cutoff energies, number of relaxed (unfrozen) atoms, and step size for displacement when calculating energies/forces. Vibrational frequencies were calculated numerically by displacing atoms to calculate second derivatives. Higher cutoff energies give more accurate energies since the basis set is more complete but require more time. Our strategy involved low/high cutoff energies (300/600 Ry). Because these systems were rather large and we did use large cutoff energies, we selectively froze atoms beyond the adsorption site in order to ensure the vibrational calculations were manageable. Frozen atoms were

typically 6-7 Å away from the C atom at the adsorption site. This resulted in a smaller set of atoms displaced during vibrational frequency calculation (in the range of 40-50 atoms), but allowed the atoms that could more directly influence the CO/CO_2 frequencies to affect calculation of the second derivatives. Our tests determined appropriate cutoff energies as well as the number of atoms that should be relaxed in order to obtain reasonable frequencies.

As shown in Table A.4, geometry optimization at the higher cutoff energies of 600 Ry followed by a vibrational frequency calculations at 600 Ry were required to obtain accurate frequencies close to the earlier reported experimental and DFT calculated frequencies. For instance, linear CO_2 adsorbed on TiO_2 was calculated to have vibrational frequencies of 2367 (asymmetric stretch) and 1351 (symmetric stretch), which agree well with both previous experimental (2355 and 1379 cm^{-1}) and DFT (2373 and 1323 cm^{-1}) values. We found that relaxing 40-50 atoms around the adsorption site was sufficient to obtain vibrational frequencies that were similar to the values obtained by relaxing one or two layers of TiO_2 slab. For instance, the difference in vibrational frequencies for adsorbed CO with the relaxed number of atoms being 42 atoms and 98 atoms (96 atoms relaxed in the top two layers of the slab and 2 atoms of CO) was only 5 cm^{-1}. We thus relaxed 40-50 atoms around the adsorption site for all our reported frequencies in the main text. With respect to the step size during the finite difference approach, we used $1.0E^{-3}$ Bohr. Tests between $1.0E^{-3}$ and $1.0E^{-2}$ Bohr for CO_2 bent/linear adsorption showed the mean absolute difference to be small (12 cm^{-1}) for adsorbed CO_2 vibrational frequencies. The final settings we used for vibrational calculations were a cutoff of 600Ry, relaxing 40-50 atoms around adsorption site, a step size of $1.0E^{-3}$ Bohr, and a tighter electronic convergence criteria of $1.0E^{-7}$ Hartree. Using these settings the mean absolute difference between our DFT calculated and experimental gas phase CO_2 and CO frequencies were 12 cm^{-1} and 5 cm^{-1} respectively.[8] Our DFT values for linearly adsorbed CO_2 were in good agreement with the experimental values,[9] with a mean absolute difference of 20 cm^{-1} for the asymmetric and symmetric stretching modes.

Table A.3: Effect of cutoff energy, number of relaxed atoms during frequency calculations ($N_{relaxed}$) and step size on calculated frequencies. All calculations for adsorbed CO_2 were on pure TiO_2 surfaces, while adsorbed CO were on Cu/TiO_2 surfaces. * indicates the experimentally observed Fermi resonance that shifts the bending frequency to a higher 1271 cm^{-1} value.[10,11] This resonance is not correctly described by the DFT calculations.

	Geo. Opt. Cutoff (Ry)	**Vib. Freq. Cutoff (Ry)**	$\mathbf{N_{relaxed}}$	**Step Size (Bohr)**	**Frequency (cm^{-1})**
CO (gas)	600	600	2	1.0E-3	2178
Experimental Reference[8]	—	—	—	—	2169
	300	600	98	$1.0E^{-3}$	2072
Adsorbed CO	600	600	98	$1.0E^{-3}$	2102
	600	600	42	1.0E-3	2097
CO_2 (gas)	600	600	3	$1.0E^{-3}$	2358, 1300, 664, 664
Theoretical Reference[12]	—	—	—	—	2365, 1318, 633, 633
Experimental Reference[8]	—	—	—	—	2349, 1333, 667, 667
	300	600	195	$1.0E^{-3}$	2371, 1337, 673, 657
	300	600	99	$1.0E^{-3}$	2372, 1335, 674, 642
Linear CO_2	600	600	42	1.0E-3	2367, 1351, 667, 688
	600	600	42	$1.0E^{-2}$	2370, 1349, 656, 650
Theoretical Reference[12]	—	—	—	—	2373, 1323, 615, 611
Experimental Reference[9]	—	—	—	—	2355, 1379, 1271*
	300	600	195	$1.0E^{-3}$	1730, 1260, 790, 875
	300	600	99	$1.0E^{-3}$	1731, 1260, 791, 872
Bent CO_2	600	600	43	$1.0E^{-3}$	1709, 1277, 822, 718
	600	600	43	$1.0E^{-2}$	1700, 1273, 801, 725
Theoretical Reference[12]	—	—	—		1719, 1249, 785, 730

A.4 Most Stable Spin State

We calculated the most stable spin state of both gas phase Cu_x clusters and adsorbed Cu_x/TiO_2 geometries. We find that in all the cases, the lowest spin state with minimum number of unpaired electrons (multiplicity of 1 or 2) are the most stable spin state as shown in Table A.5.

Table A.4: Relative energies (in eV) with respect to the most stable spin state. Zero relative energy correspond to most stable spin state.

	Cu_1	Cu_3	Cu_1/TiO_2	Cu_3/TiO_2
Multiplicity 2	0.00	0.00	0.00	0.00
Multiplicity 4	5.27	1.16	0.85	1.31
	Cu_2	**Cu_4**	**Cu_2/TiO_2**	**Cu_4/TiO_2**
Multiplicity 1	0.00	0.00	0.00	0.00
Multiplicity 3	1.58	0.61	0.43	0.02

A.5 Effect of DFT+U

A.5.1 Effect of the U Correction on Adsorption Energies

DFT+U has become a standard way to correct self interaction errors inherent in DFT using generalized gradient approximation exchange-correlation functionals.[13] Earlier DFT studies showed that the effect of U correction on the adsorption energies of adsorbates like formaldehyde or methanol on $CeO_2(111)$,[14] oxygen molecule on TiO_2 rutile (110),[15] and Au_{20}/TiO_2 rutile(110)[16] was small (less than 0.1 eV). However, Garcia and Deskins[17] reported that the adsorption of O_2 on the anatase TiO_2 (101) with oxygen vacancy was strongly destabilized ($\sim$0.8 eV) with increasing U value of up to 10 eV. In the case of adsorption of CO_2, He et

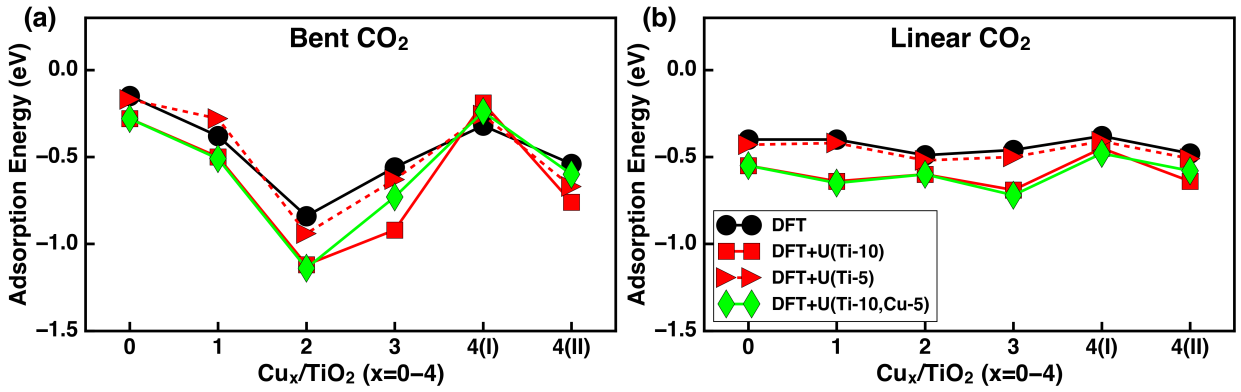

Figure A.1: Effect of different U corrections on the adsorption energies of most stable (as discussed in the main text) bent (a) and linear (b) CO_2 adsorption configurations on Cu_x/TiO_2. Shown are results for pure DFT and DFT with U corrections. For example, U(Ti-10,Cu-5) represents a U correction of 10.0 eV applied to Ti and 5.0 eV applied Cu atoms.

al.[18] showed that the energy to convert linear CO_2 to bent CO_2 on the anatase TiO_2 (101) surface differed by only 0.03 eV between DFT and DFT+U (U=4.5 eV). One complication is that the appropriate U value choice depends on the basis set, pseudopotential, the target property (adsorption energy in our case), and the catalyst under consideration. We thus used various U values to determine the DFT+U effect on O_{2c} adsorption over Cu_x/TiO_2 catalysts.

We used three different DFT+U schemes: a U correction (U values reported here are effective U, U_{eff} = U - J) applied to just Ti (5.0 eV), U correction applied to just Ti (10.0 eV), and U corrections applied to both Ti (10.0 eV) and Cu (5.0 eV). All corrections were applied to d electrons. Similar large U values were earlier used in modeling TiO_2 using CP2K.[16,17,19] In the case of Cu, literature suggests that the application of U to Cu atoms in different oxidation states such as in CuO, Cu_2O, and Cu_4O_3 can be challenging.[20,21] Electronic properties such as the band gap of Cu_4O_3 and CuO, direct or indirect band gap in Cu_2O, and location of defect levels in defective bulk Cu_2O were reported to be incorrectly described by DFT+U techniques.[20–22] Nonetheless, in order to test the effect of U on Cu, we chose a representative U value for Cu as 5.0 eV, which is similar to the value of 5.2 eV

used earlier.[22,23]

We found that DFT+U predominantly gives more negative adsorption energies compared to DFT as Figure A.0 shows. The exception is bent CO_2 on the Cu4(I) structure, where inclusion of U resulted in slight (by less than around 0.1 eV) endothermic adsorption energies compared to the DFT value. The difference between DFT and DFT+U for both bent and linear CO_2 adsorption was small (up to 0.1 eV) when U of 5 eV was applied to Ti, while it was larger (in the range of 0.1 to 0.4 eV) when a U value of 10 eV was applied. Applying a U correction to Cu had almost no effect on bent CO_2 adsorption energies when compared to U of 10 eV applied to Ti, except for the Cu_3 and Cu_4(II) clusters. These clusters where less stable by 0.19 eV, Cu_3, and 0.16 eV, Cu_4(II), when the U correction was also applied to Cu. Only in the case of Cu_4(II) did applying the U correction to Cu have an effect in destabilizing adsorbed linear CO_2, although the effect appears small (0.06 eV). It appears therefore that DFT+U may only meaningfully affect the nature of larger Cu clusters, although this effect is small for the clusters we used. In the case of Cu_4(I), DFT+U results showed that bent CO_2 adsorption is 0.15-0.26 eV less stable than linear CO_2, while DFT results showed this difference between bent and linear CO_2 adsorption to be 0.06 eV. The trends in adsorption energies however are similar regardless of U value choice. Our calculated DFT adsorption energies agree with the literature values. The linear and bent CO_2 adsorption energies reported earlier using DFT[12] were -0.48 eV and -0.01 eV, which are close to our DFT values of -0.40 and -0.15 eV respectively. We therefore present only the DFT adsorption energies in the main text.

A.5.2 Effect of U Correction on Atomic Charges

We also calculated DDEC6 charges of adsorbed CO_2, as well as Cu_x clusters with and without adsorbed CO_2 using DFT and DFT+U (U of 10 eV on Ti atoms). We found that the DDEC6 charges were predominantly weakly affected (<0.1 electrons) when U corrections

are applied (see Table A.6). For instance, Cu_3 and Cu_4/TiO_2 charges before CO_2 adsorption were almost the same. The only considerable difference between DFT and DFT+U results was for the case of a single Cu atom. When linear CO_2 was adsorbed, the charge of the Cu atom from DFT was 0.48, compared to 0.65 using DFT+U. When bent CO_2 was adsorbed, the charge of the Cu atom from DFT was 0.59, compared to 0.82 using DFT+U. Otherwise, most charges were similar between DFT and DFT+U. The mean absolute difference in CO_2 charges between DFT and DFT+U was 0.08 electrons. The mean absolute differences in Cu charges between DFT and DFT+U was 0.08 electrons (no CO_2 adsorbed) and 0.13 electrons (CO_2 adsorbed). DFT charges are therefore presented in the main text.

Table A.5: DDEC6 charges of linear/bent CO_2 and Cu atoms using the DFT and DFT+U methods. Here, a U correction of 10 eV was applied to the Ti 3d electrons.

No. Cu atoms (Cu_x/TiO_2)	**CO_2 Geometry**	**C, O, O Charges**	**Cu_x Charges (Before Adsorption)**	**Cu_x Charges (After Adsorption)**
		DFT Results		
	CO_2 (gas)	0.70,-0.35,-0.35	–	–
0	linear	0.75, -0.31, -0.37	–	–
	bent	0.79,-0.55, -0.54	–	–
1	linear	0.78, -0.40, -0.32	0.53	0.48
	bent	0.79, -0.58, -0.52	–	0.59
2	linear	0.77, -0.40, -0.33	0.13, -0.07	0.13, -0.06
	bent	0.33, -0.53, -0.36	–	0.29, 0.30
3	linear	0.75, -0.29, -0.32	0.24, 0.24, 0.03	0.18, 0.23, -0.01
	bent	0.86, -0.59, -0.45	–	0.16, 0.15, 0.04
4(I)	linear	0.76, -0.32, -0.38	0.52, 0.20, 0.23, -0.07	0.52, 0.21, 0.23, -0.08
	bent	0.83, -0.52, -0.43	–	0.51, 0.16, 0.27, -0.08
4(II)	linear	0.76, -0.33, -0.30	0.42, 0.12, 0.45, -0.06	0.38, 0.10, 0.46, -0.07
	bent	0.82, -0.58, -0.43	–	0.39, -0.01, 0.15, 0.41
		DFT+U Results		
0	Linear	0.79, -0.30, -0.42	–	–
	Bent	0.82, -0.58, -0.58	–	–
1	Linear	0.80, -0.43, -0.31	0.58	0.65
	Bent	0.83, -0.65, -0.55	–	0.82
2	Linear	0.80, -0.42, -0.32	0.10, -0.15	0.10, -0.16
	Bent	0.36, -0.61, -0.36	–	0.27, 0.23
3	Linear	0.77, -0.32, -0.39	0.27, 0.27, 0.03	0.27, 0.22, 0.00
	Bent	0.89, -0.61, -0.44	–	0.18, 0.28, 0.01
4(I)	Linear	0.77, -0.31, -0.39	0.50, 0.18, 0.21, -0.10	0.50, 0.19, 0.21, -0.12
	Bent	0.85, -0.53, -0.41	–	0.48, 0.16, 0.24, -0.14
4(II)	Linear	0.77, -0.34, -0.29	0.41, 0.07, 0.44, -0.07	0.37, 0.06, 0.45, -0.10
	Bent	0.84, -0.64, -0.41	–	0.39, 0.15, 0.34, -0.02

A.5.3 Effect of the U Correction on Electronic States

We also determined how U value choice impacts the electronic structure by examining the density of states of adsorbed Cu at different U values. Yan et al. reported that the significant Cu states are present at the valence band maximum edge.[24] We find that a U value of 5.0 eV applied to Ti describes the Cu/TiO_2 electronic states correctly similar to what Yan et al. have reported and also gives a reasonable band gap of 1.66 eV (see Figure A.1). A large U value of 10 eV applied to Ti resulted in Cu states pushed to lower (more negative) energies within the valence band, which is not agreement with previous literature.[24] We thus used a U correction of 5.0 eV to Ti for all our density of states calculations.

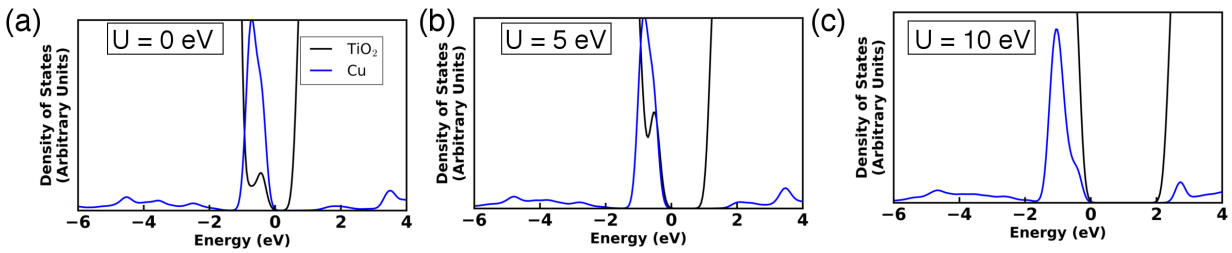

Figure A.2: Sited-projected density of states (DOS) for Cu/TiO_2 calculated using U values of 0, 5, and 10 eV (all applied to Ti). The valence band edge for each system has been set to 0 eV in the plots.

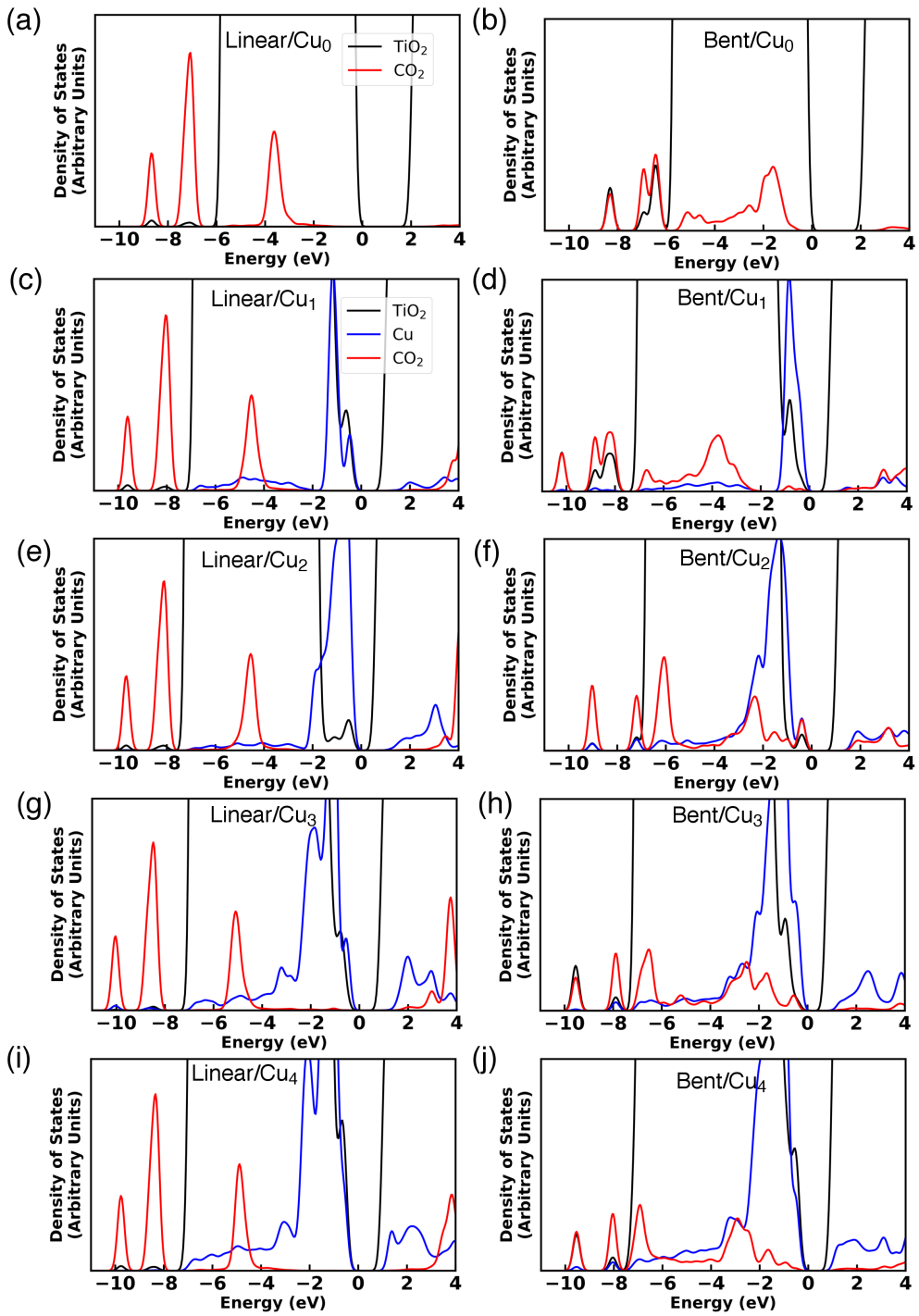

Figure A.3: Sited-projected density of states (DOS) for linear and bent CO_2 adsorbed on Cu_x/TiO_2 for a U value of 5 eV applied to Ti. The left plots show linear CO_2 while the right plots show bent CO_2. The valence band edge for each system has been set to 0 eV in the plots.

In Figure A.2, we show all the results for bent and linear CO_2 adsorption on Cu_x/TiO_2 (x=0-4) with a U value of 5.0 eV. The three characteristic localized peaks of linear CO_2 (at locations $\sim$ -9.7, -8.1, -4.5 eV in Cu_x/TiO_2) are preserved regardless of Cu cluster, although the peaks are slightly shifted up in energy over pure TiO_2. Similarly, for bent CO_2, the delocalized character of the CO_2 peaks are preserved for bent CO_2 on TiO_2 with and without Cu clusters present. On the pure TiO_2 surface, the linear and bent CO_2 states extend within the valence band down to $\sim$ -9 eV. In the presence of Cu, the CO_2 states are pushed to lower energies extending up to -11 eV (see for example Bent CO_2 on Cu1). As mentioned in the main text, we consistently find strong hybridization between bent CO_2 and Cu states in the valence band as indicated by the overlap of delocalized Cu and bent CO_2 states (between 0 and $\sim$ -8 eV). In contrast, the linear CO_2 states are localized between -4 and -6 eV indicating weak hybridization with the Cu states.

A.6 CO adsorption on Cu_x/TiO_2

The most stable CO adsorption sites on Cu_x/TiO_2 are shown in Figure A.3. We found the most stable adsorption site for CO on Cu/TiO_2 to involve a linear O-C-Cu bond at the top site of Cu atom with an adsorption energy of -1.96 eV. The bond distance of C-Cu was found to be 1.82 Å. The Cu atom was displaced significantly upon CO adsorption (by 0.57Å).

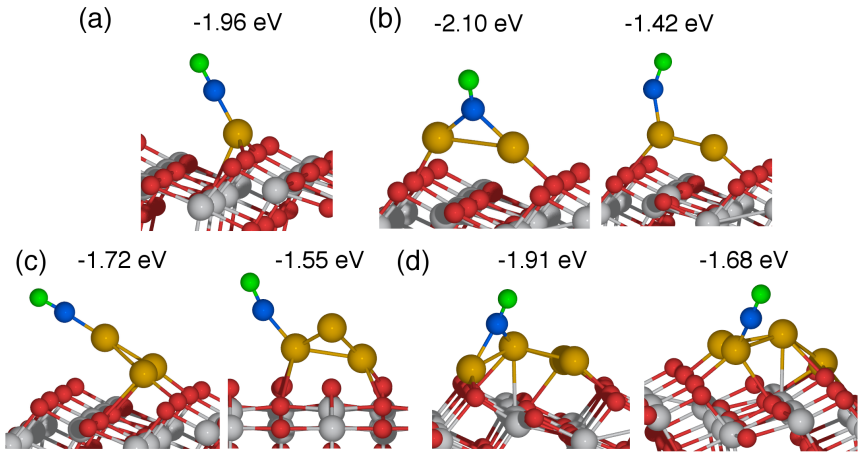

Figure A.4: Most stable adsorption sites of CO on Cu_x/TiO_2 with x=1 (a), 2 (b), 3(c), and 4(I)(d). The numbers above each structure correspond to the adsorption energy of CO for that structure. Color scheme of atoms are the same as in previous Figures.

When CO adsorbs on Cu_2/TiO_2, the most stable site of adsorption was determined to be the bridge site where the C atom bonds with both Cu atoms and has an adsorption energy of -2.10 eV (see A.3). This adsorption energy is also the largest among the CO adsorption energies over all Cu_x/TiO_2. The strong adsorption energy for Cu_2 again indicates the reactive nature of the Cu dimer, as was observed for CO_2 adsorption. The bond distances of both C-Cu bonds were 1.89Å. Adsorption of CO at the bridge site also results in the Cu-Cu bond distance to elongate from 2.30Å to 2.80Å. We also show the next most stable top site adsorption configuration on Cu_2/TiO_2 in Figure A.3b. CO was found to be non-linearly bonded (the bond angle of Cu-C-O was 151^o) with an adsorption energy of -1.42 eV. Adsorption of CO at the top site is significantly less stable than when CO adsorbs at the bridge site.

We adsorbed CO on several different adsorption sites over Cu_3/TiO_2. In the most stable configuration CO binds to the top Cu atom. The C-Cu bond distance was found to be 1.85Å and the adsorption energy was -1.72 eV. The next most stable adsorption site had

an adsorption energy of -1.55 eV where CO bonded to a Cu atom that interacted with the surface. Several adsorption sites were tested for CO adsorption on $Cu_4(I)/TiO_2$, and the two most stable sites are shown in Figure A.3d. The most stable adsorption site involved CO bridging between Cu_a and Cu_d atoms with a C-Cu bond distance of 1.92 and 1.97 Å, respectively. The next stable adsorption site consisted of CO adsorbing on top of a Cu_c atom with a C-Cu bond distance of 1.84 Å. This configuration had an adsorption energy of 1.68 eV. It was also found that CO adsorption in the top configuration bonded to any other Cu atom of $Cu_4(I)/TiO_2$ had adsorption energies between -1.57 to -1.68 eV.

A.7 Determining the Oxidation State of Cu using DDEC6

Table A.6: DDEC6 charges (in electrons) for Cu^{2+} and Cu^{1+} complexes, as well as CuF/CuF_2 and CuO/Cu_2O (bulk and molecule).

Species	**DDEC6 charge**
Cu^{1+}	
Cu-CN-$(H_2O)_3$	0.33
Cu-Cl-$(H_2O)_3$	0.35
Cu-OH-$(H_2O)_3$	0.29
Cu-F-$(H_2O)_3$	0.41
Cu-CN-$(NH_3)_3$	0.25
Cu-Cl-$(NH_3)_3$	0.30
Cu-OH-$(NH_3)_3$	0.27
Cu-F-$(NH_3)_3$	0.30
Cu-CN-$(N_2)_3$	0.34
Cu-Cl-$(N_2)_3$	0.42
Cu-OH-$(N_2)_3$	0.46
Cu-F-$(N_2)_3$	0.52
Cu_2O (bulk)	0.33
Cu_2O (molecule)	0.28
CuF	0.50

Table A.6: Continued: DDEC6 charges (in electrons) for Cu^{2+} and Cu^{1+} complexes, as well as CuF/CuF_2 and CuO/Cu_2O (bulk and molecule).

Species	**DDEC6 charge**
Cu^{2+}	
Cu-$(CN)_2$-$(H_2O)_4$	0.78
Cu-Cl_2-$(H_2O)_4$	0.95
Cu-$(OH)_2$-$(H_2O)_4$	1.02
Cu-F_2-$(H_2O)_4$	1.10
Cu-$(CN)_2$-$(NH_3)_4$	0.67
Cu-Cl_2-$(NH_3)_4$	0.85
Cu-$(OH)_2$-$(NH_3)_4$	0.85
Cu-F_2-$(NH_3)_4$	1.01
Cu-$(CN)_2$-$(N_2)_4$	0.68
Cu-Cl_2-$(N_2)_4$	0.83
Cu-$(OH)_2$-$(N_2)_4$	0.67
Cu-F_2-$(N_2)_4$	1.02
CuO (bulk)	0.94
CuO (molecule)	0.44
CuF_2	0.93

We used DDEC6 charge analysis to calculate oxidation states of Cu. In order to identify the Cu states, we modeled several known Cu^{1+} and Cu^{2+} complexes. The geometries of Cu^{2+} (or Cu^{1+}) coordination complexes are known to adopt an octahedral (or tetrahedral) coordination with Cu at the center of these complexes.[25] For both complexes we considered several anionic and neutral ligands in different combinations. The neutral ligands considered were dinitrogen (N_2), water, and ammonia, while anionic ligands considered were Cl, F, CN,

and OH. In octahedral complexes, out of the six vertices (four equatorial and two axial), two equatorial sites contained the anionic ligands for describing Cu^{2+} species with the rest of the four sites occupied by neutral ligands. In the case of the tetrahedral complexes, one of the four vertices contained an anionic ligand and other three contained a neutral ligand. The calculated DDEC6 charges are shown in Table A.8. Besides these Cu coordination complexes, we also considered other systems such as CuO (bulk and molecule), Cu_2O (bulk and molecule), molecular CuF, and molecular CuF_2. We determined average DDEC6 charges for Cu in the various formal oxidation states. For the Cu^{2+} species the average DDEC6 charge was 0.85 with a standard deviation of 0.17, while for the Cu^{1+} species the average DDEC6 charge was 0.36 with a standard deviation of 0.08. The range of DDEC6 charges for Cu^{2+} was 0.44 to 1.10, while the range of charges for Cu+ was 0.25 to 0.52.

A.8 Diffusion of Adsorbed Cu Atoms

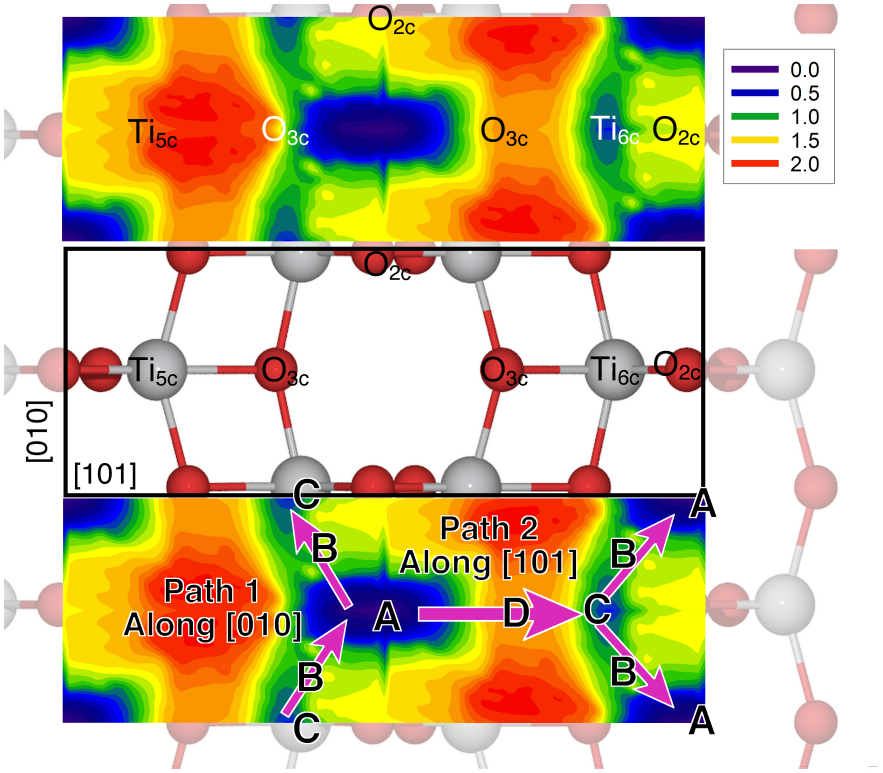

Figure A.5: Potential energy surface for Cu adsorbed on the TiO_2 anatase(101). The contour of the energy surface is shown in the top panel and the corresponding top view of the TiO_2 surface is indicated by the black box in the middle panel. The minimum energy pathway is shown in the bottom panel along [010] and [101] directions through sites A/B/C/B/A and A/D/C/B/A respectively. For clarity only the top layer of the TiO_2 surface slab is shown. Surface atoms on the top and middle panels are labeled. The contour legend shows the relative energies compared to most stable adsorption site in eV.

Cu2 was found to stabilize CO_2 very strongly, but questions remain on its stability. We found the Cu2 formation energy to be 0.94 eV (2 $Cu/TiO_2 \longrightarrow Cu_2/TiO_2 + TiO_2$). We also calculated the potential energy surface of a Cu atom bound to the anatase (101) surface, as shown in Figure A.3, in order to understand Cu diffusion on the surface. Cu diffusion

is necessary for lone Cu atoms to form dimers. We adsorbed a Cu atom at different points on the surface by freezing the x- and y-coordinates of the Cu atom while allowing the z-coordinate of the Cu atom to relax. The bottom four O-Ti-O layers (192 atoms) of the surface slab were also frozen. The Cu atom was placed at different points on the surface with a spacing of 0.2Å between points. After considering the surface symmetry, we modeled a total of 263 geometries. Test calculations showed that freezing the bottom four and two layers produced results that were very comparable. The largest difference in energy between freezing four and two layers for the adsorption of Cu at different sites (e.g. bridge site between O_{2c} atoms or top sites was <0.13 eV).

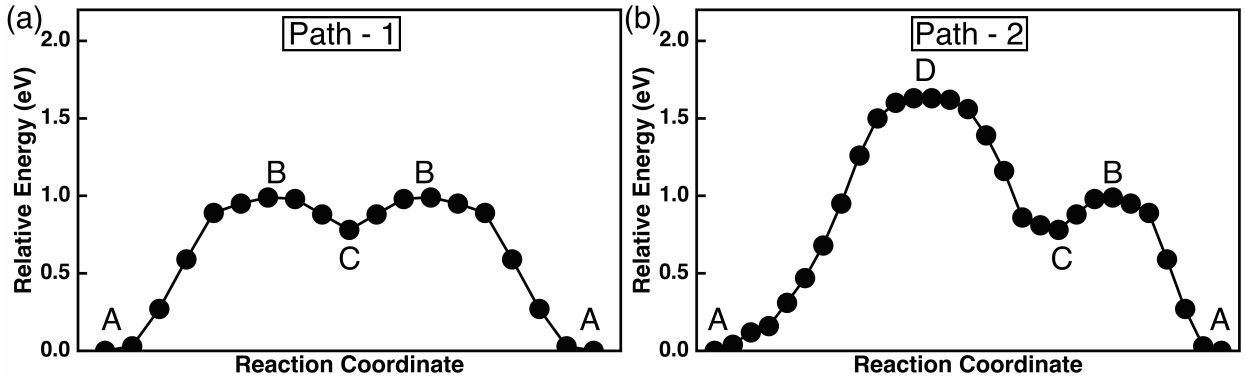

Figure A.6: Diffusion barriers for Cu along Path 1 and Path 2 (shown in Figure A.3 over the TiO_2 anatase(101) surface.)

The most stable site for Cu adsorption was at the bridge site between two O_{2c} atoms (indicated as point A in the bottom plot of Figure A.3), which corresponds to the deepest energy well with an adsorption energy of -2.60 eV. The energy corresponding to this site represents the zero energy reference in the contour plots. The second most stable site of adsorption (site C) is at a top site above a Ti_{6c} atom, whose energy is 0.78 eV higher in energy than the most stable adsorption site A. In order for an atom to diffuse from a site A to another site A, it can follow one of the pathways indicated in the bottom plot of Figure A.3.

Path 1 moves along the [010] direction and follows the pathway indicated: A $\longrightarrow$ B $\longrightarrow$ C $\longrightarrow$ B $\longrightarrow$ A. The energy barrier for Path I was calculated to be 0.99 eV as the atom crossed from site A to site B (see Figure A.4). Path 2 along moves in a general [101] direction and follows the indicated pathway: A $\longrightarrow$ D $\longrightarrow$ C $\longrightarrow$ B $\longrightarrow$ A. The energy barrier for Cu diffusion along this direction moves from site A to site D with an activation barrier of 1.63 eV. The lowest barrier for diffusion moves along the [010] direction with a value of 0.99 eV, which would indicate that Cu diffusion along the (101) surface should be relatively slow.

Bibliography

[1] N. G. Limas and T. A. Manz, *RSC Adv.*, 2016, **6**, 45727–45747.

[2] T. A. Manz and D. S. Sholl, *J. Chem. Theory Comput.*, 2010, **6**, 2455–2468.

[3] D. Koch and S. Manzhos, *J. Phys. Chem. Letters*, 2017, **8**, 1593–1598.

[4] R. F. Bader, *Atoms in molecules: a quantum theory*, 1990.

[5] G. Henkelman, A. Arnaldsson and H. Jónsson, *Comput. Mater. Sci.*, 2006, **36**, 354–360.

[6] G. Kresse and J. Furthmüller, *Physical review. B, Condensed matter*, 1996, **54**, 11169–11186.

[7] G. Kresse and J. Furthmüller, *Computational Materials Science*, 1996, **6**, 15–50.

[8] T. Shimanouchi, *Natl. Bur. Stand.*, 1972.

[9] G. Ramis, G. Busca and V. Lorenzelli, *Mater. Chem. Phys.*, 1991, **29**, 425–435.

[10] L. Mino, G. Spoto and A. M. Ferrari, *J. Phys. Chem. C*, 2014, **118**, 25016–25026.

[11] H. Y. T. Chen, S. Tosoni and G. Pacchioni, *Surf. Sci.*, 2016, **652**, 163–171.

[12] D. C. Sorescu, W. A. Al-Saidi and K. D. Jordan, *J. Chem. Phys.*, 2011, **135**, 124701.

[13] G. Pacchioni, *J. Chem. Phys.*, 2008, **128**, 182505.

[14] M. Capdevila-Cortada, Z. Łodziana and N. López, *ACS Catal.*, 2016, **6**, 8370–8379.

[15] N. A. Deskins, R. Rousseau and M. Dupuis, *J. Phys. Chem. C*, 2010, **114**, 5891–5897.

[16] Y. G. Wang, Y. Yoon, V. A. Glezakou, J. Li and R. Rousseau, *J. Am. Chem. Soc.*, 2013, **135**, 10673–10683.

[17] J. C. Garcia and N. A. Deskins, *J. Phys. Chem. C*, 2012, **116**, 16573–16581.

[18] H. He, P. Zapol and L. a. Curtiss, *Energy Environ. Sci.*, 2012, **5**, 6196.

[19] Y. G. Wang, D. C. Cantu, M. S. Lee, J. Li, V. A. Glezakou and R. Rousseau, *J. Am. Chem. Soc.*, 2016, **138**, 10467–10476.

[20] Y. Wang, S. Lany, J. Ghanbaja, Y. Fagot-Revurat, Y. P. Chen, F. Soldera, D. Horwat, F. Mücklich and J. F. Pierson, *Phys. Rev. B*, 2016, **94**, 245418.

[21] M. Heinemann, B. Eifert and C. Heiliger, *Phys. Rev. B - Condensed Matter and Materials Physics*, 2013, **87**, 3–7.

[22] D. O. Scanlon, A. Walsh, B. J. Morgan, G. W. Watson, D. J. Payne and R. G. Egdell, *Phys. Rev. B - Condensed Matter and Materials Physics*, 2009, **79**, 1–7.

[23] N. Seriani, C. Pinilla and Y. Crespo, *J. Phys. Chem. C*, 2015, **119**, 6696–6702.

[24] Y. Yan, Y. Yu, S. Huang, Y. Yang, X. Yang, S. Yin and Y. Cao, *The Journal of Physical Chemistry C*, 2017, **121**, 1089–1098.

[25] D. B. Rorabacher, *Chemical Reviews*, 2004, **104**, 651–698.

Appendix B

Supporting Information - Quantifying Support Interactions and Reactivity Trends of Single Metal Atom Catalysts over TiO_2

B.1 Electronic properties of Cu and Zn group elements

The projected density of states (PDOS) of Cu and Zn group elements supported on TiO_2 are shown in Figure B.1. In order to understand why Cu was different from other Cu group elements, we examined the PDOS of Cu, Ag, and Au when they were not interacting with the TiO_2 surface, or the transition metal atom was 6 Å above the surface O_{2c} atom. This system mimics the lone atom and bare surface, while ensuring the orbitals share a common energy reference. The PDOS of the non-interacting systems are shown in Figure B.2. See

the main text for discussion on this.

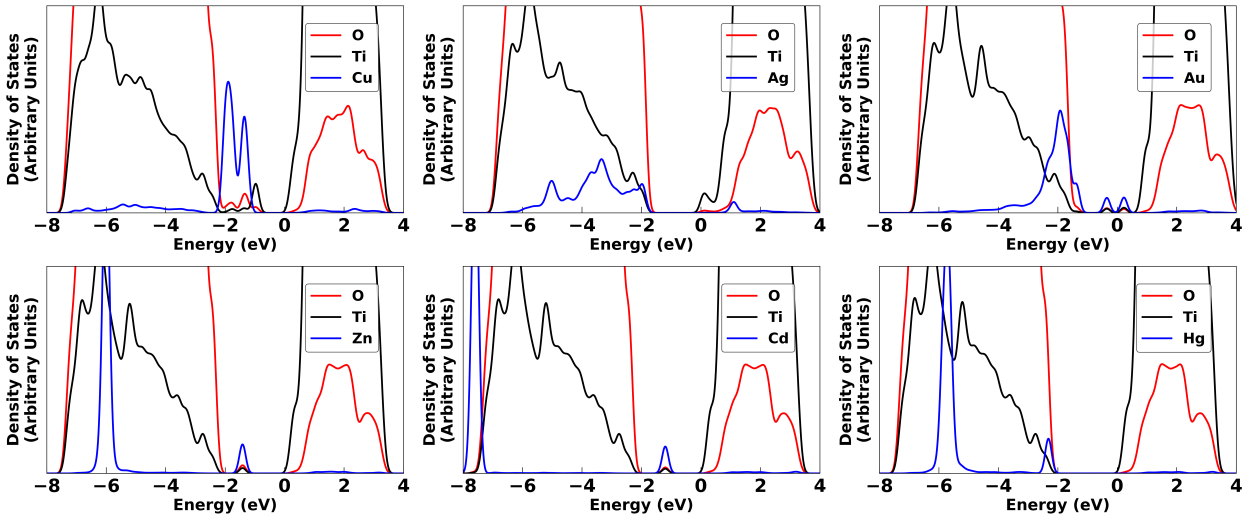

Figure B.1: Projected density of states (PDOS) of Cu group (upper panel) and Zn group (lower panel) transition metal atoms supported on TiO_2.

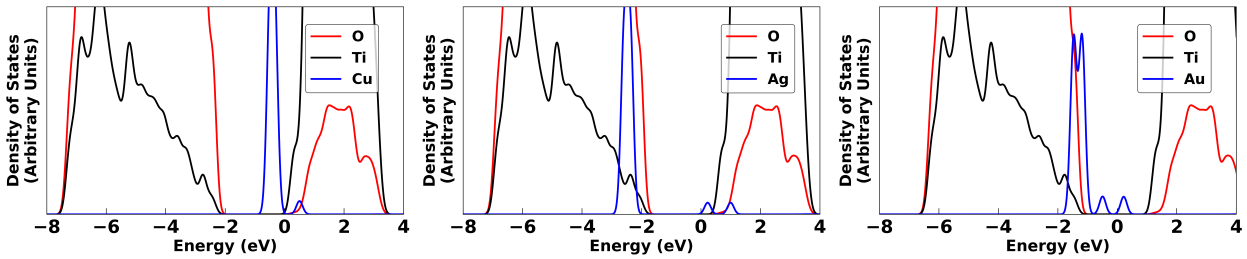

Figure B.2: Projected density of states (PDOS) of Cu group transition metal atoms 6 Å above the surface or not interacting with TiO_2. Zero eV is set at the conduction band minimum.

B.2 Transition metal adatom diffusion on TiO_2

In Figure B.3 we show that there is a correlation between the DFT-calculated diffusion barriers of metal adatoms on the anatase TiO_2 (101) surface for 8 transition metals (calculated

by Alghannam et al.[1]) and the adsorption energy difference between the two most stable adsorption sites of these adatoms as calculated by us. Alghannam et al.[1] studied three different surface diffusion pathways on the anatase (101) surface. Out of these three reported pathways, we show that both the largest and smallest diffusion barriers on the surface can be estimated from simple adsorption energy calculations of the two most stable adsorption sites. This provides a simple and computationally inexpensive approach to estimate diffusion barriers estimation compared to computationally intensive transition state finding methods.

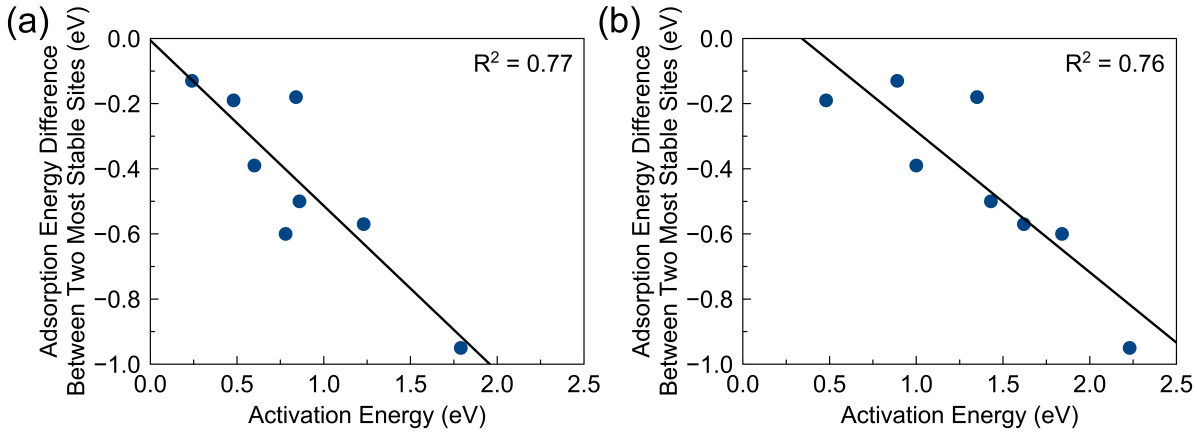

Figure B.3: Correlation between the energy difference of the two most stable adsorption sites and calculated diffusion barriers. Results are for eight transition metal adatoms on TiO_2. Shown are the (a) largest and (b) smallest barriers as calculated by Alghannam et al.[1]

B.3 Electronic properties of supported transition metals

Projected density of states for all transition metals are given in Figure B.4. The Bader charges of the transition metal atoms supported on TiO_2 are given in Figure B.5). The charges generally decreased with increasing atomic number. Linear fits of group number

compared to adsorption energy results in R^2 values of 0.85, 0.91, and 0.87 for Row 4, 5, and 6 transition metals, respectively.

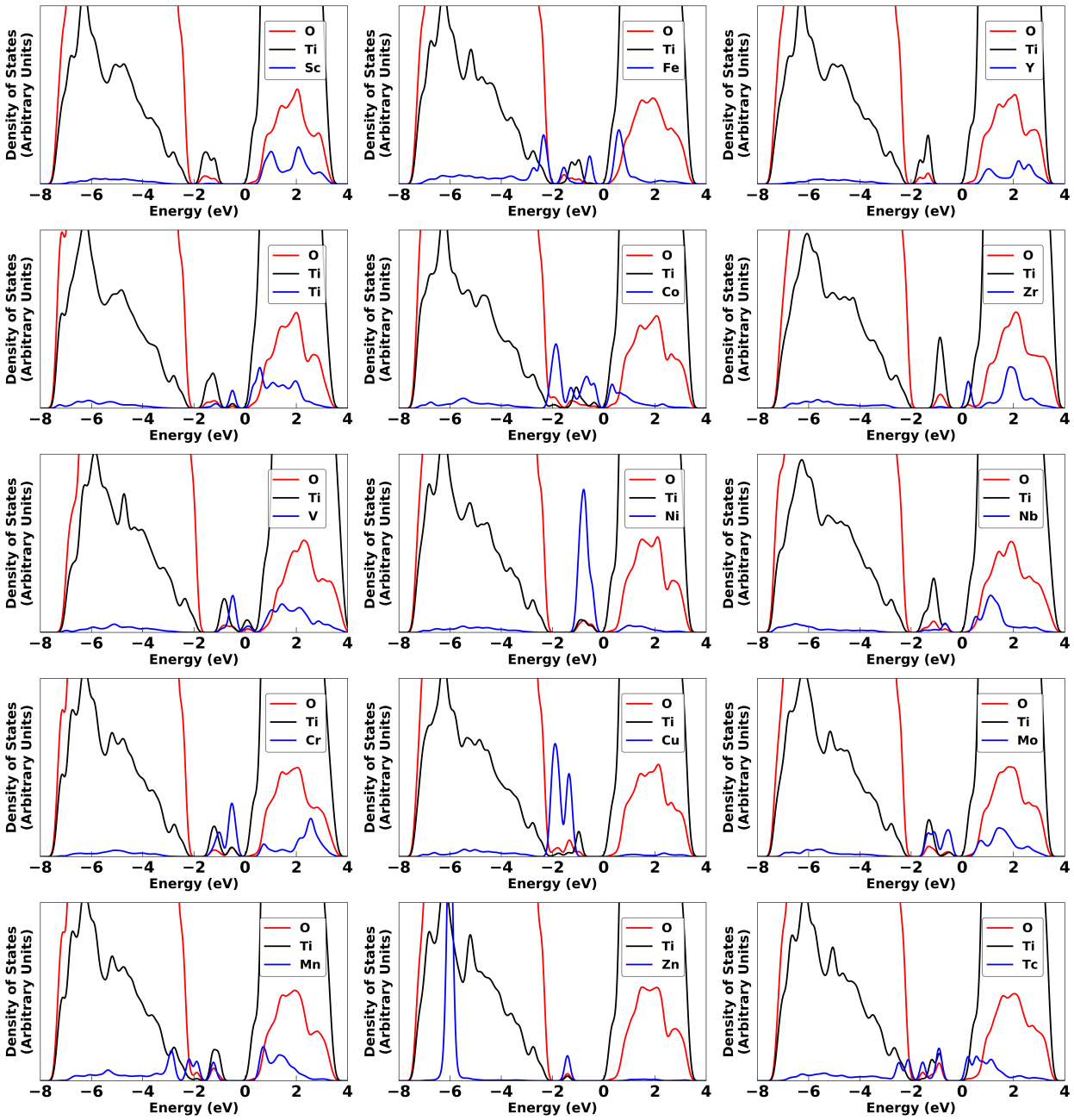

Figure B.4: Projected density of states of all 29 transition metal atom adsorbed on TiO_2. Zero eV is set at the conduction band minimum.

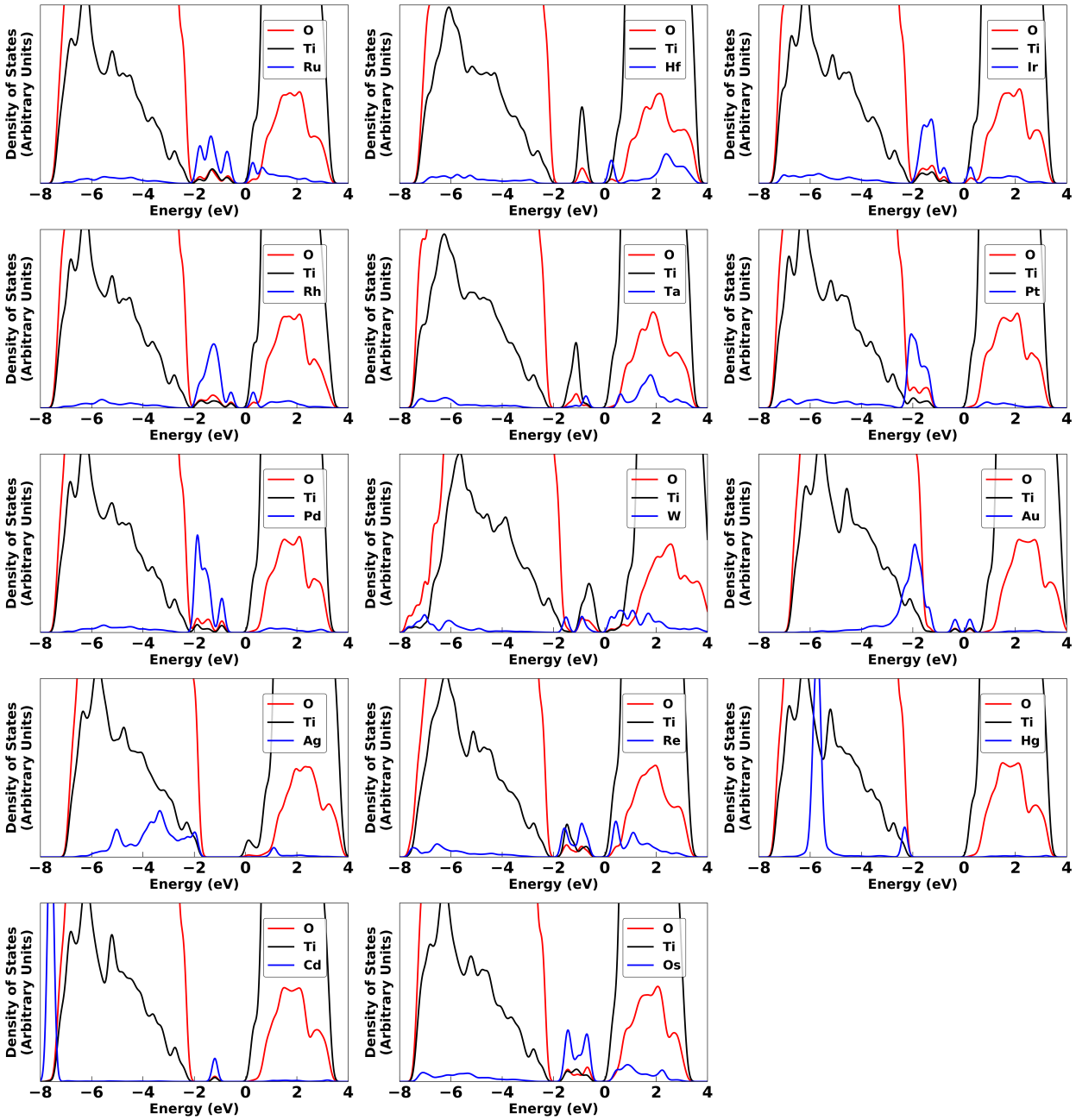

Figure B.4: Continued: Projected density of states of all 29 transition metal atom adsorbed on TiO_2. Zero eV is set at the conduction band minimum.

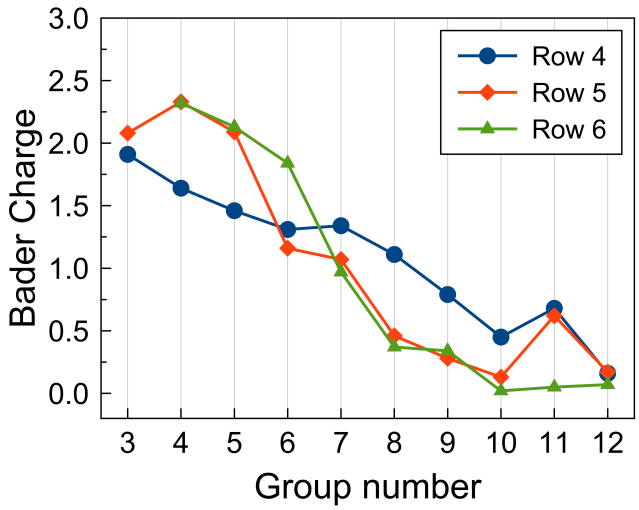

Figure B.5: Bader charges of transition metal atoms adsorbed on TiO_2.

B.4 Analyzing metal adsorption

In order to understand the transition metal adatom adsorption energy trends on TiO_2, we examined various descriptors of the transition metal atoms. A summary of these descriptors can be found in Table B.1. These descriptors include mostly tabulated values[2,3] and also DFT-derived properties like d-band center of the transition metal atom. We calculated two different d-band centers. The first was the d-band center of the combined transition metal atom adsorbed on TiO_2 (M/TiO_2) system and the other was d band center of only the adsorbed transition metal atom. In the latter case, since the transition metal atom primarily induced gap states, valence band or conduction band edge states within the energy limits of -4 to +2 eV, we computed the d-band center of M in M/TiO_2 within this energy range. Here, the energy was referenced to the Fermi energy ($E\text{-}E_{Fermi}$). This procedure was similar to that reported by Garcia-Mota et al.[4] A simple linear regression of metal atom adsorption energy against each of these descriptors were performed one at a time. The results shown in

Table B.2 clearly indicate that metal atom adsorption energies were strongly correlated with number of d electrons (which is closely related to group number), metal-oxygen dissociation energy, and d-band center of the adsorbed transition metal atom.

Table B.1: Various descriptors and their values used in the regression and in the Lasso shrinkage models for metal adsorption and CO_2 adsorption. References for the source of the data are given in the column headings.

Atomic Number	Van der Waals Radius[3] Å	Covalent Å Radius[3] Å	Electronegativity (Pauling Scale)[3]	Ionization Energy[3] (eV)	Electron Affinity[3] (eV)
21	2.15	1.59	1.36	6.56	0.188
22	2.11	1.48	1.54	6.83	0.079
23	2.07	1.44	1.63	6.75	0.525
24	2.06	1.3	1.66	6.77	0.666
25	2.05	1.29	1.55	7.43	-0.52
26	2.04	1.24	1.83	7.9	0.151
27	2	1.18	1.88	7.88	0.662
28	1.97	1.17	1.91	7.64	1.156
29	1.96	1.22	1.9	7.73	1.235
30	2.01	1.2	1.65	9.39	-0.63
39	2.32	1.76	1.22	6.22	0.307
40	2.23	1.64	1.33	6.63	0.426
41	2.18	1.56	1.6	6.76	0.893
42	2.17	1.46	2.16	7.09	0.748
43	2.16	1.38	2.1	7.28	0.55
44	2.1	1.34	2.2	7.36	1.05
45	2.1	1.34	2.28	7.46	1.137
46	2.1	1.3	2.2	8.34	0.562
47	2.11	1.36	1.93	7.58	1.302
48	2.18	1.4	1.69	8.99	-0.73
72	2.23	1.64	1.3	6.83	0.014
73	2.22	1.58	1.5	7.55	0.322
74	2.18	1.5	1.7	7.86	0.815
75	2.16	1.41	1.9	7.83	0.15
76	2.16	1.36	2.2	8.44	1.1
77	1.93	1.42	2.2	8.97	1.5638
78	2.13	1.3	2.2	8.96	2.128
79	2.14	1.3	2.4	9.23	2.30863
80	2.23	1.32	1.9	10.44	-0.52

Table B.1: Continued. Various descriptors and their values used in the Lasso shrinkage model and regression. M refers to the transition metal atom and M/TiO_2 refers to metal atom adsorbed on TiO_2.

Number of d electrons	Cohesive Energy[2] (eV)	M-O Dissociation Energy[3] (eV)	Polarizability[3] (10^{-24}cm^3)	d band center of M/TiO_2 (eV)	d band center of M in M/TiO_2 (eV)
1	3.9	6.96	14.4	-5.16	0.99
2	4.85	6.91	9.4	-5.13	0.74
3	5.31	6.53	10.1	-4.64	0.49
5	4.1	4.78	8.9	-4.89	-0.34
5	2.92	3.75	9.9	-5.02	-0.60
6	4.28	4.22	9.47	-4.94	-0.96
7	4.39	4.12	8.55	-4.78	-0.91
8	4.44	3.79	7.57	-4.61	-0.65
10	3.49	3.04	8.7	-4.69	-1.73
10	1.35	1.65	5.75	-5.49	-2.34
1	4.37	7.4	24.1	-5.16	0.74
2	6.25	7.94	16.6	-4.83	0.88
4	7.57	7.53	14.5	-5.02	0.74
5	6.82	5.2	12.9	-4.99	0.22
5	6.85	5.68	11.9	-4.89	-0.57
7	6.74	5.47	9.6	-4.90	-0.75
8	5.75	4.2	1.6	-4.84	-0.97
10	3.89	2.47	4.8	-4.82	-1.50
10	2.95	2.29	6.8	-4.65	-3.00
10	1.16	2.45	7.36	-5.80	-1.72
2	6.44	8.3	12.4	-4.87	0.00
3	8.1	8.7	8.6	-5.03	0.96
4	8.9	7.46	11.1	-4.48	0.35
5	8.03	6.5	9.05	-4.98	-0.10
6	8.17	5.96	8.5	-4.94	-0.55
7	6.94	4.25	7.6	-4.84	-1.05
9	5.84	4.34	6.5	-4.93	-1.68
10	3.81	2.31	4.13	-4.25	-2.04
10	0.67	2.79	5.08	-5.44	-2.22

Table B.2: Summary of linear regression models for predicting transition metal atom adsorption energies using various descriptors. R^2 values for models with the descriptors are given.

Descriptors	**R^2**
Atomic Number	0.01
van der Waals Radius	0.16
Covalent Radius	0.61
Electronegativity	0.42
Ionization Energy	0.55
Electron Affinity	0.01
Number of d electrons	0.84
Cohesive Energy	0.32
M-O Dissociation Energy	0.86

Table B.1: Continued. Various descriptors and their values in the Lasso shrinkage model and regression. M refers to the transition metal atom.

Group Number	Workfunction[5] (eV)	M atom adsorption energy (eV)	Bent CO_2 adsorption energy (eV)
3	3.5	-6.7	-1.72
4	3.96	-6.15	-2.32
5	4.3	-4.96	-1.61
6	4.5	-3.2	-0.71
7	4.1	-3.37	-1.03
8	4.5	-3.42	-0.63
9	4.92	-3.13	-0.86
10	5.15	-3.26	-0.97
11	4.65	-2.31	-0.44
12	4.33	-0.53	-1.06
3	3.1	-6.82	-1.56
4	4.05	-7.03	-1.68
5	4.3	-6.2	-2.21
6	4.6	-3.31	-2.11
7	4.82	-3.33	-1.32
8	4.71	-3.19	-1.74
9	4.98	-3.11	-1.04
10	5.12	-2.03	-0.9
11	4.26	-0.91	-0.87
12	4.22	-0.53	0.05
4	3.9	-7.64	-1.75
5	4.25	-7.41	-2.04
6	4.55	-4.74	-2.03
7	4.96	-3.16	-1.86
8	4.83	-3.33	-2
9	5.27	-3.62	-1.17
10	5.65	-3.26	-0.86
11	5.1	-0.86	-0.58
12	4.49	-0.41	-0.22

In the main text, we discuss a correlation between the metal atom adsorption energies and the bond dissociation energies of gas phase diatomic metal-oxygen molecules, which was found to be the best model. In the literature, adsorption energies of Row 4 transition metal atoms on the MgO(100) surface were reported to correlate with the cohesive energies of 3d metals.[6] However, we did not find a strong correlation ($R^2 = 0.32$) between metal adsorption energies and cohesive energies. This difference is potentially due to the chemically different nature of TiO_2 (a reducible oxide) and MgO (a non-reducible oxide). The oxygen atoms in MgO are almost fully reduced as O^{2-} anions with a minimal tendency of O to gain electrons from the adatom, while oxygen atoms in TiO_2 are not fully reduced with a larger tendency O to gain electrons from the adatom.[7]

B.5 Comparison of different DFT methods

Table B.3 shows all the adsorption energies of transition metal atoms adsorbed at Site A (see main text for this geometry) using four different levels of theory compared with PBE results.

Table B.3: Metal adsorption energies at the PBE level and difference in adsorption energies (compared to PBE) at three other levels of theory (PBE+U, PBE+D3, and PBE+D3+U). Also given are the average differences, standard deviations of the average differences, mean absolute differences (MAD), standard deviations of the absolute differences, and squared correlation coefficients compared to the PBE results.

	Adsorption Energy (eV)	**Difference in Adsorption Energy (eV)**		
Element name	**PBE**	**PBE+U**	**PBE+D3**	**PBE+D3+U**
Sc	-5.91	-0.25	-0.45	-0.79
Ti	-5.55	-0.23	-0.49	-0.60
V	-4.91	-0.01	0.06	-0.05
Cr	-2.62	-0.16	-0.41	-0.58
Mn	-2.61	-0.42	-0.45	-0.76
Fe	-2.87	-0.15	-0.34	-0.55
Co	-2.29	-0.58	-0.31	-0.84
Ni	-3.00	0.10	-0.37	-0.26
Cu	-1.88	-0.07	-0.40	-0.43
Zn	-0.11	-0.06	-0.34	-0.42
Y	-5.77	-0.72	-0.46	-1.05
Zr	-6.01	-0.64	-0.50	-1.02
Nb	-4.80	-0.88	-0.57	-1.40
Mo	-2.97	0.15	-0.31	-0.34
Tc	-3.39	0.72	0.20	0.06
Ru	-3.33	0.65	-0.01	0.14
Rh	-2.78	0.13	-0.47	-0.33
Pd	-1.57	0.00	-0.47	-0.46
Ag	-0.66	0.14	-0.42	-0.25
Cd	-0.10	-0.06	-0.36	-0.43
Hf	-6.62	-0.66	-0.46	-1.02
Ta	-5.98	-1.06	-0.48	-1.43
W	-4.10	-0.20	-0.45	-0.64
Re	-3.19	0.87	-0.52	0.03
Os	-3.73	0.81	-0.52	0.40
Ir	-3.24	0.11	-0.51	-0.38
Pt	-2.69	-0.07	-0.52	-0.57
Au	-0.34	-0.14	-0.36	-0.52
Hg	-0.07	-0.03	-0.30	-0.34
Avg. Diff.	–	-0.09	-0.38	-0.51
Avg. Diff. Std. Dev.	–	0.47	0.18	0.43
MAD	–	0.35	0.40	0.55
Abs. Diff. Std. Dev.	–	0.32	0.13	0.37
R^2	–	0.96	0.99	0.97

B.6 Further details on CO_2 adsorption

Figure B.6 shows the different sites we modeled for linear CO_2, and Figure B.7 provides the adsorption energies for linear CO_2 at these sites. We found that the L1 adsorption geometry of CO_2, where O_{CO_2} was bound to a Ti_{5c} atom, was a stable configuration for all transition metals. The L1 site also resembled the most stable adsorption site of linear CO_2 on the TiO_2 anatase (101) surface.[8] For most of the metals (except Ti, Cr, Mn, Zr, Ru, and Hf), the L1 site had the strongest adsorption energies. The average L1 adsorption energy over all M/TiO_2 surfaces was -0.54 eV. On the TiO_2 anatase(101) surface the linear CO_2 adsorption energy was -0.40 eV[8]). We also found two other linear CO_2 adsorption configurations with O_{CO_2} bound directly to the metal adatom. Linear CO_2 adsorbing in the L2 and L3 configurations was only slightly ($\leq$ 0.15 eV) more stable than the L1 site for select metals (Ti, Cr, Mn, Zr, Ru, and Hf). These results indicate that in general the metal adatoms do not increase linear CO_2 binding.

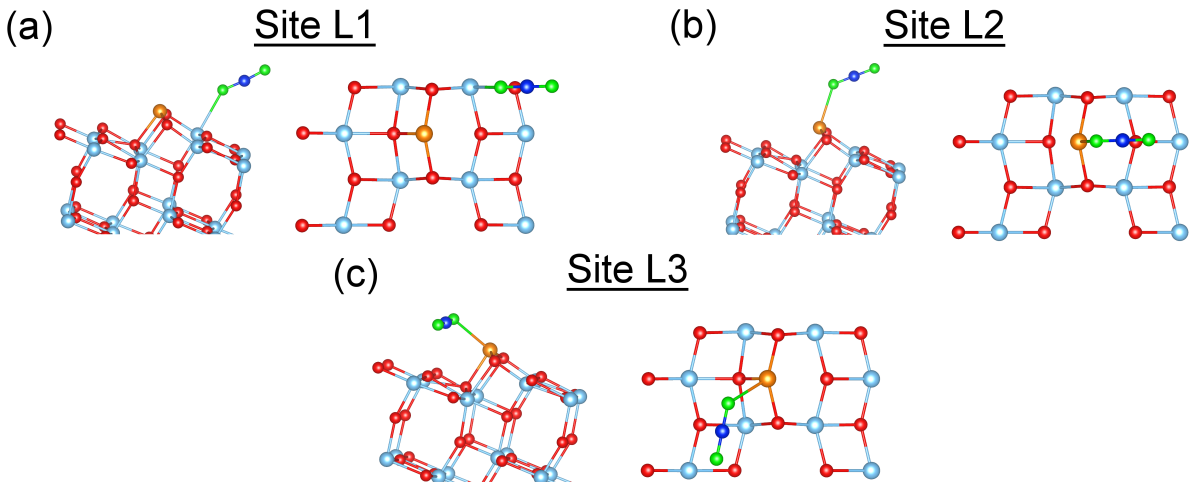

Figure B.6: Stable adsorption geometries for linear CO_2 over M/TiO_2 surfaces.

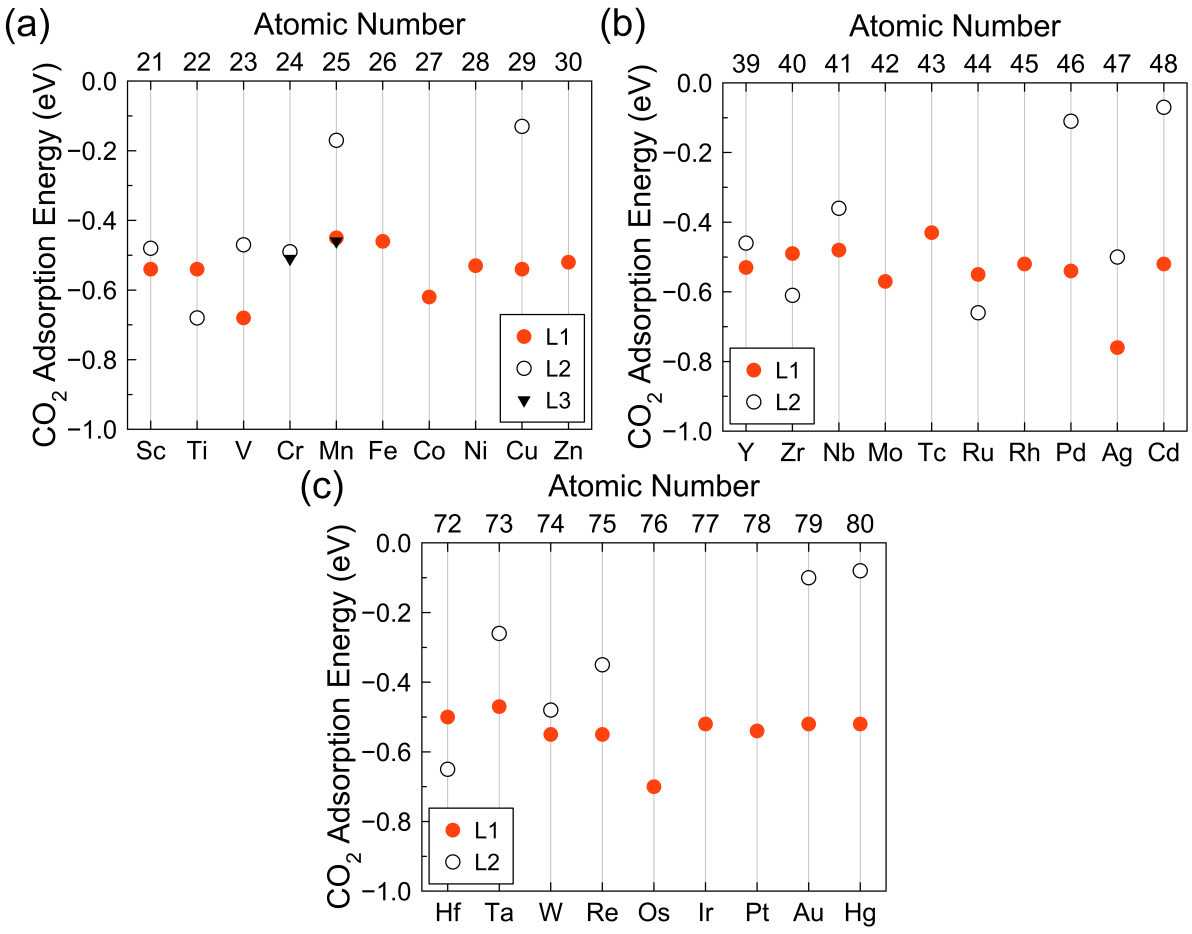

Figure B.7: Stable adsorption energies for linear CO_2 over M/TiO_2 surfaces.

In the case of bent CO_2 adsorption we modeled several geometries, including at the interface between metal adatom and TiO_2 surface, on top of the metal adatom (bent CO_2 only interacting with metal adatom), and on TiO_2 surface (bent CO_2 only interacting with TiO_2 surface atoms). We show stable adsorption sites for bent CO_2 in Figure B.8 and the corresponding adsorption energies in Figure B.9. We found that not all adsorption configurations were stable for every metal. For instance, site B4 was not stable for the late transition metals, and sites B3, B5, and B7 were stable for only select metals. On the other hand sites B1 and B2 were stable for most of the transition metals. For all the transition

metals (except Ni, Re, Ir, Pt, Au, and Hg) either B1 or B2 sites were the most stable adsorption sites. On Ni, Ir, Pt (late transition metals), B3 was the most stable adsorption site. On Re and Au, site B5 was the most stable configuration. In the case of Hg, we found the most stable adsorption configuration to be similar to B1 but without any direct interaction between Hg and CO_2 (the Hg-O_{CO_2} distance was 4.50 Å). This configuration is denoted as B6. The adsorption energy of this configuration was -0.22 eV. Another site which interacted with only TiO2 was site B7 that consisted of C-O_{2c} and O_{CO_2}-Ti_{5c} interaction. Both B6 and B7 (except Hg) were always less stable than the most stable bent CO2 adsorption configuration. We also modeled bent CO_2 interacting directly only with the metal adatom. For the row 4 transition metals, this adsorption configuration was stable only for V and Co but they were less stable (adsorption energy was -0.87 and -0.41 eV) than the most stable configurations (site B2 and B1 in Figure B.9a). Since both V and Co resulted in less stable adsorption energies, we did not model bent CO_2 interacting only with the metal atoms from row 5 and 6.

Adsorption energies ranged from very strong (-2.32 eV for Ti at site B2), to very weak (+0.05 eV for Cd at site B2). We note that for comparison the most stable bent CO_2 adsorption energy over pure TiO_2 was found to be -0.15 eV.[8] In contrast, linear adsorption energies of CO_2 were in the range of -0.43 and -0.76 eV as Figure B.7 shows. These values were close to the most stable linear CO_2 adsorption on pure TiO_2 (adsorption energy of -0.40 eV[8]). Comparison of the linear and bent CO_2 adsorption energies shows that bent CO_2 is stabilized compared to linear CO_2 on most of the transition metal adatoms. Thus, compared to pure TiO_2, most of the transition metal adatoms stabilize activated CO_2. Our results for the most stable B2 configuration of bent CO_2 on Rh, Ru, Pt, and Pd/TiO_2 are consistent with the most stable geometry reported by Ma et al.,[9] except for Pt/TiO_2. On Pt/TiO_2, we find the B3 structure to be 0.16 eV more stable than the B2 structure, which was assumed to be the most stable site by Ma et al. Their bent CO_2 adsorption energies

were -0.54 eV (Rh), -0.90 eV (Ru), -0.17 eV (Pt), -0.53 eV (Pd) eV. Our adsorption energies for these species are more negative, which is most likely due to the inclusion of dispersion corrections in our work. The trends between these different metals is similar in our work and the work of Ma et al. Our bent CO_2 adsorption energies were -1.04 eV (Rh), -1.74 eV (Ru), -0.86 eV (Pt), and -0.90 eV (Rh).

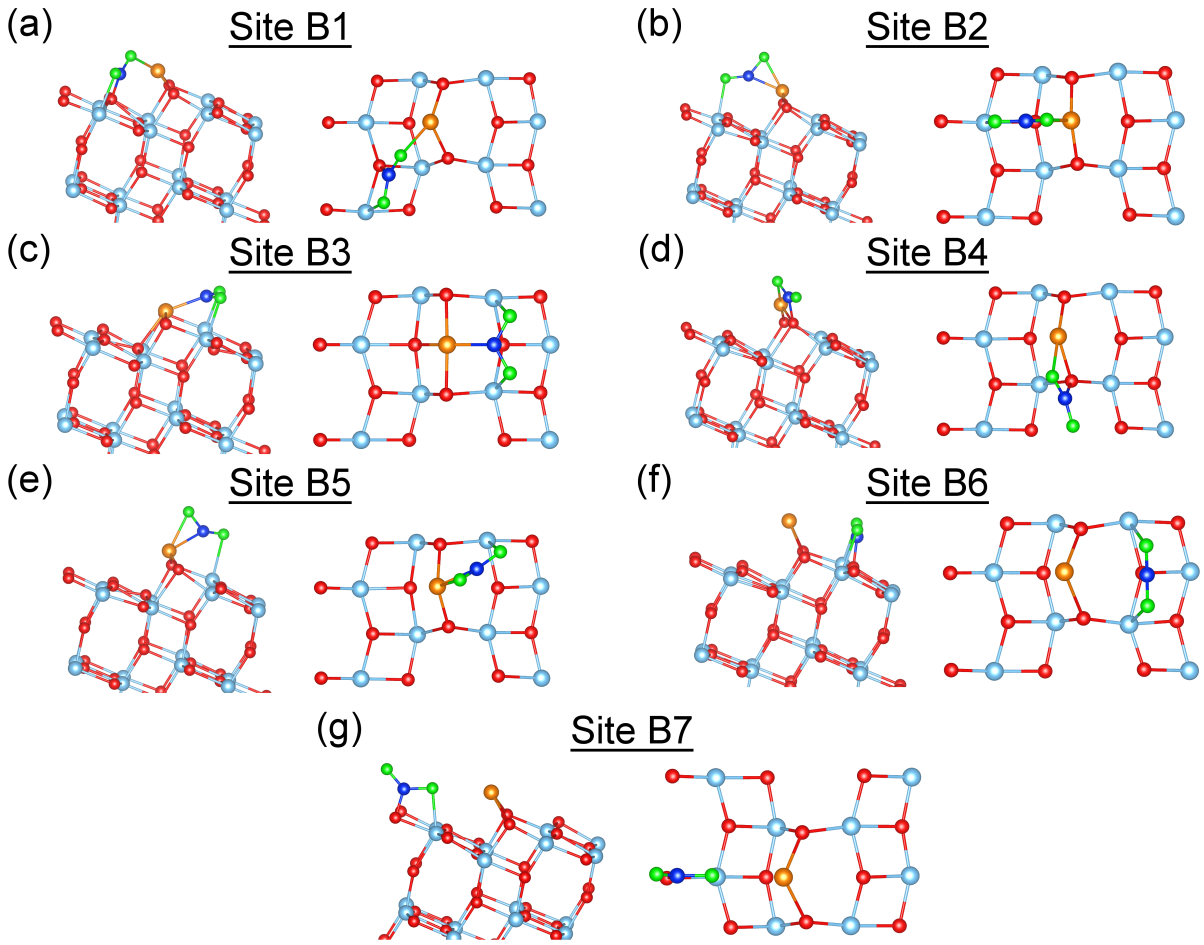

Figure B.8: Stable adsorption geometries for bent CO_2 over M/TiO_2 surfaces.

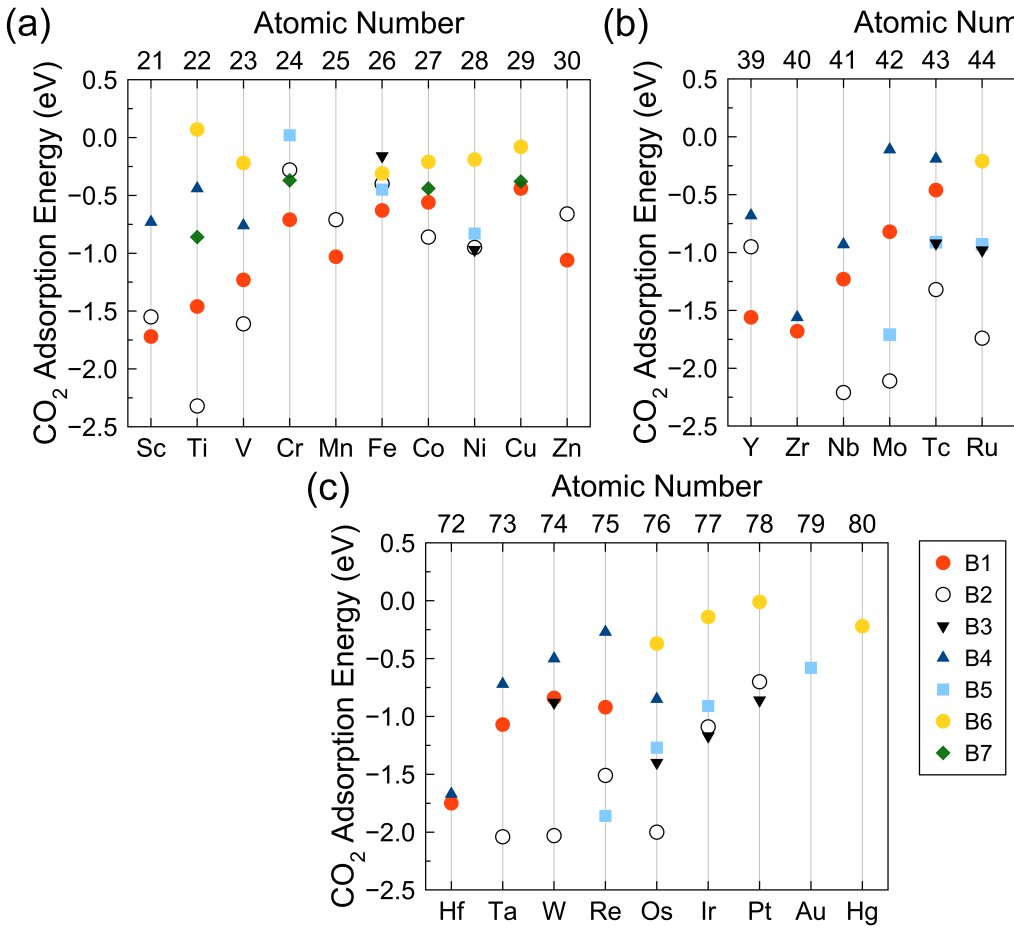

Figure B.9: Adsorption energies for bent CO_2 over M/TiO_2 surfaces of row 4 (a), row 5 (b), and row 6 (c) transition metal atoms.

In Figure B.10 we show the Bader charges of linear and bent CO_2. There is negligible charge transfer in the case of linear CO_2 adsorption. Bent CO_2 were always negatively charged. However, when bent CO_2 forms on the surface two types of CO_2 charges exist. One type of bent CO_2 gained 0.19 to 0.26 e^-. The other type of bent CO_2 gained a larger number of electrons in the range of 0.43 (Au) to 1.02 (Ta) e^-. These two types of CO_2 are directly related to the interactions of bent CO_2 with the transition metal adatom. In the first case with less negative charge, CO_2 is in the B1 configuration, where no interaction

between C and transition metal adatom occurs. The second type of bent CO_2, however, occurred with the C atom directly interacting with the transition metal adatom (B2-B5), and the electron transfer to the CO_2 was much larger.

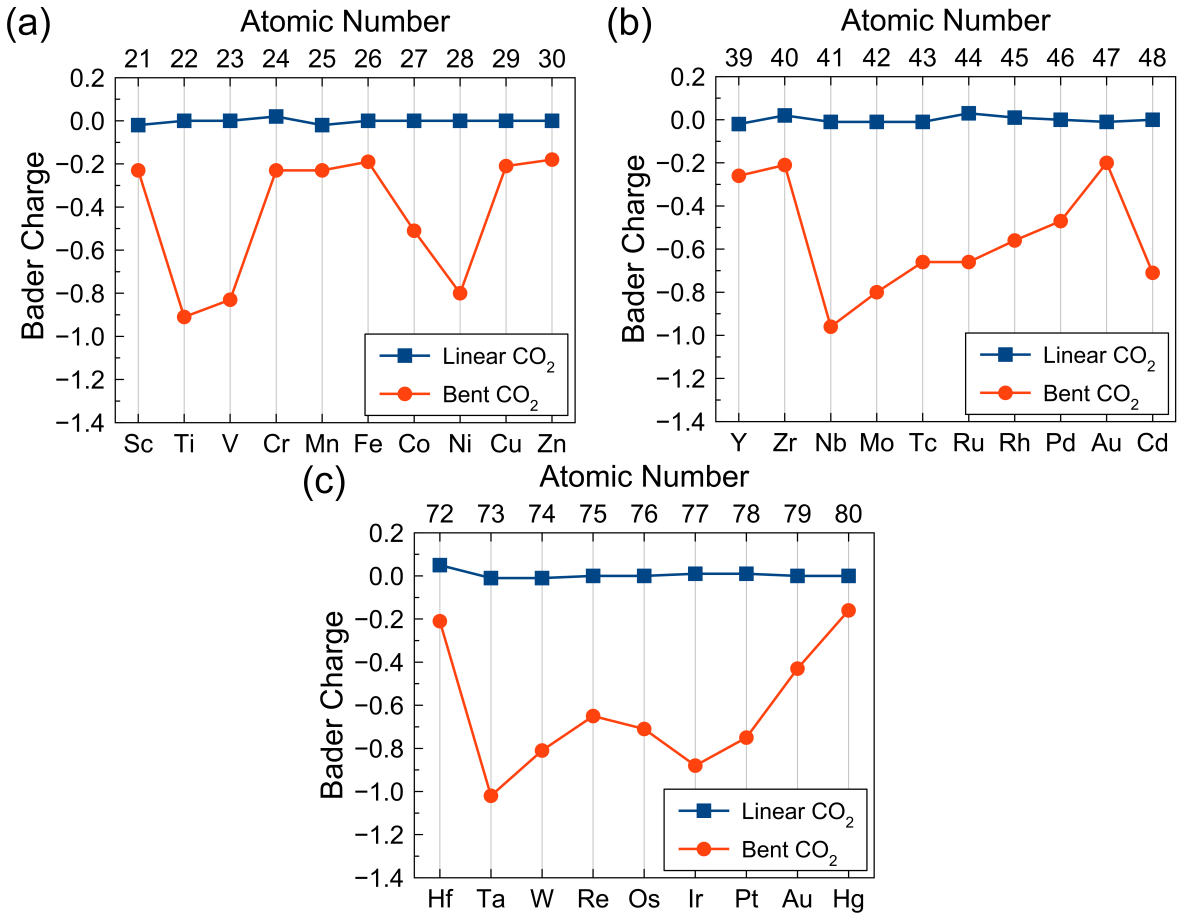

Figure B.10: Bader charge (number of electrons) of bent and linear CO_2 adsorbed over various transition metals in row 4 (a), row 5 (b), and row 6 (c) adsorbed on TiO_2. Shown are results for the most stable CO_2 geometries.

B.7 Analyzing CO_2 adsorption

As mentioned in the main text, we used linear regression and Lasso[10] for understanding and predicting the bent CO_2 adsorption energies. Table B.1 shows all the tabulated and DFT-derived predictors used in analysis. A summary of the different linear regression models using one independent descriptor is found in Table B.4. In Lasso regression, the coefficients of the fitted model are found by minimizing the function $\mathrm{RSS} + \lambda \sum_{\mathrm{i}}^{\mathrm{p}} \beta_{\mathrm{i}}$, where RSS is the residual sum of squares, the second term is the shrinkage penalty, λ is the tunable parameter, β is the coefficient of each descriptor, and p is the number of descriptors.[11] The value of λ was chosen by cross validation comparison. Due to the small dataset, we used leave-one-out cross validation (LOOCV) as the resampling method to fit our dataset containing 29 samples (or transition metal atoms). In this approach n-1 samples are used to train the model and this model is used to predict the one excluded sample. This process is repeated n times (yielding n models) to predict n different samples. From n different predictions, we obtain an overall model performance as the average mean squared error ($1/\mathrm{n} \sum_{\mathrm{i}}^{\mathrm{n}} \mathrm{MSE_i}$). The λ value was chosen based on the smallest average MSE. Note that all the data for the descriptors were standardized (zero mean and unit standard deviation) before Lasso and regression analysis.

Corresponding to this optimum λ value, we found the significant descriptors based on their non-zero coefficients (β). Larger values of β indicate more important descriptors in predicting the bent CO_2 adsorption energies. The important descriptors were found to be cohesive energy, group number, d-band center of the combined M/TiO_2 system, d-band center of lone adsorbed metal atom, and workfunction of transition metal atoms. Using these 5 descriptors the adjusted R^2 was 0.78. Using five descriptors with only 29 samples could suffer from overfitting. We thus searched for the minimum number of descriptors that could explain the data well. We found that a multiple linear regression model using cohesive energy and workfunction (the best combination of these five descriptors) resulted

in an adjusted R^2 of 0.76.

Table B.4: Summary of linear regression models with one descriptor compared to the bent CO_2 adsorption energies. R^2 values for the linear regression of various descriptors compared to the adsorption energy of bent CO_2 on M/TiO_2.

Descriptors	$\mathbf{R^2}$
Atomic Number	0.00
van der Waals Radius	0.13
Covalent Radius	0.38
Electronegativity	0.08
Ionization Energy	0.34
Electron Affinity	0.00
Number of d electrons	0.56
Cohesive Energy	0.58
M-O Dissociation Energy	0.67
Polarizability	0.24
d band center of M/TiO_2	0.02
d band center of M in M/TiO_2	0.61
Group Number	0.59
Workfunction	0.08
Metal Atom Adsorption Energy	0.53

B.8 Post Transition Metal Atoms

The adsorption energies of post transition metal atoms are shown in Figure B.11 for various stable adsorption configurations. Bader charges of the site A adsorption of post transition metal atoms are shown in Figure B.12. As described in the main text, out of the several

descriptors we tested (Table B.5), we found the best set of descriptors using Lasso to describe metal adsorption energy at the most stable adsorption site (site A) were the M-O dissociation energies and group number.

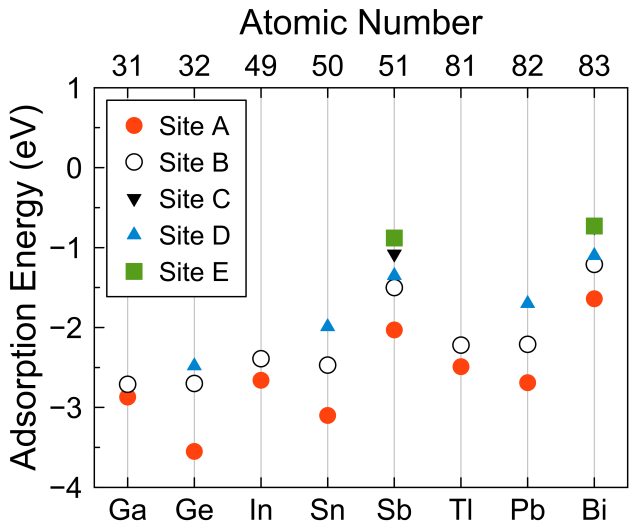

Figure B.11: Adsorption energies of post transition metal atoms adsorbed on TiO_2. Different stable adsorption configurations are labeled. Refer to the main text for the geometries.

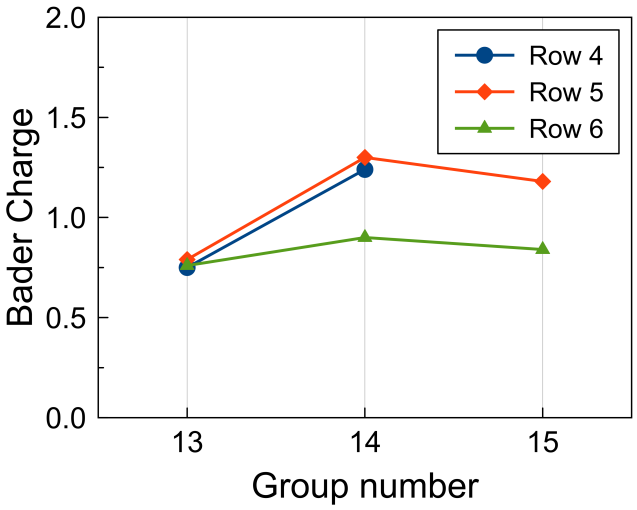

Figure B.12: Bader charges (in e^-) of post transition metals with site A adsorption configurations.

Figure B.13, shows the adsorption energies of the most stable linear and bent CO_2 configurations on TiO_2-supported post transition metal adatom. For the case of bent CO_2, we report the stable adsorption configurations of bent CO_2 in Figure B.14. Adsorption configurations of Site B1-B7 were shown in Figure B.8. The Bader charges of CO_2 in their most stable adsorption configurations are presented in Figure B.15. A summary of linear regression using various descriptors against the bent CO_2 adsorption energies is shown in Table B.6.

Table B.5: Various descriptors and their values used in the regression and in the Lasso shrinkage models for post transition metal atom adsorption. References for the source of the data are given in the column headings.

Atomic Number	van der Waals Radius[3] (Å)	Covalent Å Radius[3] (Å)	Electronegativity (Pauling Scale)[3]	Ionization Energy[3] (eV)	Electron Affinity[3] (eV)
31	1.87	1.23	1.81	6	0.43
32	2.11	1.2	2.01	7.9	1.232712
49	1.93	1.42	1.78	5.79	0.3
50	2.17	1.4	1.96	7.34	1.112067
51	2.06	1.4	2.05	8.61	1.046
81	1.96	1.44	1.8	6.11	0.2
82	2.02	1.45	1.8	7.42	0.364
83	2.07	1.50	1.90	7.29	0.946

Atomic Number	Cohesive Energy[2] (eV)	M-O Dissociation Energy[3] (eV)	Polarizability[3] (10^{-24}cm^3)	Group Number	Workfunction (eV)
31	2.81	3.88	8.12	13	4.2
32	3.85	6.81	5.84	14	5
49	2.52	3.59	10.2	13	4.12
50	3.14	5.47	7.84	14	4.3
51	2.75	4.5	6.6	15	4.55
81	1.88	2.21	7.6	13	3.84
82	2.03	3.96	6.98	14	4.25
83	2.18	3.49	7.4	15	4.22

Atomic Number	Adsorption Energy (eV)
31	-2.87
32	-3.55
49	-2.66
50	-3.10
51	-2.03
81	-2.49
82	-2.69
83	-1.64

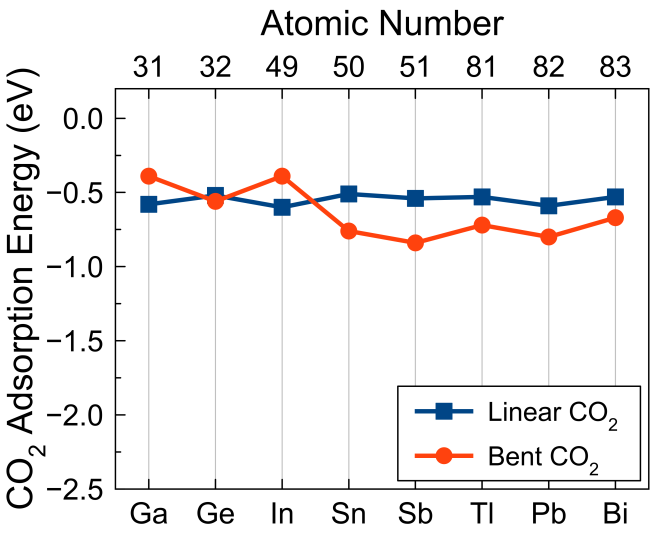

Figure B.13: Most stable bent and linear CO_2 adsorption energy on TiO_2 supported post-transition metal atoms.

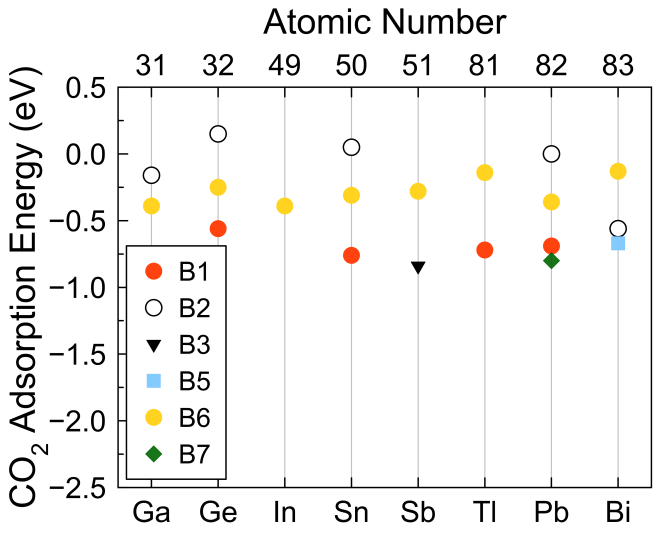

Figure B.14: The stable adsorption energies of different bent CO_2 adsorption configurations on post-transition metal atoms on TiO_2.

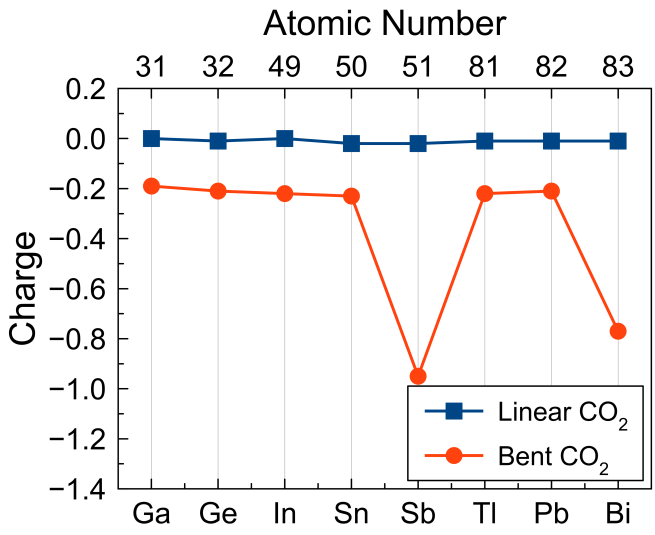

Figure B.15: Bader charges (in e^-) of the most stable linear and bent CO_2 adsorption sites on post-transition metal atoms on TiO_2.

Table B.6: Linear regression using various descriptors to estimate the bent CO_2 adsorption energies on TiO_2 supported post-transition metal atoms.

	$\mathbf{R}^2$
Atomic Number	0.32
van der Waals Radius	0.38
Covalent Radius	0.26
Electronegativity	0.19
Ionization Energy	0.47
Electron Affinity	0.09
Cohesive Energy	0.06
M-O Dissociation Energy	0.00
Polarizability	0.33
Group Number	0.40
Workfunction	0.00
Metal Atom Adsorption Energy	0.10

Bibliography

[1] A. Alghannam, C. L. Muhich and C. Musgrave, *Phys. Chem. Chem. Phys.*, 2017, **19**, 4541–4552.

[2] C. Kittel, *Introduction to Solid State Physics*, Wiley: New York, 1996.

[3] *CRC Handbook of Chemistry and Physics*, ed. J. R. Rumble, CRC Press/Taylor & Francis, Boca Raton, FL., 98th edn., 2017.

[4] M. García-Mota, A. Vojvodic, F. Abild-Pedersen and J. K. Nørskov, *J. Phys. Chem. C*, 2013, **117**, 460–465.

[5] T. J. Drummond, https://www.osti.gov/biblio/3597.

[6] S. Fernandez, A. Markovits, F. Fuster and C. Minot, *J. Phys. Chem. C*, 2007, **111**, 6781–6788.

[7] G. Pacchioni, *Phys. Chem. Chem. Phys.*, 2013, **15**, 1737–57.

[8] S. K. Iyemperumal and N. A. Deskins, *Phys. Chem. Chem. Phys.*, 2017, **19**, 28788–28807.

[9] S. Ma, W. Song, B. Liu, H. Zheng, J. Deng, W. Zhong, J. Liu, X.-Q. Gong and Z. Zhao, *Catal. Sci. Technol.*, 2016, **6**, 6128–6136.

[10] R. Tibshirani, *J. R. Stat. Soc.: Ser. B*, 1996, **58**, 267–288.

[11] G. James, D. Witten, T. Hastie and R. Tibshirani, *An Introduction to Statistical Learning: with Applications in R*, Springer New York, 2014.

Appendix C

Supporting Information - The Fate of Supported Atomic-Size Catalysts in Reactive Environments

C.1 Surface Slab of TiO2 Anatase (101)

The anatase (101) surface slab used in the work with six layers thick is shown in Figure C.1.

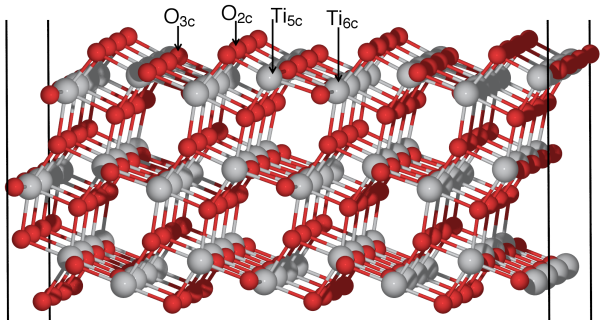

Figure C.1: The anatase(101) surface slab used in the present work. The undercoordinated atoms on the surface are labelled as O_{2c}, O_{3c}, Ti_{5c}, and Ti_{6c}, where nc refers to n coordinations. Gray and red spheres represent Ti and O atoms.

C.2 Gas Phase Cu Clusters

A genetic algorithm as implemented within the atomistic simulation environment (ASE) package[1] was used to help identify stable cluster geometries. We performed a geometry search using a two step process similar to previous work.[2] We first used a genetic algorithm with DFT using small basis sets (3-21G for oxygen and LANL2DZ for metal atoms) to determine top stable geometries, followed by an accurate basis set optimization (MOLOPT double ζ basis sets) of these most stable geometries. The first step involving the genetic algorithm was performed using NWChem[3] since it readily works with the ASE package. We used CP2K to determine final Cu cluster geometries in the second step. In this second step, we chose the geometries within 1 eV of the most stable structure identified in step 1, and optimized them again using CP2K at the level of theory discussed in the Methodology section in the main text.

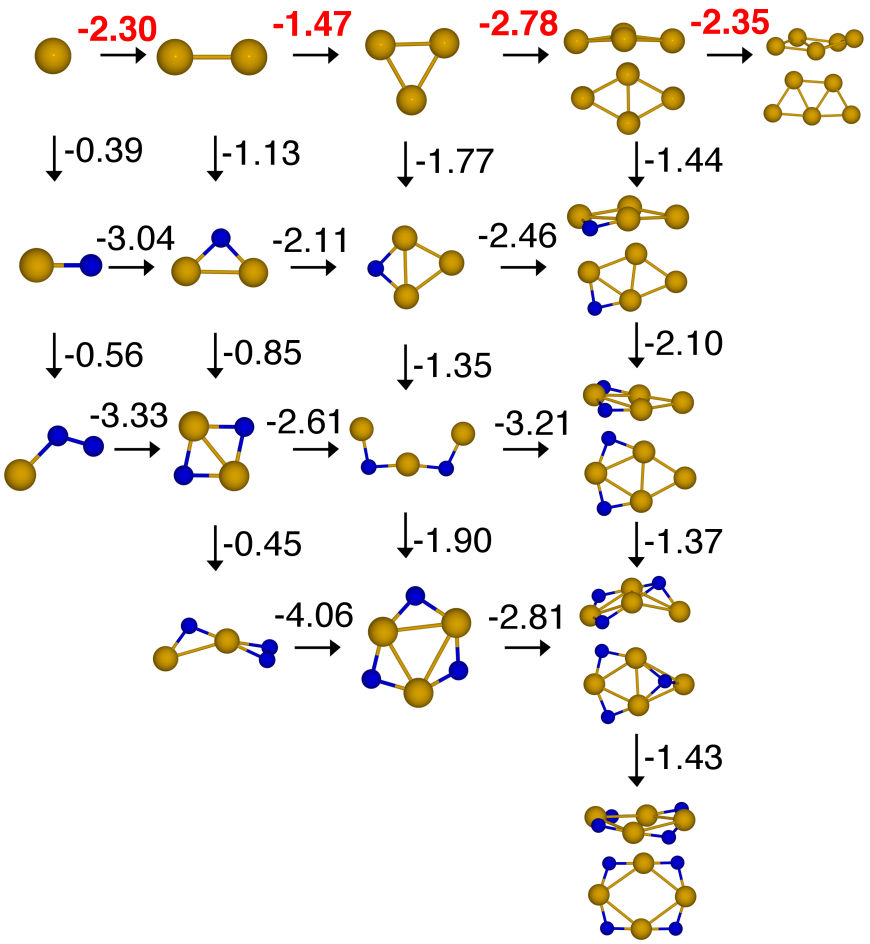

Figure C.2: Reaction pathways for formation of Cu_x/Cu_xO_y clusters in the gas phase. The numbers indicate reaction energies for each reaction step (in eV). A horizontal reaction is Cu addition, while vertical reactions are O addition (from 1/2 O_2 molecule). Numbers in red show the most favorable pathway. Cu and O atoms are represented in yellow and blue spheres respectively.

Our calculated geometries are consistent with reported stable Cu_xO_y geometries.[4–10] For metallic clusters up to 5 Cu atoms, our most stable planar geometries are similar to those reported by Jiang et al.[8] Small clusters such as CuO_2 and Cu_2O, are similar to geometries reported earlier.[4,10] For CuO, Cu_2O_2, Cu_2O_3, Cu_3O_2 and Cu_3O_3 geometries, our most

stable geometries were similar to those reported by Bae,[7] while for Cu_3O, our most stable planar geometry was 0.02 eV more stable than the pyramidal geometry reported by Bae. This difference may be due to their use of different basis set (LANL2DZ for both Cu and O) and exchange correlation functional (B3LYP). Our Cu_4O_2 structure was also consistent with Trinchero et al.[11] where O atoms prefer the adjacent edges of Cu_4 unit of Cu_4O_2 geometry. In the case of Cu_4O_4, we found a ring-like structure to be the most stable geometry unlike the three dimensional structure reported by Bae et al.[6] Our ring-like structure of Cu_4O_4 cluster consisted of alternating Cu-O-Cu bonds. Bae et al. reported their Cu_4O_4 to consist of a planar Cu_2O_4 unit with the extra two Cu atoms above and below the plane of Cu_2O_4. Our most stable structure was 1.31 eV more stable than the structure of Bae et al. Our test calculations showed that the difference in the two geometries was primarily due to the use of different exchange correlation functionals. When using B3LYP functional these two geometries became closer in energy (a difference of 0.21 eV). A ring-like Cu_4O_4 cluster was also reported earlier by Jin et al.[12]

Figure C.2 shows the reaction pathways for Cu aggregation/oxidation in the gas phase. We calculated the formation energy of gas phase Cu oxide clusters as shown in Figure C.3. The definition of formation energy of Cu oxide clusters and further discussion is presented in main text.

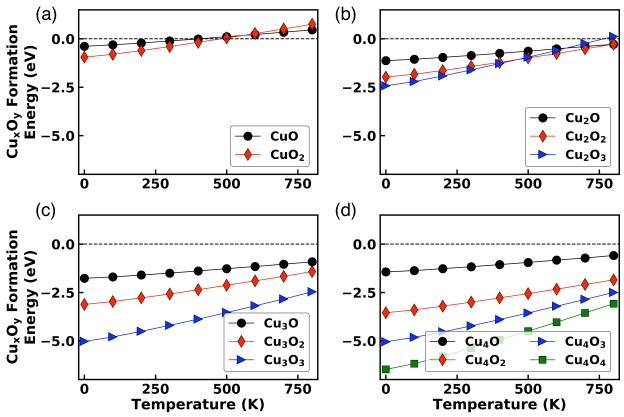

Figure C.3: Formation energies of oxidized gas phase Cu clusters in the presence of gas phase O_2 as a function of temperature.

C.3 Gas Phase Pt Clusters

For clusters with four or more atoms we searched for the most stable geometries using a genetic algorithm. For smaller clusters, we manually created initial configurations, as the configurational space was relatively small for these small clusters. The most stable geometries of Pt oxide clusters are shown in Figure C.4. The cluster geometries of PtO_2, Pt_2O, Pt_3O, and Pt_2O_2 were similar to the geometries reported by Xu et al.[13] In other cases (Pt_3O_2 and Pt_3O_3), we found our geometries to be more stable than those reported by Xu et al. The reaction energies of Pt aggregation and oxidation steps were calculated to find the preferred growth pathway. The corresponding most stable Pt oxide cluster geometries are also shown in Figure C.4. We discuss the results in the main text.

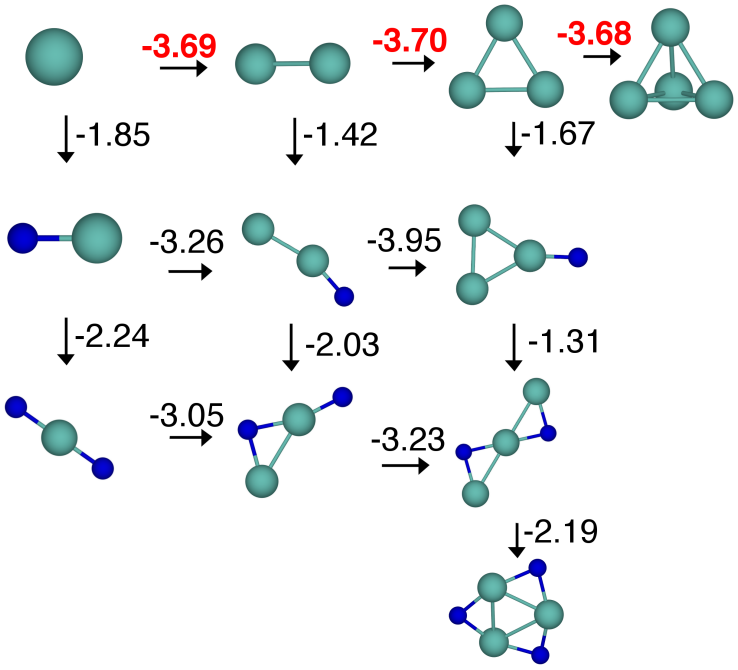

Figure C.4: Reaction pathways for formation of Pt_x/Pt_xO_y clusters in the gas phase. The numbers indicate reaction energies for each reaction step (in eV). A horizontal reaction is Cu addition, while vertical reactions are O addition (from 1/2 O_2 molecule). Numbers in red show the most favorable pathway. Pt and O atoms in Pt_xO_y are shown as turquoise and blue spheres respectively.

C.4 Adsorption of M_xO_y clusters on TiO_2

The adsorption energies of all the metal oxide clusters we studied in this work are given in Table C.1.

Bibliography

[1] L. B. Vilhelmsen and B. Hammer, *The Journal of Chemical Physics*, 2014, **141**, 044711.

Table C.1: Adsorption energies of M_xO_y clusters on TiO_2.

Cu_xO_y	**ΔE_{ads} (eV)**	**Pt_xO_y**	**ΔE_{ads} (eV)**	**MO_y (y=1,2)**	**ΔE_{ads} (eV)**
Cu	-2.56	Pt	-3.42	Co	-4.25
CuO	-3.87	PtO	-2.11	CoO	-4.40
CuO_2	-3.04	PtO_2	-1.14	CoO_2	-2.72
Cu_2	-1.89	Pt_2	-3.59	Rh	-2.92
Cu_2O	-4.40	Pt_2O	-3.05	RhO	-2.71
Cu_2O_2	-4.68	Pt_2O_2	-3.02	RhO_2	-2.16
Cu_2O_3	-3.43	Pt_3	-4.14	Ir	-4.39
Cu_3	-3.95	Pt_3O	-3.81	IrO	-3.74
Cu_3O	-4.94	Pt_3O_2	-4.86	IrO_2	-1.95
Cu_3O_2	-5.68	Pt_3O_3	-3.06	Ni	-3.78
Cu_3O_3	-4.63			NiO	-3.95
Cu_4	-4.12			NiO_2	-2.44
Cu_4O	-4.97			Pd	-1.91
Cu_4O_2	-3.71			PdO	-2.99
Cu_4O_3	-4.98			PdO_2	-2.50
Cu_4O_4	-3.55			Ag	-1.52
				AgO	-2.82
				AgO_2	-2.15
				Au	-0.73
				AuO	-2.25
				AuO_2	-1.75

[2] S. Schafer, B. Assadollahzadeh, M. Mehring, P. Schwerdtfeger and R. Schafer, *The Journal of Physical Chemistry A*, 2008, **112**, 12312–12319.

[3] M. Valiev, E. J. Bylaska, N. Govind, K. Kowalski, T. P. Straatsma, H. J. J. Van Dam, D. Wang, J. Nieplocha, E. Apra, T. L. Windus and W. a. De Jong, *Computer Physics Communications*, 2010, **181**, 1477–1489.

[4] Y. Pouillon, C. Massobrio and M. Celino, *Computational Materials Science*, 2000, **17**, 539–543.

[5] Y. Gong, M. Zhou and L. Andrews, *Chemical Reviews*, 2009, **109**, 6765–6808.

[6] G. T. Bae, B. Dellinger and R. W. Hall, *Journal of Physical Chemistry A*, 2011, **115**, 2087–2095.

[7] G.-T. Bae, *Bulletin of the Korean Chemical Society*, 2016, **37**, 638–642.

[8] M. Jiang, Q. Zeng, T. Zhang, M. Yang and K. A. Jackson, *The Journal of Chemical Physics*, 2012, **136**, 104501.

[9] B. Dai, L. Tian and J. Yang, *The Journal of chemical physics*, 2004, **120**, 2746–51.

[10] L.-s. Wang, H. Wu, S. R. Desai and L. Lou, *Physical Review B*, 1996, **53**, 8028–8031.

[11] A. Trinchero, S. Klacar, L. O. Paz-Borbón, A. Hellman and H. Grönbeck, *The Journal of Physical Chemistry C*, 2015, **119**, 10797–10803.

[12] Q. Jin, M. Fujishima, A. Iwaszuk, M. Nolan and H. Tada, *Journal of Physical Chemistry C*, 2013, **117**, 23848–23857.

[13] Y. Xu, R. B. Getman, W. A. Shelton and W. F. Schneider, *Physical chemistry chemical physics : PCCP*, 2008, **10**, 6009–6018.

Appendix D

Evaluating Solvent Effects at the Aqueous/Pt(111) Interface

D.1 Introduction

The presence of a liquid, such as water, can have a large effect on the surface chemistry and properties of metals. In heterogeneous catalysis the role of water on metal surfaces can be crucial, such as for oxidation reactions (e.g. alcohol[1–3] or CO[4,5] oxidation), Fischer-Tropsch reactions,[6] biomass reforming,[7–11] and electrocatalytic reactions.[12–14] The presence of aqueous phase at the metal surface can increase the rate of reaction, open up new favorable reaction pathways, or increase the selectivity of products.[6,15–24] However, water can also negatively affect some catalytic reactions.[22–29] Hence, understanding the role of water and other liquids in chemical reactions at the metal-liquid interface is of both fundamental and technological interest.

Extracting atomic details of surfaces with in-situ experiments (especially for metal surfaces in the presence of water) is quite challenging, and density functional theory (DFT) sim-

ulations have aided in explaining many details in surface science and catalysis studies. DFT has for instance been useful in providing valuable insights on the nature of aqueous phase reactions over metal surfaces.[3,6,17,30–37] Still, while DFT can be used to simulate aqueous phase chemistry, modeling the aqueous phase over metal surfaces has been a challenge owing to the difficulty in accurately describing complex systems that may involve simultaneous metal-water, adsorbate-water, adsorbate-metal, and water-water interactions. The addition of solvent may lead to large systems that have a number of possible thermodynamic and geometrical configurations. Due to these complications, often the aqueous phase for DFT surface simulations is ignored and approximated by vacuum. Better, efficient approaches are needed to more accurately model solid-liquid interfaces.

There are several approaches to treating liquid solvents within DFT. In an explicit solvation model (illustrated in Figure D.1), the solvent (such as water molecules) is simulated as other molecules (e.g. modeling the water molecules at the DFT level). Because of the complexity of modeling water layers near the metal surface, water has often been approximated as having a hexagonal ice-like bilayer structure.[19,38–46] Another approach is to only model a few water molecules close to the solute.[47–55] Ab initio molecular dynamics (AIMD) simulations have also been used to generate equilibrium water solvation structures around reaction intermediates over periodic solid surfaces.[17,33,56–60,60–64] The major challenge with the explicit approach is the computationally expensive task of averaging out the thermodynamic properties over several solvent configurations as well as the increased computational requirements for large systems. Accurate descriptions of the liquid-metal interface using the explicit approach are not trivial.

A second approach is the use of an implicit (or continuum) solvent model,[65,66] where the solvent is approximated by a continuum surrounding the solute molecules (see Figure D.1). The solutes are placed in a cavity, and the solvent continuum outside the cavity exhibits the average properties of the solvent. Such a treatment of the solvent can be much more

computationally cheaper compared to explicit models, as it avoids directly modeling solvent molecules. Implicit solvation also mimics the long range electrostatic interactions, which may not be accurately determined in explicit solvation, except possibly for very large simulation sizes.[66] In spite of these advantages, the implicit solvation comes at a potential cost, since specific solute-solvent interactions may not be fully described. For example, hydrogen bond interactions may not be correctly represented by the implicit approach.[67,68] This means that caution must be exercised when using implicit solvation models. Finally, we mention that there have been some attempts to combine explicit and implicit solvation models through a hybrid (or cluster-continuum) approach.[10,32,57,69]

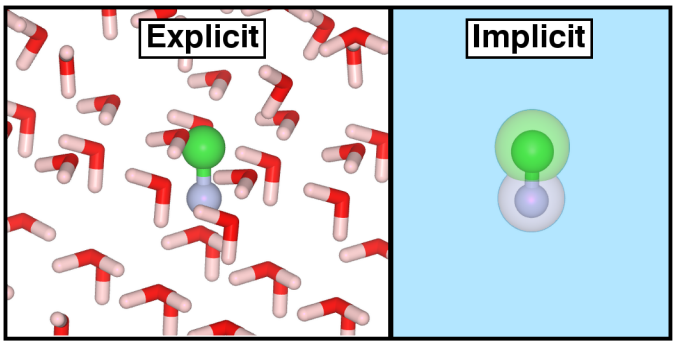

Figure D.1: Illustration of explicit (left) and implicit (right) solvation models. In this example, CO (shown with a ball and stick model) is surrounded by H_2O molecules (shown with stick models) in the explicit model. In the implicit model, the water molecules are treated by a continuum (blue background) and the CO is placed in a cavity (shown as the union of larger atomic spheres).

The computational advantages of implicit solvation models however warrant their potential application and study in simulating metal-liquid interfaces. Implicit solvation models in molecular codes are mature and flexible,[70] with a number of solvation schemes available (see for instance reviews in references[65,66]). Implicit solvation models are relatively new in periodic DFT codes, and thus need more verification to become standard methods. Metal surfaces are typically modeled using two different schemes: the cluster and periodic approach. In the cluster approach, often using molecular quantum codes, a subset of the surface (the

cluster) is modeled, rather than the entire surface. On the other hand, periodic surface models are more robust in modeling extended surfaces using the slab - supercell approach (which avoids edge effects and possible errors due to a finite number of surface atoms). Recently, based on the work of Fatterbert and Gygi,[71,72] there have been several implicit solvent models developed for periodic DFT packages. Available codes include: VASP (VASPsol[73] and VASP-MGCM[74]), JDFTx,[75,76] CP2K,[77] Quantum Espresso,[78] SIESTA,[69] and others.[79] Differences between these models for instance arise from the treatment of relative permittivity across the solute-solvent interface, definition of the solute cavity, or the numerical procedure adopted. Beyond solvation models in periodic DFT codes, we note that Heyden and coworkers developed and used a solvation scheme (iSMS) in which a cluster model is used to determine the implicit solvation energy that is added to the vacuum based results of periodic surfaces.[80] This method allows robust implicit solvation models in molecular codes to be combined with periodic DFT calculations. Since various solvation methods are available in molecular and periodic DFT codes, an evaluation of different solvation methods would be useful in determining their accuracy, and also identifying reasonable approaches to considering implicit solvation.

Several recent reports have described results with implicit solvation models over metal surfaces. Heyden and coworkers used their iSMS approach and found that the solvation effects on Pd(111) and Pd(211) surface were small (not more than 0.25 eV compared to vacuum) in studies involving C-C cleavage of ethylene glycol[80] and hydrodeoxygenation of propanoic acid[81] and methyl propionate.[82,83] Over Pt(111) surface, Bodenschatz et al.[32] reported that the effect of implicit solvation on the adsorption of large polar molecules was considerably smaller (by up to 0.7 eV) than the corresponding explicit solvation. Solvent effects on the adsorption of common adsorbate like O_2, CO, and H_2O using implicit solvation models were reported to be less than a magnitude of 0.1 eV.[32,57,84] Steinmann et al.[85] compared implicit and explicit solvation models, although only for levulinic acid adsorption

on Ru(0001). Using SCCS implicit solvation, the oxygen reduction reaction was studied on Pt(111) surface and a solvation effect of up to 0.26 eV was reported.[86] Other implicit solvation models such as adaptive Poisson-Boltzmann solver (APBS) or Jaguar's Poisson-Boltzmann solver[87] have shown strong solvent effects of up to 0.9 eV on oxygen reduction reaction on Pt(111) surface.[86,88–92] These variously reported solvent effects arise due to the nature of different implicit solvation models. Implicit models require careful evaluation of their accuracy and limitations. Implicit solvation models have also been recently used in modeling electrochemical interfaces and reactions.[93–96]

Fast, accurate implicit solvation models could potentially lead to better descriptions of metal-liquid interfaces. Even though different implicit solvent models are being used across the literature, there are still questions on the quantitative differences between them and which models may be appropriate for modeling surface chemistry over metals. Particularly we are interested in the VASPsol model[73] as implemented in VASP,[97,98] since VASP is one of the most common periodic DFT codes used to model metal surfaces. The use of the periodic code JDFTx[75,99] and the molecular code NWChem[100] (with the COSMO[101] solvation model) further allows us to compare the predicted solvent effects as implemented in both periodic and molecular DFT codes. Moreover, in principle solvent corrections obtained from a molecular DFT code could be easily incorporated into periodic DFT results, as following the iSMS approach. In our work we thus compare several implicit solvent models using DFT and attempt to answer the following questions: how do results from such models differ from each other, how accurate are these models, and what is the effect of the liquid phase on metal surface chemistry? Specifically, we consider the Pt(111) surface and focus on water as a solvent. We model adsorption of several species relevant to catalysis, as well as important surface reactions.

D.2 Methodology

In this work we modeled Pt(111) surfaces with three different codes: VASP[97,98] (plane wave basis set), JDFTx[99,102,103] (plane wave basis set) and NWChem[100] (Gaussian basis set). All three codes have different implicit solvation methods that we used in the current work (discussed below). VASP and JDFTx with a plane wave basis set allowed us to model the surface using the slab approach, where a vacuum space was created in the z-direction, and the slab was infinite in the x- and y-directions (subject to periodic boundary conditions). The surface slabs were modeled with a p(3x3) cell (a total of 36 atoms per slab), which had lattice vectors of length 8.44 Å (VASP) and 8.40 Å (JDFTx). The slabs consisted of four layers with the bottom two layers frozen in bulk geometries. A sample slab is shown in Figure D.2. A vacuum separation of 20 Å was set along the surface normal. We calculated the lattice constant for bulk Pt to be 3.98 Å using VASP and 3.96Å using JDFTx, which is in agreement with previous work (3.996,[104] 3.980,[105] and 3.989[106] Å).

We used NWChem to model Pt clusters that represented the (111) surface. We considered several cluster sizes (see Figure D.2b-d). A small cluster may be inaccurate in describing adsorption due to the presence of a large number of under-coordinated edge metal atoms, while a large cluster may be computationally intractable. Jacob et al.[107–109] reported that Pt_{35} (with 14, 13, and 8 atoms in the first, second and third layers) was a suitable cluster size with minimal edge effects. It was found that the gas phase adsorption energies of several molecular adsorbates like CH_x, C_2H_y, and oxygen reduction reaction intermediates were described well. However, Faheem et al.[80] reported converged solvation energies for the C-C cleavage reaction of ethylene glycol using cluster models having at least two Pt layers with 16 atoms in each layer. In the study by Faheem et al., they reported convergence with respect to solvation energy based on two organic adsorbates - $C_2H_4O_2$ and HCOH. In order to understand the effects of cluster size (both in number of layers of the cluster, and available

cluster surface area), we modeled a broad set of adsorbates over Pt clusters. In our work, we considered a large Pt_{35} cluster, along with two other smaller Pt(111) clusters, Pt_{19} (12 atoms in first and 7 atoms in second layer) and Pt_{10} (7 atoms in first and 3 atoms in second layer).

The generalized gradient approximation Perdew-Burke-Ernzerhof (PBE) exchange correlation functional[110] was used for all the calculations. Using NWChem, Pt atoms were treated by the LANL2DZ basis set with the accompanying relativistic effective core potential that replaced the 60 innermost core electrons leaving 18 outer valence electrons (in an electronic configuration of $5s^2 5p^6 5d^9 6s^1$) modeled using DFT.[111] We chose a sufficiently large 6-311G** basis set (all electrons treated explicitly) for O, C, and H, as valence triple zeta basis sets can usually describe the valence regions of an atom better than double zeta basis sets. Core electrons are described by the projector augmented wave (PAW)[112] approach using VASP and by ultrasoft pseudopotentials (USPP)[113] obtained from the open-source pseudopotential Garrity-Bennett-Rabe-Vanderbilt (GBRV) library[114,115] using JDFTx. We performed test calculations using a plane wave kinetic energy cutoff of 800 eV with VASP for several adsorbates. The mean absolute difference in the adsorption energy of 14 different adsorbates for 800 and 450 eV cutoff energies, was found to be 0.04 eV (see Table E.1 in the Supplementary Information). Hence, all the VASP results were obtained with an energy cutoff of 450 eV. With JDFTx, we used a slightly larger cutoff energy of 544 eV, similar to the previous value used by Ozhabes et al.[116]

With VASP we used the first-order Methfessel Paxton smearing method with a smearing width of 0.15 eV.[118] The convergence criteria in VASP for the electronic self consistent field (SCF) and ionic forces were set to 10^{-5} eV and 0.05 eV/Å respectively. In the case of JDFTx, we used a smearing width of 0.27 eV. The convergence criteria using JDFTx for electronic SCF was 2.72×10^{-5} eV (1×10^{-6} Ha), and the geometry optimizations were performed till the root mean square of ionic forces were less than 0.005 eV/Å (or 0.1 mH/Bohr), respectively.

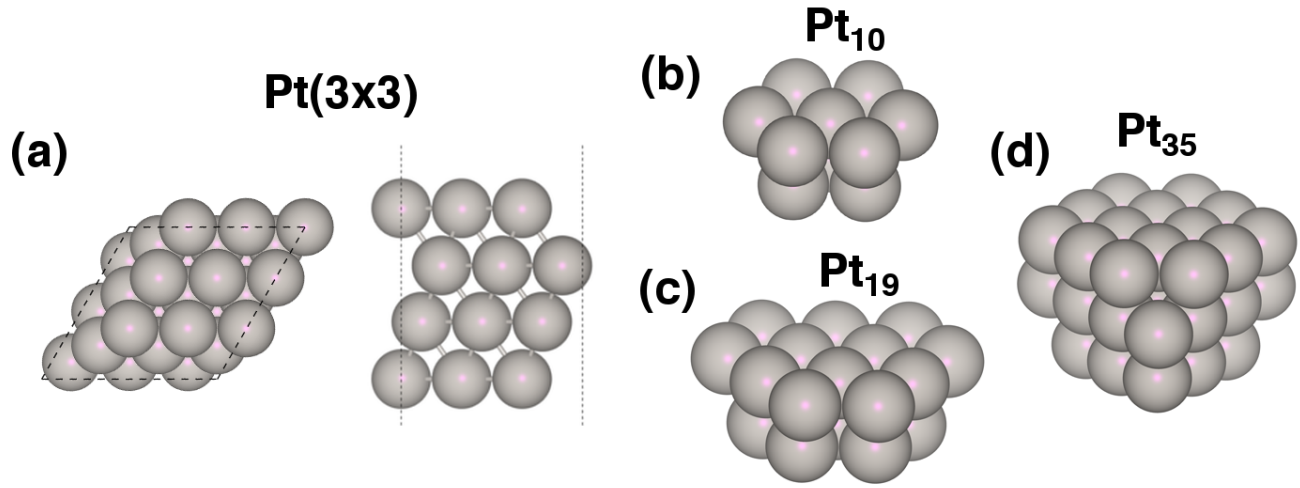

Figure D.2: Pt(111) surface models used in in the current work. The top and side views of the Pt(3x3) periodic surface is shown in (a). $Pt_{10}, Pt_{19}, Pt_{35}$ clusters are shown in (b), (c), (d), respectively. All models were drawn using VESTA-3.[117]

The reciprocal space for the VASP and JDFTx calculations were sampled with k-meshes of 3x3x1. We also tested finer k-meshes of 4x4x1 and 5x5x1 in VASP for the adsorption energies of O_2, H_2O, and HCOOH. The largest deviation in the adsorption energies of these three adsorbates calculated between 3x3x1 and 4x4x1 meshes (or 3x3x1 and 5x5x1 meshes) was 0.02 eV (or 0.09 eV). See Table E.2 in the Supplementary Information for complete data comparing different k-point meshes. NWChem calculations were performed with an electronic SCF convergence criteria of $1.36\text{x}10^{-4}$ eV ($5\text{x}10^{-6}$ Hartree) and the geometry optimization was performed until the ionic forces were less than 0.02 eV/Å (close to a previously-used value of 0.02 eV/Å[119]). To obtain better convergence, we also included a smearing width of 0.027 eV (close to a previously-used value of 0.01 eV[119]) for these metallic systems using NWChem.

For the adsorption of species on the Pt(111) clusters, Pt atoms may either be frozen in bulk geometry positions (similar to previous work[120–122]) or selected Pt atoms in the surface layer may be relaxed while keeping edge atoms frozen (also similar to previous work[92,108,109]). We found that the adsorption energy of OH, O_2, CO, and H_2O on the

Pt_{10} cluster with and without relaxing the central Pt atom of the surface layer changed by less than 0.05 eV. We also tested OH adsorption on the Pt_{35} cluster with and without relaxing the central four Pt atoms of the surface layer, and found that the adsorption energy only changed by 0.03 eV. Hence, we froze the clusters with Pt-Pt bulk bond distances of 2.807Å in all our calculations. A lattice parameter of 3.97Å (average of VASP and JDFTx lattice parameters) gives such Pt-Pt bond distances.

The Pt(111) clusters potentially have a number of unpaired electrons.[108,123] In our present work, we found the ground state of different Pt clusters to have several unpaired electrons. The values we obtained for the ground state spin (S) were 3, 3, and 8 for Pt_{10}, Pt_{19}, and Pt_{35} respectively) ; recall that a spin value of S=1 implies two unpaired electrons. These values were lower than those obtained by Jacob and Goddard[108] (S of 6 and 11 for Pt_{19} and Pt_{35} respectively). This difference could be a result of the different exchange correlation functional used by Jacob and Goddard (B3LYP). We ran test calculations that indeed showed that for a given cluster, the PBE exchange correlation functional typically predicts a lower number of unpaired electrons to be energetically more stable than that predicted by B3LYP (see Table E.3). When an adsorbate is present on the cluster, electron pairing may occur, which may lower the number of unpaired electrons for a Pt cluster.[109] We again tested several spin states for each adsorbate/cluster combination and report herein the results using the lowest energy structures. Our analysis of spin states allows us to be more confident that we have obtained the proper ground-state energies for the cluster systems.

With all three DFT codes we studied implicit solvation. Implicit / continuum solvent models are characterized by the presence of a cavity containing the solute surrounded by a continuum representing the solvent. Here, VASPsol[73] (the implicit solvation model implemented in VASP) and JDFTx[75] were used to model implicit solvation for the periodic Pt(111) surfaces, while the COnductor-like Screening MOdel (COSMO)[101] in NWChem was used to model implicit solvation for the Pt cluster models. All these solvation models are

based on the concept of the Polarizable Continuum Model (PCM),[66] where the response of the presence of solvent on the solute electronic density is captured through polarization charges at the solute-solvent interface. Although all the solvation models are based on the PCM approach, there are some differences among each of them. In COSMO the shape of the cavity enclosing the solute is determined by the union of rigid atomic spheres, unlike in VASPsol and JDFTx where the self consistent determination of cavity shape is based on the solute electronic density. We use the optimized atomic radii reported by Klamt et al.[124] : H = 1.30 Å, C = 2.00 Å, O = 1.72 Å, and Pt = 2.223 Å for the COSMO calculations. Another difference between COSMO and VASPsol/JDFTx is with respect to the description of the dielectric constant at the solute-solvent interface. The switching of dielectric constant from solute to solvent regime is discontinuous in the case of COSMO, while it switches smoothly as a functional of solute electron density in JDFTx and VASPsol. All three solvation models however modify the Hamiltonian in the Kohn-Sham equations within the self consistent cycle to determine the ground state energy of the combined-solute solvent system. In the case of implicit solvation in VASPsol and JDFTx, both adopt the theoretical framework from joint density functional theory.[125] In joint density functional theory, the usual Kohn-Sham electron density functional is appended with functionals describing the bulk solvent and the solute-solvent interactions such that, now a combined solute-solvent system is described. Here, the bulk solvent surrounding the solute is described using a classical DFT picture in terms of molecular density of the solvent (see for example Ref[126]), while the solute-solvent interaction is taken into account through the solvent polarization. In COSMO, the polarization charges on the cavity surface are used to construct the corresponding potential that enters the Kohn-Sham equations.[127]

In vacuum (Equation D.1) or using implicit solvation (Equation D.2), adsorption energies can be calculated as,

$$\Delta E_{ads}^{vac} = E(X*) - E(*) - E(X) \tag{D.1}$$

$$\Delta E_{ads}^{imp} = E(X*^{imp}) - E(*^{imp}) - E(X^{imp}) \tag{D.2}$$

where, * refers to the bare Pt surface, X* to the Pt surface with adsorbate, and X to the free molecule or atom. The superscript "imp" indicates the energies are calculated using implicit solvation. In Equation D.2, we chose to define the adsorption energy in the presence of solvent to indicate a real-solvated situation, where a solvated free species (X^{imp}) adsorbs on a solvated metal surface ($*^{imp}$) to form the solvated metal-adsorbate system ($X*^{imp}$). Typically, the free species are modeled without solvent, but we chose to solvent these species in our work in order to better mimic reality where such species are likely in bulk solvent. The difference in Equation D.2 between using solvated free species and gas-phase free species is simply the solvation energy of the lone molecule or atom. The energies with superscript "imp" contain both the electrostatic and the non-electrostatic (cavitation and dispersion) contributions upon solvation. All the energies reported using implicit solvation were calculated with the default numerical settings in all the three DFT codes. Steinmann et al.[85] reported results using $\tau = 0$, or no cavitation energy, due to convergence issues. We experienced no such issues in our study and report all results with cavitation energies. For atomic adsorbates like H, O, and N, the energy of the free adsorbate we used was 1/2 the energy of the gas-phase dimer. In the case of C and S also we choose 1/2 the energy of the gas-phase dimer as the energy of free adsorbate to be consistent with the definition of other elemental adsorbates. The difference in the adsorption energies for the solvated case (equation D.2) and the vacuum case (equation D.1) represents the change in adsorption energy upon applying solvation, a term we call the 'adsorption solvation energy', or $\Delta\Delta E_{ads}^{solv}$.

$$\Delta\Delta E_{ads}^{solv} = \Delta E_{ads}^{imp} - \Delta E_{ads}^{vac}$$

$$= \Delta E_{solv}(X*) - \Delta E_{solv}(X) - \Delta E_{solv}(*) \tag{D.3}$$

This value quantifies the effect of solvation on adsorption energy values. Negative values of $\Delta\Delta E_{ads}^{solv}$ indicate that solvation is more favorable in the presence of solvent, while positive values indicate that solvation is more favorable in gas phase.

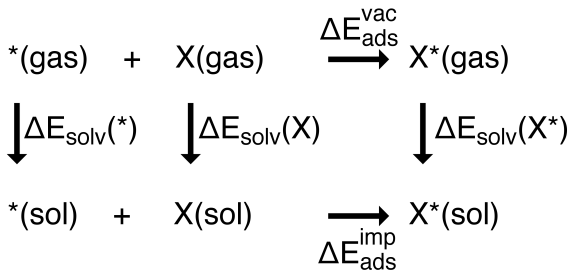

Scheme D.1: Thermodynamic cycle for the solvation process during adsorption of a species on a metal surface.

Another way to consider the solvation process during adsorption is shown in Scheme D.1. The top process shows adsorption of species X from the gas-phase, while the lower reaction shows adsorption of species X in the presence of solvent. The vertical energy changes in the thermodynamic cycle correspond to (from left to right) the solvation energy of the clean surface [$\Delta E_{solv}(*)$], solvation energy of the free adsorbate [$\Delta E_{solv}(X)$], and solvation energy of the combined adsorbate/metal surface [$\Delta E_{solv}(X*)$]. Analysis of these three solvation energies can provide useful insight on what solvation effects dominate the adsorption process. For instance, if $\Delta E_{solv}(X*)$ is very negative, while $\Delta E_{solv}(*)$ and $\Delta E_{solv}(X)$ are both close to zero, the solvation energy of adsorption will be very negative, implying that solvation of the combined adsorbate/surface system is dominant for the adsorption process.

D.3 Results and Discussion

D.3.1 Comparison of Implicit Solvated Cluster Models

Motivated by the work of Heyden and coworkers,[80] which used metal clusters with implicit solvation to treat solvation effects, we modeled several different Pt clusters to represent the

(111) surface. We sought to determine solvation effects on the adsorption of common ORR intermediates, as well as CO (a common catalyst poison or intermediate). In the literature, properties like adsorption and reaction energies in the gas phase have often been used to assess cluster-size effects.[92,107,108,120–122] However, relatively limited amount of work[80,128] is available on understanding the effect of cluster size on surface processes in the presence of implicit solvation. We first sought to determine which Pt cluster would be appropriate for this work.

On the different Pt clusters, we considered the following adsorbates and adsorption sites: H(top), O(fcc), OH(top), O_2(bridge), CO(fcc), and H_2O(top). See Figure E.1 in the Supplementary Information for illustrations of the different adsorption sites. These adsorption sites for H, O, OH, O_2, CO, and H_2O are the most stable sites as found in previous literature (see references[104,106,129,130]). Due to the small size of the Pt_{10} cluster, the adsorption of O atom at the fcc site resulted in a shifting of the O atom to the top site upon optimization. We thus relaxed the O atom at the fcc site only along the surface normal direction (the O atom was frozen in x and y directions) to find the minimum geometry for O adsorbed at the fcc site. A similar approach was also used by Jacob et al.[107] We show the adsorption energies for the different clusters in vacuum and with implicit solvation in Figure D.3. The adsorption energies are predominantly found to converge to common values with increasing Pt cluster size. It can also be seen that for adsorbates like H, OH, and H_2O, the adsorption energies converge relatively smoothly with increasing cluster size when compared to adsorbates like O, O_2, and CO.

We find that the adsorption energies of different clusters depend on the local environment around the adsorption site. When adsorbates bind at fcc (O and CO) or bridge sites (O_2), the local environment over Pt_{10} and Pt_{19} clusters are significantly different from Pt_{35} clusters. For the Pt_{10} and Pt_{19} clusters, the adsorbates at fcc/bridge sites bond to edge Pt atom(s) because of the small cluster sizes. In contrast no edge Pt atoms are involved in bonding

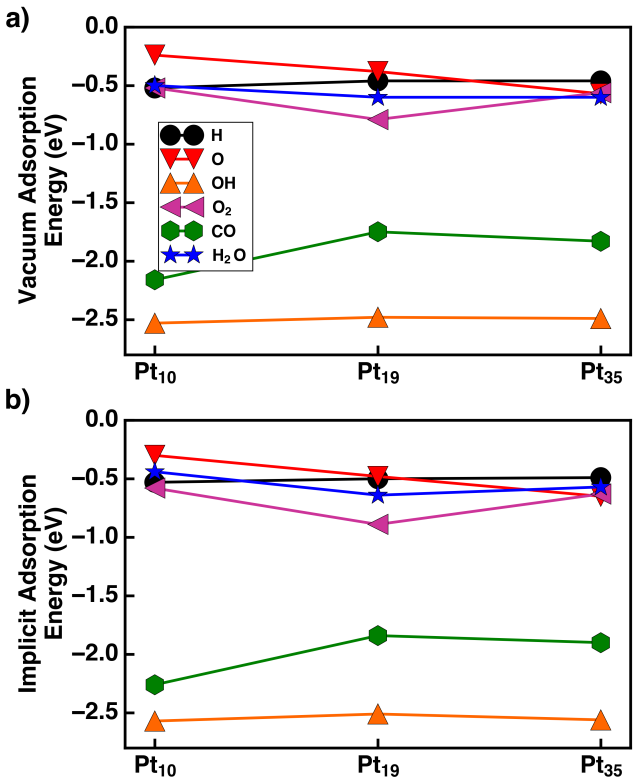

Figure D.3: Calculated adsorption energies in the presence of vacuum (a) and implicit solvation (b) as a function of Pt cluster size. COSMO was used to treat solvation with the NWChem DFT code.

over Pt_{35} clusters. In addition to these edge effects, indirect effects due to the absence Pt atoms in the third layer may also affect the adsorption energies calculated using the two layer Pt_{10}/Pt_{19} clusters. Jacob et al.[107] also found that two-layer cluster surfaces may not represent the adsorption properties well. Pt_{35} is three layers thick and may better describe the bulk-like nature of the Pt surface. Furthermore adsorbate-Pt bond distances differ by up to 0.1 Å for the Pt_{10}/Pt_{19} clusters compared to the Pt_{35} cluster. The mean absolute difference between Pt_{35} and Pt_{19} clusters for both the adsorption energies in vacuum (ΔE_{ads}^{vac}) and in the presence of implicit solvation (ΔE_{ads}^{imp}) was 0.09 eV. In the remainder of the work, we use the Pt_{35} cluster as it showed minimal edge and layer effects when compared to the Pt_{19} and Pt_{10} clusters.

D.3.2 Comparison of Implicit Solvation Models for Adsorption

In this section we consider the effect of implicit solvation on the adsorption of several adsorbates using Pt clusters with NWChem, as well as two other implicit solvation models as implemented in the periodic DFT codes, VASP and JDFTx. We simulated adsorption of a number of possible adsorbates, such as atomic species, organic molecules, and inorganic molecules. We chose such adsorbates as they represent common adsorbates that may be present for typical catalytic reactions. Figure D.4 shows the calculated adsorption solvation energies as calculated using VASP, NWChem, and JDFTx. We calculated these energies with Equation D.3. We used the following adsorption sites: H (top), O (fcc), C (fcc), S(fcc), N(fcc), OH (top), CH (fcc), CH_2(bridge), CH_3 (top), NH (fcc), NH_2(bridge), NH_3(top), NO (fcc), CO (fcc), O_2 (bridge), and H_2O (top). These sites were chosen as they were reported to be the most stable adsorption sites based on the previous DFT studies[106,129–131] (see Table E.5 in the Supplementary Information for more details).

The effect of implicit solvation on adsorption as shown in Figure D.4 can be classified into three types based on the relative solvation effect: weak ($\leq$0.05 eV), moderate ($\sim$0.1 eV), and strong ($\geq$0.20 eV). Several adsorption solvation energies fall into the weak regime using all three implicit solvation models. VASP results show that solvation energies for OH and CH are moderately positive, while solvation energies for NH and NH_2 are moderately negative. Adsorption of ammonia showed a strong solvent effect, with an adsorption solvation energy of -0.32 eV using VASPsol. We find that JDFTx results are very close to those calculated using VASPsol (mean absolute difference of 0.02 eV). In the case of COSMO, most solvation energies were weak. Moderate negative adsorption solvation energies were found for O, CO, and O_2 using COSMO, while weak solvation effects were calculated for these same species using VASP/JDFTx. However, COSMO also predicts strong solvent effects for ammonia (-0.20 eV) consistent with VASP/JDFTx results.

To better understand the differences between these three solvent models, we analyzed

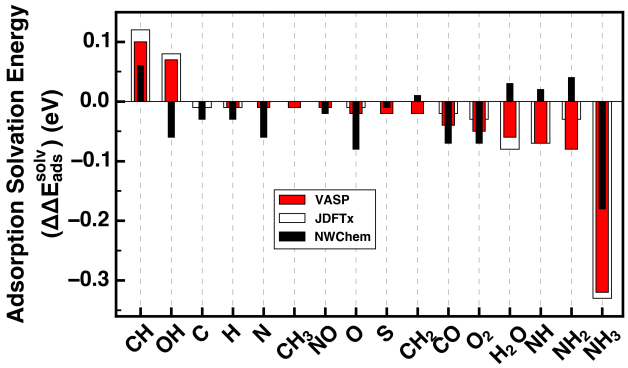

Figure D.4: Adsorption solvation energies for several adsorbates calculated using VASP, JDFTx, and NWChem. The results with NWChem were obtained using Pt_{35} clusters.

the different solvation energy terms shown in Scheme D.1. We note that solvation energies of free adsorbates, or the energy to place a gas-phase molecule in solvent, $\Delta E_{solv}(X)$, calculated using the three different solvent models are in good agreement with each other: the mean absolute difference between VASP and JDFTx was 0.01 eV, VASP and NWChem was 0.03 eV and JDFTx and NWChem was 0.03 eV. These results show that all three implicit solvent models describe solvation of free species in a similar manner. The experimental solvation energies for free adsorbates like molecular nitrogen, ammonia, carbon monoxide, water, methane, ethanol, methanol, acetone, benzene, toluene, and aniline were reported earlier.[132,133] The mean absolute difference in implicit solvation energy between our results and the experimental data for the above adsorbates was found to be 0.04 eV, giving confidence to our approach. Likewise, our results for implicit solvation energies also agree well (mean absolute difference of 0.04 eV) with the values obtained by Marenich et al.,[134] who used the SMD implicit solvation model. Marenich et al. modeled molecular hydrogen, ammonia, water, water dimer, acetic acid, methane, isopropyl alcohol, ethanol, methanol, acetone, benzene, toluene, and aniline.

All the solvation energy terms in Scheme D.1 [$\Delta E_{solv}(X)$, $\Delta E_{solv}(*)$, and $\Delta E_{solv}(X*)$] calculated using VASPsol and JDFTx are almost identical to each other (see for example

Table D.1). We attribute this small difference to the similarity of the solvation models implemented in these codes, as well as other similar parameters (e.g. basis set). Therefore, in the following discussion we will focus on comparing results between NWChem/COSMO and VASP/VASPsol. Values of $\Delta E_{solv}(X)$ calculated by using the three codes are similar (see Table E.4), with a mean absolute difference of 0.03 eV between VASP and NWChem. The largest difference between the two codes was 0.10 eV. The $\Delta E_{solv}(*)$ values of 0.04, 0.05, and -0.02 eV for VASP, JDFTx, and NWChem, respectively, indicating a difference of 0.06 eV between VASP and NWChem. It follows that when the differences in the adsorption solvation energies estimated by VASP and NWChem are considerable, for example, around 0.1 eV for OH, NH_x(x=13), and H_2O, this difference was largely due to different $\Delta E_{solv}(X^*)$ values calculated by VASP and NWChem.

We note that VASP/VASPsol tends to produce more positive solvation energies than NWChem/COSMO for systems with metal surfaces. This small difference in solvation energies between VASP and NWChem could potentially be attributed to the finite size of the Pt cluster used in NWChem, or differences in the two implicit solvation models. These differences include how the shape of the cavity is determined and how the bulk dielectric constant of the solvent is treated across the solute solvent interface (see the Methods Section for more details). For several metal/adsorbate systems (e.g. O, OH, CO, O_2, and N), VASP shows solvation energies $\Delta E_{solv}(X^*)$ to be around 0.1 eV more positive compared to NWChem. On the other hand, for adsorbates such as NH2, NH3 , and the weakly adsorbed water molecule, VASP results in solvation energies that are around 0.1 eV more negative compared to NWChem. The mean absolute difference between the solvation energies of VASP and NWChem for the adsorbates listed in Table 1 is 0.06 eV, with the largest deviation (0.13 eV) for OH. Overall, VASP and NWChem solvation energies are consistent with each other for several adsorbates. More importantly, the adsorbates that showed large solvation energies in Table 1, such as water and ammonia, were predicted in a consistent manner with

Table D.1: Solvation energies $\Delta E_{solv}(X^*)$ in eV for Pt surface with different adsorbates. Values of $\Delta E_{solv}(^*)$ and $\Delta E_{solv}(X)$ for the different codes are discussed in the text. Scheme D.1 and Equation D.3 provide a description of these different variables.

	VASPsol	**COSMO**	**JDFTx**
H*	0.03	-0.01	0.04
O*	0.03	-0.06	0.05
C*	0.04	-0.02	0.06
S*	0.03	0.02	0.07
N*	0.03	-0.05	0.05
OH*	-0.10	-0.23	-0.08
CH*	-0.01	-0.01	0.03
CH_2*	-0.01	-0.02	0.01
CH_3*	0.02	-0.01	0.04
NH*	-0.13	-0.09	-0.12
NH_2*	-0.21	-0.14	-0.20
NH_3*	-0.47	-0.38	-0.46
NO*	0.02	-0.01	0.05
CO*	0.00	-0.07	0.02
O_2*	0.01	-0.06	0.04
H_2O*	-0.34	-0.26	-0.34

the two solvation models.

The adsorption solvation energies, $\Delta\Delta E_{ads}^{solv}$, for several adsorbates are generally small (less than 0.1 eV) as Figure D.4 indicates. Small adsorption solvation energies (less than 0.1 eV) using COSMO for intermediates like O_2, O, OH, CO and H_2O were also reported on Pt(111)[84] and a Al-Pt core shell cluster.[135] Behtash et al.[82] modeled the Pd(111) surface and used a slightly different definition of adsorption solvation energy, where they considered the free adsorbate to be in the gas phase, rather than solvated like we have done. This definition is equivalent to using $\Delta E_{solv}(X)$ equal to zero in Equation D.3. We used our data to recalculate adsorption solvation energies using their modified approach and find the adsorption solvation energies to be 0.01, -0.20, -0.05, -0.23, 0.01, 0.01 eV for H, OH, CO, H_2O, CH_2, and CH_3, respectively. Behtash et al. calculated the values to be -0.01, -0.05, -0.08, -0.12, 0.02, 0.03 eV for these same species. While our work used the Pt(111) surface and Behtash et al. used the Pd(111) surface, the adsorption solvation energies are of very

similar magnitude. Using VASPsol, Sakong et al.[57] reported the adsorption solvation energy of water on Pt(111) to be -0.08 eV, which is in good agreement with our value of -0.06 eV. Bodenschatz et al.[32] also reported a modified adsorption solvation energy (Equation D.3 with $\Delta E_{solv}(X)$ equal to zero), using VASPsol, for CO at the top site on Pt(111) to be -0.02 eV. We recalculated the modified adsorption solvation energy value to be -0.02 eV for CO, which is in close agreement with their value.

Our results, however, are in contrast to work which used the Jaguar[87] Poisson-Boltzmann solver, where they reported an adsorption solvation energy of up to 1.3 eV for ORR intermediates on Pt(111).[91,92,136] We surmise that the strong solvation effects in these other results could be due to the electrostatic potential (ESP) fitting to obtain atomic charges used in calculating the electrostatic contribution of the solvation energy. Our results also differ from the APBS solvation model used by Sha et al.,[88] who reported a larger adsorption solvation energy for the adsorption of H (-0.07), O (-0.70), OH (-0.54), O_2 (-0.32), and H_2O (-0.36 eV). As described in Section D.2, COSMO, VASPsol, and JDFTx calculate the solvent effects based on a self-consistent approach. Solvent effects calculated by Sha et al. involve a post-hoc correction to a gas-phase electron density. As also mentioned by Behtash et al.,[82] solvation energies in the work of Sha et al. included only the electrostatic component of solvation energy, which may perhaps be another source of discrepancy between our results and that of Sha et al. Although cavitation and dispersion energies are important for obtaining accurate solvation energies, our results showed that the cavitation energies were generally small (around 0.1 eV). Sha et al. used Gaussian basis functions along with norm-conserving pseudopotentials, and a (2x2) unit cell. These simulation parameters are different from the parameters used in our present work, which may also explain the contrasting solvation energies between our work and theirs. Nonetheless, the adsorption solvation energies calculated in our work over Pt surfaces are consistent with a large number of previous data.[32,57,82,84,135]

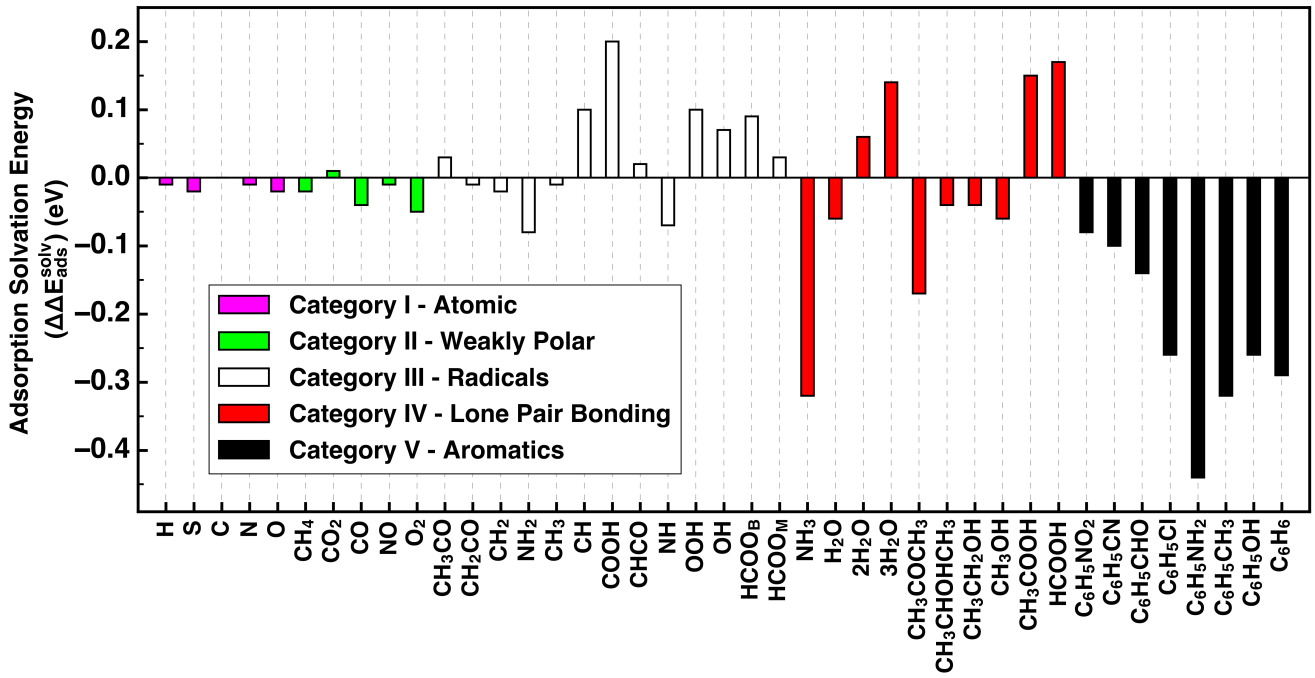

Figure D.5: Adsorption solvation energies calculated using VASPsol for different species classified into five categories based on chemical nature of the adsorbate.

D.3.3 Comparison of solvation energies for different classes of adsorbates using VASPsol

Periodic DFT modeling is a standard method for simulating metal surfaces. The advantage of using periodic DFT is that realistic surface structures can be simulated, which can often lead to very good agreement with experimental data. Our results suggest that the two codes with periodic basis functions, JDFTx and VASP, give very similar solvation results. We thus focus in this section on studying a broad number of adsorbates using VASP in order to better understand how its solvation scheme (i.e. VASPsol) performs. We chose a wide variety of adsorbates that may find applications in, for instance, the catalytic conversion of hydrocarbons, catalytic poisoning, oxygen reduction reaction, formic acid/methanol/ethanol oxidation reactions, and aromatic hydrogenation or dehydrogenation. Our results cover a broad class of adsorbates such as atomic adsorbates, organic/inorganic radicals, water clus-

ters, carbonyls, alcohols, aromatics, and other hydrocarbons. We chose the adsorption sites over Pt based on the most stable geometries in vacuum as reported in the literature (see Table E.5 in Supplementary Information for further details of the adsorbates studied). In Figure D.5 we show the calculated adsorption solvation energies, $\Delta\Delta E_{ads}^{solv}$, of many adsorbates using VASPsol. In order to understand the trends in adsorption solvation energies, we classified the adsorbates into five categories: I (atomic), II (weakly polar), III (radicals), IV (closed shell species with lone pair bonding to the Pt surface), and V (aromatics).

The category I adsorbates are atomic species. For all the five atomic adsorbates studied, the implicit water solvation shows negligible effect on adsorption energies. Although small in magnitude, the adsorption solvation energies of the atomic adsorbates tend to be slightly negative (-0.04 eV to 0.00 eV). Weakly polar adsorbates (category II) include non-polar molecules such as CH_4, CO_2, and O_2 and weakly polar diatomic molecules such as CO, and NO. The gas phase dipole moment of any adsorbate within these category does not exceed 0.22 D. Similar to category I results, the magnitude of adsorption solvation energies are weak (-0.05 eV to 0.01 eV). Most of these adsorption solvation energies are slightly negative. Both Category I and II species interact weakly with the solvent, likely due to small cavity size, leading to small solvent-solute interactions, and/or small electronic polarizability/dipole moment, also leading to small solvent-solute interactions.

Unlike category I and II results, the radical adsorbates in category III show adsorption solvation energies that have a variety of values. The absolute values range from weak ($\leq$0.05 eV), to moderate (around 0.1-0.2 eV), and to strong ($\geq$0.2 eV). Several adsorbates like CH_xCO (x=1-3), CH_x (x=2-3), and $HCOO_M$ (the 'M' subscript indicates HCOO bonding to Pt through one O-Pt bond in monodentate configuration) show weak solvation effects. Adsorbates exhibiting moderate solvation effect include NH_x (x=1-2), CH, OH, OOH, and $HCOO_B$ (the 'B' subscript indicates HCOO bonding to Pt through two O-Pt bonds in bidentate configuration). Among these adsorbates, only NH and NH_2 show a negative adsorption

solvation energy of around -0.1 eV. A strong adsorption solvation energy of 0.20 eV was found for COOH (an intermediate in CO oxidation[137] and formic acid oxidation[36]) and is similar to a recent value reported by Steinmann et al.[85] of 0.28 eV for levulinic acid bound to Ru(0001) surface through the COOH group. The adsorption solvation energy of formate with different binding modes ($HCOO_M$ and $HCOO_B$) differing by 0.06 eV indicates that the solvent effect is dependent on the adsorbate moieties exposed to the implicit solvent. A similar observation in DMF solvent and water solvent on different binding modes of oxalate and levulinic acid on Ni(111) and Ru(0001) respectively was reported earlier.[85,95] All the adsorbed species, other than weakly solvated CH_x (x=1-3), show a favorable solute-solvent interaction due to a large solute polarizability/dipoles and/or large solute cavity.

The next set of adsorbates are category IV, which are closed-shell molecules that bond to the Pt surface primarily through lone pair electrons. We considered a few inorganic (e.g. ammonia and water clusters) and organic adsorbates (e.g. ketone, alcohol, and acid). Figure D.5 shows that adsorption of ammonia in the presence of water is more favorable with an adsorption solvation energy of -0.32 eV. The adsorption solvation energy is weakly favorable for a water monomer (-0.06 eV). We modeled water dimer and water trimer on Pt similar to the work of Sakong et al.[57] The adsorption geometry of water dimer (or trimer) involves one chemisorbed water molecule interacting directly with the Pt surface, while the other water molecules are around 3.3 Å above the metal surface and hydrogen bond to the chemisorbed water. For modeling adsorption of dimer and trimer, similar to Sakong et al., we used a single water molecule as the reference, or reactant state. When the size of the water cluster increases from monomer to dimer and trimer, the adsorption in the presence of water becomes unfavorable with adsorption solvation energies of 0.06 and 0.14 eV respectively. The organic adsorbates in category IV comprise a ketone (acetone), alcohols (methanol, ethanol, and isopropanol), and acid adsorbates (formic and acetic acid). Acetone and alcohol adsorbates show favorable adsorption in the presence of water. However, our results show

that acetone binds stronger in the presence of water compared to the alcohol adsorbates. The similar adsorption solvation energies of around -0.05 eV for different alcohols indicates that the change in alkyl chain length or the chain type (primary and secondary alcohol) does not affect the solvation of the adsorbed species, since these chains are hydrophobic. Montemore et al.[68] also found similar solvation effects for alkyl adsorbates of differing chain lengths adsorbed on Cu(111). The adsorption solvation energies of formic and acetic acid however, are strongly positive (around 0.15 eV) in the presence of water. Again, the increase in chain length from formic to acetic acid did not affect the adsorption solvation energies. All the adsorbates in this category show strong solute-solvent interactions.

The category V adsorbates are aromatic compounds: nitro- benzene, benzonitrile, benzaldehyde, chlorobenzene, aniline, toluene, phenol, and benzene (from left to right in Figure 5). For all these adsorbates, the aromatic rings lie flat on the Pt surface, which was earlier reported to be the most stable adsorption configuration.[21,138–141]The negative adsorption solvation energies for all the adsorbates indicate a favorable effect of water on their adsorption. Nitrobenzene, benzonitrile, and benzaldehyde have moderate adsorption solvation energies of around -0.1 eV. For the rest of the adsorbates, however, high adsorption solvation energies were calculated in the range of -0.26 to -0.44 eV, and aniline has the highest solvation energy. The high polarity (as reported below in terms of Bader charges, which are 0.10, 0.28, 0.17, 0.21, and 0.17, respectively) that is induced when aromatic adsorbates such as chlorobenzene, aniline, toluene, phenol, and benzene are adsorbed in the presence of water result in strong polarization of the surrounding solvent. Furthermore, the larger cavity of these aromatic adsorbates results in stronger interactions with the surrounding solvent, which lead to significant solvation energies. In the continuum solvent model these interactions are determined by integrating over the surface area of the solute molecule. All the adsorption solvation energies of the aromatic species are negative, indicative of favorable adsorption in the presence of an aqueous phase. These molecules prefer to be in the adsorbed

state, rather than in water. Furthermore, the hydrophobic aromatic rings drive them onto the Pt surface.

We now discuss the calculated adsorption solvation energies of the various categories, and analyze the trends and reasons for these solvation energies. Recall Scheme D.1 which shows the relationship between the adsorption solvation energy, and other various defined solvation energies. Equation D.3 indicates the mathematics of this process, where $\Delta\Delta E_{ads}^{solv}$ = $\Delta E_{solv}(X*)$ - $\Delta E_{solv}(X)$ - $\Delta E_{solv}(*)$. In other words, each of the calculated solvation energies contributes to the final adsorption solvation energy. The solvation energy of the Pt surface, $\Delta E_{solv}(*)$, is small (0.04 eV), which indicates that the adsorption solvation energies in Figure D.5 can be largely understood by comparing the solvation energies of adsorbed and free species as shown in Equation D.4.

$$\Delta\Delta E_{ads}^{solv} \sim \Delta E_{solv}(X*) - \Delta E_{solv}(X) \tag{D.4}$$

The second term on the right hand side of Equation D.4, the solvation energy of a free adsorbate, simply describes the energy to solvate the gas-phase species. We find that the solvation energy of a given atom/molecule is correlated to its gas-phase dipole moment (calculated at the PBE/6-311G** level and taken from the NIST Computational Chemistry Database[142]). A larger dipole moment tends to lead to more favorable solvation. Similar correlations have been observed before.[143,144] A larger dipole moment on a molecule indicates that the surrounding solvent medium could be strongly polarized, which in turn leads to a favorable solute-solvent interaction causing favorable solvation of the molecule.

Category I adsorbates (atomic) have no dipole moments while Category II (weakly polar) have small dipole moments (less than around 0.2 D). Correspondingly, all the free adsorbate solvation energies are small for these two categories, with absolute values of around 0.1 eV or smaller. Radical adsorbates (category III) include molecules with very low to very large

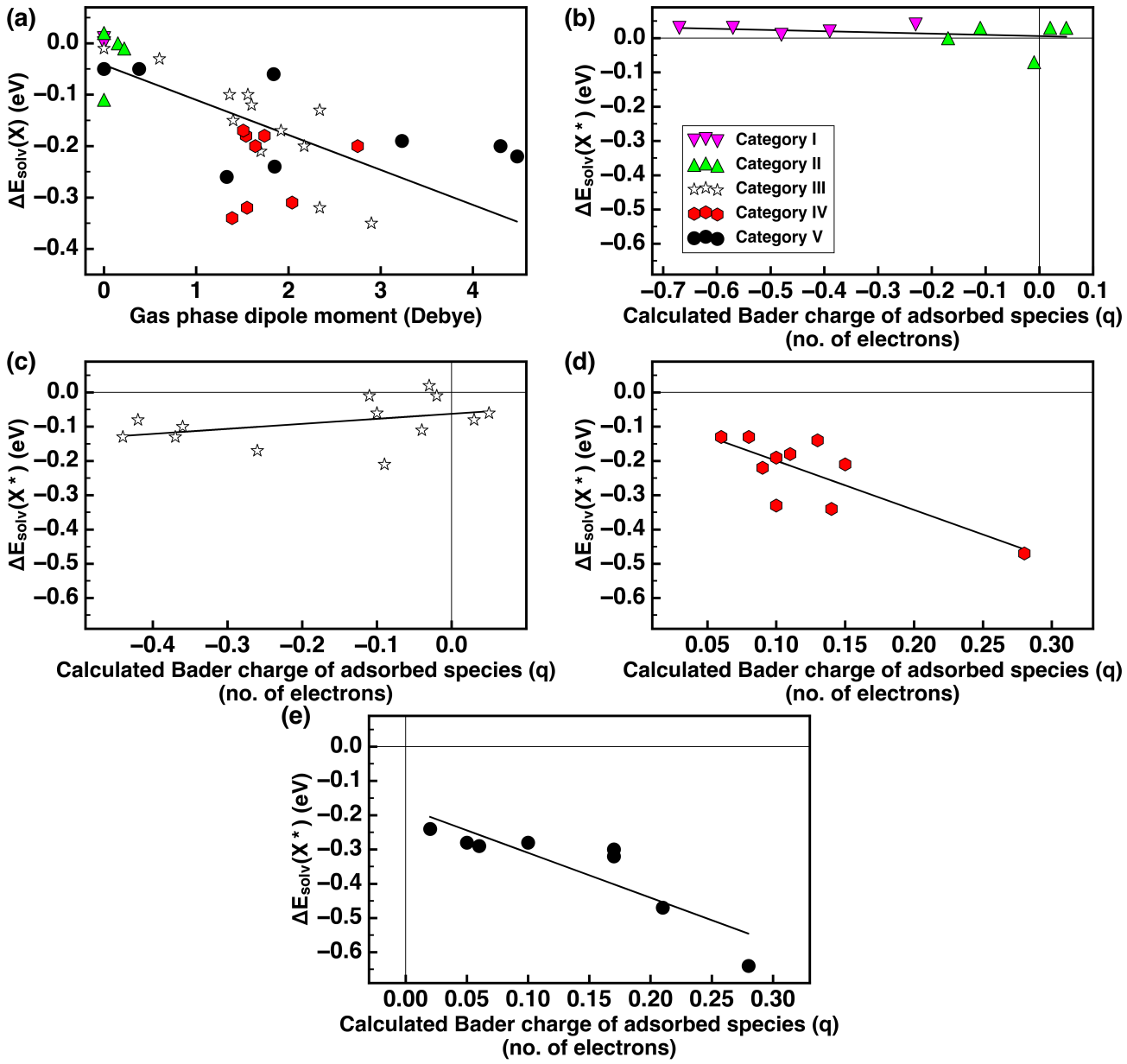

Figure D.6: Correlations between calculated solvation energies and parameters of the relevant molecules. (a) Solvation energies of gas phase molecules compared to calculated (PBE/6-311G**) gas phase dipole moments.[142] Plots (b), (c), and (d) show the solvation energies of adsorbed molecules compared to calculated Bader charges of these adsorbed species. The dashed lines indicate the best linear fits.

dipole moments. Here, CH_3 (no dipole) and CH_2 (0.6 D) have low free adsorbate solvation energies of -0.01 and -0.03 eV, respectively. On the other hand NH_2, HCOO, OOH, CH_3CO, and COOH possess large dipole moments of more than 1.9 D, with larger solvation energies up to -0.35 eV. The remainder of the radical molecules have dipole moments in the range of 1.3 to 1.7 D, corresponding to free molecule solvation energies near -0.1 to -0.2 eV.

In category IV, inorganic adsorbates like ammonia (1.7 D) and water (2.0 D) have solvation energies of -0.18 and -0.31 eV, respectively. Organic adsorbates such as acid and alcohols have dipole moments of 1.4 to 1.6 D, while the dipole moment of acetone is 2.7 D. The solvation energies of the alcohol and acetone free molecules are around -0.2 eV, but the acid adsorbates have free molecule solvation energies near -0.3 eV. The acid species have more negative solvation energies that strongly deviate from the best linear fit line in Figure D.6a. This deviation may be related to the presence of the COOH group, which is strongly solvated in formic and acetic acid. For example, methyl (CH_3) and carboxylic acid (COOH) moieties (the constituents of acetic acid) have calculated solvation energies of -0.01 and -0.35 eV. Thus for acetic acid, which has these two moieties, the solvation effect is strong due to the presence of COOH group, rather than solvation of the methyl group. Finally, for category V species, benzene and toluene have low dipole moments and low free solvation energies (-0.05 eV each). However, aniline has a larger dipole moment of 1.8 D and shows a larger solvation energy of -0.24 eV. In summary, category I and II species all tend to have very low dipole moments, and thus have small free species solvation energies. Category III consisted of molecules with a range of small to large dipole moments and correspondingly a range of small to large free molecule solvation energies. Category IV species tend to have larger dipole moments, and thus large free molecule solvation energies. Category V molecules show both large and small dipole moments. Our results show that a key parameter for interpreting the free molecule solvation energy is the dipole moment of the gas-phase species.

Next we examined the first term on the right hand side of Equation D.4, the solvation

energy of adsorbed species. We relate the solvation energies of the adsorbed species to their calculated Bader charges[145,146] (q) in (Figure D.6b,c,d). A positive (negative) q value indicates a positively (negatively) charged adsorbed species. We expect that a large charge on an adsorbed species could lead to the surrounding solvent being strongly polarized, which may lead to strong solvent effects. The Bader charges of adsorbed species and the different solvation energy terms are given in Table E.5 in the Supplementary Information. In a similar fashion, Jacob and Goddard[92] explained that the favorable solvation effects they observed for H_2 and O_2 adsorption in the presence of implicit solvation could be related to the charge transferred to adsorbed H_2 and O_2.

We find that for categories I and II (atomic and weakly polar species) the adsorbate solvation energies of the atoms and molecules are nearly independent of the Bader charge on the adsorbate. These solvation energies of adsorbed species are also not strong. This small solvation energy is either due to the small cavity size of the adsorbates (e.g. atoms) or due to the small dipole moment of the adsorbates (e.g. atoms or weakly polar molecules). The small cavity size or small dipole moment (i.e. weak polarity) results in a small interaction between the adsorbate and surrounding implicit solvent, regardless of the charge of the adsorbed species. Combined, both the small solvation energies of adsorbed species and the small solvation energies of free adsorbates (see Figure D.6a) resulted in small adsorption solvation energies for category I and II species, since their difference is approximately the adsorption solvation energy (see Eq. D.4).

The solvation energies of adsorbed species in category III also appear to be weakly correlated with the Bader charge of the adsorbed species (see Figure D.6c). We do however observe that as charge decreases to more negative values, the solvation energy tends to be become slightly more negative. Although the charges can be as large as -0.46, the solvation energies of these adsorbed species in category III only range from 0.02 to -0.21 eV. This weak correlation between q and solvation energy may be due to the radical adsorbates binding to

the Pt surface with strong adsorption (see adsorption energies in Table E.5 in the Supplementary Information). Because of the strong binding, the Pt surface electronic states may partly screen the favorable solvation effects for the category III radical adsorbates, leading to a weak correlation with the Bader charges. The solvation energies of adsorbed radical species tend to be in the range of 0.02 eV to -0.21 eV. However, the solvation energies of corresponding free adsorbates (Figure D.6a) ranged from around -0.01 eV to -0.35 eV. Thus, as per Equation D.4, several adsorbates in category III showed a positive adsorption solvation energy (see Figure D.5), while a few species had small negative adsorption solvation energies.

Figure D.6d shows a strong correlation between the solvation energy and adsorbate charge for categories IV and V. All these species become positively charged upon adsorption, in contrast to other category I, II, and III species. We find that as charge increases to more positive values, the solvation energies become larger in magnitude. As the adsorbed species become more charged, stronger interactions between the surrounding solvent occur, which results in the more favorable solvation effects. The solvation energies of adsorbed ammonia and water were found to be -0.47 and -0.34 eV. Since the solvation energies of free ammonia and water were -0.18 and -0.31 eV, the adsorption solvation energy of ammonia was strongly negative while that for water was weakly negative (see Figure D.5). As the size of the water cluster increased, the total charge on the water monomer, water dimer, and water trimer slightly decreased from +0.26 to +0.24 to +0.22 respectively. Since only one water molecule in the water sets interacts with the Pt surface, adding more water molecules does not significantly change the total water cluster charge. The adsorbed monomer (-0.34 eV) is most favorably solvated, followed by the dimer (-0.21 eV) and then trimer (-0.14 eV). The solvation energy of the free water monomer, which was the reference state for all water cluster adsorbates, was -0.31 eV. Thus, the adsorption solvation energy for water monomer was negative and as the cluster size was increased, the adsorption solvation energy resulted

in more positive values (Figure D.5).

In the case of organic adsorbates, the solvation energies of adsorbed acids were around -0.1 eV, while solvation energies of free adsorbates were around -0.3 eV. This led to strongly negative adsorption solvation energies for the acids. The solvation energies of adsorbed and free alcohols were close to each other (around 0.2 eV), giving adsorption solvation energies with small magnitude (-0.06 to -0.04 eV). In the case of acetone, the solvation energy of adsorbed acetone (around -0.3 eV) was more favorable than free acetone (around -0.2 eV) which resulted in a negative adsorption solvation energy. Overall for category IV species, we find that the solvation energies of adsorbed species are correlated to the charge on the adsorbate, and that adsorbed inorganic species, like water and ammonia, tend to have more pronounced solvation energies than organic adsorbates.

Solvation energies of category V adsorbates are very negative, and these aromatics have large positive charges. Adsorbed benzene and toluene show solvation energies around -0.3 eV, which is significantly more negative than their free molecule counterparts (-0.05 eV each). This in turn leads to very negative adsorption solvation energies. Adsorbed aniline has a very positive charge (+0.63) and a solvation energy of -0.64 eV, leading to a highly negative adsorption solvation energy, since free aniline has a solvation energy of only -0.24 eV. The charge on adsorbed aniline is more positive than benzene and toluene by around 0.2. The more positive charge in aniline is due to the presence of electron rich center (-NH_2 group with a lone pair electron) that results in larger charge transfer from aniline to the metal surface, whereas in benzene and toluene such an electron rich center is absent.

The results described in this section cover a broad spectrum of various kinds of adsorbates, and provide valuable insights into understanding the performance of implicit solvation models. Using VASPsol, the effect of solvent on the adsorption process could be explained by comparing the solvation energies of free and adsorbed species. We found that the solvation energies of free adsorbates could be related to the gas phase dipole moments. The

solvation energies of certain adsorbed species were found to be related to their charges upon adsorption (radical, lone-pair bonding, and aromatic adsorbates). Thus our results indicate when the solvation effects may be important and may even rationally predict such effects.

Our results generally agree with published DFT results using implicit solvation models. Behtash et al. modeled CH_xCH_yCO (x=1-3, y=0-2), CH_3, and CH_2 on Pd(111) and used a slightly different solvation energy method than we report. They used free molecules in vacuum as reference (rather than solvated molecules), such that $E_{solv}(X)$ in Equation D.3 is zero. As explained in our methodology, we chose to solvate free species, as this closer mimics the real-world adsorption process. Our re-calculated corresponding solvation energy values using the vacuum free species reference state are in the range of -0.02 to -0.12 eV for CH_xCO and CH_x (x=1-3), which are close to the values reported by Behtash et al. Our calculated adsorption solvation energies of water and methanol (using vacuum reference molecules) are also close to the earlier VASPsol work of Garcia-Rátes and López,[74] with differences in adsorption solvation energies of less than 0.1 eV. The adsorption solvation energies of acetic acid and alcohols (ethanol and methanol) were reported to be 0.2 and ∼0.3 eV earlier.[69,147] Our calculated values agree well (difference of 0.03 eV) for acetic acid but deviate for the alcohol adsorbates by around 0.3-0.4 eV, perhaps due to the atomic orbital basis set used by Wang and Liu when compared to the plane wave basis set used in VASPsol. Finally, the works of Sha et al.[88,90] showed some differences from our current results. The mean absolute difference between our work and theirs for adsorption solvation energies of six ORR intermediates (H, O, OH, O_2, OOH, H_2O) was 0.36 eV with the largest difference being around 0.7 eV for atomic oxygen adsorption. As described earlier in Section D.3.2, we hypothesize that the large solvent effects obtained by Sha et al. may be due to the non-self-consistent determination of solvation energies. Other possible reasons for the differences may be the simulation parameters used by Sha et al., such as Gaussian basis set, norm-conserving pseudopotentials, and a smaller (2x2) unit cell, which are different from the settings used in

our current work.

We also compared our implicit solvation results to explicit solvation results and found good agreement in adsorption solvation energies for several adsorbates. The adsorption solvation energy (with gas phase free adsorbate reference) of -0.23 and -0.21 eV for ethanol and isopropyl alcohol using implicit solvation compares well with that reported explicit adsorption solvation values of -0.27 and -0.26 eV.[148,149] The adsorption solvation energy (again with gas phase free adsorbate reference) of acetone using implicit solvation was calculated in our present work to be -0.37 eV, which is more negative than the -0.18 eV value calculated using explicit solvation on Ru(0001).[10] It is unclear if this difference is due to the solvation model, or the different metal surfaces (Pt versus Ru). In the presence of explicit liquid water, Bodenschatz et al.[32] reported a favorable solvation energy (again with gas phase free adsorbate reference) of -0.12 for the adsorption of CO on Pt(111). Our corresponding implicit solvation energy of -0.04 eV is in reasonable agreement with their explicit liquid solvation results. Rossmeisl et al.[13] reported solvent effects for the adsorption of H, O, and OH species on Pt(111) by modeling the surrounding explicit water as an ice-like bilayer. Rossmeisl et al. reported adsorption/dissociation energies in their work according to the following processes: $1/2H_2 + * \longrightarrow H^*$, $H_2O + * \longrightarrow O^* + H_2$, and $H_2O + * \longrightarrow OH^* + 1/2H_2$. The reference state in these reactions was chosen to be gas phase H_2O and H_2 for both solvated and unsolvated reactions. The corresponding reaction solvation energies (for the above steps, defined as the reaction energy in solvent minus the reaction energy in vacuum) was reported to be 0.00, -0.03, and -0.59 eV respectively. Our respective corresponding reaction solvation energies using implicit solvation were calculated to be 0.00, -0.01, and -0.15 eV. Our results appear to underestimate solvation effects for OH*.

One aspect that is not well described by implicit solvation models is hydrogen bonding, as the literature highlights.[32,66,67,150] Hydrogen bonding, which may occur when using explicit solvation, for instance leads to new adsorption geometries for alcohols as reported by Chibani

et al.[148] and Loffreda et al.[149] Both works reported that the presence of water can change the most stable adsorbed ethanol geometry. Chibani et al.[148] and Loffreda et al.[149] found that the most stable explicitly solvated ethanol does not bind to Pt directly but rather hydrogen bonds with a chemisorbed water molecule. This ethanol geometry was reported to bind 0.27 eV stronger than the unsolvated ethanol.[148] In contrast we observed no such configuration and find that in implicit solvent, ethanol prefers to bind directly to the Pt surface.

Implicit solvation however describes solvent effects for the non-polar adsorbates H* and O* well (with largest deviation of 0.02 eV), as compared to the explicit solvation results of Rossmeisl et al.[13] The good performance of implicit solvation may possibly be due to relatively small interactions between H*/O* with surrounding water. This is in contrast to OH*, which strongly interacts with surrounding water through multiple hydrogen bonds, as several papers using explicit solvation showed.[13,151–153] In order to directly compare the solvent effects predicted by our implicit solvation with explicit solvation of a strongly hydrogen bonding adsorbate like OH*, we modeled OH* in the presence of four water ice-bilayer similar to previous work.[13,32,152] The adsorption solvation energy calculated using explicit solvation for OH* was determined to be -0.33 eV, which is more negative by -0.39 eV compared to implicit solvation (more details in Supplementary information). These comparisons suggest that explicit models may describe solvation differently than implicit models for certain molecules, such as OH* or alcohols, where hydrogen bonding between water and such molecules is important.

D.3.4 Estimation of Adsorption Solvation Energies by using an Artificial Neural Network

We further analyzed our data using machine learning techniques to develop a model to predict adsorption solvation energies $\Delta E_{ads}^{solv}(X^*)$. We used the Weka program[162] with

artificial neural network (ANN) algorithms implementing the feed-forward multilayer perceptron learning method.[163] Our dataset was split so that 66% of our calculated data points were used as a training dataset, and the other 33% as a testing dataset. We considered a number of descriptors as potential inputs to the artificial neural network, including the Bader charge q of adsorbed species in the absence of solvent, gas-phase solvation energy $\Delta E_{solv}(X)$, gas-phase dipole moment, gas-phase polarizability, adsorption energy in vacuum ΔE_{ads}^{vac}, and molecular surface area. We calculated q, ΔE_{ads}^{vac}, and $\Delta E_{solv}(X)$ using VASP/VASPsol, and we obtained the molecular surface area using the COSMO solvation model in NWChem. The gas-phase dipole moment and polarizability were obtained from the NIST computational chemistry database at the PBE/6-311G** level of theory.[150] We created several ANN models, each of which had a different number of potential descriptors as inputs. In each of these models, we tested up to two hidden layers between the input and output layers, each of which contained up to six nodes. We determined that one hidden layer with two nodes showed the least errors in predicting the adsorption solvation energy (further details can be found in the Supporting Information). Our final model that we report had the least number of descriptors while still giving a good fit to our data.

Figure 7 show the results of our best ANN model, in which q, $\Delta E_{solv}(X)$, dipole moment, and surface area were used as input descriptors. This model had a correlation coefficient R of 0.93 with a mean absolute error of 0.037 eV. We also tried other combinations of input descriptors and found that another model with q, $\Delta E_{solv}(X)$, dipole moment, and polarizability as inputs had a correlation coefficient of 0.89 with a mean abso- lute error of 0.037 eV. The relative absolute error was 37.5% for the model in Figure 7. This relatively large absolute error could be attributed to several potential factors. The mean absolute errors are small (<0.04 eV), but the target ΔE_{ads}^{solv} values are ads also small (-0.29 to 0.17 eV), and hence relative absolute errors are on the order of 37%. Moreover, our training dataset only contains 41 data points, and a more robust dataset may lead to a better model. Finally,

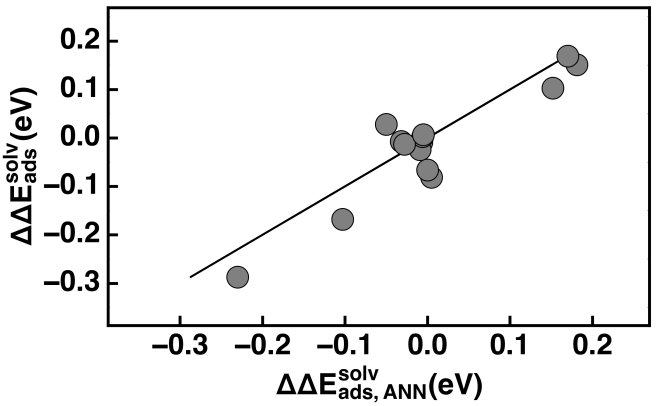

Figure D.7: Comparison of adsorption solvation energies ΔE_{ads}^{solv} calculated by the artificial neural network and from our DFT calculations. Shown are data from the testing set. The Bader charge of adsorbed species with no solvent present q, solvation energy of free species $\Delta E_{solv}(X)$, gas-phase dipole moment, and molecular surface area of the free species were used as inputs to the model.

it is possible that there may be other, unspecified effective input descriptors. Nonetheless, our model does obtain a suitable fit to the DFT data and indicates that several gas-phase descriptors (as well as adsorbate charge) may be useful in determining adsorption solvation effects. These descriptors (e.g. charge of adsorbed molecules, dipole moment, and molecular surface area) are all expected to influence solvation energies. This work gives insight into how molecular properties can influence solvation effects for adsorbed species, and these properties can even be used to predict these effects, as shown in Figure 7.

D.3.5 Implicit Solvation for Reactions

The role of aqueous phase for reactions on metal surfaces could be crucial, as the presence of water could affect the reaction energy landscape significantly. We looked at the effect of water on various reactions compared to simply ignoring the water phase. We considered several reactions that were relevant for fuel cells, such as oxygen reduction reaction (ORR), formic acid oxidation, and alcohol oxidation (C-H and C-C cleavage steps). We also studied the effect of liquid-phase on the water gas shift reaction, which finds important applications in H_2

production and Fischer-Tropsch synthesis. All the reported solvent effects were determined using VASP/VASPsol with water solvent. Figure D.8 shows a summary of our results for vacuum and water-solvated surfaces. All the surface species appearing in the reactions shown in Figure D.8 were adsorbed in the most stable adsorption sites based on previous literature. More information on these adsorption sites can be found in Table E.5 in the Supplementary Information.

Oxygen Reduction Reaction The oxygen reduction reaction is a widely studied and important electrocatalytic reaction. The ORR can occur through several different pathways such as direct dissociation of O_2, formation of intermediates like OOH (hydroperoxy), or formation of HOOH (hydrogen peroxide) which undergoes O-O bond cleavage to form hydroxyl/atomic oxygen. Tripkovic et al.[37] reported that the ORR mechanism involving the formation of the hydroperoxy radical is thermodynamically and kinetically more favorable compared to other mechanisms. We thus chose this pathway involving hydroperoxy radical in our work to study the effect of the presence of water on ORR.

The potential energy surface (PES) of the ORR through the hydroperoxy intermediate is shown in Figure D.8a. The zero energy level corresponds to the state of free H_2, free O_2, and clean Pt(111) surface, which are either unsolvated or solvated depending upon the PES in vacuum or in water respectively. The clean surface formed in a reaction (e.g. O_2*+4H* $\longrightarrow$ OOH*+3H*+*) is not shown for clarity. The reaction starts by the adsorption of O_2 and $2H_2$ with $2H_2$ dissociating into 4H*. For simplicity these two reactions are combined and represented as O_2*+4H*. These surface H* species are consumed during the reduction of O_2*. The following reaction involves hydrogenation of O_2* to form a hydroperoxy (OOH*) radical. The hydroperoxy radical then undergoes O-O cleavage to form O* and OH*. The OH* intermediate is subsequently reduced to form H_2O*, which eventually desorbs. The O* intermediate forms OH* in reaction step 6, which is further reduced to H_2O*, and finally

desorbed H_2O. We found our results in vacuum to be in good agreement with the work of Xiao et al.[135] The mean absolute difference between the reaction energies for the above listed reactions that we calculated and Xiao et al. was found to be 0.12 eV.

For the current discussion we use the term reaction energy to mean the difference in energy of one energy level in the PES (e.g. OOH*+3H*) and the previous energy level (e.g. O_2*+4H*), or the energy for a specific reaction step (O_2* + 4H* $\longrightarrow$ OOH*+3H*+*). We quantify the solvent effect on a reaction energy by calculating the difference in reaction energy in vacuum and in solvent for a given reaction step i, as given in Equation D.5.

$$\Delta\Delta E^{solv}_{rxn-i} = \Delta E_{rxn-i}(solv) - \Delta E_{rxn-i}(vacuum) \tag{D.5}$$

A negative value of $\Delta\Delta E^{solv}_{rxn-OOH*}$ indicates the reaction step is more favorable in the presence of water, while a positive value indicates an unfavorable effect on the reaction step in the presence of water. Since different reactants may be at different energy levels in vacuum and solvent, $\Delta\Delta E^{solv}_{rxn-OOH*}$ values allow a direct comparison of how solvent effects a particular reaction. The effect of water on the PES and on the reaction energies within the PES is shown in the left and right columns of Figure D.8 respectively. Individual energy levels (relative to the appropriate reference states) may change in vacuum or solvent, as the left plots show. The reaction energies (differences in energies for intermediate states) may also change in solvent, as the right plots in Figure D.8 show.

We observe that generally the PES levels for ORR are all more negative in solvent when compared to vacuum, as indicated by the red lines (solvent) being lower in level than black lines (vacuum). The solvated PES is strongly downhill compared to vacuum energy levels after reaction step 4 when adsorbed or free water appear as products. This large solvation effect on the latter reaction steps is largely a result of the strong solvation energy for the free water (-0.31 eV) and the adsorbed water (-0.34 eV). Whenever water is a product, this

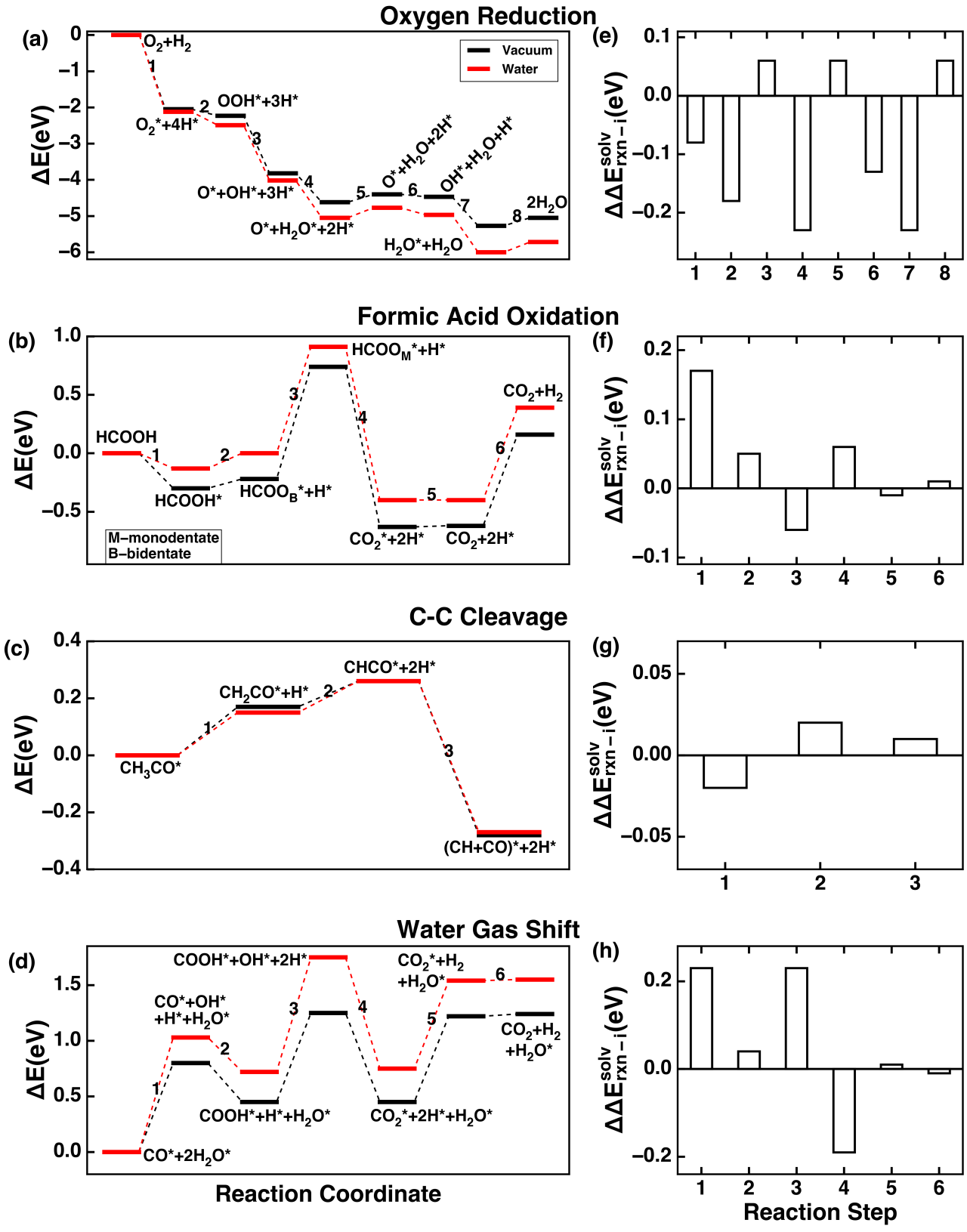

Figure D.8: Potential energy surfaces (left plots) in the presence of implicit water (red lines) and vacuum (black lines), and solvation energies for individual reaction steps (right plots). Each row corresponds to one reaction: (a) and (e) oxygen reduction reaction, (b) and (f) formic acid decomposition, (c) and (g) C–C cleavage of a C_2 organic molecule, and (d) and (h) water gas shift reaction. The reaction steps i in the right plots correspond to the numbered reactions in the left plots. The energies corresponding to zero eV are described in

solvent effect lowers the solvated energy levels, which is why the later steps of the PES are much lower in energy in solvent compared to in vacuum. In the PES only certain reaction steps such as 2, 4, 6, and 7 are affected strongly by water as shown in Figure D.8e. OOH* formation (reaction step 2), H_2O* formation (reaction steps 4 and 7), and OH* formation (reaction step 6) were all found to be more favorable in water with $\Delta\Delta E^{solv}_{rxn-i}$ values of -0.18, -0.23, and -0.13 eV respectively. The effect of water solvent on all the other reaction steps was small, with magnitudes of ≤ 0.08 eV. In addition to the formation of adsorbed or free water as products, formation of OOH* and OH* as products in the presence of water resulted in favorable $\Delta\Delta E^{solv}_{rxn-i}$ values since OOH* and OH* adsorbates are favorably solvated in water. These three adsorbates are polar adsorbates that result in favorable solute-solvent interactions leading to favorable solvation effects on the oxygen reduction reaction.

The solvent effects predicted by our work are in good agreement with results reported by Fortunelli et al.[86] using the SCCS solvation model.[78] The mean absolute difference in $\Delta\Delta E^{solv}_{rxn-i}$ values for a set of reactions was found to be 0.04 eV. These reactions included O_2 dissociation (O_2*$\longrightarrow$ 2O*), OOH formation, OOH dissociation, H_2O formation, OH formation, and O hydration (O*+H_2O* $\longrightarrow$ 2OH*). However, the solvent effects that we observed are significantly smaller compared to the results obtained from the APBS solvation model[86,88] and Jaguar's Poisson Boltzmann solver,[91,136] possibly for reasons mentioned in Section D.3.2. We also compared the reaction energies of the above listed reactions with results by Zope et al.[3] who modeled the reactions in the presence of explicit solvation consisting of four layers of ice-like bilayers. For the reactions O_2 dissociation, OH formation, H_2O formation, OOH formation, O_2 hydration (O_2*+H_2O* $\longrightarrow$ OOH*+OH*), and OOH dissociation, the mean absolute difference between their explicit and our implicit $\Delta\Delta E^{solv}_{rxn-i}$ energies is 0.15 eV. Here, $\Delta\Delta E^{solv}_{rxn-i}$ for the above listed reactions from our work (and the results of Zope et al.) in order are 0.01 (0.04), -0.13 (-0.34), -0.23 (-0.29), -0.18 (-0.32), 0.05 (-0.34), and 0.06 (0.02) eV. The solvent effects calculated using the implicit solvation is

comparable for several reactions except O_2 hydration that differs by 0.39 eV from the explicit solvation results of Zope et al. In contrast, the $\Delta\Delta E^{solv}_{rxn-i}$ energy for O_2* dissociation was found to be -1.2/-1.4 eV by APBS/Poison implicit solvation models. The close agreement between our implicit and Zope et al.'s explicit solvation results for O_2 dissociation maybe due to non-polar O_2* and O* appearing in this reaction, which are described well by implicit solvation. In the case of H_2O formation (OH*+H*$\longrightarrow$ H_2O*) and OOH dissociation (OOH* $\longrightarrow$ OH*+H*), the very close solvent effects between our implicit solvation model and explicit solvation results of Zope et al. may be due to cancellation of strong solvent effects of explicitly solvated OH*/H_2O* and OOH*/OH* in each reaction. Such a cancellation of strong solvent effects does not occur in the case of O_2 hydration (O_2*+H_2O* $\longrightarrow$ OOH*+OH*), as all the adsorbates other than O_2 are capable of forming strong hydrogen bonds under explicit solvation. The hydrogen bonding of reactants and products thus do not cancel and there is a larger number of hydrogen bonds for products. This indicates one potential shortcoming of implicit solvation in describing chemical species where hydrogen bonding may be involved.

Formic acid oxidation We next consider formic acid oxidation, which is an important electrocatalytic reaction in formic acid fuel cells. Experimental results have shown adsorbed formate on Pt surface to be an important intermediate that is formed during the oxidation of formic acid.[154] DFT studies focused on the formic acid oxidation pathway involving the formation of formate species suggested that oxidation of formic acid to a bidentate formate and subsequent rotation to a monodentate formate followed by dehydrogenation to CO_2 was the favorable reaction pathway.[155–157] Based on these experimental and DFT results, we consider the reaction pathway involving bidentate and monodentate formate in our present work.

The PES for formic acid oxidation is shown in Figure D.8b. The zero energy level corresponds to the sum of the energy of free formic acid and clean Pt(111) surface. Formic acid

oxidation begins with the adsorption of HCOOH on Pt(111), which is exothermic with a value of -0.30 eV in vacuum. The adsorption is followed by a slightly endothermic dehydrogenation step (0.09 eV) leading to the formate species adsorbed through two O-Pt bonds in a bidentate configuration ($HCOO_B$). The next reaction step is thermodynamically unfavorable as this step is uphill by 0.96 eV in vacuum, where the bidentate configuration rotates to form a monodentate configuration ($HCOO_M$) with a single O-Pt bond. The subsequent reaction step is dehydrogenation of $HCOO_M$ to form CO_2*, which easily desorbs to form the final product CO_2. Our reaction energies for the adsorption of formic acid, dehydrogenation reactions, rotation of monodentate to bidentate formate, and CO_2 formation in vacuum are in close agreement with the work of Hu et al.[157] with a mean absolute difference of 0.05 eV.

Water solvent increases the energy levels in the PES relative to vacuum. Of all the reaction steps however, only reaction step 1 (HCOOH adsorption) is strongly affected by water solvent, with a $\Delta\Delta E^{solv}_{rxn-i}$ value of 0.17 eV, as shown in Figure D.8f. For all the subsequent reactions, the effect of solvent on the reaction energies is negligible. The absolute mean $\Delta\Delta E^{solv}_{rxn-i}$ value for the steps involving adsorbed species (i.e. surface reactions) was 0.04 eV. The smallest $\Delta\Delta E^{solv}_{rxn-i}$ value was 0.01 eV (for H_2 formation), while the largest $\Delta\Delta E^{solv}_{rxn-i}$ value was -0.06 eV (for $HCOO_M$ formation). The small solvent effect from reaction step 2 shows that the offset in the PES between vacuum and solvent results is due to the first step, HCOOH adsorption. Essentially our results show that reaction steps on the surface involving formate, CO_2, and H species are all weakly affected by any aqueous phase. The large HCOO* molecule has weak interactions with the solvent, as the favorable solvent-solute interactions between the polar part of the molecule (O-C-O) and surrounding solvent may be screened by the Pt surface. CO_2* and H* also weakly interact with the solvent due to a combination of low dipole moment and small size of solute cavity.

Other DFT work using an explicit solvation approach to study formic acid oxidation[69,155,156] however showed stronger solvation effects. The $\Delta\Delta E^{solv}_{rxn-i}$ values reported by Gao et al.[155,156]

using one ice-like bilayer for the C-H cleavage of adsorbed monodentate formate or O-H cleavage of adsorbed formic acid were reported to be 0.34 eV and -0.33 eV respectively. For the latter reaction (O-H cleavage of formic acid), $\Delta\Delta E^{solv}_{rxn-i}$ values of -0.1 to -0.2 eV were reported by Wang and Liu[69] using a hybrid solvation model (a combination of implicit and explicit solvation) with up to six water molecules. On the contrary, the $\Delta\Delta E^{solv}_{rxn-i}$ values for O-H cleavage of adsorbed monodentate and C-H cleavage of adsorbed formic acid are estimated in the current work using implicit solvent to be 0.05 (reaction step 2) and 0.06 eV (reaction step 4), respectively. Our implicit solvation effects are thus different from previous work using explicit solvation for O-H and C-H cleavage reactions. Strong hydrogen bonding was reported to occur, and such hydrogen bonding is not well described by implicit solvation approaches.

C-C cleavage in alcohol oxidation The next reaction we studied is C-C cleavage, which can be an important step in higher alcohol oxidation. C-C cleavage is believed to be the rate determining step in electrocatalytic ethanol oxidation,[17,158–160] which may occur at the anode of a fuel cell. On Pt(111), the C-C bond of ethanol has been reported to break through intermediates such as CH_xCO*(x=1-3).[158,160–162] We consider the effect of water on C-C cleavage through a CHCO* intermediate (starting with CH_3CO which dehydrogenates to form CHCO), which was reported to have a lower activation barrier compared to other CH_xCO intermediates for ethanol decomposition.[161,162]

We started the reaction process with an adsorbed intermediate CH_3CO; previous steps involving ethanol were ignored in our comparison. The PES's of CH_3CO* formation of coadsorbed (CH+CO)* in the presence of vacuum and water are shown in Figure D.8c. The zero energy level corresponds to the sum of energies of CH_3CO* and clean Pt(111) surface. The PES of the C-C cleavage reaction consists of two endothermic steps where C-H bonds of CH_xCO* species are cleaved successively, with reaction energies of 0.17 and 0.09 eV in

vacuum.C-C cleavage of CHCO* to form coadsorbed CH*(hcp site) and CO*(top site) was exothermic with a vacuum reaction energy of -0.54 eV. Our values are in close agreement with Sheng et al.,[161] with the largest deviation being 0.04 eV for the dehydrogenation of CH_2CO*. The effect of water does not affect the PES much, as both solvated and vacuum PES's lie very close in energy. This small solvent effect is also shown in terms of $\Delta\Delta E^{solv}_{rxn-i}$ values, which are all less than a magnitude of 0.02 eV, as shown in Figure D.8g. We attribute this small solvent effect to the weakly polar nature of CH_x and CO species. Figure D.5 shows that CH_3 and CH_2 have small adsorption solvation energies, as does CO. Our results are similar to the work of Behtash et al.,[81] who reported a small implicit solvent effect (less than 0.1 eV) on the C-H and C-C cleavage reactions of propanoic acid on Pd(111).

The literature suggests that the type of chemical group of an adsorbate that is exposed to the aqueous environment for hydrogen bonding may affect reaction energies. Herron et al.[163] reported dehydrogenation of methanol in the presence of explicit solvation on Pt(111) using AIMD. Under explicit solvation, the hydroxyl group (OH) in both adsorbed methanol and hydroxymethyl (CH_2OH*) was exposed to the aqueous environment and formed a hydrogen bond with the neighboring water molecule. Adsorbed methoxy on the other hand, with exposed methyl group away from the surface into the aqueous environment, showed no hydrogen bonds with neighboring water molecules. The small solvent effect ($\Delta\Delta E^{solv}_{rxn-i}$=0.06eV) in the dehydrogenation of adsorbed methanol to hydroxymethyl is a result of similar solvent effects on both the reactant and the product species, which all have one hydrogen bond. However, the solvent effect on the dehydrogenation of adsorbed methanol to methoxy was strong ($\Delta\Delta E^{solv}_{rxn-i}$=0.77 eV), which Herron et al. attribute to the reactant being more stabilized by the hydrogen bond compared to the product species that does not form a hydrogen bond. To directly compare the performance of implicit solvation, we calculated the same reaction and found the $\Delta\Delta E^{solv}_{rxn-i}$ to be 0.20 eV, which predicts the trend correctly but it underestimates the solvation effect by 0.57 eV compared to the values of Herron et al.

Zope et al.[3] reported explicit solvation results of oxygen reduction reaction, which also showed strong solvent effects on reactions when the stabilization through hydrogen bonding of reactants compared to products is different. For example, the $\Delta\Delta E^{solv}_{rxn-i}$ for the reaction O*+H* $\longrightarrow$ OH* was -0.34 eV, while $\Delta\Delta E^{solv}_{rxn-i}$ for the reaction OOH*$\longrightarrow$ OH*+O* was 0.02 eV. Zope et al. did not discuss hydrogen bonding, but in the two reactions OH* and OOH* are likely strongly stabilized through hydrogen bonds as shown by Jinnouchi et al[151] and Tripkovic et al.[37] Other reaction species are less stabilized by hydrogen bonding which results in a favorable solvation effect for the OH* formation reaction while the favorable solvent effects cancel out in the OOH* dissociation reaction. It appears that implicit solvation may work well for reactions where the stabilization of the reactant and product species by aqueous phase are similar. However, as shown above for the dehydrogenation of methanol to methoxy, when the aqueous phase stabilization of one reactant or product differs from that of the other reactants or products, implicit solvation may underestimate the solvent effects. A similar explanation based on change in number of hydrogen bonds between the reactant and transition state was reported by Zope et al.[3] for explaining the solvent effect on the activation energies of alcohol oxidation.

Water gas shift Finally we considered the role of solvation on the water gas shift reaction. Grabow et al.[164] examined several pathways for the water gas shift reaction on Pt(111). They reported that the most energetically favorable mechanism proceeds through a COOH* intermediate assisted by OH* to form CO_2 and H_2O. We therefore modeled this reaction mechanism. In Figure D.8d, the zero energy level corresponds to CO* and $2H_2O$*. In vacuum, the reaction proceeds via H_2O* dissociation to form OH* and H*, which was uphill by 0.80 eV. The water-dissociated OH* reacts with CO* to form COOH* in reaction step 2, which is exothermic by -0.35 eV. Once COOH* forms, the other H_2O* dissociates in reaction step 3 to provide OH* that reacts with COOH* to form CO_2* in reaction step 4. Reaction

step 4 was exothermic by -0.81 eV indicating the reaction of OH* with COOH* to form CO_2* is favorable. The 2H* and CO_2* subsequently desorbs as H_2 and CO_2 in reaction step 5 and 6 with a reaction energy of 0.77 and 0.01 eV respectively.

Figure D.8d shows the effect of implicit water on the PES. Overall, the PES solvated energy levels lie above vacuum levels, indicating a potential unfavorable solvent effect. However, only certain reaction steps are significantly affected by the presence of water. The reaction steps 1, 3, and 4 are the most affected by the presence of water with $\Delta\Delta E^{solv}_{rxn-i}$ values of 0.23, 0.23, and -0.19 eV, respectively, as shown in Figure D.8h. The reaction steps 1 and 3 are both water dissociation steps, where the energy levels of the products (OH*+H*) are higher in the presence of water compared to vacuum. In the case of reaction step 4, COOH* oxidation in the presence of water is more favorable than vacuum as the solvated energy levels are lower. Since the polar adsorbate H_2O* induces strong solvent effects, H_2O* appearing as a product (or a reactant) in reaction step 4 (or reaction steps 1 and 3) makes the reaction more (or less) favorable in water compared to vacuum.

Gong et al.[137] modeled the water gas shift reaction proceeding through the COOH intermediate in the presence of explicit water. The $\Delta\Delta E^{solv}_{rxn-i}$ value for CO*+OH* $\longrightarrow$ COOH* in the presence of explicit water was reported to be positive by around 0.5 eV. Our results on the reaction energy for the same reaction using implicit solvation was found to be almost thermoneutral (0.04 eV) indicating that our implicit solvation effects are underestimated compared to the reported explicit solvation values. The reported positive solvent effect may be due to the stronger stabilization of the reactant OH* through strong hydrogen bonding compared to the stabilization of the solvated product COOH*. Such an effect associated with strong hydrogen bonding seems to be not captured well by implicit solvation.

D.3.6 Role of Different Implicit Solvents

Up to this point we have only reported results using water as the solvent. We now briefly examine how the implicit solvation model treats other solvents. While water is the most common liquid phase present in catalysis, other liquids may also be used. For instance, it was recently reported by Fortunelli et al.[86,165] that tuning the solvent dielectric constant can result in a faster ORR rate. We considered three different characteristic solvents: CCl_4 (non-polar), CH_3CN (polar aprotic), and H_2O (polar protic). A primary parameter controlling the solvent model in the implicit approach is the solvent dielectric constant. The dielectric constants used for these solvents were 2.2, 38.8, and 78.4 for CCl_4, CH_3CN, and H_2O, respectively.

Figure D.9 shows the effect of changing the solvent dielectric constant on the adsorption of different species over Pt. The magnitude (or absolute value) of adsorption solvation energies monotonously increase from the low dielectric solvent (carbon tetrachloride) to the high dielectric solvent (water). The results show that adsorption solvation energies that are positive in CCl_4 tend to become more positive with increasing dielectric constant, while adsorption solvation energies that are negative in CCl_4 tend to become more negative with increasing dielectric constant. Moreover, the adsorption solvation energies at a moderate dielectric constant (38.8) are very similar to these energies at higher dielectric constant (78.4). The mean absolute difference between adsorption solvation energies in water and acetonitrile is 0.04 eV.

The differences in the adsorption solvation energies at low and high dielectric constant can be explained in part by the extent to which the solvent polarizes the solute. The polarization of a solute, such as an adsorbed or free adsorbate, in a low dielectric constant solvent, such as carbon tetrachloride, is weak. To understand this further, as before, the adsorption solvation energy can be decomposed into solvation energy of the free species $\Delta E_{solv}(X)$, clean Pt(111) surface $\Delta E_{solv}(*)$, and adsorbed species $\Delta E_{solv}(X*)$ (see Scheme D.1 and Equation D.3). We

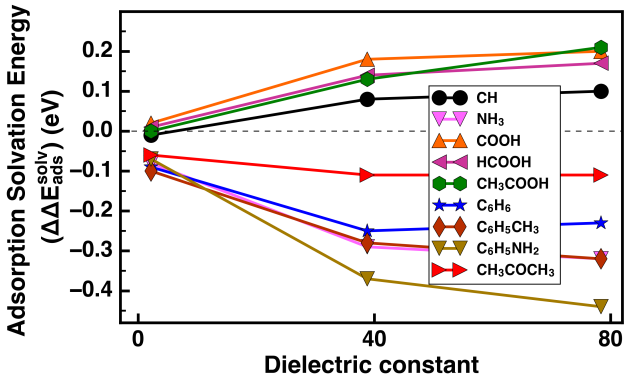

Figure D.9: Calculated adsorption solvation energies of different adsorbed species as a function of dielectric constant, characteristic of three different solvents: CCl_4, CH_3CN, and H_2O with dielectric constants 2.2, 38.8, and 78.4 respectively.

found that in carbon tetrachloride absolute values for the free adsorbate solvation energies and clean surface solvation energies were less 0.06 eV and 0.07 eV, respectively. This small effect of the solvent is due to the non-polar nature of carbon tetrachloride, which does not polarize the solute significantly. The solvation energies of any adsorbed species in carbon tetrachloride were calculated to be near -0.2 eV or smaller, which in comparison to water as solvent is relatively weak. In water, for instance solvation energies of adsorbates are as large as -0.64 eV (see Figure D.6d).

We do also observe a change in the electronic properties of the adsorbates when comparing one solvent versus another. For instance, some adsorbates showed strong solvent effects in water. We found that the Bader charges of adsorbed ammonia, toluene, and aniline decreased from -0.39, -0.41, -0.63 to -0.30, -0.20, -0.31 electrons, respectively, when the solvent changed from high dielectric constant (water) to low dielectric constant (carbon tetrachloride).

The trends obtained in our work related to different solvents are consistent with the previous work of Gunceler et al.[75] using JDFTx, who reported a monotonously increasing effect of solvent on ionic surfaces with increasing solvent dielectric constant. A stronger solvent effect for solvents with higher dielectric constant compared to solvents with lower dielectric

constant has also been reported earlier.[81,82,166] Adsorption solvation energies calculated in our work agree with the values reported by Fortunelli et al.[165] (who used the APBS solvation model) at the lower dielectric limit (∼2). However, at higher dielectric values, they observe a significantly larger solvation effect compared to our results. A possible cause of this discrepancy is discussed in Section D.3.2. Zuo et al.[166] in contrast to our work reported a reduction in the magnitude of Mulliken charge by around 0.2 electrons for CO adsorbed on Cu surfaces when solvent changed from low dielectric constant (liquid paraffin) to higher dielectric constant (chloroform). This may possibly be due to the Mulliken charge analysis in their work, which is sensitive to the choice of basis set.

D.4 Conclusions

We have assessed how solvation models can be used to describe chemistry and catalysis on a Pt(111) surface in contact with an aqueous phase. The implicit solvent models implemented in VASP (VASPsol), JDFTx, and NWChem (COSMO) were compared, and all of these solvent models predict fairly consistent solvation effects for adsorption. Studying the role of solvation in the adsorption of 41 representative adsorbates on Pt(111) using VASP allowed us to find correlations and trends in the solvation energies. We found that both dipole moment and charge of adsorbed species could explain solvation behavior on adsorption for several types of atomic and molecular species. Our results may thus indicate when solvent effects may be important and when they may be negligible on the basis of the adsorbate and its chemical nature. We further found good prediction of adsorption solvation energies by using an artificial neural network with descriptors such as Bader charge, solvation energy of the free adsorbate, dipole moments, and molecular surface area/polarizability. We also examined the role of solvation in several reactions: oxygen reduction, formic acid oxidation, C-C cleavage, and water gas shift. Our results show that solvation changes reaction energies by up to 0.23

eV. Implicit solvation results agree with explicit solvation results from the literature when adsorption or a reaction involves nonpolar adsorbates. However, our results do suggest that certain cases in which hydrogen bonding may be important are not described well by implicit solvation models. When implicit solvation fails for hydrogen bonding, a possible way to account for the hydrogen-bonding effects may be by including a few explicit water molecules along with implicit solvation (a hybrid approach). Finally, we briefly studied solvents other than water and found that solvation effects decrease with decreasing dielectric constant. Our work not only provides useful insights into and guidelines on how to better model aqueous phases over metals, which are important for a number of catalytic and industrially relevant systems, but also assesses the utility of computationally cheap implicit solvation models implemented in several popular DFT codes.

Bibliography

[1] M. Besson and P. Gallezot, *Catalysis Today*, 2000, **57**, 127–141.

[2] T. Mallat and A. Baiker, *Chemical Reviews*, 2004, **104**, 3037–3058.

[3] B. N. Zope, D. D. Hibbitts, M. Neurock and R. J. Davis, *Science (New York, N.Y.)*, 2010, **330**, 74–8.

[4] R. A. Ojifinni, N. S. Froemming, J. Gong, M. Pan, T. S. Kim, J. M. White, G. Henkelman and C. B. Mullins, *Journal of the American Chemical Society*, 2008, **130**, 6801–6812.

[5] J. Gong, *Chemical reviews*, 2011, **112**, 2987–3054.

[6] D. D. Hibbitts, B. T. Loveless, M. Neurock and E. Iglesia, *Angewandte Chemie - International Edition*, 2013, **52**, 12273–12278.

[7] R. D. Cortright, R. R. Davda and J. A. Dumesic, *Nature*, 2002, **418**, 964–7.

[8] R. R. Davda, J. W. Shabaker, G. W. Huber, R. D. Cortright and J. a. Dumesic, *Applied Catalysis B: Environmental*, 2005, **56**, 171–186.

[9] M. a. Mellmer, J. M. R. Gallo, D. Martin Alonso and J. a. Dumesic, *ACS Catalysis*, 2015, 3354–3359.

[10] C. Michel, J. Zaffran, A. M. Ruppert, J. Matras-Michalska, M. Jedrzejczyk, J. Grams and P. Sautet, *Chem. Commun.*, 2014, **50**, 12450–12453.

[11] J. N. Chheda, Y. Roman-Leshkov and J. a. Dumesic, *Green Chemistry*, 2007, **9**, 342.

[12] J. K. Nø rskov, J. Rossmeisl, A. Logadottir, L. Lindqvist, J. R. Kitchin, T. Bligaard and H. Jónsson, *Journal of Physical Chemistry B*, 2004, **108**, 17886–17892.

[13] J. Rossmeisl, J. K. Nø rskov, C. D. Taylor, M. J. Janik and M. Neurock, *The journal of physical chemistry. B*, 2006, **110**, 21833–21839.

[14] M. J. Janik, C. D. Taylor and M. Neurock, *Journal of The Electrochemical Society*, 2009, **156**, B126.

[15] A. Frassoldati, C. Pinel and M. Besson, *Catalysis Today*, 2011, **173**, 81–88.

[16] M. Daté, M. Okumura, S. Tsubota and M. Haruta, *Angewandte Chemie International Edition*, 2004, **43**, 2129–2132.

[17] R. Kavanagh, X. M. Cao, W. F. Lin, C. Hardacre and P. Hu, *Angewandte Chemie - International Edition*, 2012, **51**, 1572–1575.

[18] C. Michel, F. Auneau, F. Delbecq and P. Sautet, *ACS Catalysis*, 2011, **1**, 1430–1440.

[19] X. Nie, W. Luo, M. J. Janik and A. Asthagiri, *Journal of Catalysis*, 2014, **312**, 108–122.

[20] X. Nie, M. R. Esopi, M. J. Janik and A. Asthagiri, *Angewandte Chemie (International ed. in English)*, 2013, **52**, 2459–62.

[21] Y. Yoon, R. Rousseau, R. S. Weber, D. Mei and J. a. Lercher, *Journal of the American Chemical Society*, 2014, **136**, 10287–10298.

[22] S. Storsater, O. Borg, E. Blekkan and A. Holmen, *Journal of Catalysis*, 2005, **231**, 405–419.

[23] M. Daté and M. Haruta, *Journal of Catalysis*, 2001, **201**, 221–224.

[24] A. K. Dalai and B. H. Davis, *Applied Catalysis A: General*, 2008, **348**, 1–15.

[25] N. E. Tsakoumis, M. Rønning, Ø. Borg, E. Rytter and A. Holmen, *Catalysis Today*, 2010, **154**, 162–182.

[26] A. M. Hilmen, D. Schanke, K. F. Hanssen and A. Holmen, *Applied Catalysis A: General*, 1999, **186**, 169 – 188.

[27] P. J. Van Berge, J. Van De Loosdrecht, S. Barradas and A. M. Van Der Kraan, *Catalysis Today*, 2000, **58**, 321–334.

[28] D. a. H. Cunningham, W. Vogel and M. Haruta, *Catalysis Letters*, 1999, **63**, 43–47.

[29] M. a. Bollinger and M. A. Vannice, *Applied Catalysis B: Environmental*, 1996, **8**, 417–443.

[30] D. Cao, G. Q. Lu, a. Wieckowski, S. a. Wasileski and M. Neurock, *Journal of Physical Chemistry B*, 2005, **109**, 11622–11633.

[31] A. Wieckowski and M. Neurock, *Advances in Physical Chemistry*, 2011, **2011**, No. 907129.

[32] C. J. Bodenschatz, S. Sarupria and R. B. Getman, *The Journal of Physical Chemistry C*, 2015, **119**, 13642–13651.

[33] B. S. Akpa, C. D'Agostino, L. F. Gladden, K. Hindle, H. Manyar, J. McGregor, R. Li, M. Neurock, N. Sinha, E. H. Stitt, D. Weber, J. A. Zeitler and D. W. Rooney, *Journal of Catalysis*, 2012, **289**, 30–41.

[34] T. Sheng, W.-F. Lin, C. Hardacre and P. Hu, *The Journal of Physical Chemistry C*, 2014, **118**, 5762–5772.

[35] Y. Gohda, S. Schnur and A. Groß, *Faraday Discussions*, 2009, **140**, 233.

[36] M. Neurock, M. Janik and A. Wieckowski, *Faraday Discuss.*, 2009, **140**, 363–378.

[37] V. Tripković, E. Skúlason, S. Siahrostami, J. K. Nø rskov and J. Rossmeisl, *Electrochimica Acta*, 2010, **55**, 7975–7981.

[38] P. J. Feibelman, *Science (New York, N.Y.)*, 2002, **295**, 99–102.

[39] a. Michaelides, *Applied Physics A: Materials Science and Processing*, 2006, **85**, 415–425.

[40] C. D. Taylor and M. Neurock, *Current Opinion in Solid State and Materials Science*, 2005, **9**, 49–65.

[41] K.-Y. Yeh, S. a. Wasileski and M. J. Janik, *Physical chemistry chemical physics : PCCP*, 2009, **11**, 10108–10117.

[42] S. Schnur and A. Groß, *New Journal of Physics*, 2009, **11**, 125003.

[43] I. Hamada and Y. Morikawa, *Journal of Physical Chemistry C*, 2008, **112**, 10889–10898.

[44] L. Árnadóttir, E. M. Stuve and H. Jónsson, *Chemical Physics Letters*, 2012, **541**, 32–38.

[45] S. Wippermann and W. G. Schmidt, *Physical Review B*, 2008, **78**, 235439.

[46] B. M. Ward and R. B. Getman, *Molecular Simulation*, 2014, **40**, 678–689.

[47] C. Hartnig, J. Grimminger and E. Spohr, *Journal of Electroanalytical Chemistry*, 2007, **607**, 133–139.

[48] C. Hartnig, J. Grimminger and E. Spohr, *Electrochimica Acta*, 2007, **52**, 2236–2243.

[49] C. Hartnig and E. Spohr, *Chemical Physics*, 2005, **319**, 185–191.

[50] Y. Qi, J. Gao, D. Zhang and C. Liu, *RSC Adv.*, 2015, **5**, 21170–21177.

[51] K. a. Schwarz, R. Sundararaman, T. P. Moffat and T. Allison, *Phys. Chem. Chem. Phys.*, 2015, **17**, 20805–20813.

[52] P. O. Bedolla, G. Feldbauer, M. Wolloch, C. Gruber, S. J. Eder, N. Doerr, P. Mohn, J. Redinger and A. Vernes, *Journal of Physical Chemistry C*, 2014, **118**, 21428–21437.

[53] R. Cortese, R. Schimmenti, N. Armata, F. Ferrante, A. Prestianni, D. Duca and D. Y. Murzin, *Journal of Physical Chemistry C*, 2015, **119**, 17182–17192.

[54] L. Árnadóttir, E. M. Stuve and H. Jónsson, *Surface Science*, 2012, **606**, 233–238.

[55] Y.-C. Zhang, R.-P. Ren, S.-Z. Liu, Z.-J. Zuo and Y.-K. Lv, *RSC Adv.*, 2016, **6**, 15127–15136.

[56] T. Roman and A. Groß, *Catalysis Today*, 2013, **202**, 183–190.

[57] S. Sakong, M. Naderian, K. Mathew, R. G. Hennig and A. Groß, *The Journal of Chemical Physics*, 2015, **142**, 234107.

[58] L. Yu, X. Pan, X. Cao, P. Hu and X. Bao, *Journal of Catalysis*, 2011, **282**, 183–190.

[59] Y. J. Wang, P. Hu and X. L. Ma, *Physical chemistry chemical physics : PCCP*, 2013, **15**, 17112–7.

[60] J. Liu, X.-M. Cao and P. Hu, *Phys. Chem. Chem. Phys.*, 2014, **16**, 4176–4185.

[61] P. B. Balbuena, R. Callejas-Tovar, P. Hirunsit, J. M. Martínez De La Hoz, Y. Ma and G. E. Ramírez-Caballero, *Topics in Catalysis*, 2012, **55**, 322–325.

[62] A. Lyalin, A. Nakayama, K. Uosaki and T. Taketsugu, *Physical chemistry chemical physics : PCCP*, 2013, **15**, 2809–20.

[63] Y. Okamoto, O. Sugino, Y. Mochizuki, T. Ikeshoji and Y. Morikawa, *Chemical Physics Letters*, 2003, **377**, 236–242.

[64] T. R. Mattsson and S. J. Paddison, *Surface Science*, 2003, **544**, 1–6.

[65] C. J. Cramer and D. G. Truhlar, *Chemical Reviews*, 1999, **99**, 2161–2200.

[66] J. Tomasi, B. Mennucci and R. Cammi, *Chemical Reviews*, 2005, **105**, 2999–3094.

[67] R. Jinnouchi and a. B. Anderson, *J. Phys. Chem. C*, 2008, **112**, 8747–8750.

[68] M. M. Montemore, O. Andreussi and J. W. Medlin, *The Journal of Chemical Physics*, 2016, **145**, 074702.

[69] H.-f. Wang and Z.-p. Liu, *The Journal of Physical Chemistry C*, 2009, **113**, 17502–17508.

[70] T. He, F. Pan, Z. Xi, X. Zhang, H. Zhang, Z. Wang, M. Zhao, S. Yan and Y. Xia, *Journal of Physical Chemistry C*, 2010, **114**, 9234–9238.

[71] J.-L. Fattebert and F. Gygi, *Journal of computational chemistry*, 2002, **23**, 662–6.

[72] J. L. Fattebert and F. Gygi, *International Journal of Quantum Chemistry*, 2003, **93**, 139–147.

[73] K. Mathew, R. Sundararaman, K. Letchworth-Weaver, T. a. Arias and R. G. Hennig, *The Journal of chemical physics*, 2014, **140**, 084106.

[74] M. Garcia-Ratés and N. López, *Journal of Chemical Theory and Computation*, 2016, **12**, 1331–1341.

[75] D. Gunceler, K. Letchworth-Weaver, R. Sundararaman, K. a. Schwarz and T. a. Arias, *Modelling and Simulation in Materials Science and Engineering*, 2013, **21**, 074005.

[76] S. A. Petrosyan, A. A. Rigos and T. A. Arias, *The journal of physical chemistry. B*, 2005, **109**, 15436–44.

[77] W.-J. Yin, M. Krack, B. Wen, S.-Y. Ma and L.-M. Liu, *The Journal of Physical Chemistry Letters*, 2015, **6**, 2538–2545.

[78] O. Andreussi, I. Dabo and N. Marzari, *Journal of Chemical Physics*, 2012, **136**, 064102.

[79] R. Jinnouchi and A. Anderson, *Physical Review B*, 2008, **77**, 245417.

[80] M. Faheem, S. Suthirakun and A. Heyden, *The Journal of Physical Chemistry C*, 2012, **116**, 22458–22462.

[81] S. Behtash, J. Lu, M. Faheem and A. Heyden, *Green Chemistry*, 2014, **16**, 605.

[82] S. Behtash, J. Lu, E. Walker, O. Mamun and A. Heyden, *Journal of Catalysis*, 2016, **333**, 171–183.

[83] S. Behtash, J. Lu, O. Mamun, C. T. Williams, J. R. Monnier and A. Heyden, *The Journal of Physical Chemistry C*, 2016, **120**, 2724–2736.

[84] H. Dong, B. Lin, K. Gilmore, T. Hou, S.-T. Lee and Y. Li, *Journal of Power Sources*, 2015, **299**, 371–379.

[85] S. Steinmann, P. Sautet and C. MICHEL, *Phys. Chem. Chem. Phys.*, 2016.

[86] A. Fortunelli, W. a. Goddard, Y. Sha, T. H. Yu, L. Sementa, G. Barcaro and O. Andreussi, *Angewandte Chemie - International Edition*, 2014, **53**, 6669–6672.

[87] *Jaguar, Schrodinger, LLC, New York, NY*, 2007.

[88] Y. Sha, T. H. Yu, Y. Liu, B. V. Merinov and W. a. Goddard, *The Journal of Physical Chemistry Letters*, 2010, **1**, 856–861.

[89] Y. Sha, T. H. Yu, B. V. Merinov, P. Shirvanian and W. a. Goddard, *The Journal of Physical Chemistry Letters*, 2011, **2**, 572–576.

[90] Y. Sha, T. H. Yu, B. V. Merinov and W. a. Goddard, *ACS Catalysis*, 2014, **4**, 1189–1197.

[91] J. a. Keith, G. Jerkiewicz and T. Jacob, *Chemphyschem : a European journal of chemical physics and physical chemistry*, 2010, **11**, 2779–94.

[92] T. Jacob and W. a. Goddard, *Chemphyschem : a European journal of chemical physics and physical chemistry*, 2006, **7**, 992–1005.

[93] I. T. McCrum and M. J. Janik, *Journal of Physical Chemistry C*, 2016, **120**, 457–471.

[94] S. Sakong and A. Groß, *ACS Catalysis*, 2016, **6**, 5575–5586.

[95] S. N. Steinmann, C. Michel, R. Schwiedernoch and P. Sautet, *Phys. Chem. Chem. Phys.*, 2015, **17**, 13949–13963.

[96] N. Lespes and J. S. Filhol, *Journal of Chemical Theory and Computation*, 2015, **11**, 3375–3382.

[97] G. Kresse and J. Furthmüller, *Physical review. B, Condensed matter*, 1996, **54**, 11169–11186.

[98] G. Kresse and J. Furthmüller, *Computational Materials Science*, 1996, **6**, 15–50.

[99] S. Ismail-Beigi and T. a. Arias, *Computer Physics Communications*, 2000, **128**, 1–45.

[100] M. Valiev, E. J. Bylaska, N. Govind, K. Kowalski, T. P. Straatsma, H. J. J. Van Dam, D. Wang, J. Nieplocha, E. Apra, T. L. Windus and W. a. De Jong, *Computer Physics Communications*, 2010, **181**, 1477–1489.

[101] A. Klamt and G. Schüürmann, *Journal of the Chemical Society-Perkin Transactions 2*, 1993, 799–805.

[102] R. Sundararaman, K. Letchworth-Weaver, K. Schwarz and A. TA, 2012, http://jdftx.sourceforge.net/.

[103] T. Arias, M. Payne and J. Joannopoulos, *Physical Review Letters*, 1992, **69**, 1077–1080.

[104] A. Phatak and W. Delgass, *The Journal of Physical Chemistry C*, 2009, **113**, 7269–7276.

[105] P. Boski and N. López, *Journal of Physical Chemistry C*, 2012, **116**, 15484–15492.

[106] P. J. Feibelman, B. Hammer, F. Wagner, M. Scheffler, R. Stumpf, R. Watwe and J. Dumesic, *The Journal of Physical Chemistry B*, 2001, **105**, 4018–4025.

[107] T. Jacob, R. P. Muller and W. a. Goddard, *Journal of Physical Chemistry B*, 2003, **107**, 9465–9476.

[108] T. Jacob and W. a. Goddard, *The journal of physical chemistry. B*, 2005, **109**, 297–311.

[109] T. Jacob, *Fuel Cells*, 2006, **6**, 159–181.

[110] J. P. Perdew, K. Burke, M. Ernzerhof, D. of Physics and N. O. L. . J. Quantum Theory Group Tulane University, *Physical Review Letters*, 1996, **77**, 3865–3868.

[111] W. R. Wadt and P. J. Hay, *The Journal of Chemical Physics*, 1985, **82**, 284–298.

[112] G. Kresse and D. Joubert, *Physical Review B*, 1999, **59**, 1758–1775.

[113] D. Vanderbilt, *Physical Review B*, 1990, **41**, 7892–7895.

[114] K. F. Garrity, J. W. Bennett, K. M. Rabe and D. Vanderbilt, *Computational Materials Science*, 2014, **81**, 446–452.

[115] http://www.physics.rutgers.edu/ dhv/uspp/.

[116] Y. Ozhabes, D. Gunceler and T. a. Arias, *arXiv*, 2015, **1504.05799**, 1–7.

[117] K. Momma and F. Izumi, *Journal of Applied Crystallography*, 2011, **44**, 1272–1276.

[118] M. Methfessel and A. T. Paxton, *Physical Review B*, 1989, **40**, 3616–3621.

[119] E. Aprà and A. Fortunelli, *The Journal of Physical Chemistry A*, 2003, **107**, 2934–2942.

[120] D. A. Daramola and G. G. Botte, *Journal of Colloid and Interface Science*, 2013, **402**, 204–214.

[121] R. Blanco and J. Orts, *Electrochimica Acta*, 2008, **53**, 7796–7804.

[122] G. Cui, S. Song, P. K. Shen, A. Kowal and C. Bianchini, *The Journal of Physical Chemistry C*, 2009, **113**, 15639–15642.

[123] I. Katsounaros, W. B. Schneider, J. C. Meier, U. Benedikt, P. U. Biedermann, A. Cuesta, A. a. Auer and K. J. J. Mayrhofer, *Physical chemistry chemical physics : PCCP*, 2013, **15**, 8058–68.

[124] A. Klamt, V. Jonas, T. Bürger and J. C. W. Lohrenz, *The Journal of Physical Chemistry A*, 1998, **102**, 5074–5085.

[125] S. A. Petrosyan, J. F. Briere, D. Roundy and T. A. Arias, *Physical Review B - Condensed Matter and Materials Physics*, 2007, **75**, 1–6.

[126] R. Sundararaman and T. A. Arias, *Computer Physics Communications*, 2014, **185**, 818–825.

[127] A. Schäfer, A. Klamt, D. Sattel, J. C. W. Lohrenz and F. Eckert, *Physical Chemistry Chemical Physics*, 2000, **2**, 2187–2193.

[128] K. Dhar and C. Cavallotti, *The journal of physical chemistry. A*, 2014, **118**, 8676–88.

[129] D. Ford, Y. Xu and M. Mavrikakis, *Surface Science*, 2005, **587**, 159–174.

[130] a. Eichler, F. Mittendorfer and J. Hafner, *Physical Review B*, 2000, **62**, 4744–4755.

[131] S. Meng, E. Wang and S. Gao, *Physical Review B*, 2004, **69**, 195404.

[132] C. Amovilli and B. Mennucci, *The Journal of Physical Chemistry B*, 1997, **101**, 1051–1057.

[133] A. Ben-Naim and Y. Marcus, *The Journal of Chemical Physics*, 1984, **81**, 2016.

[134] A. V. Marenich, C. J. Cramer and D. G. Truhlar, *The journal of physical chemistry. B*, 2009, **113**, 6378–96.

[135] B. B. Xiao, Y. F. Zhu, X. Y. Lang, Z. Wen and Q. Jiang, *Scientific Reports*, 2014, **4**, 5205.

[136] J. a. Keith and T. Jacob, *Angewandte Chemie - International Edition*, 2010, **49**, 9521–9525.

[137] X. Q. Gong, P. Hu and R. Raval, *Journal of Chemical Physics*, 2003, **119**, 6324–6334.

[138] C. Morin, D. Simon and P. Sautet, *Journal of Physical Chemistry B*, 2003, **107**, 2995–3002.

[139] T. Sheng, Y. J. Qi, X. Lin, P. Hu, S. G. Sun and W. F. Lin, *Chemical Engineering Journal*, 2016, **293**, 337–344.

[140] R. Peköz, K. Johnston and D. Donadio, *Journal of Physical Chemistry C*, 2014, **118**, 6235–6241.

[141] M. D. Rasmussen, L. M. Molina and B. Hammer, *Journal of Chemical Physics*, 2004, **120**, 988–997.

[142] Johnson III, R, *NIST Computational Chemistry Comparison and Benchmark Database, NIST Standard Reference Database Number 101*, Release 17b September, 2015, http://cccbdb.nist.gov/.

[143] J. Andzelm, C. Kolmel and A. Klamt, *The Journal of Chemical Physics*, 1995, **103**, 9312.

[144] Y. H. Jang, W. A. G. Iii, K. T. Noyes and L. C. Sowers, *J. Phys. Chem. B*, 2003, **107**, 344–357.

[145] R. F. Bader, *Atoms in molecules: a quantum theory*, 1990.

[146] G. Henkelman, A. Arnaldsson and H. Jónsson, *Computational Materials Science*, 2006, **36**, 354–360.

[147] Y.-H. Fang and Z.-P. Liu, *Surface Science*, 2015, **631**, 42–47.

[148] S. Chibani, C. Michel, F. Delbecq, C. Pinel and M. Besson, *Catalysis Science & Technology*, 2013, **3**, 339–350.

[149] D. Loffreda, C. Michel, F. Delbecq and P. Sautet, *Journal of Catalysis*, 2013, **308**, 374–385.

[150] V. S. Bryantsev, M. S. Diallo and W. a. Goddard, *The journal of physical chemistry. B*, 2008, **112**, 9709–19.

[151] R. Jinnouchi, K. Kodama and Y. Morimoto, *Journal of Electroanalytical Chemistry*, 2014, **716**, 31–44.

[152] D. D. Hibbitts and M. Neurock, *Journal of Catalysis*, 2013, **299**, 261–271.

[153] J. G. Wang and B. Hammer, *The Journal of Chemical Physics*, 2006, **124**, 184704.

[154] M. Osawa, K. I. Komatsu, G. Samjeské, T. Uchida, T. Ikeshoji, A. Cuesta and C. Gutiérrez, *Angewandte Chemie - International Edition*, 2011, **50**, 1159–1163.

[155] W. Gao, J. a. Keith, J. Anton and T. Jacob, *Journal of the American Chemical Society*, 2010, **132**, 18377–18385.

[156] W. Gao, J. A. Keith, J. Anton and T. Jacob, *Dalton transactions (Cambridge, England : 2003)*, 2010, **39**, 8450–8456.

[157] C. Hu, S.-W. Ting, K.-Y. Chan and W. Huang, *International Journal of Hydrogen Energy*, 2012, **37**, 15956–15965.

[158] H.-F. Wang and Z.-P. Liu, *Journal of the American Chemical Society*, 2008, **130**, 10996–1004.

[159] P. Ferrin, D. Simonetti, S. Kandoi, E. Kunkes, J. a. Dumesic, J. K. Nø rskov and M. Mavrikakis, *Journal of the American Chemical Society*, 2009, **131**, 5809–15.

[160] J. E. Sutton and D. G. Vlachos, *Industrial & Engineering Chemistry Research*, 2015, **54**, 4213–4225.

[161] T. Sheng, W.-F. Lin, C. Hardacre and P. Hu, *Physical chemistry chemical physics : PCCP*, 2014, **16**, 13248–54.

[162] R. Alcalá, M. Mavrikakis and J. a. Dumesic, *Journal of Catalysis*, 2003, **218**, 178–190.

[163] J. A. Herron, Y. Morikawa and M. Mavrikakis, *Proceedings of the National Academy of Sciences*, 2016, **113**, E4937–E4945.

[164] L. C. Grabow, A. A. Gokhale, S. T. Evans, J. a. Dumesic and M. Mavrikakis, *Journal of Physical Chemistry C*, 2008, **112**, 4608–4617.

[165] A. Fortunelli, W. a. Goddard III, L. Sementa and G. Barcaro, *Nanoscale*, 2015, **7**, 4514–4521.

[166] Z. Zuo, L. L. Sun, W. Huang, P. Han and Z. Li, *Applied Catalysis A: General*, 2010, **375**, 181–187.

Appendix E

Supporting Information - Evaluating Solvent Effects at the Aqueous/Pt(111) Interface

We have performed several tests in order to verify that our simulation parameters were reasonably converged. We compared a cutoff energy of 450 eV and 800 eV in VASP for the calculating the adsorption energies in the presence of implicit solvation using VASPsol in Table E.1. The results show that a cutoff energy of 450 eV was sufficient to obtain converged adsorption energies compared to a cutoff energy of 800 eV. The mean absolute difference in adsorption energies was 0.04 eV between the two cutoff energies.

Table E.1: Adsorption energies (in eV) of different species calculated with VASPsol at two cutoff energies.

Adsorbate	**450 eV**	**800 eV**
C	-3.51	-3.47
S	-2.49	-2.45
N	0.42	0.46
OH	-2.10	-2.06
CH	-6.55	-6.51
CH_2	-4.04	-4.02
CH_3	-1.97	-1.93
NH	-4.04	-4.00
NH_2	-2.47	-2.43
NH_3	-1.17	-1.14
NO	-1.73	-1.69
CO	-1.77	-1.73
$C_6H_5CH_3$	-0.99	-0.94
$CH_3CHOHCH_3$	-0.28	-0.18

Adsorption energies for select adsorbates in vacuum and in the presence of an implicit water solvent using different k-point meshes with VASP are shown in Table E.2. The mean absolute difference in the adsorption energies calculated using 3x3x1 and 4x4x1 kpoints in vacuum (implicit water) was 0.02 eV (and 0.01 eV). The largest difference in adsorption energy using 3x3x1 and 4x4x1 meshes was 0.02 eV (for H_2O adsorption in vacuum). The mean absolute difference in the adsorption energies for 3x3x1 and 5x5x1 meshes in vacuum (implicit solvent) was 0.04 eV (0.05 eV). The largest difference in adsorption energy using 3x3x1 and 5x5x1 meshes was 0.08 eV for the adsorption of O_2 in both vacuum and implicit

water. The adsorption energies calculated using 3x3x1 kpoints are close to results with denser k-point meshes of 4x4x1 or 5x5x1, and we used a 3x3x1 k-point mesh in our work.

Table E.2: Adsorption energies (in eV) in vacuum and implicit solvation calculated using different k-point meshes with VASP.

	3x3x1		**4x4x1**		**5x5x1**	
	vacuum	**implicit**	**vacuum**	**implicit**	**vacuum**	**implicit**
O_2*	-0.50	-0.55	-0.49	-0.54	-0.58	-0.63
H_2O*	-0.22	-0.28	-0.20	-0.28	-0.24	-0.32
HCOOH*	-0.30	-0.13	-0.29	-0.13	-0.33	-0.17

We also analyzed the ground spin states of the Pt clusters in our work. Jacob et al.[1,2] reported a ground state spin of 7 and 11 for Pt_{19} and Pt_{35} clusters respectively. In our work however, we found the ground state spin to be 3, 3, 8 for Pt_{10}, Pt_{19}, Pt_{35} clusters, respectively. The reason for the discrepancy between our work and Jacob et al. is due to the use of different exchange correlation functional. Indeed, when we calculated the ground state spin using the B3LYP functional, we obtained the same ground state spin as reported by Jacob et al. (see Table E.3). The PBE exchange correlation functional results in a lower number of unpaired electrons compared to the B3LYP functional.

Table E.3: Total energies (in Hartree) of Pt(111) clusters calculated using the B3LYP and PBE exchange-correlation functionals at different spin states.

	B3LYP			**PBE**		
Spin	Pt_{10}	Pt_{19}	Pt_{35}	Pt_{10}	Pt_{19}	Pt_{35}
0				-1191.81461	-2264.79137	-4172.49455
1				-1191.82152	-2264.79395	-4172.50045
2	-1191.68091	-2264.40638		-1191.82515	-2264.79796	-4172.50151
3	-1191.67962	-2264.41584		**-1191.82887**	**-2264.80045**	-4172.50202
4	**-1191.68966**	-2264.40653		-1191.82194	-2264.79675	-4172.50406
5	-1191.67207	-2264.42855		-1191.80154	-2264.79418	-4172.50476
6		-2264.44144	-4171.69263	-1191.78142	-2264.79433	-4172.50370
7		**-2264.44441**	-4171.68917	-1191.72688	-2264.79329	-4172.50461
8		-2264.41614	-4171.68969	-1191.66854	-2264.77913	**-4172.50685**
9		-2264.40173	-4171.70272	-1191.60809	-2264.76554	-4172.50590
10		-2264.39599	-4171.71023	-1191.50996	-2264.74285	-4172.50365
11		-2264.34428	**-4171.71385**	-1191.38606	-2264.70800	-4172.50054
12			-4171.71719	-1191.23851	-2264.64891	-4172.49674
13			-4171.70949	-1191.06966	-2264.58995	-4172.49328
14			-4171.69654	-1190.89787	-2264.52255	-4172.48228
15			-4171.68175	-1190.69546	-2264.45514	-4172.46647
16				-1190.47622	-2264.36477	-4172.44579

Table E.4: Solvation energies of free adsorbate ($\Delta E_{solv}(X)$) using three different solvation models. All three solvation models show comparable solvation energies.

	VASP	**NWChem**	**JDFTx**
H_2	0.00	0.04	0.00
O_2	0.01	0.04	0.01
C_2	0.00	0.03	0.01
S_2	0.01	0.05	0.01
N_2	0.00	0.04	0.00
OH	-0.21	-0.14	-0.20
CH	-0.15	-0.05	-0.14
CH_2	-0.03	-0.01	-0.03
CH_3	-0.01	0.01	-0.01
NH	-0.10	-0.08	-0.10
NH_2	-0.17	-0.16	-0.22
NH_3	-0.18	-0.18	-0.18
NO	0.00	0.03	0.00
CO	-0.01	0.03	-0.01
O_2	0.02	0.04	0.02
H_2O	-0.31	-0.26	-0.31

Figure E.1 shows the different adsorption sites that were used in our work over the Pt_{35} cluster. We have provided a summary of our adsorption results in Table E.5. Adsorbate sites were taken from literature sources. Adsorption energies in vacuum (ΔE_{ads}^{vac}), calculated Bader charges (q) of adsorbates, solvation energies of adsorbed species ($\Delta E_{solv}(X*)$), solvation energies of unadsorbed species ($\Delta E_{solv}(X)$), and adsorption solvation energies ($\Delta\Delta E_{ads}^{solv}$) are all provided.

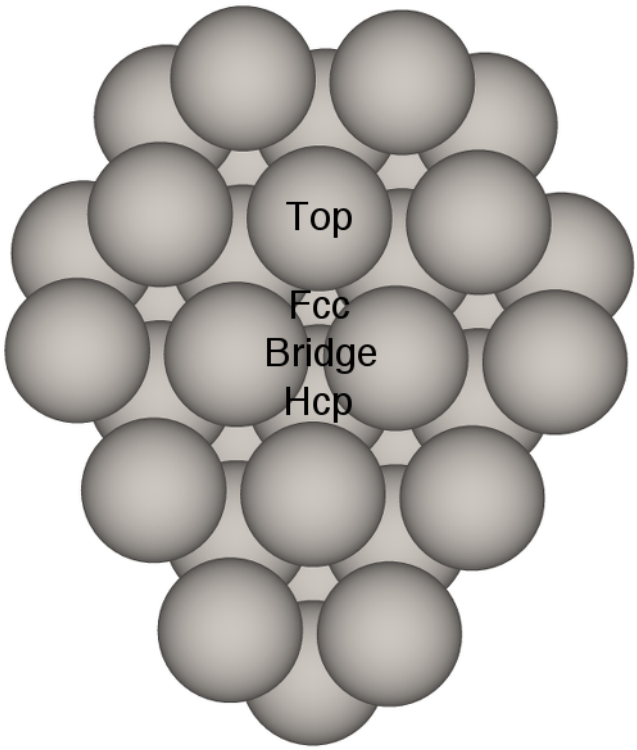

Figure E.1: Pt_{35} cluster model of the Pt(111) surface showing the top, fcc, bridge, and hcp adsorption sites.

Table E.5: A summary of adsorbate states and properties as calculated in our work. All energies are in eV, except for the calculated Bader charge (q).

Category	**Adsorbates**	**Adsorption site**	ΔE_{ads}^{vac}	**q**	$\Delta E_{solv}(X*)$	$\Delta E_{solv}(X)$	$\Delta\Delta E_{ads}^{solv}$
	O	fcc[3]	-1.10	-0.69	0.03	0.01	-0.02
	N	fcc[3]	0.43	-0.59	0.03	0.00	-0.01
I	C	fcc[3]	-3.51	-0.23	0.04	0.00	0.00
	S	fcc[3]	-2.46	-0.11	0.03	0.01	-0.02
	H	top[3]	-0.39	0.07	0.03	0.00	-0.01
---	---	---	---	---	---	---	---
	O_2	bridge[4]	-0.50	-0.54	0.01	0.02	-0.05
	NO	fcc[3]	-1.72	-0.41	0.02	0.00	-0.01
II	CO	fcc[3]	-1.73	-0.22	0.00	-0.01	-0.04
	CO_2	phyisorbed[5]	-0.01	-0.01	-0.07	-0.11	0.01
	CH_4	phyisorbed[5]	-0.01	0.02	0.03	0.02	-0.02
---	---	---	---	---	---	---	---
	$HCOO_M$	bridge[6]	-1.56	-0.46	-0.13	-0.20	0.03
	$HCOO_B$	bridge[6]	-2.52	-0.39	-0.08	-0.20	0.09
	OH	top[3]	-2.14	-0.36	-0.10	-0.21	0.07
	OOH	top[7]	-1.06	-0.29	-0.17	-0.32	0.10
	NH	fcc[3]	-3.98	-0.29	-0.13	-0.10	-0.07
	CHCO	fcc[8]	-3.38	-0.10	-0.06	-0.12	0.02
III	COOH	top[6]	-2.69	-0.08	-0.11	-0.35	0.20
	CH	fcc[3]	-6.64	-0.07	-0.01	-0.15	0.10
	CH_3	top[3]	-1.95	0.00	0.02	-0.01	-0.01
	NH_2	bridge[3]	-2.38	0.01	-0.21	-0.17	-0.08
	CH_2	bridge[3]	-4.03	0.02	-0.01	-0.03	-0.02
	CH_2CO	bridge[8]	-1.41	0.05	-0.08	-0.10	-0.01
	CH_3CO	top[8]	-2.22	0.09	-0.06	-0.13	0.03
---	---	---	---	---	---	---	---
	HCOOH	top[9]	-0.30	0.10	-0.13	-0.34	0.17
	CH_3COOH	top[9]	-0.34	0.13	-0.13	-0.32	0.15
	CH_3OH	top[10]	-0.24	0.17	-0.22	-0.20	-0.06
	CH_3CH_2OH	top[8]	-0.23	0.18	-0.19	-0.18	-0.04
IV	$CH_3CHOHCH_3$	top[11]	-0.24	0.19	-0.18	-0.17	-0.04
	CH_3COCH_3	top[11]	-0.10	0.22	-0.33	-0.20	-0.17
	$3H_2O$	top[12]	-0.41	0.22	-0.14	-0.31	0.14
	$2H_2O$	top[12]	-0.36	0.24	-0.21	-0.31	0.06
	H_2O	top[12]	-0.22	0.26	-0.34	-0.31	-0.06
	NH_3	top[3]	-0.85	0.39	-0.47	-0.18	-0.32
---	---	---	---	---	---	---	---
	C_6H_6	bridge[13]	-0.79	0.40	-0.30	-0.05	-0.29
V	$C_6H_5CH_3$	bridge	-0.67	0.41	-0.32	-0.05	-0.32
	$C_6H_5NH_2$	bridge	-0.88	0.63	-0.64	-0.24	-0.44

In order to assess the solvation effects of a hydrogen bonding species (OH*) in the presence of explicit water, we modeled a Pt surface with four ice-bilayers, similar to previous work.[14–16] An ice-bilayer consisted of a hexagonal hydrogen-bonded network of water molecules, where the water molecules have their molecular planes lying either parallel or perpendicular to metal surface in an alternating pattern. A common approach of modeling ice-bilayer solvation is by using an ice-bilayer structure where the O-H bonds of water point away from the surface as shown in Figure E.2.[16,17] To solvate OH*, one of the water molecules with its molecular plane lying perpendicular to the surface was replaced by OH since this geometry was 0.25 eV more stable than when OH replaced the water molecule that lies with its molecular plane parallel to the surface. OH* replaces a water molecule in the first bilayer because the OH* prefers a Pt top site, which is where the water molecules also adsorb. Our model had 24 water molecules, and the adsorption energy in the presence of explicit solvation, similar to previous work,[18] becomes the following.

$$\Delta E_{ads}^{exp} = E_{OH*[23H_2O]} + 1/24(E_{*[24H_2O]} - E_*) - E_{*[24H_2O]} - E_{OH^{imp}}$$

In this equation $E_{OH*[23H_2O]}$ is the energy of OH* solvated by the ice-bilayers which contain 23 water molecules, $1/24(E_{*[24H_2O]} - E_*)$ is the average energy of a solvated water molecule in an adsorbed ice-bilayer, $E_{*[24H_2O]}$ is the energy of an adsorbed ice-bilayer with 24 water molecules, and $E_{OH^{imp}}$ is the energy of implicitly solvated free OH. The second term in the above equation, $1/24(E_{*[24H_2O]} - E_*)$, contains the energy of four adsorbed ice-bilayers ($E_{*[24H_2O]}$) minus the energy of a clean surface without any adsorbed molecules (E_*). This term gives the average energy of an adsorbed solvent water molecule. The difference between ΔE_{ads}^{exp} - ΔE_{ads}^{vac} is the explicit adsorption solvation energy.

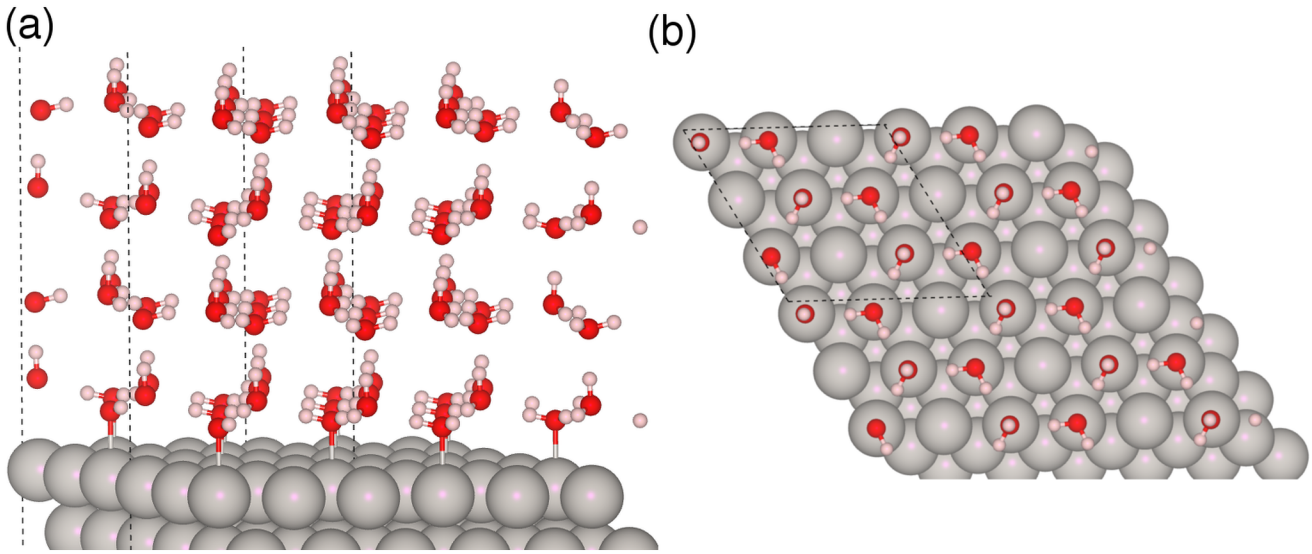

Figure E.2: Four ice-bilayers adsorbed on Pt(111) in side (a) and top (b) views. Dotted lines represent the unit cell. Periodic images are shown to visualize the hydrogen bonding network. Pt, O, and H atoms are shown as gray, red, and white spheres, respectively.

Bibliography

[1] T. Jacob and W. a. Goddard, *The journal of physical chemistry. B*, 2005, **109**, 297–311.

[2] T. Jacob, R. P. Muller and W. a. Goddard, *Journal of Physical Chemistry B*, 2003, **107**, 9465–9476.

[3] D. Ford, Y. Xu and M. Mavrikakis, *Surface Science*, 2005, **587**, 159–174.

[4] a. Eichler, F. Mittendorfer and J. Hafner, *Physical Review B*, 2000, **62**, 4744–4755.

[5] C. Shi, C. P. O'Grady, A. a. Peterson, H. a. Hansen and J. K. Nørskov, *Physical chemistry chemical physics : PCCP*, 2013, **15**, 7114–22.

[6] C. Hu, S.-W. Ting, K.-Y. Chan and W. Huang, *International Journal of Hydrogen Energy*, 2012, **37**, 15956–15965.

[7] T. Jacob and W. a. Goddard, *Chemphyschem : a European journal of chemical physics and physical chemistry*, 2006, **7**, 992–1005.

[8] R. Alcalá, M. Mavrikakis and J. a. Dumesic, *Journal of Catalysis*, 2003, **218**, 178–190.

[9] M. Salciccioli, S. M. Edie and D. G. Vlachos, *Journal of Physical Chemistry C*, 2012, **116**, 1873–1886.

[10] S. K. Desai, M. Neurock and K. Kourtakis, *Journal of Physical Chemistry B*, 2002, **106**, 2559–2568.

[11] C. Michel, J. Zaffran, A. M. Ruppert, J. Matras-Michalska, M. Jedrzejczyk, J. Grams and P. Sautet, *Chem. Commun.*, 2014, **50**, 12450–12453.

[12] L. Árnadóttir, E. M. Stuve and H. Jónsson, *Surface Science*, 2012, **606**, 233–238.

[13] C. Morin, D. Simon and P. Sautet, *Journal of Physical Chemistry B*, 2003, **107**, 2995–3002.

[14] J. Rossmeisl, J. K. Nø rskov, C. D. Taylor, M. J. Janik and M. Neurock, *The journal of physical chemistry. B*, 2006, **110**, 21833–21839.

[15] D. D. Hibbitts and M. Neurock, *Journal of Catalysis*, 2013, **299**, 261–271.

[16] C. J. Bodenschatz, S. Sarupria and R. B. Getman, *The Journal of Physical Chemistry C*, 2015, **119**, 13642–13651.

[17] K.-Y. Yeh, S. a. Wasileski and M. J. Janik, *Physical chemistry chemical physics : PCCP*, 2009, **11**, 10108–10117.

[18] V. Tripković, E. Skúlason, S. Siahrostami, J. K. Nø rskov and J. Rossmeisl, *Electrochimica Acta*, 2010, **55**, 7975–7981.